

**Evolutionary Algorithm Simulation Study of MnO₂
Nanoclusters**

by

PHALA WESLEY MASOGA

THESIS

submitted in fulfilment of the requirements for the degree of

DOCTOR OF PHILOSOPHY

in

Physics

in the

FACULTY OF SCIENCE AND AGRICULTURE

(School of Physical and Mineral Sciences)

at the

University of Limpopo

Supervisor: Prof. H.R. Chauke

Co-Supervisor: Prof. P.E. Ngoepe

2023

DECLARATION

I declare that the thesis hereby submitted to the University of Limpopo (Turfloop Campus) for the degree of Doctor of Philosophy (PhD) has not previously been submitted by me for a degree at this or any other university; that it is my work both in design and execution, and that all material contained herein has been duly acknowledged.

Signature

A handwritten signature in black ink, appearing to read 'P.W. Masoga', enclosed within a large, loopy oval flourish.

Mr P.W. Masoga

Date: 14 / 04 / 2023

Acknowledgements

The research study presented in this Ph.D. thesis was carried out under the supervision of Prof. H.R. Chauke and Prof. P.E. Ngoepe from the Materials Modelling Centre at the University of Limpopo. My gratitude also goes to Sir Prof. C.R.A. Catlow and the research group at the University College London in the United Kingdom for their assistance. A special thanks goes to my main supervisor Prof. H.R. Chauke for the exceptional support provided to me throughout this study.

I would also like to recognise my Masters supervisor Prof. R.R. Maphanga from the Council for Scientific and Industrial Research (CSIR) for the knowledge she imparted on me during the Masters portion of this study. Additionally, I would like to thank all my fellow researchers at the MMC for the support and input they have given me towards the completion of this study.

I offer my gratitude to the National Research Foundation (NRF) for the financial support provided to me and the University of Limpopo for its financial support. My thanks also go to the Centre for High Performance Computing in Cape Town for their computational resources utilised towards the successful completion of this study. The authors also acknowledge the support provided by the Titanium Centre of Competence (TiCoC), and the Royal Society Advanced Fellowship Newton Grant (NA140447). The support of the South African Research Chair Initiative of the Department of Science and Innovation is also appreciated.

I would like to give a special thanks to my mother **Lisbeth Masoga** and the whole Masoga family for supporting me throughout this study.

Dedication

This Ph.D. study is dedicated to the whole **Masoga** family for their unwavering support and encouragement towards the completion of this research study for my PhD.

This work is also dedicated to my beloved wife **Dimakatso Masoga** and my first-born son **Tshephiso Gift Masoga**.

In memory of my loving Father; **Madidimalo Stephen Masoga** who passed on in 2018. Rest in peace Mothokoa. Thank you for the unwavering support and encouragement.

Abstract

Transition metal-oxides have garnered significant attention due to their different allotropic polymorphs with unique structural and electronic properties necessary for the creation of new and improved rechargeable battery systems. The increasing demand for rechargeable batteries with high energy densities has fuelled interest in the research, development and manufacturing of new battery systems capable of powering high-powered machinery as well as portable household appliances. These demands have led to the heavy reliance on non-renewable fossil fuels. Consequentially, these have resulted in the unavoidable environmental pollution, which has in turn led to dangerous climatic conditions and unwanted health threats to human beings hence the need for renewable energy.

Manganese dioxide is one of the most promising materials in rechargeable lithium-ion batteries. Specifically, pyrolusite ($\beta\text{-MnO}_2$) as the most stable and abundant polymorph of MnO_2 is selected for this purpose. In this study, evolutionary algorithm and first principle methods were used to generate $(\text{MnO}_2)_{n=2-20}$ nanoclusters. Firstly, the $\beta\text{-MnO}_2$ bulk structure was optimised using existing interatomic potentials (IP). The selected IP parameters successfully reproduced the $\beta\text{-MnO}_2$ bulk structure to within 0.43 % of experimental data.

The XRD patterns of the $\beta\text{-MnO}_2$ bulk structure were compatible to experimental data displaying similar peak intensities, 2θ positioning and Miller indexes such as the (110), (101), (200) and (211) peaks. The verified IP parameters were then used in conjunction with the Buckingham potential and the 12-6 Lennard-Jones potential to

generate subsets of stable nanoclusters using the Knowledge Led Master Code (KLMC) software.

A combination of global search techniques and density functional theory (DFT) based codes such as FHI-aims, CASTEP and VASP were used to refine the energy ordering of the generated nanoclusters in an effort to determine the global minima of the nanoclusters for all the concerned atomic sizes i.e., $n = 2$ to $n = 20$. The predicted order of stability for the nanoclusters was found to be similar to those predicted for isostructural ZrO_2 , SiO_2 and TiO_2 nanoclusters. Furthermore, the larger stable nanoclusters adopted compact ring configurations as they grew larger in atomic size. Additionally, they displayed improved stability and electrical conductivity as seen by the shorter band-gap energy of 0.113 eV for the stable n_{20} nanocluster.

Secondly, the effect of temperature changes on the stability of the nanoclusters was investigated using the NVE ensemble in CASTEP and the molecular dynamics code DMol³. The nanoclusters showed a preference towards compact circular bonding configurations at higher temperatures as seen by the decreased bond lengths and inward bending of the exterior terminal oxygen atoms. An indirect relationship where the binding energy decreased with increasing temperatures was observed showing that high temperatures weakened the bonds in the n_{3-01} nanocluster.

The results also predicted that the nanoclusters have metallic characteristics with the density of states (DOS) curves being continuous at the Fermi level with minimal band-gaps between the valence and conduction bands indicating a good conductive nature. The XRD patterns for the most stable n_3 nanoclusters revealed common peaks such as the (001), (101) and (200) indicative of the tetragonal phase signifying the stable rutile β - MnO_2 . Moreover, the stable nanoclusters showed a prevalence towards a

cubic bonding configuration composed of two manganese atoms bonded to two oxygen atoms.

The atomistic substitutional doping technique proved to be a better strategy as compared to the virtual crystal approximation (VCA) technique using Fe, Co and Ni. The doping was preferential on the central manganese atom with the highest coordination denoted as Mn₂. Nickel was the most favourable dopant due to its better binding energy with smaller bond lengths. However, the cobalt-doped nanoclusters were shown to be the better electrical conductors even though they were not as stable as the nickel-doped nanoclusters. Dual doping with nickel and cobalt did not sufficiently improve the stability and conductivity of the smaller nanoclusters. However, the simultaneous doping using Fe, Co and Ni may succeed in improving the stability of the larger nanoclusters as compared to singular doping.

Lastly, the electronic charge density differences of the Ni-doped n₃-01 nanoclusters displayed considerable occurrences of covalent bonding. However, the weaker ionic bonding was observed with singular Fe-doping and Co-doping. The Ni-doped nanoclusters on the Mn₂ atomic position with the highest coordination had the highest voltage potential of 3.038 V showing that nickel is indeed the most preferable dopant. Fe-doped nanoclusters had the lowest potential below the Co-doped nanoclusters. Furthermore, all the doped nanoclusters had an operational voltage range between 2.7 V and 3.9 V showing their efficacy for energy storage.

The aims of the study were achieved hence the study can be considered a success. Recommendations are made to continue the work towards improving future rechargeable batteries.

Table of Contents

Declaration.....	ii
Acknowledgements.....	iii
Dedication.....	iv
Abstract.....	v
List of Figures	xv
List of Tables	xx
Chapter 1: Introduction.....	1
1.1. Background.....	1
The Ontologies of computer simulations in science research.....	6
1.2. Structural properties of pyrolusite (β -MnO ₂).....	7
1.3. Intentions of the Study	9
1.4. Motivation for the study.....	10
1.5. Research hypothesis.....	13
Research questions	13
1.6. Aim and objectives.....	14
1.7. Outline.....	15
Chapter 2: Literature review.....	18

2.1. Evolution of batteries	18
2.2. Metal oxide nanostructures.....	21
2.3. MnO ₂ nanostructures.....	24
2.4. Simulated nanoclusters	26
2.5. Doping of nanostructures.....	30
2.6. Electronic properties of nanostructures	32
Chapter 3: Methodology	34
3.1. Evolutionary algorithm.....	35
3.2. Atomistic potentials model	38
3.2.1. Long range interactions	39
3.2.2 Short range interactions.....	41
3.2.3 The atomistic potentials method	46
3.3. Density functional theory.....	48
3.3.1. Local density approximation	52
3.3.2. Generalised gradient approximation	54
3.4. Plane-wave pseudopotential method	56
3.4.1. Plane-wave basis.....	56
3.4.2. Pseudopotential approximation.....	58
3.5. Projector augmented-wave method	61
3.6. k-point sampling.....	63
3.7. Electronic properties of β -MnO ₂	65

3.8. Molecular dynamics	69
3.9. X-Ray diffraction spectroscopy	74
3.10. Binding energy and relative stability	76
3.11. Doping of the bulk structure and the nanoclusters	77
3.11.1. Virtual crystal approximation method	78
3.11.2. Substitutional method of doping	80
3.12. Charge density differences	81
3.12.1. Hirshfeld charges	83
3.12.2. Analysis of the Mulliken atomic populations	84
3.13. Implementation of computational software codes	87
3.13.1. GULP	87
3.13.2. Knowledge-Led Master Code	88
3.13.3. FHI-aims	90
3.13.4. Materials Studio	90
3.13.4.1 CASTEP	91
3.13.4.2 Reflex code	92
3.13.4.3 DMol ³ code	93
Chapter 4: β-MnO₂ bulk Structure	96
4.1. Convergence tests: cut-off energy and k-points	96
4.1.1. Cut-off energy	97
4.1.2. k-point mesh	98

4.1.3. Optimisation of the β -MnO ₂ bulk structure	101
4.2. X-Ray diffraction patterns for the bulk β -MnO ₂ structure.....	104
4.3. Effect of temperature on the stability of the bulk β -MnO ₂ structure	107
4.4. Doping of the β -MnO ₂ bulk structure	114
4.4.1. Virtual crystal approximation method.....	115
4.4.2. Substitutional method of doping.....	120
Chapter 5: Generation and stability of β-MnO₂ nanoclusters.....	127
5.1. Generation of the MnO ₂ nanoclusters	127
5.1.1. Energy landscape	128
5.1.2. Convergence parameters for the k-point mesh.....	129
5.2. Stability of the nanoclusters	132
5.3. Band-gap energy and Fermi energy	137
5.4. Density and binding energy.....	138
Chapter 6: Effect of temperature on the stability of the MnO₂ nanoclusters .	144
6.1. Bonding patterns.....	145
6.1.1. Bond lengths.....	150
6.1.2. Bond angles.....	154
6.2. Binding energy	156
6.3. Fermi energy.....	161
6.4. Band-gap energy	163
Chapter 7: X-Ray diffraction.....	166

7.1.1. X-Ray diffraction of the undoped n3 nanoclusters	166
7.1.2. XRD patterns of the n3-01 nanocluster at varying temperatures	171
7.1.3. XRD spectroscopy of the doped n3-01 nanoclusters	174
Chapter 8: The effect of doping on the electronic properties of MnO₂ nanoclusters	178
8.1. Doping of the n3-01 nanocluster	178
8.1.1. Preferred doping position	179
8.2.1. Iron doping of the n3-01 nanocluster	180
8.2.2. Cobalt doping of the n3-01 nanocluster	182
8.2.3. Nickel doping of the n3-01 nanocluster	184
8.3. Dual doping of the n3-01 nanocluster	188
8.4. Density of states of the doped n3-01 nanocluster	191
8.4.1. TDOS of the IP and DFT n3-01 nanocluster	192
8.4.2. TDOS of the Fe-doped n3-01 nanocluster	193
8.4.3. TDOS of the Co-doped n3-01 nanocluster	194
8.4.4. TDOS of the Ni-doped n3-01 nanocluster	195
8.4.5. Fermi energy	198
Chapter 9: Charge density differences	201
9.1. Undoped n3-01 nanocluster	201
9.2. Doped n3-01 nanocluster	203
9.2.1. Fe-doping	204

9.2.3. Co-doping	207
9.2.4. Ni-doping	209
9.3. Bond lengths	211
9.3.1. Effect of Fe-doping on bond lengths	212
9.3.2. Effect of Co-doping on bond lengths.....	215
9.3.3. Effect of Ni-doping on bond lengths.....	219
9.4. Electronic atomic orbital contributions.....	222
9.5. Voltage profiles of the n3-01 nanocluster.....	234
9.6. Charge density differences of the dual doped n3-01 nanocluster	241
Chapter 10.....	245
SUMMARY and CONCLUSIONS	245
Recommendations	253
Appendices	299
Appendix A	299
Appendix B1-1: Mn ₂ O ₄	300
Appendix B1-2: Mn ₃ O ₆	300
Appendix B1-3: Mn ₄ O ₈	300
Appendix B1-4: Mn ₅ O ₁₀	301
Appendix B1-5: Mn ₆ O ₁₂	301
Appendix B1-6: Mn ₇ O ₁₄	302
Appendix B1-7: Mn ₈ O ₁₆	302

Appendix B1-8: Mn ₉ O ₁₈	303
Appendix B1-9: Mn ₁₀ O ₂₀	303
Appendix B1-10: Mn ₁₁ O ₂₂	304
Appendix B1-11: Mn ₁₂ O ₂₄	304
Appendix B1-12: Mn ₁₃ O ₂₆	305
Appendix B1-13: Mn ₁₄ O ₂₈	305
Appendix B1-14: Mn ₁₅ O ₃₀	306
Appendix B1-15: Mn ₁₆ O ₃₂	306
Appendix B1-16: Mn ₁₇ O ₃₄	307
Appendix B1-17: Mn ₁₈ O ₃₆	307
Appendix B1-18: Mn ₁₉ O ₃₈	308
Appendix B1-19: Mn ₂₀ O ₄₀	308
Appendix C: Presentations, awards and publications	310
Local/National Conference Presentations.....	310
International Conference Presentations.....	311
Publications	312
Achievements	313
Awards.....	314

List of Figures

Figure 1: Pure β -MnO ₂ structure displaying bond lengths between the neighbouring manganese (purple) and oxygen (red) atoms	7
Figure 2: β -MnO ₂ bulk structure	8
Figure 3: Flow chart of the multi-stages used to investigate the nanoclusters of (MnO ₂) _n . Each rectangle represents an input/output for the codes employed: a script that calls GULP in stages 1 and 2, FHI AIMS in stages 3, 4 and 5 and lastly CASTEP in stage 3 and 5 [139, 140].....	37
Figure 4: Schematic representation of the shell model [157].....	41
Figure 5: Illustration showing the equilibrium distance of the Lennard-Jones potential [152].	44
Figure 6: Extract of a script used to generate the Mn _n O _{2n} ; (n=2) nanoclusters as employed in KLMC.....	47
Figure 7: Schematic illustration of all-electron potential (blue line) and pseudo-electron potential (red line) with the corresponding valence wavefunction (ψ_v) and pseudo-wave function (ψ_{pseudo}) [185].....	60
Figure 8: Band structure of (a) metal, (b) insulator and (c) semiconductor [195]....	67
Figure 9: Flow chart of the computational codes used and the properties measured	95
Figure 10: The plot for the total energy versus energy cut-off of the β -MnO ₂ bulk structure.	97
Figure 11: Plot for total energy vs k-points of the β -MnO ₂ bulk structure	100
Figure 12: Atomic arrangement of the DFT optimised β -MnO ₂ bulk structure displaying the Mn (purple) and O (red) atoms	103

Figure 13: XRD patterns comparing (a) simulated XRD patterns of the bulk β -MnO ₂ structure generated using the Reflex module and (b) an experimental study [241].	105
Figure 14: Plot illustrating the behaviour of the bulk structure with respect to increasing temperatures. The horizontal temperature scale is in the multiple of ten (K x 10).	108
Figure 15: Bond length from the central Mn atom to the exterior corner Mn atom of the β -MnO ₂ bulk structure drawn against temperature from 200 K to 1400 K	113
Figure 16: Comparison of energy landscape as determined by the Basin Hopping, Genetic Algorithm, CASTEP and GULP codes for the 20 most stable (MnO ₂) _{n=6} nanoclusters.....	128
Figure 17: Plot depicting the total energy of the increasing k-point separations...	131
Figure 18: A plot of the Density against the atomic number for all the generated nanoclusters (n = 2 - 20)	139
Figure 19: A plot for the Density against the total energy for all the generated nanoclusters.....	140
Figure 20: Band-gap energy plotted against the binding energy of the DFT optimised nanoclusters; n=2-20.....	141
Figure 21: A plot of the binding energies drawn against the atomic number	142
Figure 22: Illustration of the numberings of the atoms in the n ₃ -01 manganese dioxide nanocluster after optimisation with DFT optimisation	145
Figure 23: Bond length measurements of the n ₃ -01 nanocluster as the temperatures was varied from 200 K to 1400 K	153
Figure 24: Total Energies of the n ₃ -01 nanocluster drawn against the temperature ranging from 100 K to 1500 K.	158

Figure 25: Plot depicting the Binding energy vs Temperature of the most stable nanocluster consisting of 3 manganese atoms and 6 oxygen atoms ranging from 100 K to 1500 K.	160
Figure 26: Plot depicting the Fermi Energy vs Temperature of the most stable nanocluster consisting of 3 manganese atoms and 6 oxygen atoms ranging from 100 K to 1500 K.	161
Figure 27: Plot depicting the band-gap energy of the n3-01 nanocluster measured against increasing temperatures from 100 K to 1500 K.....	163
Figure 28: XRD patterns for the three most stable (MnO ₂) n=3 nanoclusters developed using IP techniques.	167
Figure 29: XRD pattern from a previous study by Augustine <i>et al.</i> [244] depicting different MnO _x species	168
Figure 30: XRD patterns of a rutile-type pyrolusite product synthesised from mixed manganese dioxide mixtures crystallised under acidic hydrothermal conditions [263].	169
Figure 31: XRD patterns of the n3-01 nanocluster optimised at varying temperatures from 200 K to 1400 K.	172
Figure 32: Extract from a study by McMurdie <i>et al.</i> [243] indicating the XRD pattern of an ore containing pyrolusite.	173
Figure 33: A comparison of the XRD patterns of the (a) undoped n3-01 nanocluster with XRD patterns of the n3-01 nanoclusters doped with (a) Fe, (b) Co and (d) Ni on the Mn ₂ atomic position.	175
Figure 34: The n3-01 nanocluster indicating the labelled atomic positions before doping	180

Figure 35: (a) The dual doped n3-01 nanocluster with Ni substituted on the Mn2 atomic position and Co substituted on the Mn1 atomic position, (b) The dual doped n3-01 nanocluster with Co substituted on the Mn2 atomic position and Ni substituted on the Mn1 atomic position. In-text labels distinguish the position of the atoms. . 189

Figure 36: The Total Density of States (TDOS) plot of A) The original n3-01 nanocluster generated by KLMC and B) The optimised n3-01 nanocluster by CASTEP..... 192

Figure 37: The Total Density of States (TDOS) plot of the Fe-doped n3-01 nanocluster substituted at A) The Mn1 atomic position and B) The Mn2 atomic position..... 194

Figure 38: The Total Density of States (TDOS) plot of the Co-doped n3-01 nanocluster substituted at A) The Mn1 atomic position and B) The Mn2 atomic position..... 195

Figure 39: The Total Density of States (TDOS) plot of the Ni-doped n3-01 nanocluster substituted at A) The Mn1 atomic position and B) The Mn2 atomic position 196

Figure 40: Total Density Of States (TDOS) of the most stable nanoclusters, (MnO₂); n = 2 atoms to n = 6 atoms..... 198

Figure 41: Charge density differences depiction of an undoped n3-01 nanocluster indicating the gain (blue) and loss (yellow) of electrons. The Mn1, Mn2 and Mn3 cations are labelled accordingly. 202

Figure 42: Charge density differences of the Fe-doped n3-01 nanocluster at (a) On the right fragment Mn1 and (b) The Central manganese position Mn2. Different angles are displayed to fully show the charge density difference regions. 206

Figure 43: Charge density differences of the Co-doped n3-01 nanocluster at (a) Mn1 and (b) Mn2..... 208

Figure 44: Charge density differences of the Ni-doped n3-01 nanocluster at (a) Mn1 and (b) Mn2.....	210
Figure 45: Depiction of the Fe-doped n3-01 nanocluster showing bond lengths doped at (a) Mn1 and (b) Mn2.....	212
Figure 46: Depiction of the Co-doped n3-01 nanocluster with labelled bond lengths at (a) Mn1 and (b) Mn2.....	216
Figure 47: Depiction of the Ni-doped n3-01 nanocluster at (a) Mn1 and (b) Mn2 with labelled bond lengths	220
Figure 48: End to end bond length of the exterior terminal oxygen atoms from the doped n3-01 nanocluster.....	230
Figure 49: Mulliken bond populations of the dopants compared per doping site..	231
Figure 50: Plot depicting the voltage profiles of the undoped β -MnO ₂ , the Fe-doped, Co-doped and Ni-doped bulk β -Mn ₂ O ₄ bulk structures.....	238
Figure 51: Plot depicting the voltage profiles of the undoped β -MnO ₂ , the Fe-doped, Co-doped and Ni-doped bulk β -Mn ₂ O ₄ bulk structures.....	239
Figure 52: Charge density differences of the simultaneous dual doping of the n3-01 nanocluster with Ni and Co. (a) The n3-01 nanocluster doped with Ni on the Mn2 atomic position and Co on the Mn1 atomic position. (b) The n3-01 nanocluster doped with Co on the Mn2 atomic position and Ni on the Mn1 atomic position.....	242
Figure 53: Close-up images of the interaction of the dopant impurities focusing on the type of bonds formed between oxygen with either Ni or Co	243
Figure 54: Original Bulk structure of β -MnO ₂	299
Figure 55: β -MnO ₂ bulk structure after optimisation to the ground state	299

List of Tables

Table 1: k-points at 500eV cut-off energy of the β -MnO ₂	99
Table 2: Comparison of the lattice parameters (Å), cell volume (Å ³), bond length (Å) and density (g/cm ³) of the bulk β -MnO ₂ Structure	102
Table 3: Binding Energy and Fermi Energy of the β -MnO ₂ Bulk structure ranging from 100 K to 1500 K	110
Table 4: Structural properties of the doped bulk β -MnO ₂ structures.....	115
Table 5: Depicted below in the table are the bulk structures doped with 10 % and 20 % of the dopants; iron, cobalt and nickel.....	118
Table 6: Substitutional doping of the β -MnO ₂ bulk structure on the central manganese atom	121
Table 7: Atomistic substitutional doping of the β -MnO ₂ bulk structure on the corner manganese atoms, 25 % of each making one whole atom	123
Table 8: Central and corner atomic substitutional doping of the manganese atoms displayed side-by-side for iron, cobalt and nickel dopants.	124
Table 9: Total Energies of the randomly selected nanocluster with varying k-point separations.....	130
Table 10: Suitable cell volumes determined to accurately minimise the nanoclusters to their most accurate ground state	132
Table 11: A display of the most stable nanoclusters (n =2 – 20) generated by the IP-based KLMC and optimised by the DFT-based CASTEP.	133
Table 12: Structural properties of the most stable nanocluster composed of 3 manganese atoms and 6 oxygen atoms focusing on the Binding and Fermi energies	146

Table 13: Comparison of the bond lengths in the n3-01 nanocluster calculated by IP and DFT techniques at varied temperatures ranging from 200 K to 1400 K.....	151
Table 14: Comparison of the bond angles in the n3-01 nanocluster optimised by IP and DFT techniques and calculated at varied temperatures from 200 K to 400 K.	155
Table 15: Total energies, binding energies, Fermi energies and the energy band-gap between the valence band edge and the conduction band edge with respect to the increasing temperature from 100 K to 1500 K.....	157
Table 16: Electronic properties of the pure and Fe-doped n3-01 nanocluster showing their Fermi energies, band-gap energies and binding energies.	181
Table 17: Electronic properties of the Co-doped n3-01 nanocluster	183
Table 18: Electronic properties of the Ni-doped n3-01 nanocluster.....	185
Table 19: Electronic properties of the dual-doped n3-01 nanocluster using the Ni- and Co- dopants.....	190
Table 20: Table indicating the values of the Density of States at Fermi level for the pure n3-01 nanocluster and the doped n3-01 nanoclusters	197
Table 21: Bond lengths of the atomic interactions present in the Fe-doped n3-01 nanocluster.....	214
Table 22: Bond lengths of the atomic interactions present in the Co-doped n3-01 nanocluster.....	217
Table 23: Bond lengths of the atomic interactions present in the Ni-doped n3-01 nanocluster.....	221
Table 24: Comparisons of the electronic contributions to the total atomic populations of the Fe-doped n3-01 nanocluster on site Mn1 and Mn2.	222

Table 25: Charge density differences of the Fe-doped n3-01 nanocluster substituted at the two atomic positions at Mn1 and Mn2 with their Hirshfeld and Mulliken charges	224
Table 26: Electronic contributions to the total atomic populations of the Co-doped n3-01 nanocluster on Mn1 and Mn2.....	225
Table 27: Charge density differences of the Co-doped n3-01 nanocluster substituted at the two atomic positions at Mn1 and Mn2 with their Hirshfeld and Mulliken charges	226
Table 28: Comparisons of the electronic contributions to the total atomic populations of the Ni-doped n3-01 nanocluster on the Mn1 and Mn2 sites.....	227
Table 29: Charge density differences of the Ni-doped n3-01 nanocluster substituted at the two atomic positions at Mn1 and Mn2 with their Hirshfeld and Mulliken charges	228
Table 30: Binding energies of all the structures	235
Table 31: Voltage profiles of the undoped, the Fe-doped, Co-doped and Ni-doped β -Mn ₂ O ₄ bulk structures.	237
Table 32: Voltage profiles of the undoped, the Fe-doped, Co-doped and Ni-doped n3-01 nanoclusters.....	238

Chapter 1: Introduction

This chapter discusses the history of manganese dioxide in South Africa for the specific use as a cathode material in secondary rechargeable batteries. Particular focus will be mainly on the structural properties of the stable polymorph of manganese dioxide, i.e., pyrolusite. Furthermore, a brief synopsis on the literature and background behind this topic is also given. The aim, objectives, intentions and motivations of this study are also detailed in this chapter.

1.1. Background

The growing demand for energy worldwide has necessitated an increase in scientific research focusing on optimising renewable and rechargeable energy supplies. This is done to alleviate the pressure on fossil fuels, which are mainly found on the African continent. Moreover, the dependence on fossil fuels as the main source of energy and fuel for powering the industrial revolution has contributed immeasurable damage to the environment [1]. The inevitable depletion of these fossil fuels has seen an increase in their cost and deemed the research into cleaner and higher density forms of energy very important [2].

Many vehicle manufacturers and oil companies have invested a substantial amount of resources into the research and manufacturing of new technologies with the aim of subverting the ever-increasing pressure on fossil fuels. These endeavours have already begun producing results as evident in the production of hybrid electric vehicles (HEVs) and plug-in electric vehicles (PHEV) [3]. The focus is mainly on the research and development of green energy sources, as well as energy storage systems that will have the capacity to store the produced power over an extended

period of time and distributing that power efficiently when required [4]. Current demands for energy have led to high costs in natural resources needed to produce fuel for motor vehicles and electricity production worldwide and in South Africa specifically [5].

Generally, there are four types of energy storage devices or batteries in existence today; primary batteries, secondary batteries, reserve batteries and fuel cells [6]. Recent secondary batteries have attracted the most attention as they are characterised by high energy density and high-power density. Moreover, they last longer and are environmentally friendly, hence their preference in consumer electronic devices [7]. However, rechargeable batteries for electric vehicles require higher capacities and large serial-parallel numbers.

Limiting factors affecting the use of rechargeable batteries are problems with their safety, production cost, uniformity and durability. This imposes some difficult limitations on the wide use of lithium-ion batteries in electric vehicles [8]. Consequently, improvements in the energy output and power density of these lithium-ion batteries are urgently required to meet the rapid development of electric vehicles and portable electronic devices. One of the difficulties encountered with improving the performance of secondary batteries to meet the increasing requirements for energy storage and optimal performance is the production of suitable cathode materials [9].

Cathode materials used in secondary batteries are usually transition metal oxides metals, capable of undergoing oxidation since they exist in various oxidation states such as 2⁺, 3⁺ and 4⁺. Transition metal oxides such as MnO₂ and TiO₂ are subject to intensive investigations due to their wide range of applications in various fields

including solar panels, catalysts, cosmetics, sensors, biomedical industry, optical-electronic devices, magnetism and rechargeable batteries [10]. The transition metal oxide, manganese dioxide (MnO_2) contains different allotropic polymorphs denoted by α - MnO_2 (hollandite), β - MnO_2 (pyrolusite), γ - MnO_2 (nsutite), R- MnO_2 (Ramsdellite), ϵ - MnO_2 (Akhtenskite), etc. These polymorphs mostly differ in the way in which the manganese atoms are located on the octahedral sites [11].

MnO_2 compounds are interesting as potential materials in secondary batteries due to their low cost and toxicity. Pyrolusite (β - MnO_2) is regarded as the most stable polymorph of MnO_2 [12]. The demand for pyrolusite in South Africa began in the mid-fifties as an oxidising agent for the production of Uranium [13]. In 1973, The Delta Manganese mining corporation established a 28 000 t/a electrolytic manganese plant at Nelspruit in the Mpumalanga province with the aim of increasing capacity and production annually.

South Africa is home to the highest grades of manganese ores in the world and, remarkably nearly 70% of all global manganese reserves are contained in the Kalahari Basin of the Northern Cape Province [14]. However, most of the produced manganese is exported to other countries for post processing and beneficiation. The ferrous metal manganese is an irreplaceable element in current industrial economies and it is required in large quantities by all industrialised nations. It is a potentially mobile element which occurs in three oxidation states (+2, +3, +4) [15].

Despite the abundance of pyrolusite and its indicated use as a cathode material in lithium-ion rechargeable batteries, pyrolusite suffers from some structural defects and impurities that hinder its optimal use [16]. The dominant defect species in the β - MnO_2 structure are cation vacancies at high oxygen activities and manganese interstitials

at low oxygen activities. Increasing the temperature of a system increases the chemical activity of the individual atoms thereby increasing the entropy (disorder/movement) of the atoms [17]. Recent studies have shown that nanostructural refinement can be used to correct the structural defects present in other rutile structures [18].

Materials at the nano scale display physical and chemical characteristics that differ from their counterpart bulk systems [19]. Nanostructuring is expected to play a crucial role in fabricating the next generation of nano devices. Specifically, nanostructures can be used as both building units and interconnectors. They also offer unique opportunities to explore the novel optical, mechanical, magnetic and electronic properties of materials. The physical and chemical properties of nanostructures are determined by their extremely large specific surface area (surface to volume ratio). These properties differ essentially from those of the macroscopic phase of the same material and depend on the size and shape of the nanostructure [20].

Several nanostructured MnO_2 , including nanocrystals of different shapes; i.e., nanowires, nanotubes, nanoclusters and nanobelts, have been synthesised for potential applications in catalysis, rechargeable batteries, ion-sieves and supercapacitors in recent years [21]. Thus, there has been unprecedented efforts focused on the synthesis, [22] structure [23, 24], properties [25, 26] and applications [27, 28, 29] of nanomaterials. However, some structural features existing at the nanoscale are difficult to characterise experimentally in the laboratories. Therefore, atomistic computer simulations offer a unique window of exploration into nanostructures, particularly the synthesis and stabilities of nanoclusters [30]. The great advances achieved in computational resources and experimental tools have

had an overwhelming improvement in the quality of research done on nanostructures [31, 32].

Unit nanostructures having at least one dimension between 1 and 10 nanometres with a narrow size distribution are termed nanoclusters. Nanoclusters consisting of up to a couple of hundred atoms and larger aggregates containing a thousand or more atoms are referred to as nanoparticles. Properties of nanoparticles are intermediary to those of bulk materials [33]. Nanoclusters have properties and structures which are very sensitive to their composition and size, which leads to new and interesting properties contrasting those of the bulk material. Nanoclusters are considered to be the transitional state between atoms and nanoparticles. Furthermore, they exhibit molecule-like properties due to the gradual emergence of discrete electronic states [34].

Nanoclusters offer the ability to investigate and alter the properties of the material or proffer new properties by simply adjusting the size. Nanostructured MnO_2 morphologies, such as nanoclusters can provide a large specific surface area that shortens the path of ions and electrons, improving the electrochemical performance. The ultra-small size of the nanoclusters results in a large surface area which makes interaction with the surrounding particles more efficient [35]. Oxides of MnO_2 and TiO_2 nanoclusters are an appealing option for research because of their nontoxicity, stability and narrow band-gap which makes them good electrical conductors.

MnO_2 nanoclusters exhibit improved electronic and optical properties compared to their bulk equivalents as a result many methods have been developed to synthesise the nanoclusters experimentally and to generate them using global optimisation techniques [36]. The experimental synthesis of nanoclusters is challenging due to the

control of side reactions occurring at the nanoscale whereby the use of computational simulation techniques has seen an increased use in shedding light on this field [37].

The understanding of all possible changes that can occur to the coordination and bonds of each atom at the sub-nano scale is important. This understanding goes a long way in explaining the changes that occur to the nanoclusters structure when exposed to different environmental conditions. Computer simulations offer scientists the observe these sub-nano scale atomic interactions. Furthermore, computer simulations give experimental researchers the option to save the actual minerals while accurately determining the properties of those minerals in question [38].

The Ontologies of computer simulations in science research

Computer simulations can be described as methods for investigating systems that are best modelled with analytical equations. This systematic process involves the selection of a particular model and determining efficient ways of applying them, thereafter, making deductions from the data output received and finally validating the studied models to the actual physical, target system [39]. Winsberg [40] purported that the need for computational simulations is due to the unavailability of data on a particular topic of scientific interest. In such cases, computer simulations may be used to replace or add on to the information gathered from conventional hands-on practical experimentation [41].

This study seeks to employ a multi-modal approach to address factors that hinder the stability and electrochemical activity of manganese dioxide when used as a cathode material in secondary batteries. In particular, to investigate the electronic properties, the structural stability, the electrical conductivity and the evolution of the manganese dioxide nanoclusters as their size is increased from $n=2$ to $n=20$ atoms.

1.2. Structural properties of pyrolusite ($\beta\text{-MnO}_2$)

The structure of pyrolusite ($\beta\text{-MnO}_2$) may be described as an infinite chain of edge-sharing MnO_6 octahedral connected to other single chains. The oxygen atoms form a slightly distorted hexagonal closed packed (hcp) array, half the closed-packed rows of octahedral interstices are occupied by Mn^{4+} ions. It has a rutile-type, tetragonal crystal structure where the anions form coordinated octahedrals around the cations as shown in Figures 1 and 2. In the bulk $\beta\text{-MnO}_2$ lattice, each manganese atom has six neighbouring atoms and each oxygen atom has three nearest manganese neighbours [21].

Pyrolusite crystallises into the rutile crystal structure with three-coordinate oxides and octahedral metal centres. The atomic Wyckoff positions for manganese and oxygen atoms are 2a and 4f, respectively. Moreover, it belongs to the ditetragonal dipyramidal class ($4/mmm - 4/m 2/m 2/m$) with the $P42/MNM$ space group. Its density has been measured to be in the range of $5.04 - 5.19 \text{ g/cm}^3$ [25]. Figure 1 displays the pure $\beta\text{-MnO}_2$ bulk structure in its natural unit form.

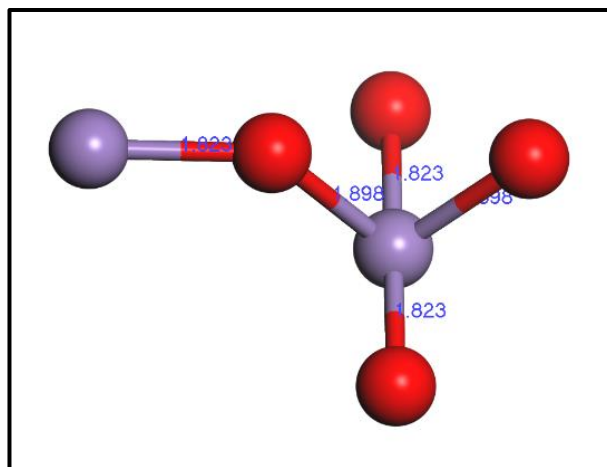


Figure 1: Pure $\beta\text{-MnO}_2$ structure displaying bond lengths between the neighbouring manganese (purple) and oxygen (red) atoms

The crystal model of the bulk structure is presented in figure 2 [26]. The lattice parameters were found to be $a=b= 4.414 \text{ \AA}$, $c = 2.860 \text{ \AA}$ and $\alpha=\beta=\gamma = 90.0^\circ$, with a unit cell volume of 55.56 \AA^3 .

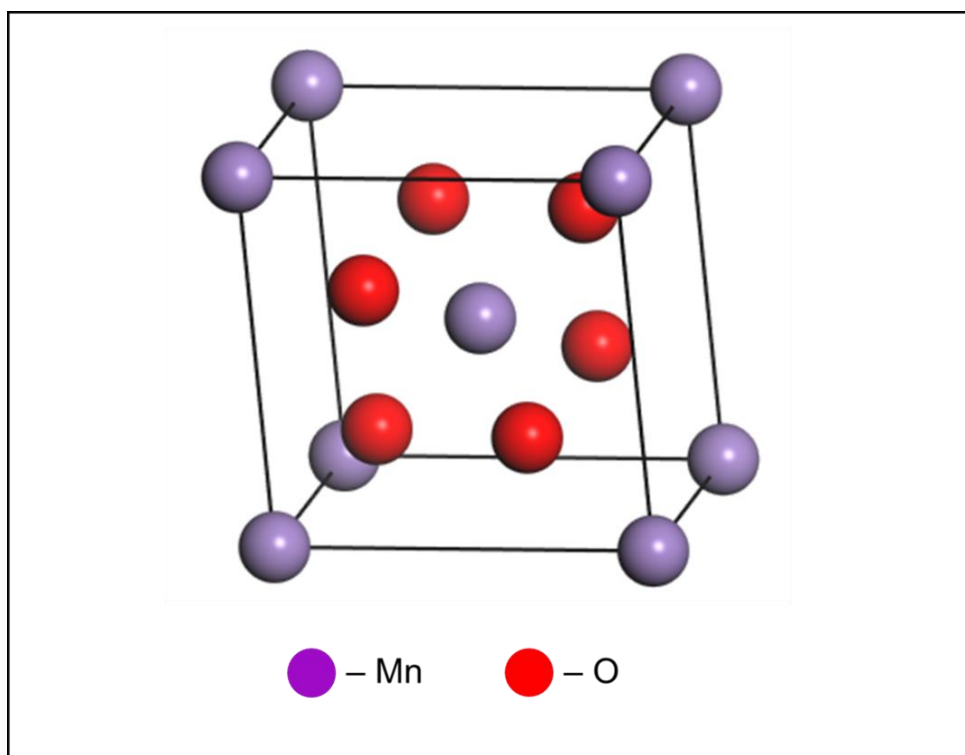


Figure 2: β - MnO_2 bulk structure

The synthetic β - MnO_2 is the most stable, stoichiometric isotype and ordered form with a tetragonal rutile structure of manganese dioxide. The anion-cation-anion angle towards the shared anion-anion edge varies from 75° to 85° . The two apical Mn-O bonds are longer than the four equatorial bonds (apically elongated) thus resulting in the same type of distortion as observed in TiO_2 [42].

The atomic number of manganese is 25 with an oxidation state of +4 in MnO_2 . Oxygen has an atomic number of 8 and an oxidation number of -2, but since oxygen exists as a diatomic gas it has an overall oxidation number of -4. This means MnO_2

is a neutrally charged compound due to the equality of the oxidation numbers when all summed up.

1.3. Intentions of the Study

This study intends to understand the evolution of β -MnO₂ structures at the nano scale and to mimic their stabilities in an effort to applying them to the macro structures. The nanoclusters are generated and evaluated using evolutionary algorithm techniques, then they are optimised using different DFT methodologies to produce the most efficient and stable nanoclusters of pyrolusite.

- i. Firstly, the interatomic potential (IP) code; the General Utility Lattice Program (GULP) [43] is used to refine the original interatomic potentials. Specifically, the GULP code is employed within the Knowledge–Led Master Code software (KLMC) [44, 45]. These refined potentials are then used to generate and rank the MnO₂ nanoclusters from $n=2$ to $n=20$ atomic numbers.
- ii. Secondly, the density functional theory (DFT) based code; the Cambridge Serial Total Energy Package (CASTEP) [27] is used to optimise the generated nanoclusters and rank them according to their stability. The NVE ensemble [46] is utilised to study the behaviour of the nanoclusters as temperature is increased from 100 K to 1500 K.
- iii. Thirdly, other DFT-based codes such as the Vienna Ab-initio Simulation Package (VASP) [26, 47], the “Fritz-Haber Institute ab-initio molecular simulations” (FHI-aims) software suit [48, 49] and Reflex [50] are used to investigate properties of interest from these stable nanoclusters which include the density of states (DOS), charge densities and X-ray diffraction patterns (XRD).

- iv. Lastly, the molecular dynamics (MD) based code D-Mol³ [51] is employed to evaluate the effect of doping the nanoclusters with iron, cobalt and nickel. Furthermore, the Highest Occupied Molecular Orbital-Lowest Unoccupied Molecular Orbital (HOMO-LUMO) energy band-gap and the conductivity of the nanoclusters will also be calculated using the DMol³ code.

The β -MnO₂ bulk structure and the generated stable nanoclusters are exposed to different temperatures with the aim of investigating their tolerance to different extreme conditions. Furthermore, the effect of doping is explored to determine the activity and stability of the nanocluster structures. This aspect is critical for evaluating the effect of natural impurities on pyrolusite when used as a cathode material in secondary rechargeable batteries. The dopants under focus in this study are iron, cobalt and nickel because they have shown potential when used to dope similar manganese oxide structures [52, 53, 54].

The quest of this study is to establish how conventional interatomic potentials (IP) can effectively enhance the β -MnO₂ bulk and nanocluster structures to achieve reliable data which can be applied experimentally.

1.4. Motivation for the study

The rapidly increasing market for portable electronic devices has resulted in a heavy demand for secondary batteries with high energy densities such as the batteries in electric vehicles (EV) and hybrid electric vehicles [8]. Advanced rechargeable energy storage systems are currently highly needed to mitigate current energy shortages caused by the depletion of fossil fuels and increasing population numbers [2]. The increasing need for high energy density secondary rechargeable batteries has

increased the interest in the research, development and manufacturing of new battery materials and technologies [7]. Specifically, the onset of continuous electricity cut-offs (loadshedding) in South Africa, further highlights the importance of effective energy storage devices to mitigate the effects of the regular power cuts.

Significant advances in materials and devices are necessary in order to realise the potential impact of nanostructuring. It is envisaged that the research and development of advanced materials may lead to new, cost effective, environmentally friendly, reliable and stable energy storage materials. It is widely reported that nanostructural stability relies on the targeted size dependent properties that can be exploited for a finite period of time considering that all nanostructures are thermodynamically and energetically unfavourable in comparison to bulk states [55].

Furthermore, nanostructured electrode materials feature keenly in the advancement of future energy technologies, as they display considerably higher capacities and better response rates than traditional materials [56]. The future of batteries relies on the creation of multifunctional electrode materials with distinctive nano-architectures [9]. In recent studies, MnO_2 has been shown to be a suitable cathode material capable of improving current performance in rechargeable batteries [57, 58, 59].

The majority of the previous work focused on the bulk and to a lesser extent on the MnO_2 nanostructures material [60]. However, converting MnO_2 into nanostructures is particularly challenging because only near-surface atoms participate in the redox reactions with the cations in the electrolyte. Nanostructured electrodes have previously exhibited improved capacitance and increased electron mobility in the electrode [35]. The potential importance of rutile MnO_2 in energy storage and catalytic applications has provided further impetus on this research. Combining this

information with experimental understanding promises to speed up the research into these materials while saving as much of the naturally occurring material as possible.

The impact of doping on the stability and performance of metal oxides was studied previously and showed some considerable success [61, 62, 63]. Doping has been shown to create different electrochemically active MnO_2 crystalline phases which result in the doped MnO_2 electrode having a higher charge-discharge reversibility with increased specific capacitance [64, 65]. Previous studies have indicated that there was less lithium-ion intercalation with the bulk $\beta\text{-MnO}_2$ systems [66, 67].

Cobalt-nickel composites were shown to improve the capacitance in MnO_2 multi-walled nanotubes [68]. This necessitates investigating the effect of doping in this current study. Specifically, this study will investigate the doping site preferences in order to determine the optimal atomic position to perform the doping on. The dopants of interest in this study are iron, cobalt and nickel due to their potential as previous studies have indicated some promise when they were used in other nanostructural investigations [52, 53, 54].

It is intended that this study will show that nanostructuring can improve the capability of these manganese dioxide systems by shortening the diffusion distance between the electrode and the electrolyte [38]. Manganese dioxide has been synthesised as various nanostructures, including dendritic clusters [69], nanocrystals [70, 71, 72], nanowires [7, 73], nanotubes [74], nanobelts [75] and nanoflowers [59]. Considerable success has also been achieved in the computer simulation of MnO_2 focusing on the nanoparticle, nanosheet, nanorod and mesoporous [76, 77].

Previous studies [3, 23, 24, 78] have shown that MnO_2 is one of the most promising cathode materials for application in lithium-ion battery systems. MnO_2 is an electrode

material and catalyst that is easier to prepare, cheaper and less toxic to the environment. However, this material is also characterised with inherent poor conductivity and poor charge/discharge cyclability, which limits their widespread use for energy storage [79]. This study aims to investigate novel architectures for the smaller sized MnO₂ nanoclusters, which could lead to higher energy densities, improved conductivity and faster charge/discharge cycles. These are all vital features of current and future research in energy storage.

1.5. Research hypothesis

Evolutionary algorithm methodologies can be utilised to generate β -MnO₂ nanoclusters. Density functional theory techniques are capable of optimising the β -MnO₂ bulk structure and the generated nanoclusters. Nanostructuring improves the stability of the β -MnO₂ nanoclusters. Doping improves the stability, electrochemical activity and conduction of β -MnO₂ nanoclusters.

Research questions

- i. Which optimisation technique is optimal for the β -MnO₂ bulk structure and nanoclusters?
- ii. How can the stability and electrochemical activity of the β -MnO₂ bulk structure and the nanoclusters be enhanced?
- iii. What effect does doping have on the β -MnO₂ bulk structure and nanoclusters
 - a. Does doping improve the stability of the bulk structure?
 - b. How does doping affect the structural integrity of β -MnO₂ bulk structure and the nanoclusters at high temperatures?
 - c. Which doping site and dopant is most preferred?

- d. Between the two doping techniques employed in this study; virtual crystal approximation method and substitution method, which doping technique produces the most stable structures?
 - e. How does doping affect the electronic behaviour of the nanoclusters with regards to the charge-electron transfer?
- iv. How does temperature impact the β -MnO₂ bulk structure and the nanoclusters?

1.6. Aim and objectives

This study aims to investigate the structural properties of the β -MnO₂ bulk structure and the evolution of the nanoclusters employing DFT and IA. The study will also investigate the electronic properties, thermodynamic properties and the effect of doping. In particular, the effect of doping on the stability, electrochemical activity and conductivity on the specified nanoclusters.

The objectives of this study are to:

- i. Evaluate existing interatomic potential parameters of β -MnO₂ and utilise them to create and optimise the β -MnO₂ bulk structure.
- ii. Generate β -MnO₂ nanoclusters using the validated interatomic potential parameters with KLMC.
- iii. Determine X-ray diffraction patterns of the β -MnO₂ bulk structures and the nanoclusters, then compare them with previous studies.
- iv. Determine the effect of doping (with Fe, Co, Ni) on the stability, electrochemical activity and conductivity of the stable nanoclusters.

- v. Determine the structural properties of $(\beta\text{-MnO}_2)_n$, $n=2\text{-}20$ nanoclusters using DFT techniques, i.e., lattice parameters, atomic coordination and bond lengths
- vi. Calculate electronic properties of the most stable nanoclusters, i.e., total density of states, band-gap energies and charge density differences.
- vii. Determine the thermodynamic properties of the $\beta\text{-MnO}_2$ bulk structure and the nanoclusters, i.e., the effect of temperature on the stability.
- viii. Determine the charge density differences of a selected stable nanocluster to investigate localisation of electrons during doping.
- ix. Calculate and compare the voltage profiles of the bulk structures and the doped nanoclusters.

1.7. Outline

Chapter 1 gives background information on the use of pyrolusite when used in rechargeable batteries. It discusses the structural properties of $\beta\text{-MnO}_2$ and a brief introduction about similar studies. Also included in this chapter are the intentions and objectives of the study which specify the actual work that was carried out during this study.

Chapter 2 focuses on the literature review; it discusses the methodologies and outcomes of previous studies that are related to this current study. Key findings from previous studies are discussed to guide the scope and direction of this study.

Chapter 3 discusses the theory behind the methodologies of the techniques employed in this study. Furthermore, all the computational software codes used in this study are discussed in detail. The methodologies are the IP, DFT and MD. The computational codes are GULP, CASTEP, KLMC, FHI-aims, Reflex and DMol³.

Chapter 4 focuses on the stability of the β -MnO₂ bulk structure at different temperatures. This chapter also discusses the doping of the bulk structure with iron, cobalt and nickel, in order to deduce which dopant is preferable and which doping technique produces the most stable and compact β -MnO₂ bulk structure.

Chapter 5 focuses on the generation of the β -MnO₂ nanoclusters from $n=2$ to $n=20$ atoms. Furthermore, the nanoclusters are optimised using DFT and molecular dynamics techniques.

Chapter 6 is focused on exploring the effect of temperature changes on the stability of the selected optimised nanoclusters. The behaviour of the nanocluster at the reported melting region of pyrolusite is also analysed. Furthermore, the formation of other phases of manganese dioxide at higher temperatures is explored.

Chapter 7 focuses on the X-ray diffraction patterns of the selected optimised nanoclusters. The XRD patterns of the selected nanoclusters are discussed in comparison to the XRD bulk structure and relevant previous studies.

Chapter 8 focuses on the effect of doping on the stability of the selected nanoclusters i.e., n3-01. Specifically, the properties in question are the bond lengths, band-gap energies and Fermi energies. Furthermore, this chapter also determines the most compatible and preferable dopant element for the MnO₂ nanoclusters. The dopants under focus are Fe, Co and Ni.

Chapter 9 investigates the electronic charge density differences of the stable manganese dioxide nanocluster, i.e., n3-01. The charge density difference of the pure undoped n3-01 nanocluster is compared with the singularly doped nanoclusters.

Furthermore, the charge density differences of the dual doped n3-01 nanocluster with Co and Ni is also explored.

Chapter 10 presents the summary and Conclusion of the study. It draws out the key findings from the analysis and discussions undertaken in the result chapters (4-9) to make substantive conclusions on this study. Furthermore, recommendations are made for future research based on the findings from this study.

A reference section follows after the recommendations. This acknowledges in full, all the literature, sources and references used in this study.

Lastly, the appendix section is found at the end of thesis. Appendix A and B contain all the structures and data generated from this study. Appendix C contains all the major presentations at national and international conferences, publications and achievements garnered during the study.

Chapter 2: Literature review

This chapter surveys and reviews scholarly sources in this field and provides an overview of previous and current knowledge. This allows the authors to identify relevant theories, methodologies and gaps in the existing research [80]. In particular, the focus is on the advancements made in the production and performance of rechargeable batteries over the years. The literature review centres on the challenges and improvements made in metal oxide nanostructures for use in secondary batteries, specifically manganese dioxide cathode batteries. Previous research articles with similar interests and relatable objectives are reviewed to guide the direction and execution of this study.

2.1. Evolution of batteries

A battery or an electrical cell is a device that generates electrical energy from a chemical reaction. It is composed of a positive electrode, negative electrode, an electrolyte, a separator and an ionic conductor. In 1774, while employed at the Royal school as a professor of physics in his native Como, in Italy; Alessandro Volta invented the electrophorus, which produced static electricity. He later designed the voltaic pile which served as the foundation for a great deal of early scientific research into the generation of electricity [81].

There are generally four types of batteries in existence today: primary batteries, secondary batteries, reserve batteries and fuel cells. **Primary batteries** are used once then discarded and cannot be recharged. They are extremely uneconomical because they produce only about 2% of the power used during their manufacture. Primary batteries are used in household appliances such as toys, flashlights and

radios which do not require special disposable methods [6]. An example of a primary battery is the alkaline/manganese dioxide battery.

Secondary batteries are simply rechargeable batteries. Encouragingly, they can be recharged after depletion to their original pre-use condition by passing current through the circuit in the opposite direction to the current flow during discharge. They have the advantage of being more cost-effective over the long-term although the individual batteries are more expensive than primary batteries. Some examples of these batteries are the lithium-ion batteries, used in power tools, laptops, mobile phones, cameras. This study focuses on the cathode component of this rechargeable batteries. Specifically on manganese dioxide as the core material in the cathode for its intended use in secondary batteries.

The third battery category is the **reserve battery**. This battery structure is commonly observed in thermal batteries where the electrolyte is kept inactive in a solid state before the melting point of the electrolyte is reached hence allowing ionic conduction and activation of the battery. Same as the primary batteries, most reserve batteries are used only once then discarded. They are used in timing, temperature and pressure sensitive detonation devices; found in missiles and other weapon systems.

Fuel cells represent the fourth category of batteries. Fuel cells differ from other battery systems because they possess the capability to produce electrical energy as long as active materials are provided to the electrodes. A well-reported application of fuel cells is in cryogenic fuels used in rockets and space crafts [82, 83].

Currently, conventional secondary batteries are inadequate to meet the demands placed on them, therefore advanced materials with high capacity and fast charge/discharge are critical for the next generation of secondary batteries [84].

Previously, various transition metal (Mn, Co, Cr and Ni) oxides were investigated as possible cathode materials for future batteries. Conventional battery systems have significant disadvantages that hinder their use. For example, the LiCoO_2 cathode that is predominantly used in lithium-ion batteries is expensive and difficult to dispose due to its high level of toxicity. Consequently, nanostructured lithium manganese-based oxides such as LiMn_2O_4 are studied extensively in order to replace the LiCoO_2 electrode material. However, the disadvantage of LiMn_2O_4 lies in the slow dissolution of manganese ions in the electrolyte during charge cycling. Compared to LiCoO_2 , MnO_2 systems have several advantages, i.e., less toxicity, greater abundance, availability, better thermal stability and lower cost [7, 56].

The quest for safer, cheaper and more efficient energy storage materials has necessitated the considerable research on manganese oxides and their extended surfaces [85, 60]. There has been an increased interest in manganese dioxide nanostructures for their potential applications in rechargeable lithium-ion batteries. Nanostructuring of MnO_2 has brought new ideas into the improvement of existing battery systems [86]. Several experimental methods such as thermal decomposition, electrochemical deposition, sol-gels and molten salts have been developed to synthesise MnO_2 nanostructures. However, the experimental organisation of MnO_2 nanostructures including nanowires, nanorods, nanoneedles, nanobelts and nanosheets into hierarchical super structures still remains a challenge [87].

The low-temperature hydrothermal method was employed experimentally to synthesise uniform nanoclusters of $\gamma\text{-MnO}_2$. Li ions were treated with MnO_2 nanoclusters without any intercalation to further investigate the effect of lithium ions on the morphology, particle size and charge/discharge behaviours of the synthesised MnO_2 [88]. It was reported that the solid-state treatment can change the morphology

and particle size of γ -MnO₂ nanoclusters, without considerable change in the phase composition. The sensitive control of morphologies, reactions, sizes, architectures and patterns of the nanocrystals have become a central theme in material sciences since these parameters are very key in determining their physical characteristics.

Low-dimensional nanostructures have garnered more attention because of their novel electrical, magnetic, optical and catalytic properties. Bruce *et al.* [89] demonstrated the chemistry of nanomaterials for future research on rechargeable lithium-ion batteries. Their study showed that future generations of rechargeable lithium-ion batteries could exhibit higher energy capacities that depend crucially on the use of nanostructured materials as electrodes and electrolytes. The ultimate expression of the nanoscale in rechargeable lithium-ion batteries is the formation of 3D nano-architected cells.

Previous studies on bulk β -MnO₂ showed no significant lithium-ion intercalation [67]. Moreover, the mesoporous and needle-like MnO₂ nanostructures exhibited good lithium intercalation with high capacities of up to 320 mAhg⁻¹ and good cycling stability [23, 60, 90]. Furthermore, the pore size and wall thickness of the nanostructures have been shown to improve the rate capability [91].

2.2. Metal oxide nanostructures

Transition metal oxides are an integral group of materials based on to their varying mechanical, electronic and chemical properties. They are important because of their stability at elevated temperatures. Transition metal oxide electrode materials have drawn great and extensive research attention due to their large specific capacitance, resulting from fast and reversible redox reactions at the surface of active materials [92]. Nanostructured transition-metal oxides are expected to enhance the rate

capability of cathode materials because of their remarkably higher effective interfacial area between the nano-sized metal oxide and the electrolyte and its shorter lithium diffusion distance during the charge/discharge cycle [93].

Titanium dioxide exists in various polymorphs (rutile, anatase and brookite). These polymorphs have been widely investigated as a lithium-ion battery materials, due to their advantages in terms of cost, safety and rate capability [94, 95]. TiO_2 is isostructural to MnO_2 and favours lithium insertion as a host electrode material with good lithium-storage capacity. Hence, it is considered as a promising electrode material for lithium-ion batteries due to its induced cycling stability and safety against overcharging [96].

The electrochemical performance of TiO_2 electrode materials strongly depends on their surface area, crystallite size and shape [97], hence the need for nanostructuring to improve structural stability. As a result, TiO_2 nanostructures have been favourably reported as good electrode materials with favourable rate performances for lithium-ion batteries [98, 99, 100].

Among the mesoporous transition metal oxides, crystalline titanium dioxide with a high surface area is a favourable material due to its well-reported activity in catalytic reactions [101]. Mesoporous TiO_2 exhibited high charging/discharging capabilities and remarkable stability. Moreover, it displayed excellent extraction capabilities and high de-insertion properties [102]. The stability of the TiO_2 nanostructured materials further highlights the potential of rutile polymorphs of transition metal oxides as electrodes in lithium-ion batteries [103].

Pan *et al.* [104] investigated one-dimensional SnO_2 nanostructures for use as an anode material in lithium-ion batteries. The study reported that the abrupt capacity

fading caused by volume variation in the bulk material could be effectively reduced when operating at the nanoscale level. Furthermore, this yielded a higher theoretical capacity and higher operating voltage as compared to traditional carbonaceous anode active materials. The self-catalytic SnO₂ nanowires in particular, provided more reaction sites on the surface and enhanced the charge transfer in the electrochemical reactions. Additionally, the SnO₂-based heterostructures are a very promising strategy to achieve a higher-power and a higher energy density when used in lithium-ion batteries.

Hamad *et al.* [22] studied the effect of nano-structuring on the photochemistry of TiO₂ using a combination of simulated annealing techniques, i.e., Monte Carlo Basin Hopping simulation and Genetic Algorithms methods. The techniques provided the global minima of small (TiO₂)_{n=1-15}. The stable structures were then refined by DFT techniques. The results from the two techniques correlate fairly well, although the interatomic potentials methods were unable to describe some subtle effects. The produced global minima subset consisted of compact structures, with titanium atoms reaching a higher coordination rapidly as the size of the nanocluster increased.

Chibisov *et al.* [105] used DFT-based techniques to investigate the atomic structure and elastic properties of titanium nanowires. They utilised the GGA with spin polarisation to relax the atomic structure until the interatomic forces were less than 0.005 eV/Å. It was determined that the value of the Young's modulus for the titanium nanowire was three times greater than the value reported for the bulk material. This showed that the nanowire was proven to be more stable and ductile as compared to the bulk material.

2.3. MnO₂ nanostructures

Previous studies have shown that nanostructuring has the capability to improve the performance and storage properties of rutile MnO₂ when used in lithium-ion batteries, supercapacitors and as catalysts in lithium-air batteries [57, 58, 59, 60, 106]. Thus, it has been established that battery performance is highly dependent on MnO₂ morphologies and crystallographic forms. However, mechanisms for improved performance are not fully understood, particularly at the atomic and nano scale.

Subramanian *et al.* [57] investigated MnO₂ nanostructures with the emphasis on structural, morphological, compositional and electrochemical properties in electrode materials. Qiu *et al.* [107] synthesised MnO₂ nanostructures by hydrothermal treatment and investigated their catalytical and electrochemical properties. Cheng *et al.* [76] synthesised MnO₂ nanostructures of different crystallographic types and crystal morphology via a facile hydrothermal route and investigated their electrochemical properties as active cathode materials in primary and secondary batteries. Their studies showed improved performance of MnO₂ nanostructured electrodes when compared to other compounds experimentally.

Kalubarme *et al.* [108] synthesised MnO₂ nanorods by hydrothermal method, where different morphologies were obtained. Effects of the crystal structure of MnO₂ on the catalytic activity for O₂ reduction were investigated. They displayed a good catalytic activity for oxygen reduction when used in a non-aqueous medium for a Li/O₂ battery. Tang *et al.* [109] showed that manganese dioxide and its composite materials delivered high-rate capability, excellent capacitance and a superior charge/discharge cycling stability when applied in battery systems.

Sugantha *et al.* [3] synthesised manganese (IV) oxide nanorods and nanofibers of varying dimensions by combining a sol–gel synthetic route with a template-based nanofiber fabrication. Diffraction studies and inductively coupled plasma analysis indicated that the product formed was an α - MnO_2 polymorph which crystallised into a hollandite-type structure. The discharge capacity during charge/discharge cycles of the Li/ MnO_2 cells showed higher values compared to that of bulk α - MnO_2 . This behaviour was attributed to the large surface area of the nano-sized electrode material.

Previous studies on rutile MnO_2 applications in supercapacitors showed some limitation in success when using bulk crystallites, which delivered capacities of approximately 9 Fg^{-1} [110]. However, Zang *et al.* [111] demonstrated that the formation of nanostructured particles dramatically enhanced the capacitance to 294 Fg^{-1} . In particular, this showed that nanostructuring does indeed show considerable success in the quest for improved capacitance and conductivity.

Sayle *et al.* [23] used computer simulation techniques to predict the electrochemical properties of MnO_2 nanomaterials for use in rechargeable Li-ion batteries. It was established that to maximise the electrochemical properties: (i) the β - MnO_2 host should be symmetrically porous, (ii) heavily twinned and (iii) the critical wall thickness should lie between 10 and 100 nm for β - MnO_2 and greater than 100 nm for α - MnO_2 . These findings explain why certain nano-formations of MnO_2 are electrochemically active, while others are inactive. Specifically, this showed that properties of MnO_2 nanostructures can be fine-tuned to desirable preferences differing to the bulk (parent) material by simply altering the size of one or more dimensions in the nano scale [23].

Tompsett *et al.* [16] computationally investigated the electronic structure of rutile β - MnO_2 surfaces using DFT based techniques. Their studied showed a preferred configuration toward a rod-like structure. This was noted as important for the formation of nano-morphologies showing promising electrochemical performance as battery cathodes, oxygen reduction catalysts and supercapacitors. In addition, it was established that the surfaces of the nanostructured rutile MnO_2 were electronically conducting contrasting those of the bulk material, which were reported to be insulating [24, 16].

Kong *et al.* [112] found that nanostructuring of MnO_2 created surface and edge structural distortions, characterised by emerging unsaturated surface ions. The ions are highly mobile and can easily migrate to form new bonds with neighbouring ions. Moreover, they reported that MnO_2 nanostructuring weakens the charge transfer between Mn and O ions located at the outer layers, thus bringing in more reductive Mn ions which enable oxygen vacancy formations. This ultimately enhances the catalytic activity of manganese oxides.

2.4. Simulated nanoclusters

The ground state of $(\text{SiO}_2)_n$ nanoclusters ranging from $n=2$ to 27 were predicted by extensive global optimisation searches using the Monte Carlo-Basin Hopping algorithm technique by Catlow *et al.* [113]. The technique is considered to be one of the least hindered global optimisation methods with respect to the specific topology of the potential energy surface. The reported silica nanoclusters formed four-coordinated tetrahedral networks with a high structural complexity. Clusters consisting of two-ring chains terminated at either end by a silanone group, were

discovered to be dominant in the make-up of the most stable structures of $(\text{SiO}_2)_n$ up to $n=6$ atoms.

Iwaszuk *et al.* [114] investigated the photocatalytic behaviour of TiO_2 using first principles techniques. They performed DFT simulations on the TiO_2 rutile (110) surface modified with TiO_2 nanoclusters ($(\text{TiO}_2)_n$: Ti_5O_{10} , Ti_6O_{12} , Ti_8O_{16} , $\text{Ti}_{16}\text{O}_{32}$, $\text{Ti}_{30}\text{O}_{60}$), with diameters reaching up to 1.5 nm. This cluster size is readily achievable experimentally. Furthermore, it was determined that the clusters adsorbed strongly at the surface giving adsorption energies from -2.7 eV to -6.7 eV. The valence and conduction band composition of the heterostructures favoured spatial separation of electrons thus giving improved photocatalytic properties.

Nagarajan *et al.* [115] investigated the nanostructures of cubic and monoclinic phases of zirconia nanoclusters which were optimised using the B3LYP/ LanL2DZ basis set. The stable $(\text{ZrO}_2)_{n=1-8}$ nanoclusters were generated through data mining plausible $(\text{TiO}_2)_n$ structures by global optimisation techniques. Their structural stabilities were determined from various electronic properties (including HOMO–LUMO band-gaps, ionisation potential and electron affinity), chemical hardness and chemical potential. A greater amount of energy was absorbed or released only in the cationic state of zirconia nanoclusters. It was reported that there was no significant energy absorbed or released by the remaining states in the ZrO_2 nanoclusters.

Gould *et al.* [116] studied segregation effects on the properties of $(\text{AuAg})_{147}$ nanoclusters using empirical potentials utilising an atomic-swap basin-hopping search technique to optimise the elemental distributions. The lowest energy structural arrangements were then re-minimised using DFT. The force-field calculations showed that Gold (Au) atoms preferentially occupied sub-surface positions in the

bimetallic structures. Au was found to favourably occupy sub-vertex positions within the alloy nanoclusters, as this maximised stronger Au–Ag interactions. However, at the DFT level, an Ag core surrounded by an Au shell was energetically favoured. The electronic charge densities were drawn more readily when Au atoms were positioned on the nanocluster surface resulting in a partial negative charge. Both structures were assumed to be energetically stable due to the slight differences in their binding energies and covalency.

The structures and electronic properties of Ti_nV ($n=1-16$) clusters were investigated by Rodriguez-Kessler *et al.* [117] using first principles calculations employing the generalised gradient approximation. Their study showed that the Ti_nV clusters favoured compact spherical structures with similar conformations to the pure Ti clusters. Their calculations indicated that the vanadium atoms remained on the surface for atomic numbers less than 8 ($n \leq 8$) and equal to 16 ($n = 16$) while for $n = 9 - 15$, the vanadium atoms occupied the endohedral position.

Furthermore, the Ti_6V , $Ti_{12}V$ and $Ti_{14}V$ clusters were found to be more stable which is consistent with pure Ti clusters of the same size. It was also discovered that an increase in the average binding energy occurred when a single V impurity was added on to the Ti_n clusters for $n = 12$, suggesting that the $Ti_{12}V$ cluster favours the encapsulation of the V-dopant atom. These results motivated the investigation of other bimetallic clusters, which may offer opportunities for tuning the electronic properties for appropriate and specific purposes.

Meng-Hsiung *et al.* [118] investigated the thermodynamic properties of titanium dioxide $(TiO_2)_n$ ($n=1-6$) nanoclusters using first-principle molecular dynamics (MD) simulations. The configurations of the TiO_2 nanoclusters were generated by the fast

inertial relaxation engine algorithm. The derived structures were further refined by DFT to correct any subtle defects in their atomic configurations. The variation of the internal energies was used to indicate the occurrence of a phase change for $(\text{TiO}_2)_n$ ($n = 1-6$) nanoparticles with increasing temperature. For $n=3$, three different structural transforms for the motion of oxygen atoms were observed at temperatures between 1150 and 1600 K. However, no apparent structure transition was observed for $n > 3$ because of the symmetric shapes and their higher bonding energies.

The effect of pressure on the thermodynamic and structural properties of Ag-Pd nanoclusters was previously investigated by Akbarzadeh *et al.* [119]. The molecular dynamics simulations were performed in a canonical ensemble (NVT) using the Nose-Hoover thermostat, the time step of the MD simulations was set at 0.001 ps with a relaxation time of 1 ps. The cluster was more stable when the Pd atoms were located in the core and the Ag atoms in the shell of the cluster. This was attributed to the larger size and smaller cohesive energy of the bulk Ag as compared to the bulk Pd. The energy results indicated that the Pd@Ag nanocluster was more stable than the Ag@Pd cluster at different pressures and also, the surface energy of both clusters increased with increasing pressure.

Escher *et al.* [120] used evolutionary algorithm (EA) techniques to study the thermodynamically stable structures of barium oxide nanoclusters $(\text{BaO})_n$ ($n = 4 - 18$ and $n=24$). The global minima clusters with 8, 10 and 16 formula units were more stable relative to their neighbour sized clusters and other local minima configurations of the same size. Lazauskas *et al.* [121] carried out a genetic algorithm exploration on the tight-binding interatomic potential energy surface for Ti_n ($n = 2-32$) nanoclusters. The energetically stable candidate nanoclusters were further optimised

with the PBEsol exchange-correlation functional and the PBEsol0 hybrid functional. The results indicated that non-zero spin moments persisted to larger sized clusters and magnetic moments of the lowest energy structures for $n = 18, 25, 26$ and 27 had an overall spin moment of $1 \hbar$.

2.5. Doping of nanostructures

The effect of doping on the stability and electrochemical activity of metal oxides has been studied intensively throughout the years [61, 62, 63]. The studies showed that doped-manganese oxides could be used as suitable electrodes in rechargeable batteries. Vilas Boas *et al.* [122] recommended the use of doped electro-catalysts as they presented a higher performance than the reported state of the platinum-carbon catalyst. This was confirmed by Zn-air mini battery tests which showed a higher power density than a conventional MnO_2 carbon catalyst. The electrochemical results of Bismuth and Cerium doped MnO_2 showed a higher conductivity as proven by the formation of nanorod structures with lower band-gap energies.

Shalini *et al.* [123] investigated the effect of dual doping on the nanostructured TiO_2 which was formed using the hydrothermal method. It was reported that the dual doped TiO_2 showed an improvement in the efficiency value by 6% and exhibited an improved performance of 2.4 %. Rudra *et al.* [124] studied the effect of doping metal oxides using a transition metal similar to this current study. They used manganese as a dopant for the nanostructured 3-D nano-root network of zinc oxide. Their study showed a successful agglomeration of the ZnO nanoparticles as the Mn content was increased.

Liu *et al.* [125] studied the doping of manganese dioxide where the transition metal Tungsten (W) was successfully doped on δ -MnO₂. The substitution of Tungsten (W⁶⁺) with manganese in MnO₆ groups reduced the chemical valence of Mn. Moreover, this resulted in the adsorbed surface oxygen species being more active which achieved an efficient and stable activity. Previous studies have shown that doping creates different electrochemically active MnO₂ crystalline phases which results in the doped MnO₂ electrode having a higher charge/discharge reversibility with increased specific capacitance [64, 65, 66].

Jadhav *et al.* [126] investigated the doping of manganese dioxide hierarchical nanostructures with cobalt in the quest of enhancing their pseudo-capacitive properties. Their study successfully displayed an overall improvement in the electrochemical performance of manganese dioxide nanostructures by fine-tuning the structure of the partially co-doped manganese dioxide using the facile hydrothermal method. In particular, a 5% increase in the specific capacitance was achieved with the co-doped manganese dioxide sample as compared to the pure undoped manganese dioxide electrode.

Lee *et al.* [62] investigated the doping of a metal oxide using another transition metal whereby manganese was the dopant for TiO₂ nanocluster complexes. The bond lengths between Mn-O shortened as compared to the parent complex of Ti-O bonds. The most stable nanostructures typically had the introduced Mn at lower coordinated positions and some of the Mn-O bonds broke in order to maintain that low coordination. The HOMO–LUMO band-gap decreased significantly due to Mn doping showing that manganese was a suitable dopant in the quest to form and maintain compact structures with smaller bond lengths even at elevated temperatures. This

shows that transition metals will be suitable dopants for doping the MnO₂ nanoclusters in this current study.

The cuboid-like cobalt nickel phosphate/MnO₂ multi walled carbon nanotubes were studied for application as binder-free electrodes for high-performance supercapacitors by Wang *et al.* [68]. The composite showed the best capacitance when the mass ratio of MnO₂ to MWCNT was 1:1 with the total doping amount of 3.9% using 3 mol/L KOH as the electrolyte. These further shows the importance of doping on improving the stability and electrochemical performance of manganese dioxide nanostructures. Nickel, cobalt and iron have shown remarkable potential when used as dopants in other nanostructure complexes [52, 53, 54] hence they will be investigated further in this study as the selected dopants.

2.6. Electronic properties of nanostructures

Electronic properties are of importance in materials science because they help in classifying the type of material under investigation, i.e., a metal (conductor), semiconductor or an insulator. Hence electronic properties offer insight into the conduction and bonding behaviour of atoms. Electronic properties that were of concern in this current study were the Fermi Energy (E_F) and band-gap energy, binding energy (E_B) and the electronic charge density differences. Electronic properties of bulk materials and nanostructures are dominated by the movement of electrons during the bonding and anti-bonding of atoms as stipulated by the packing conditions (space group, symmetry and the approximate atomic conditions [127]).

Jassem *et al.* [128] investigated the effect of temperature changes on the structural and electronic properties of manganese oxide nanoparticles. Their study showed that

different phases of manganese dioxide are formed at different temperatures and they also showed how the optical band-gap differed between these phases. The tetragonal MnO₂ was formed and stabilised at 800 °C. It is thus vital to observe the behaviour of the current study's nanoclusters around the 800 °C region for presence of any new phases.

Krawczuk *et al.* [129] analysed electronic charge densities to gain insight on the nature and role of intermolecular interactions involved during the doping of materials. Their study showed that some important properties can be deduced from the electron densities using Hirshfeld analysis [130] and Mulliken atomic populations [131]. The electron delocalisation indices that measure the number of electron pairs shared by atomic basins were used to describe the covalency of the intermolecular bonding.

Charge densities provide valuable insight on the subtle features due to polymorphism in nanocrystals. Charge density differences are inherently aligned with X-ray diffraction and density of states calculations. Particularly to visualise the electronic distributions that occur due to the localisations of electrons during the formation of intermolecular covalent bonds. This aids in the classification of solids through topological analysis as either conductors, semiconductors or insulators [132].

Chapter 3: Methodology

This chapter discusses the theory and the techniques employed in this study as well as all the computational software codes used. The background on the techniques is discussed along with the advancements that have been done over the years to bring the techniques to their current level of functionality.

In this study, MnO₂ nanoclusters were generated using different sets of interatomic potentials, i.e., Buckingham and Lennard-Jones potentials. These nanoclusters are then analysed and compared to determine which potentials produce the more stable nanoclusters. The stability of the MnO₂ nanoclusters was further investigated using DFT methods [133, 134]. The DFT methods are employed to verify the reliability of the first stage (IP) calculations by probing the nanoclusters.

It is critical for the potential based calculations to be validated by DFT methods because the accuracy and precision of previous IA calculations were not satisfactory [135, 136]. In addition to refining and verifying the stability of the nanoclusters, the DFT methods were also used to determine the structural, physical and electronic properties of the most stable nanoclusters. The next section gives a detailed discussion on the evolutionary algorithm approach, followed by the density functional theory methodology and the molecular dynamics method.

Ground state energies of the nanoclusters are calculated using interatomic potential methods and electronic structure techniques i.e., CASTEP, Reflex, DMol3. The interatomic potential method is computationally less costly and enables for large numbers and sizes of nanoclusters to be explored. Disparagingly, they have a number of limitations and discrepancies which may result in inaccurate results.

Combining IP methods with density functional theory (DFT) has yielded some promising and insightful results in other investigations [137, 138].

IP methods are used in the initial stages to generate and explore the range of cluster sizes and structures. DFT methods are then used in the latter stages to refine the energy ordering, optimise the structures of a selected subset of nanoclusters and calculate their properties. Thus, those found to be low in energy (local minima clusters) from the IP calculations, also referred to as “first stage” are subjected to further calculations in the second stage using other techniques to refine the structures and validate their order of stability [120, 121].

3.1. Evolutionary algorithm

The evolutionary algorithm (EA) technique is a method that has been successfully applied in many fields such as functional optimisation, machine learning, process control, economical evaluation, etc. [28, 29]. This kind of algorithm has been used successfully on atomic structure simulations and produced satisfactory results compared to other techniques. The fundamental theory behind EA simulates natural selection through a process similar to ‘survival of the fittest’ and this produces stable candidate structures [139, 140].

The EA process manages the evolution of clusters in different environments where the stronger and more adaptable cluster species survive and thrive while the weakest clusters are disregarded and discarded. This method avoids many problems associated with a single starting point by setting up a population of candidate clusters. Over numerous iterations, the quality of the candidate structures improves up to a point where one of the candidates generated is the desired “best-fit” structure referred

to as the global minima and the other potential structures are called the local minimas [30].

The EA is applied through a 'Genetic Algorithm' (GA) based upon a multi-stage approach where probable approximate structures are generated. Subsequently, these probable structures are then relaxed using local optimisation routines within the GULP code [141, 43] to minimize their lattice energies. Recently, hybrid approaches have been adopted using GA and Monte Carlo Basin Hopping (MBCH) methods to predict stable structures for small-sized inorganic nanoparticles [142].

The GA typically spends over 90% of the computing time on scanning and evaluating the quality of the trial structures. The relationship between quality and ground state energy implies that the lower lattice energy for a trial structure implies it is the better candidate. Even with the recent improvements in computational resources and advances in software, the simplest way to calculate the lattice energy has still proven to be too expensive. Hence, state of the art research is necessary to improve the cost effectiveness of this approach [143]. The multi-stage approach implemented in this study was developed in accordance with ZrO₂ nanoclusters determined by Woodley *et al.* [139] and Walsh *et al.* [140] for (In₂O₃)_n nanoclusters.

Figure 3 details the evolutionary algorithm approach for the global optimisation procedure covering all the stages employed in searching for the local minima and ultimately the global minima structures in this study. The 20 lowest energy candidate structures as measured by their energy of formations are selected after each EA cycle for a given atomic size (i.e., n = 1, 2, 3 ... 20) to predict the stable and low-energy atomic configurations.

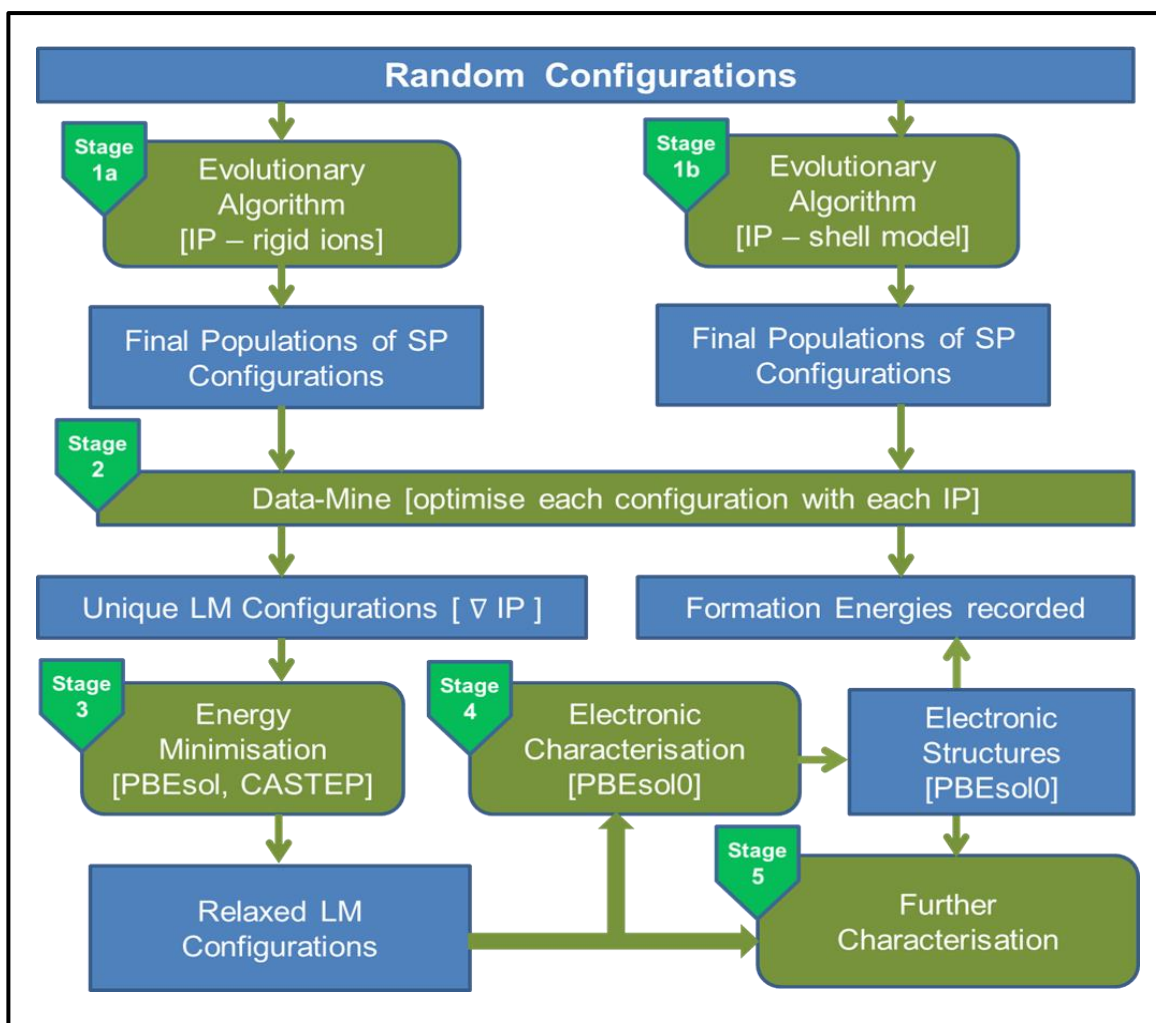


Figure 3: Flow chart of the multi-stages used to investigate the nanoclusters of $(\text{MnO}_2)_n$. Each rectangle represents an input/output for the codes employed: a script that calls GULP in stages 1 and 2, FHI AIMS in stages 3, 4 and 5 and lastly CASTEP in stage 3 and 5 [139, 140]

In stages 1a and 1b, EA relaxes all the newly created structures (whether through breeding or randomisation) in a two-step process. Firstly, the rigid model (1a) followed by the shell model (1b) according to the selected IP. The set of chosen structures from stage 1 are then refined using standard local optimisation techniques at the second stage. Stage 1 and 2 are implemented within KLMC. Stage 3 and 4 are performed using DFT platforms, FHI-aims [48] and CASTEP [27]. Furthermore, the

selected stable nanoclusters are subjected to geometry optimisation in order to investigate other subtle effects usually not identified by atomistic IP methods [144].

3.2. Atomistic potentials model

The IP method has been proven to be beneficial in structure determination, it is usually less computationally demanding, both in computing time and memory storage requirements [145]. The IPs used within GULP code are based on the Born model of ionic solids [146]. This model assumes that the energy and its derivatives can be defined as the summation of the atomistic interactions occurring within the crystal system. In particular, this includes the total net force acting on the individual atoms due to the other atoms as explained by their short range and long-range interactions. The interaction energy between the ions is given by

$$\phi_{ij} = \frac{1}{4\pi \epsilon_0} \frac{q_i q_j}{r_{ij}} + \psi (r_{ij}). \quad (3.1)$$

The term (ϕ_{ij}) represents the long-range Coulombic interactions between particle i and j , ϵ_0 gives the permittivity in free space, q_i and q_j are the ionic charges, r_{ij} gives the interatomic distance. The term, $\psi (r_{ij})$ describes the short-range interactions between ions including the repulsion due to the charged electron clouds and the attraction due to the Van der Waals forces. The total interaction energy of the system can be written in terms of the atomic positions as follows

$$\phi_i = \sum_i^N \sum_j^N \frac{1}{4\pi \epsilon_0} \frac{q_i q_j}{r_{ij}} + \sum_i^N \sum_j^N \psi (r_{ij}) + \sum_i^N \sum_j^N \sum_k^N \psi (r_{ijk}), \quad (3.2)$$

where $i \neq j \neq k$. The contribution of the point-charges to the electrostatic potential decays with $1/r$. The other terms of equation (3.2) describe the short-range interactions, which converge much faster and are thus usually calculated by a simple summation [147].

Stable local minimas on the energy landscape of formation are defined by interatomic potentials (IPs) found by employing a number of global optimisation algorithms [143]. Implementation of the IPs has been shown to reduce the computational cost incurred when locating plausible structures. This is discussed further in the next section of the methodology chapter. Searching landscapes based on IPs has been successfully applied to finding a wide range of bulk metal oxide phases [137, 138]. Similar techniques were also applied successfully to nanoclusters [148, 140].

The IPs are typically fitted in an effort to reproduce the structures and properties of the bulk phases. This could be one of the causes in the changing of the stability rankings for the clusters. Finally, the plausible structures are then refined using various DFT approaches.

3.2.1. Long range interactions

The charged particle i in equation (3.1) interacts with all other charged particles through long-range electrostatic interactions in the simulation crystal box. The Coulombic contribution ϕ_i to the interaction energy is given by

$$\phi_i = \frac{1}{2} \left(\frac{1}{4\pi \epsilon_0} \right) \sum_n \sum_{i=1}^N \sum_{j=1}^N \frac{q_i q_j}{|r_{ij} + nL|}, \quad (3.3)$$

where L represents the vectors reflecting the periodicity of the simulation crystal box over the summation of n as an ordered triple integer to defines the periodicity of the

structure in the simulation cell. q_i and q_j represent the charges on particles i and j , r_{ij} is the interatomic distance and ϵ_0 gives the permittivity in free space. The summation in equation (3.3) is slow to converge due to the $1/r$ term hence a quicker convergence and a more reliable scheme is required such as the Ewald Summation discussed below.

Ewald Summation

The Ewald Summation [149] is a preferred technique for calculating the electrostatic interactions in periodic systems between the ions and all its infinite periodic images.

The Ewald summation method assumes every particle with a charge q_i is surrounded by a spherical symmetric charge distribution of an opposite sign which cancels q_i and is usually expressed with a Gaussian distribution as ...

$$\rho_i = -q_i \left(\frac{\alpha}{\pi}\right)^{3/2} \exp(-\alpha r^2), \quad (3.4)$$

where α denotes the width of the distribution and r represents the position relative to the centre of the distribution. Therefore, only the fraction of q_i contributes to the electrostatic potential due to the particle i . This fraction rapidly converges to zero at long distances and the screened interactions resemble those of the short-ranged interactions. Hence, the electrostatic interactions between these screened charges can now be calculated by direct summation in real space [150].

3.2.2 Short range interactions

Shell Model Potential

The shell model was developed by Dick *et al.* [151] and it was it created to incorporate the polarisation of the atoms. This model of an ion is described by a core and shell. The core contains all the mass of the ion and it is attached to the shell by a harmonic spring with a certain spring constant. The core determines the position of the ion. The shell does not have any mass and it models the electronic charge density cloud. The total charge of the ion is shared between the core and the shell. The core has a positive charge and the shell has a negative charge; however there exists potentials for highly oxidized cations that have positive charges on the shell.

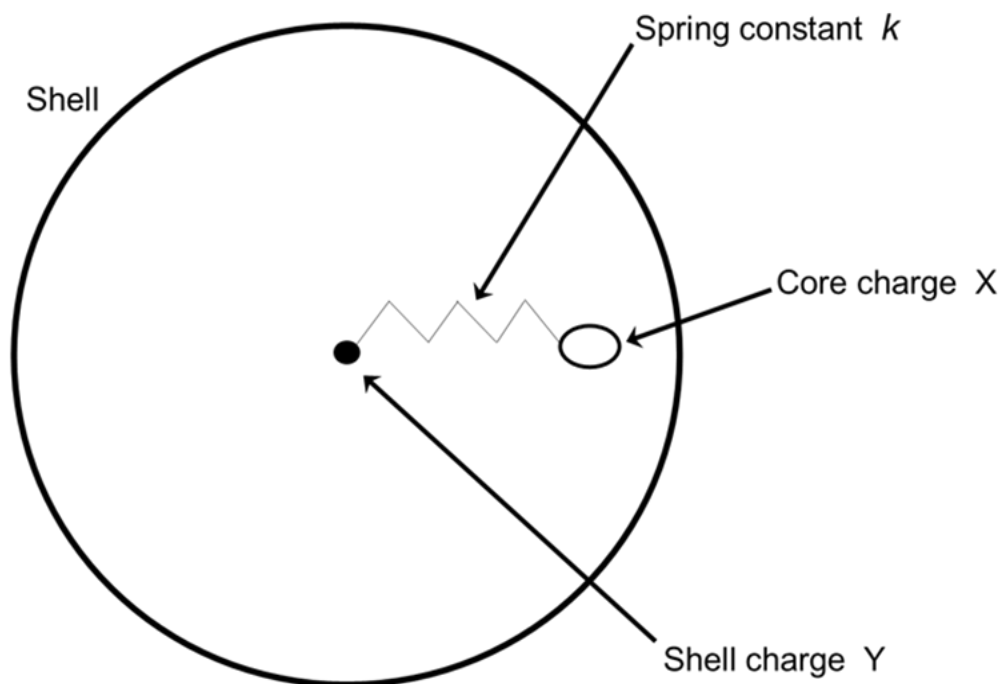


Figure 4: Schematic representation of the shell model [157]

The electronic polarizability of the ion, α , is related to the shell charge, Y and the spring constant k , by the following equation

$$\alpha = \frac{Y^2}{k} \quad (3.5)$$

The parameters Y and k are obtained by empirical fitting to dielectric constants, elastic constants and/or phonon dispersion curves. The disadvantage with the shell model is that the number of species is doubled hence the calculations become computationally expensive.

The short-range interactions consist of different contributions. At small distances, the electron charge clouds interact strongly leading to a situation where the electrons will repel each other. Also, at these distances, the dipole-dipole interactions, due to fluctuating dipoles on each ion, will result in attractive Van der Waals forces when considering covalent systems. The short-range attractive and repulsive interactions are described by simple parameterised potential functions. The potential parameters can be derived empirically by fitting to experimental data, such as crystallographic positions, elastic or dielectric properties. Charge density differences were also studied in order to analyse and discuss the transfer of electrons, localisation of charges and type of bonds formed.

The possibility of modelling nanocluster systems using potentials derived for the bulk structure and surface calculations were investigated. The efficacy of the potentials towards the manganese dioxide bulk structure and the nanoclusters was determined in this study. Furthermore, the Buckingham potentials and the Lennard-Jones potentials were used to model the interactions in the MnO_2 system. These potentials are discussed in detail in the next section.

Lennard-Jones Potential

The Lennard-Jones potential was initially proposed by Sir John Edward Lennard-Jones as a means to describe the potential energy of interaction between two non-bonding atoms or molecules based on their distance of separation [152]. The potential equation accounts for the difference between the attractive forces (dipole-dipole, dipole-induced dipole and London interactions) and the repulsive forces. The Lennard-Jones model consists of two parts; a steep repulsive term and a smoother attractive term, representing the London dispersion forces. The Lennard-Jones potential has been successfully shown to sufficiently describe the atomic interactions in metallic nanocluster systems [153, 154].

Individually, the 12-6 Lennard-Jones model [155] is not sufficiently accurate to represent of the potential energy surface. Its widespread use is due to its computational expediency since it is 4 times faster than the Buckingham potential. The 12-6 Lennard-Jones potential can be expressed as follows

$$V_{LJ} = 4\varepsilon \left[\left(\frac{\sigma}{r} \right)^{12} - \left(\frac{\sigma}{r} \right)^6 \right] = \varepsilon \left[\left(\frac{r_m}{r} \right)^{12} - 2 \left(\frac{r_m}{r} \right)^6 \right], \quad (3.6)$$

where $0 \leq n \leq m$. ε represents the potential well depth, σ represents the finite distance where the inter-particle potential is zero, r gives the distance between the particles and r_m gives the distance where the potential reaches a minimum. Equation (3.6) can be simplified and expressed as ...

$$V_{LJ} = \frac{A}{r^{12}} - \frac{B}{r^6}, \quad (3.7)$$

here $A = 4\varepsilon\sigma^{12}$ and $B = 4\varepsilon\sigma^6$.

The exponents are by default 12 and 6 [152]. The first term represents the repulsion between electronic clouds, which dominates at very short distances. The second term is the attractive part of the potential and models the van der Waals dispersion forces, which dominate at larger distances.

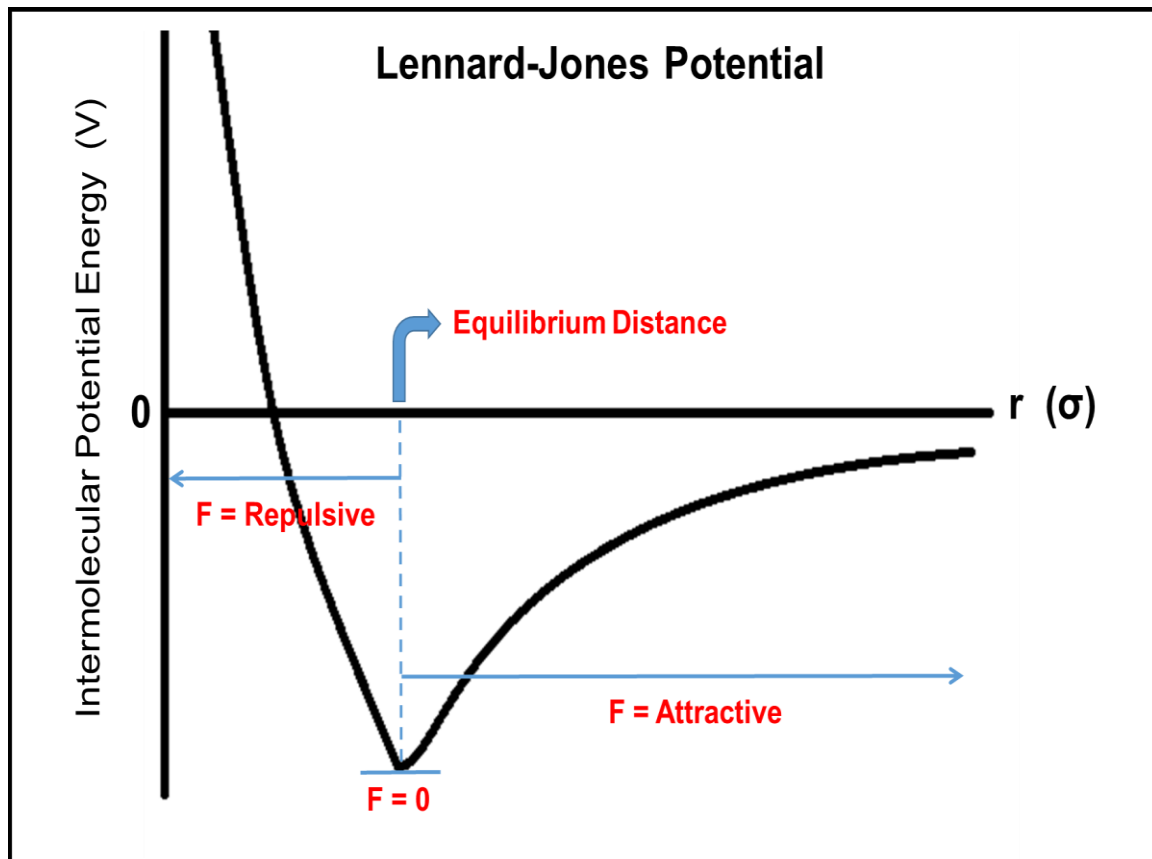


Figure 5: Illustration showing the equilibrium distance of the Lennard-Jones potential [152].

Buckingham Potential

The Lennard-Jones potential is usually improved using the Buckingham potential by incorporating an extra parameter and replacing the repulsive part by an exponential function [156]. The Buckingham potential [157] describes the van der Waals energy and the Pauli repulsion energy for the interaction of two atoms that are not directly bonded, as a function of the interatomic distance r . However, since the

Buckingham potential remains finite even at very small distances, it runs the risk of an un-physical "Buckingham catastrophe" at short range when used in simulations of charged systems. This occurs when the electrostatic attraction artificially overcomes the repulsive barrier. To overcome this, the Buckingham potential is usually used in conjunction with another interatomic potential as we have used the Lennard-Jones potential in this work [158]. The Buckingham potential is expressed as follows

$$V_r = Ae^{-\left(r/\rho\right)} - \frac{c}{r^6}, \quad (3.8)$$

where A , ρ and C are variable parameters. The first term represents the short-range repulsive interaction between the ions and the second term represents the attractive van der Waals forces. The energy for the sum of the two-body interactions is given by the analytical expression;

$$V(r_{ij}) = \frac{q_i q_j}{r_{ij}} + B_0 + B_1 r + B_2 r^2 + B_3 r^3 + B_4 r^4 + B_5 r^5, \quad (3.9)$$

where the first term is the standard Coulomb contribution to the energy between two-point charges q_i and q_j , a distance r_{ij} apart. The analytical expression for the Buckingham potential [159] employed, describes the interaction between two ions, i and j , of charge q separated by a distance r and is given by equation 3.10 below where the point charges include both cores and shells;

$$Ur_{ij} = \left[\frac{q_i q_j}{r_{ij}} + A_{ij} e^{-\left(r_{ij}/\rho_{ij}\right)} - \frac{C_{ij}}{r_{ij}^6} \right]. \quad (3.10)$$

Three-Body Potential

Another component of the interactions of covalent species is the bond-bending term, which is included to account for the energy penalties incurred for the deviations from the equilibrium value. This potential describes the lateral direction of the bonds and has a simple harmonic form;

$$U(\theta_{ijk}) = \frac{1}{2} k_{ijk} (\theta_{ijk} - \theta_0)^2 , \quad (3.11)$$

where k_{ijk} represents the three-body force constant and θ_0 is the angle of equilibrium [160].

3.2.3 The atomistic potentials method

The potential parameters used in this study were obtained by modifying the parameters developed by Matsui and Amundsen [161, 162] for isostructural TiO₂ and spinel LiMn₂O₄, respectively. The refined potentials were previously used successfully to model bulk, surfaces and nanostructures of MnO₂ [163, 164]. The potential parameters are based on the partially charged rigid ion model and the fully charged shell model where the ions are represented by point charges representing the anions and cations.

An extract of the script used to create the nanoclusters with KLMC is displayed in the figure below. The script incorporates both the Lennard-Jones potential and the Buckingham potential, along with a spring constant and other parameters. These parameters were then fine-tuned and optimised towards creating the local minima set of stable nanoclusters for the concerned atomic sizes, i.e., n=2 to n=20.

```

opti conv conj dist
cartesian
Mn   core   1.000000   1.000000   1.000000   2.2 1.0 0.0
Mn   core   1.000000   1.000000   1.000000   2.2 1.0 0.0
O    shel   1.000000   1.000000   1.000000  -1.1 1.0 0.0
O    shel   1.000000   1.000000   1.000000  -1.1 1.0 0.0
O    shel   1.000000   1.000000   1.000000  -1.1 1.0 0.0
O    shel   1.000000   1.000000   1.000000  -1.1 1.0 0.0
species
Mn   core   2.20000
O    core  -1.10000
lenn 12 6
Mn   core Mn   core   1.0 0.0 0.0 15.0
Mn   core O    core  10.0 0.0 0.0 15.0
O    core O    core   1.0 0.0 0.0 15.0
buckingham
O    core O    core  11782.760  0.2340  30.22  0.0 12.0
Mn   core O    core  15538.20  0.1950  22.00  0.0 12.0
Mn   core Mn   core  23530.500  0.1560  16.00  0.0 12.0
xtol opt   5.000000
gtol opt   5.000000
ftol opt   5.000000
switch rfo 0.05
maxcyc 10000

species
Mn   core   4.00000
O    core   0.24000
O    shel  -2.24000
buckingham
O    shel O    shel  22764.0  0.149  43.00  0.0 12.0
Mn   core O    shel  2000.986  0.3180  0.0  0.0 12.0
spring
O    9.85
xtol opt   7.000000
gtol opt   7.000000
ftol opt   7.000000
switch rfo 0.02
maxcyc 1000

```

Figure 6: Extract of a script used to generate the Mn_nO_{2n} ; ($n=2$) nanoclusters as employed in KLMC.

3.3. Density functional theory

The Density functional theory as proposed by Hohenberg and Kohn in 1964 [165] and Kohn and Sham in 1965 [166] is a quantum mechanical approach used to investigate the electronic structure of the many-electron system. In particular, on the atoms, molecules and solids in their ground-states. Due to the absence of molecular orbitals from the kinetic energy term, the accuracy and precision of early attempts were not satisfactory [167].

The first Hohenberg-Kohn (H-K) theorem represented the ground state properties of a many-electron system that were uniquely determined by an electron density that depended on only three spatial coordinates. This laid the foundation for reducing the many-body problem of N electrons with $3N$ spatial coordinates, through the use of the electron density [135].

The second H-K theorem defines the energy functional of the system and goes a long way to proving that the correct ground state electron density minimises the energy functional within the framework of the Kohn-Sham DFT. The framework solves the intractable many-body problem of non-interacting electrons moving in an effective potential. The effective potential includes the external potential and the effects of the Coulomb interactions. Modelling the latter two interactions becomes a difficulty within the Kohn-Sham DFT. The Kohn-Sham total energy functional for a set of doubly occupied electronic states ψ can be expressed as follows:

$$E = \{\psi_i\} = 2 \sum_i \left(-\frac{\hbar^2}{2m} \right) \nabla_{ion} \nabla^2 \psi_i d\vec{r} + \int v_{ion}(\vec{r}) \rho(\vec{r}) d\vec{r} + \frac{e^2}{2} \int \frac{\rho(\vec{r}) \rho(\vec{r}')}{|\vec{r} - \vec{r}'|} d\vec{r} d\vec{r}' + E_{xc}[\rho(\vec{r})] + E_{ion\{R_i\}}, \quad (3.12)$$

where E_{ion} is the coulomb energy associated with interactions among the nuclei (or ions) at positions $\{R_i\}$, v_{ion} is the static total electron-ion potential, $\rho(\vec{r})$ is the electron density and is given by:

$$\rho(\vec{r}) = 2 \sum_i |\psi_i(\vec{r})|^2 , \quad (3.13)$$

$E_{xc}[\rho(\vec{r})]$ is the exchange-correlation functional. The Kohn-Sham energy functional is equal to the ground state energy of the system of electrons with the position of the ions represented by $\{R_i\}$. In the DFT framework, the total ground state energy of a many-electron body is expressed as:

$$E = E[\rho(\vec{r}), \vec{R}_\alpha] , \quad (3.14)$$

where the electronic density ρ and total energy E depend on the type and arrangement of the atomic nuclei. The electron density is a scalar function defined at each point \vec{r} in real space i.e., $\rho = \rho(\vec{r})$. R_α denotes the positions of the nuclei α in the system. The total ground state energy can be decomposed into three terms; (i) a kinetic energy, (ii) a Coulombic energy term due to the classical electrostatic interactions among all charged particles in the system and (iii) the exchange-correlation energy term that captures all the many-body interactions. Therefore, the total energy can thus be expressed as:

$$E[\rho] = T_0[\rho] + U[\rho] + E_{xc} , \quad (3.15)$$

where T_0 is the sum of the kinetic energies of all effective electrons moving as independent particles. If each effective electron is described by a single particle wave

function ψ_i , then the kinetic energy of all the effective electrons in the system is given by:

$$T_0 = \sum n_i \int \psi_i^*(\vec{r}) \left[\frac{-\hbar^2}{2m} \nabla^2 \right] \psi_i(\vec{r}) dr , \quad (3.16)$$

where n_i is the number of electrons in the state i . The next term $U[\rho]$ in equation 3.15, is the Coulombic energy which is purely classical. It contains the electrostatic energy arising from the Coulombic attraction between the electrons and their nuclei, the classical repulsion between the electrons and also the repulsion between the nuclei i.e.,

$$U[\rho] = U_{en}[\rho] + U_{ee}[\rho] + U_{n-n} , \quad (3.17)$$

with

$$U_{en}[\rho] = - e^2 \sum_{\alpha} Z_{\alpha} \int \frac{\rho(r)}{|r-R_{\alpha}|} d\vec{r} , \quad (3.18)$$

$$U_{ee}[\rho] = e^2 \iint \frac{\rho(r)\rho(r')}{|r-r'|} d\vec{r} d\vec{r}' , \quad (3.19)$$

$$U_{n-n} = e^2 \sum_{\alpha\alpha'} \frac{Z_{\alpha}Z_{\alpha'}}{|R_{\alpha}-R_{\alpha'}|} , \quad (3.20)$$

where e is the elementary charge of a proton and Z_{α} is the atomic number of an α atom. The last term in equation (3.15), E_{XC} is the exchange correlation energy which accounts for all remaining complicated electronic contributions to the total energy. Accordingly, the Pauli Exclusion Principle deduces that each electron has a given spin and all other electrons with the same directional spin are inclined to avoid a close proximity with each other. Consequentially, the average Coulombic repulsive energy of that electron gets diminished over time. This inverse energy gain is called the exchange energy. The correlation energy is the additional many-body interaction between both having opposite spins.

Furthermore, it is important to describe the set of wavefunctions that serve to minimise the Kohn-Sham energy functional. These are resolved by the self-consistent solutions of the Kohn-Sham equations as follows:

$$\left[\frac{-\hbar^2}{2m} \nabla^2 + V_{ion}(\vec{r}) + V_H(\vec{r}) + V_{XC}(\vec{r}) \right] \psi_i(\vec{r}) = \varepsilon_i \psi_i(\vec{r}), \quad (3.21)$$

where ψ_i is the wavefunction of electronic state i , ε_i are Lagrange multipliers, which are effective one-electron Kohn-Sham eigenvalues, V_{ion} is the static total electron-ion potential and V_H is the Hartree potential of the electron which can be expressed as follows:

$$V_H = e^2 \int \frac{\rho(\vec{r}')}{|\vec{r}-\vec{r}'|} d\vec{r}'. \quad (3.22)$$

The exchange-correlation potential, $V_{XC}(\vec{r})$ is given by the following functional derivative:

$$V_{XC}(\vec{r}) = \frac{\delta E_{XC}[\rho(\vec{r})]}{\delta \rho(\vec{r})}. \quad (3.23)$$

Finally, the Kohn-Sham total-energy functional is written as the expression:

$$E = \frac{1}{2} \sum_{occ} \varepsilon_i + U_{n-n} - \frac{e^2}{2} \iint \frac{\rho(\vec{r})\rho(\vec{r}')}{|\vec{r}-\vec{r}'|} d\vec{r}d\vec{r}' + E_{XC}[\rho(\vec{r})] - \int \rho(\vec{r}) V_{XC} d\vec{r}. \quad (3.24)$$

The exchange-correlation potential cannot be obtained explicitly as the exact exchange-correlation energy is not presently known at this stage. Hence, some approximation methods must be applied in order to solve the problem. Some common methods of approximation include the local density approximation (LDA) and the generalised gradient approximation (GGA), which are discussed in the next subsections [168].

The effective potential includes the external potential and the effects of the Coulombic interactions between the electrons. The Kohn-Sham DFT shows that only the exchange-correlation as a function of the electron spin density must be approximated [169]. Hohenberg and Kohn expressed that the ground state energy of a collection of electrons in an external potential $V(\vec{r})$ is the minimum of a universal functional of the electron density $F[\rho(\vec{r})]$ where F is the universal function of the density

$$E_{ground} = \min_{n(\vec{r})} \left\{ F[\rho(\vec{r})] + \int V(\vec{r})\rho(\vec{r}) d\vec{r} \right\} . \quad (3.25)$$

Thus, if a decent approximation to $F[\rho(\vec{r})]$ was available there would be no need to work with the wavefunctions as the electron density would be sufficient. When working with metals (or metal oxides in this context), a filling factor f_i is added to the computation of the density:

$$\rho(\vec{r}) = \sum_i f_i |\psi_i(\vec{r})|^2 . \quad (3.26)$$

An artificial finite electronic temperature is introduced for efficiency reasons when working with metals with the filling factor taking immediate values between 0 and 1 [170]. The two exchange-correlation functionals in DFT are discussed in the next subsections.

3.3.1. Local density approximation

Local density approximation (LDA) gives the correct rule of the sum for the exchange correlation hole [171]. LDA is an approximation used locally to substitute the exchange-correlation energy density of an inhomogeneous system by that of an electron gas evaluated with the local density. It is one of the simpler methods used to

describe the exchange-correlation energy of an electronic system as used in total energy pseudopotential calculations.

This exchange-correlation energy depends only on the local electron density around each volume element $d\vec{r}$. The LDA is reliant upon two basic assumptions: (i) the effect of the exchange-correlation is predominantly due to the immediate vicinity of point \vec{r} and (ii) these exchange-correlation effects do not depend strongly on the variations of the electron density in the vicinity of \vec{r} . When the two conditions listed above are satisfied then the contribution from the volume element $d\vec{r}$ would be the same as if this volume element was surrounded by a constant electron density $\rho(\vec{r})$ of the same value as $d\vec{r}$. Within LDA, the expression for the exchange-correlation energy depends on the local electron density where the functional is evaluated and can be written as:

$$E_{XC}^{LDA}[\rho(\vec{r})] = \int \rho(\vec{r}) \epsilon_{XC}[\rho(\vec{r})] d\vec{r} , \quad (3.27)$$

and

$$\frac{\delta E_{XC}^{LDA}(\rho(\vec{r}))}{\delta \rho(\vec{r})} = \frac{\partial [\rho(\vec{r}) \epsilon_{XC}(\vec{r})]}{\partial \rho(\vec{r})} , \quad (3.28)$$

with

$$\epsilon_{XC}(\vec{r}) = \epsilon_{XC}[\rho(\vec{r})] , \quad (3.29)$$

where $\epsilon_{XC}[\rho(\vec{r})]$ is the exchange correlation energy per electron of a uniform electron gas. Equation (3.27) can be split into two parts as follows:

$$\epsilon_{XC}[\rho(\vec{r})] = \epsilon_X[\rho(\vec{r})] + \epsilon_C[\rho(\vec{r})] , \quad (3.30)$$

The exchange correlation energy part $\epsilon_{xc}[\rho(\vec{r})]$ can be derived analytically with the Hartree-Fock expression which can be written as:

$$\epsilon_{xc}[\rho(\vec{r})] = \frac{3}{4} \sqrt{\frac{3\rho(\vec{r})}{\pi}} . \quad (3.31)$$

The exchange correlation energy part cannot be derived analytically, but it can be calculated numerically with high accuracy by means of the Monte-Carlo simulations. When performing calculations, LDA is known to underestimate the bond length in molecules and cell parameters in crystals. The LDA uses the exchange-correlation energy for the uniform electron gas at every point in the system regardless of the inhomogeneity of the real charge density [172].

Using the formulae given in equation (3.31), the exchange-correlation potential for any electron density $\rho(\vec{r})$ can be evaluated. Both the Coulomb potential and the exchange-correlation potential in the Kohn-Sham equations depend on the charge density, which is constructed from the one-particle wavefunctions. The solution to the Kohn-Sham equation gives access to the total energy as a function of the nuclear position. One of the disadvantages with LDA is that it underestimates the exchange energies of atomic and molecular systems by roughly 10% [173]. To overcome this effect another approximation was formulated, called the generalised gradient approximation and is discussed in the next subsection.

3.3.2. Generalised gradient approximation

The generalised gradient approximation (GGA) has been widely used and declared a proven success in correcting the deficiencies of the LDA [172]. Beyond the LDA, the exchange correlation in an inhomogeneous system is non-local with respect to

the electrons it surrounds and this is referred to as gradient correction or generalised gradient approximation, which was introduced by Perdew and Wang [174]. GGA was found to overestimate bond lengths and lattice constants as a means of overcoming the deficiencies encountered within the LDA.

For non-uniform charge densities, the exchange-correlation energy can deviate from what is expected normally. The GGA functional most commonly used in physics, includes Perdew, Burke and Ernzerhof (PBE) and Perdew–Wang [175], are parameter free based on an interpolation between analytically solvable regimes [170]. GGA uses the gradient of the charge density, $|\nabla \rho(\vec{r})|$ to correct this deviation. The exchange correlation energy is expressed as:

$$E_{XC}^{GGA}(\rho) = \int dr \rho(r) \mathcal{E}_{XC}^{GGA} [\rho(r), \|\nabla\rho(r)\| , \quad (3.32)$$

where \mathcal{E}_{XC} is the exchange-correlation energy and $\nabla\rho(r)$ is the gradient term. The basic idea behind GGA to overcome the difficulties in LDA is to include the exchange-correlation expressions that account for the gradient due to the electron density and not solely on the value at each point in space. This leads to these corrections being classified as non-local potentials [176]. The Perdew-Burke-Enzerhof functional has undergone significant improvement in recent versions of the computational codes when used to predict molecular enthalpies of formation [177].

Other variations of the GGA have been developed. Finite-temperature analogues of the GGA for the non-interacting free-energy functional have been developed through the years and have yielded promising results [173]. A parameter free Meta-GGA functional that employs Laplacians of the kinetic energy densities have also been developed by Tao *et al.* [178] as well as a hyper-GGA that adds an exact energy

exchange per particle. The performance of this new hybrid GGA-based functional has improved the versatility and were also shown to provide reasonably accurate results [179].

3.4. Plane-wave pseudopotential method

The plane-wave pseudopotential method is a very useful fundamental technique that can be used to calculate with some precision the variation of the self-consistent solution in density functional theory. It has become very dependable in studying the properties of a variety of materials. The basic idea of this method is to exclude the core electrons by the assumption that their charge density is not affected by the changes in the chemical environment thereby focusing only on the valence electrons.

The method makes it possible to replace the strong electron-ion potential with a substantially reduced pseudopotential that also describes all the prominent features and relativistic effects of a valence electron moving through a solid. The use of plane waves as basis functions enables the systematic study of the complex, low-symmetry configurations of the possible atomic configurations [180].

3.4.1. Plane-wave basis

The theory behind the plane-wave pseudopotential method is explained by using Bloch's theorem, which permits electronic wavefunctions to be expanded according to a discrete set of plane-waves to overcome the effects of the infinite number of electrons. The electronic wavefunctions can be written as:

$$\psi_i(\vec{r}) = \exp[i\vec{k} \cdot \vec{r}] f_i(\vec{r}) , \quad (3.33)$$

where the function $f_i(\vec{r})$ defines the periodicity of the solid and allows for the expansion using a basis set with containing a discrete set of planes that can be written as follows:

$$f_i(\vec{r}) = \sum_G C_{i,\vec{G}} \exp[i\vec{G} \cdot \vec{r}] , \quad (3.34)$$

where \vec{G} represents the reciprocal lattice vectors of the periodic cell. \vec{G} is required for the resolution of rapid variations in the wavefunctions and charge density. Each electronic wavefunction can be written as a sum of plane waves:

$$\psi_i(\vec{r}) = \sum_G C_{i,\vec{k}+\vec{G}} \exp[i(\vec{k} + \vec{G}) \cdot \vec{r}] , \quad (3.35)$$

where $C_{i,\vec{k}+\vec{G}}$ are the coefficients for the plane waves. These coefficients are depended on the specific kinetic energy expressed as:

$$\frac{\hbar^2}{2m} |\vec{k} + \vec{G}|^2 . \quad (3.36)$$

The convergence of this expression relies on the choice of the kinetic energy cut-off although in principle, the cut-off energy should be increased until the total energy of the system reaches convergence. Only plane waves that obey the following equation are included in the basis:

$$\frac{\hbar^2}{2m} |\vec{k} + \vec{G}|^2 < E_{cut} . \quad (3.37)$$

Plane-waves implement a finite cut-off energy which usually results in an error in the computed total energy, hence the cut-off energy must be increased systematically until the total energy converges. Substituting the electronic wavefunctions given in

equation (3.37) into equation (3.12) for the self-consistent solutions of the Kohn-Sham equations gives:

$$\sum \left[\frac{-\hbar^2}{2m} |\vec{k} + \vec{G}|^2 \delta_{GG'} + V_{ion}(\vec{G} - \vec{G}') + V_H(\vec{G} - \vec{G}') + V_{XC}(\vec{G} - \vec{G}') \right] C_{i, \vec{k} + \vec{G}'} = \varepsilon_i C_{i, \vec{k} + \vec{G}} . \quad (3.38)$$

The various potential contributions are given by their Fourier transformations whereas the kinetic is diagonal. Although Bloch's theorem requires for the electronic wavefunctions to be expanded using a discrete set of plane-waves, a plane-wave basis is not suitable to expand electronic wavefunctions due to the large number of plane-waves required to grow the tightly bound core orbitals.

Considerable amounts of computational resources are necessary to adequately calculate all the generated wavefunctions and perform the required electronic calculations. This problem is discussed and remedied in section 3.4.2. using the pseudopotential approximations [181, 182]. Plane-wave basis sets are unbiased as they are independent of the atomic positions and species. They control the basis-set convergence because a single convergence criterion is sufficient [183].

3.4.2. Pseudopotential approximation

The pseudopotential approximation allows for the electronic wavefunctions to be expanded using a much smaller number of planewave basis states. The physical properties of solids depend on the valence electrons than the tightly bound core electrons. The pseudopotential approximation uses this fact to remove both the core electrons and the strong nuclear potential, then replace them with a weaker

pseudopotential which acts on a set of pseudo wavefunctions instead of the true valence wavefunctions [184].

Accounting for the weaker potential is vital because it makes the solution of the Schrödinger's equation simpler. This is achieved by allowing expansion of the wavefunctions in a relatively smaller set of plane waves. The most common form for the pseudopotential is given by:

$$V_{NL} = \sum_{lm} |lm\rangle V_l \langle lm| , \quad (3.39)$$

where lm are spherical harmonics and V_l is the pseudopotential for angular momentum l . Using this operator on the electronic wavefunction decomposes the wavefunctions into spherical harmonics, each of which is multiplied by the relevant pseudopotential V_l . A schematic diagram below illustrates a typical ionic potential, valence wavefunction with the corresponding pseudopotential and the pseudo wavefunction.

Local pseudopotentials are computationally much more efficient than non-local ones. The norm conserving pseudopotentials, are an example of non-local pseudopotential and they use a different potential for each angular momentum component of the wavefunction.

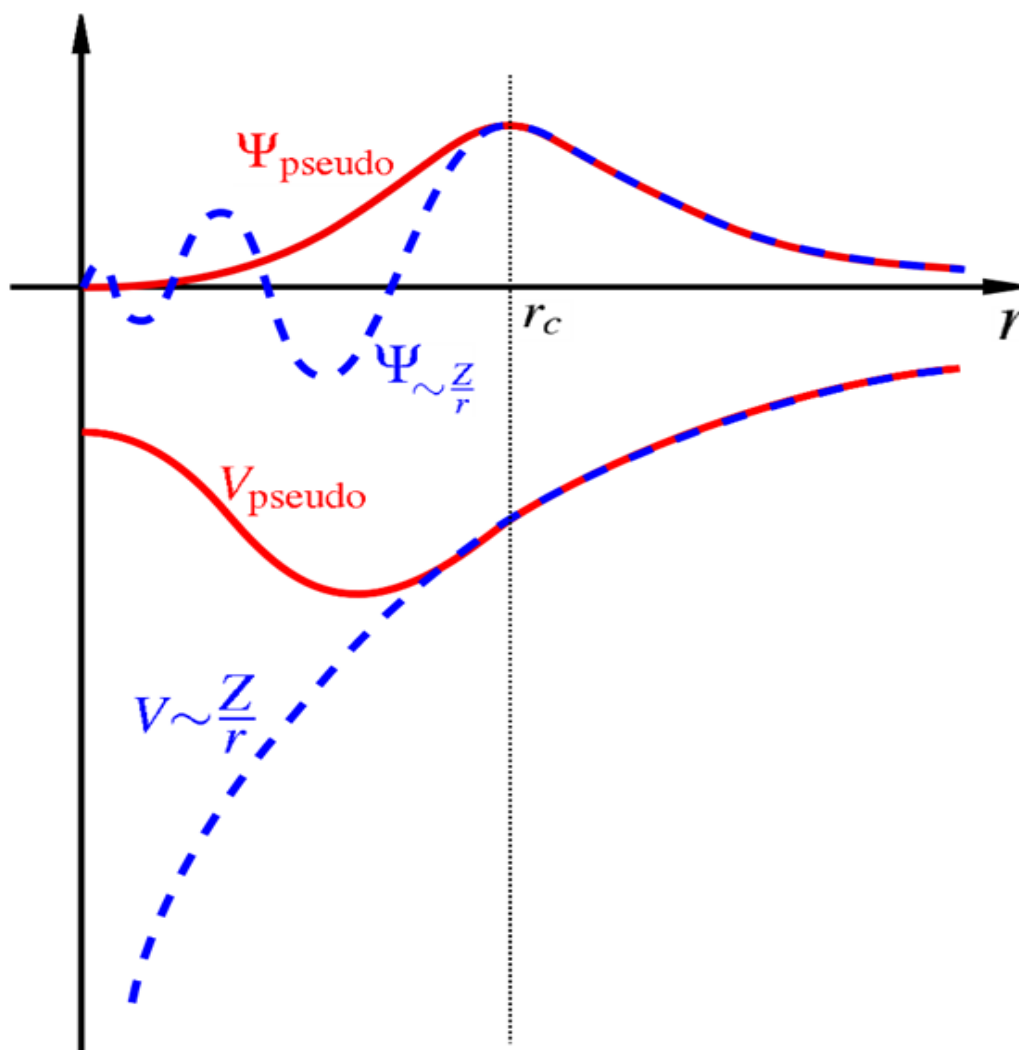


Figure 7: Schematic illustration of all-electron potential (blue line) and pseudo-electron potential (red line) with the corresponding valence wavefunction (ψ_v) and pseudo-wave function (ψ_{pseudo}) [185]

The non-local pseudopotential generally describes the scattering from the ion core. A match of the pseudo and real wavefunctions outside the core region also assures that the first-order energy dependence of the scattering is accurately described over a wide range of energy [186]. Pseudopotential approximations offer the advantage of reducing computational demands by replacing some of the basis functions with simplified analytic or numerical forms thereby reducing the time required to conduct calculations since these basis functions will be computed only once during the self-consistent field (SCF) iterations.

3.5. Projector augmented-wave method

The Projector Augmented-Wave (PAW) method combines the pseudopotential method and the Linear Augmented Plane Wave (LAPW) method in a more natural way. The PAW method's accuracy was shown to be very compatible with some of the most accurate all-electronic structure methodologies based on the LDA.

The PAW method was initially developed by Blochl with a strategy towards dividing the wave function into different constituent parts, i.e., the partial-wave expansion function within an atom atom-centred sphere and enveloped functions outside the spheres [187]. Blochl introduced a linear transformation and derived the PAW total energy functional from the nodal pseudopotential to the all-electronic wave function in a consistent manner that made it applicable with the Kohn-Sham functional [188].

The PAW method aims for a smooth transformation from the nodal structure to an auxiliary wave function with a rapid convergent plane wave expansion. The linear transformation operator \mathcal{T} is expressed using Dirac's Bra and Ket notation as follows;

$$|\psi_n\rangle = \mathcal{T}|\varphi_n\rangle, \quad (3.40)$$

Whereby $|\psi_n\rangle$ denotes the physical one-particle wave function and $|\varphi_n\rangle$ denotes the auxiliary wave function. The transformation operator \mathcal{T} must be written as a sum of the atomic contributions \mathcal{S} in order to smooth out the auxiliary wave function in each atomic region.

$$\mathcal{T} = 1 + \sum_R \mathcal{S}_R, \quad (3.41)$$

The relevant wave functions are then expressed as superpositions of the partial waves

$$\psi(r) = \sum_{i \in R} \vartheta_i(r) c_i \text{ for } |r - R_r| < r_{c,R}, \quad (3.42)$$

$$\text{And } \varphi(r) = \sum_{i \in R} \tilde{\vartheta}_i(r) \langle \tilde{p}_i | \varphi \rangle \text{ for } |r - R_r| < r_{c,R}, \quad (3.43)$$

$i \in R$ represents the partial wave functions belonging to the site index R for the position of the nucleus at R_r and $r_{c,R}$ represents the truncation radius. Each partial wave is associated with an auxiliary partial wave and they are pairwise identical up to a given limiting radius r_c . $\langle \tilde{p}_i |$ represents the projector function.

The atomic contributions can be applied to the auxiliary wave functions as follows

$$\mathcal{S}_R|\varphi\rangle = \sum_{i \in R} \mathcal{S}_R |\tilde{\vartheta}_i\rangle \langle \tilde{p}_i | \varphi \rangle = \sum_{i \in R} (|\vartheta_i\rangle - |\tilde{\vartheta}_i\rangle) \langle \tilde{p}_i | \varphi \rangle, \quad (3.44)$$

The transformation operator is thus finally

$$\mathcal{T} = 1 + \sum_i (|\vartheta_i\rangle - |\tilde{\vartheta}_i\rangle) \langle \tilde{p}_i |, \quad (3.45)$$

Similar to the wave functions, the total energy can be divided into its constituent parts as follows

$$\tilde{E}([\varphi_n], R_i) = \tilde{E} + \sum_R (E_R^1 - \tilde{E}_R^1), \quad (3.46)$$

\tilde{E} represents plane-wave part and is evaluated in real and on the reciprocal space. In contrast to the norm-conserving pseudopotential approach, the augmentation charge density is non-spherical and constructed such that they have vanishing electrostatic multi-pole moments at each atomic site as given below ...

$$n_R^1(r) + Z_R(R) - \tilde{n}_R^1(r) - \tilde{Z}_R(R), \quad (3.47)$$

where the nuclear charge density $-eZ(r)$ is defined as a sum of the wave functions on the nuclear sites with the atomic numbers $Z(r)$. The compensation charge density

$\tilde{Z}_R(R)$ is given as a summation of the angular momentum. This compensation charge density is localised within the atomic regions thus all the functionals in \tilde{E} can converge as fast as the auxiliary density making PAW computationally efficient [189].

The PAW method substantially improves the accuracy and efficiency of the plane-wave pseudopotential calculations through linear scaling and utilisation of the all-electron wavefunctions with soft node-less pseudo wavefunctions. This approach can be adapted to exhibit improved convergence properties as compared to norm-conserving pseudopotential methods in the DFT framework [136]. Implementation of the PAW method has become increasingly popular in several computational electronic structure simulation codes due to the positive correlation among the pseudo and the actual wave functions to produce reliable accurate results [190].

3.6. k-point sampling

Many calculations in crystals involve the averaging over the Brillouin zone of a periodic function of a wave vector [179]. Electronic states are accounted for only at a given set of k-points determined by the systems boundary conditions which are applicable to bulk solids. K-points denote sampling points in the first Brillouin zone of the material, i.e., the specific region of reciprocal-space which is closest to the origin (0,0,0). The need for k-points arises directly from Bloch's theorem, which states that in a periodic potential the wavefunctions have a periodic magnitude. Bloch's theorem changes the problem of calculating an infinite number of electronic wavefunctions to one of calculating a finite number of k-points.

The density of permissible a k-point mesh is proportional to the volume of the solid in question. The infinite number of electrons in the solid are accounted for by an infinite

number of k-points and only a finite number of electronic states are occupied at each k-point. Density functional theory approximates the k-space integral with a finite sampling of k-points. The most commonly used scheme is that proposed by Monkhorst and Pack [191]. They proposed a scheme where the k-points are distributed homogeneously in the Brillouin zone according to the following expression:

$$k = x_1 b_1 + x_2 b_2 + x_3 b_3 + \dots \quad (3.48)$$

where b_1, b_2 and b_3 are the reciprocal lattice vectors, and

$$x_i = \frac{l}{n_i}, \quad (3.49)$$

where $l = 1, \dots, n_i$, where n_i are the folding parameters.

This essentially means that the sampled k-points are distributed comparably and equally in the Brillouin zone, with rows or columns of k-points running parallel to the reciprocal lattice vectors that spans the Brillouin zone. The number of k-points required for a given type of calculation depends entirely on the system as their treatment requires different settings.

Metallic systems require more k-points than semiconductors and insulating systems. If the k-point sampling does not give a sufficiently converged total energy, then a much denser set of k-points must be used to reduce the errors and ensure the required convergence. Therefore, choosing a sufficiently dense k-point mesh is crucial for the convergence of the calculated results and is therefore one of the major objectives when performing convergence tests. However, the computational cost of performing a very dense sampling of the k-space increases linearly with the number of k-points in the Brillouin zone.

DFT-based codes approximate these k-space integrals with a finite sampling of k-points. Special k-point schemes have been developed to use fewer possible k-points for a given accuracy, thereby reducing the computational cost and calculation time [191].

3.7. Electronic properties of β -MnO₂

This study will investigate the electronic properties of the bulk structure and compare those results that with the electronic properties determined from the generated nanoclusters. The properties targeted are the Density of States (DOS), the Fermi energy and the gap between the Highest Occupied Molecular Orbitals and the Lowest Unoccupied Molecular Orbitals (HOMO-LUMO band-gap energy). Density of states (DOS) refers to the number of states that are available for occupation by electrons. The DOS provides numerical information on the states of availability at each energy level [192].

A high value for the density of states represents a higher probability for the energetic states to be occupied. Energy levels in a crystalline can be split into multiple levels separated by their atomic interactions. As a result of interatomic coupling, a crystal forms a single electronic system obeying Pauli's exclusion principle. Electrons usually prefer to occupy the lowest available energy states according the Aufbau principle [193].

Materials are classified into three main groups; metals, semiconductors and insulators. These classifications are distinguished by the presence and size of the band-gaps between the two highest energy bands namely; the conduction band and the valence band. The band-gap energy (E_g) refers to a forbidden space between the

maximum valence energy band (E_v) and the minimum conduction energy band (E_c). The band-gap is the minimum amount of energy that is required for an electron to separate freely from its bonded state and starts to move freely in the material causing it to be conductive. When an electron becomes conductive, a hole is left behind where the electron moved from. This hole moves in the opposite direction to the electron.

The two highest bands of energy states of an electron are the valence band and the conduction band. The valence band is the highest range of energy states of an electron that is still bound to an atom and the conduction band is the range of energy states at which the electron is stripped from the atom to flow freely through the atomic lattice of the material. This freedom of movement by this electron is what contributes to electric current [194]. The boundary between the occupied states and the unoccupied states is called the Fermi energy [195, 196]. Understanding what happens at the Fermi level and the resulting band-gap energy is very important to deduce the stability of the nanoclusters and the contributions of their individual atoms.

The Fermi level makes it possible to calculate the density of electrons and holes in a material and how they are affected by the temperature of the system. In metallic conductors, the valence is partially occupied by electrons. The valence band and the conduction band are in close proximity or they overlap causing the electrons to be conductive due to the electrons moving freely between the two bands. Semiconductors and insulators have Fermi levels lying in the forbidden band-gap and they have full valence bands restricting free movement of the electrons. Therefore, insulators have electrons with nowhere to go hence they are non-conductive. Semiconductors become conductive only at certain temperatures when more

electrons can be found in the higher energy states due to thermal excitation and increased kinetic energy.

The Fermi level and the band-gap in a solid are mainly responsible for the electrical properties of materials. In a perfect semiconductor without impurities or dopants), the Fermi level is located close to the middle of the energy band-gap. It has been shown that electrons exist below the valence band at very low temperatures, these electrons gain energy as temperature increases whereby, they can reach the conduction band and contribute significantly to the electric current. The shift of the Fermi level (E_F) with respect to the band-gap energy plays an essential role investigating the electronic properties and the change of coordination within the system [197].

The band structure of the three types of materials is given in figure 8, displaying the size of the band-gap between the valence band and the conduction band for these materials.

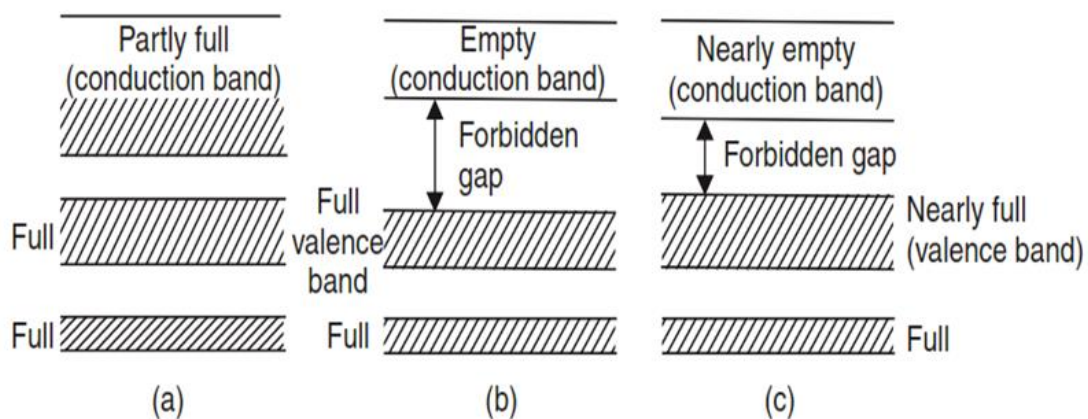


Figure 8: Band structure of (a) metal, (b) insulator and (c) semiconductor [195]

In a metal, the uppermost energy band is partially filled or the uppermost filled band and the next unoccupied band overlap in energy. Semiconductors have resistances between those of metals and insulators with a forbidden band-gap energy of 2 eV or

less between the valence band and the conduction band. In an insulator, the energy band-gap between the valence and conduction bands is very large, greater than 2 eV.

Quantum statistical mechanics [198, 199] make it possible to solve the Schrödinger equation to find the energies and wavefunctions of a particle of interest however it becomes increasingly difficult and impractical to individually solve each and every possible carrier wavefunction as well as its corresponding energy. Fortunately, it is possible to find the density of states instead of solving the Schrödinger equation multiple times. This DOS provides the total concentration of available states in that specified energy range as follows:

$$N_{interval} = \rho_{energy}(E)dE , \quad (3.50)$$

where $N_{interval}$ is the carrier density. Alternatively, equation (3.50) can be re-written as follows:

$$N_{tot} = \int_{E_1}^{E_2} \rho_{energy}(E)dE , \quad (3.51)$$

where $\rho_{energy}(E)$ is the desired density of states function in the energy range dE between the energies E_1 and E_2 . Furthermore, the density of states can be integrated over an energy range to produce the desired number of states as follows:

$$N(E) = \int_E^{\Delta E} g(E)dE , \quad (3.52)$$

where $g(E)dE$ represents the number of states between E and dE .

In this study, the density of states for the stable β -MnO₂ nanoclusters are calculated and presented, in order to understand the electronic behaviour of the generated

nanoclusters. Characteristics such as the width of the valence band, positioning of the pseudo gap, size of the band-gap-energy, Fermi energies and electronic contributions from the respective electronic orbitals will be analysed. Previous studies [200] have shown many inconsistencies between the theoretically calculated values and experimental values of Fermi energies hence the importance of this study.

3.8. Molecular dynamics

Molecular dynamics (MD) simulation is a computational technique used to study the motions of atoms in a given system (e.g., a solid material or a solid solution) in order to understand and predict the structural, dynamic, kinetic and/or equilibrium properties at chosen conditions (e.g., compositions, temperatures and pressures). The term “*ab initio*” is generally used to describe methods that are derived from first principles. The basic idea underlying *ab initio* molecular dynamics (AIMD) method is to compute the forces acting on the nuclei from electronic structure calculations that are performed [46]. Electronic structure calculations are mostly based on a time-dependent Schrödinger equation:

$$i\hbar \frac{\partial}{\partial t} \Psi (\{r_i\}, \{R_I\}; t) = \mathcal{H} \Psi (\{r_i\}, \{R_I\}; t) , \quad (3.53)$$

where i is the imaginary unit, \hbar is Planck’s constant, $\partial/\partial t$ indicates a partial derivative with respect to time t with electronic r_i and nucleic R_I degrees of freedom. \mathcal{H} represents the Hamiltonian operator for the electronic system and ψ is the position-space wavefunction. This approach neglects interactions between nucleons and relativistic effects. There are three main approaches for combining electronic structure calculations with molecular dynamics which can help overcome some of the

shortfalls associated with classical molecular dynamics. These approaches are the Born-Oppenheimer MD, Ehrenfest MD and the Car-Parrinello MD.

The dynamics task in CASTEP uses the Born-Oppenheimer MD based on the velocity Verlet algorithm for integrating the equations of motion. The efficacy of this method is brought about by considering wavefunction extrapolation between molecular dynamic steps and charge density extrapolation [201, 202]. In both Ehrenfest and Car-Parrinello schemes the explicitly treated electron dynamics limits the largest time step that can be used in order to integrate the coupled equations of motion for nuclei and electrons simultaneously. This limitation does not exist in the Born-Oppenheimer dynamics since there are explicit electron dynamics, therefore the maximum time step is simply given by the one intrinsic to nuclear motion.

The time-scale advantage of Born-Oppenheimer vs Car-Parrinello becomes evident if the nuclear dynamics become slower. The comparison of the overall performance of Car-Parrinello and Born-Oppenheimer MD in terms of computer time depends crucially on the accuracy of the conservation of the energy. Thus, the final conclusion is that the Born-Oppenheimer AIMD is the method of choice both in terms of accuracy and speed for approaches that use non-space-fixed basis to describe the electronic wavefunctions [203].

The electronic structure part in molecular dynamics is reduced to solving a time-independent quantum problem by solving the time-independent Schrödinger equation, concurrently to propagating the nuclei via classical molecular dynamics. The time-dependence of the electronic structure is a consequence of nuclear motion and not intrinsic as in Ehrenfest molecular dynamics. The resulting Born-Oppenheimer molecular dynamics method is defined by

$$M_I \ddot{R}_I(t) = -\nabla_I \min_{\downarrow} \{ \langle \Psi_0 | \mathcal{H}_e | \Psi_0 \rangle \}, \quad (3.54)$$

$$E_0 \Psi_0 = \mathcal{H}_e \Psi_0. \quad (3.55)$$

A natural and straightforward extension of ground-state Born-Oppenheimer dynamics is to apply the same scheme to any excited electronic state Ψ_k without considering any interference. This means that also the diagonal correction terms are always neglected as follows:

$$D_I^{kk}(\{R_I(t)\}) = -\int dr \Psi_k^* \nabla_I^2 \Psi_k. \quad (3.56)$$

These terms renormalise the Born-Oppenheimer potential energy surface E_k of a given state Ψ_k . It is deemed necessary to formulate the Born-Oppenheimer equations of motion for the special case of effective one-particle Hamiltonians [204]. This can be achieved by the Hartree-Fock approximation defined to be variational minimum of the energy expectation value $\langle \Psi_0 | \mathcal{H}_e | \Psi_0 \rangle$ given by a single Slater determinant:

$$\Psi_0 = \det \{ \Psi_i \}. \quad (3.57)$$

This is subject to the constraint of one-particle orbitals Ψ_i that are orthonormal and expressed as:

$$\langle \Psi_i | \Psi_j \rangle = \delta_{ij}. \quad (3.58)$$

The corresponding constraint minimization of the total energy with respect to the orbitals can be transformed into Lagrange's form:

$$\mathcal{L} = \langle \Psi_0 | \mathcal{H}_e | \Psi_0 \rangle + \sum_{ij} \Lambda_{ij} (\langle \Psi_i | \Psi_j \rangle - \delta_{ij}), \quad (3.59)$$

where Λ_{ij} is the associated Lagrangian multiplier. Unconstrained variations of the Lagrangian with respect to the molecular orbitals lead to the well-known Hartree-Fock equations:

$$\mathcal{H}_e^{HF} \Psi_i = \sum_j \Lambda_{ij} \Psi_j . \quad (3.60)$$

A similar set of equations is obtained if the Hohenberg-Kohn-Sham density functional theory is implemented. Applications of the Born-Oppenheimer molecular dynamics are performed in the framework of a semi-empirical approximation to the electronic structure problem using the *ab initio* approach. This approach has also improved the field of *ab initio* molecular dynamics by opening novel methods to treat large-scale computer simulation calculations [205]. Molecular dynamics is the preferred technique for performing statistical-mechanical simulations. MD makes it possible to determine and track the trajectories of molecules and atoms with respect to environmental changes.

The AIMD technique makes it possible to simulate the dynamic, thermal behaviour of atoms in solids by performing simulations at different temperatures and studying the displacements of the ions as a function of time which leads to predictions about diffusion coefficients and temperature dependences [46]. In practice, computer codes employ integration algorithms to solve Newton's equations using the microcanonical ensemble (NVE), canonical ensemble (NVT) and the isothermal-isobaric ensemble (NPT) as required. In the NVE ensemble, the system is isolated from variations in the amount of substance (N), volume (V) and energy (E). In NVT, amount of substance (N), volume (V) and temperature (T) are conserved. In NPT, amount of substance (N), pressure (P) and temperature (T) are conserved.

Molecular dynamics calculations result in various quantities describing the temperature-dependent behaviour of the analysed systems. In this study, AIMD is used to investigate the effect of temperature fluctuations on the stability and electrochemical activity of the manganese dioxide bulk structure and the generated stable nanoclusters. However, in AIMD simulations the resulting temperatures are not the actual melting temperatures of the systems, but rather the temperature where mechanical instability of the infinite single crystal occurs [206, 207].

Thermal energy has the ability to excite electrons across the band-gap in materials. Increasing the temperature of a material causes an increase in the number of electrons that have the required kinetic energy to be promoted into the higher conduction band. The electrical conductivity of a semiconductor increases proportionally temperature. For crystalline metal, an electron will travel through the crystal due to the applied electrical potential however it cannot travel too far because it will encounter and collide with the metal's nucleus. As the temperature of the solid increases, the atoms in the lattice become excited and acquire more kinetic energy because their positions are fixed in the lattice. However, the increased kinetic energy increases only the extent to which they are able to vibrate about their fixed positions.

At higher temperatures, the collisions between the metal nuclei with the mobile electrons occurs more frequently and with greater energy, thus decreasing the conductivity. This effect is, however, substantially smaller than the increase in conductivity with temperature exhibited by semiconductors. Doping can be used to tune the electrical properties of semiconductors by introducing small amounts of impurities that alter collisions with the electrons. If that impurity contains more valence electrons than the original atoms of the host lattice then the doped solid will have

more electrons present to conduct current than the pure host structure thereby improving its conductivity [16].

Doping is a proven way to adjust the conductivity of materials. Insulators are poor conductors because their valence bands are full. The electrical conductivity of semiconductors increases rapidly with increasing temperature, whereas the electrical conductivity of metals decreases slowly with increasing temperatures. Doping with an element with containing more valence electrons than the original host populates the conduction band, resulting in an n-type semiconductor with increased electrical conductivity [64].

Adding an element with fewer valence electrons than the atoms in the original host will generate holes in the valence band, resulting in a p-type semiconductor that also exhibits increased electrical conductivity [208]. In summary doping is capable of improving the conductivity of materials as required for materials used in the cathode of secondary rechargeable batteries.

3.9. X-Ray diffraction spectroscopy

In this section, the focus is on X-Ray diffraction spectroscopy. X-Ray diffraction (XRD) is a powerful multifunctional experimental and modelling technique used to determine the crystal structure and its lattice parameters. As previously stated, the β -MnO₂ has a tetragonal crystal structure meaning its lattice parameters are defined as $a = b \neq c$; $\alpha = \beta = \gamma = 90^\circ$. The precise scientific method of predicting the positions and arrangement of atoms in a crystal where the beams from these X-rays strike a crystal and causes the beam of light to diffract into many specific directions is referred to as X-Ray crystallography [209].

The knowledge of how atoms are arranged in crystal structures is the foundation on which the understanding of the synthesis, structure and properties of materials is built. X-ray diffraction gives valuable information on the crystallite size and the preferred orientation of the crystal [210]. In materials with a crystalline structure, X-rays are scattered coherently “in-phase” for certain directions meeting the criteria for constructive interference suggesting signal amplification and intensity. The conditions required for constructive interference can be explained by Bragg’s law;

$$n \lambda = 2 d \sin \theta . \quad (3.61)$$

For a tetragonal structure;

$$\frac{1}{d_{hkl}^2} = [h^2 + k^2 + l^2 \left(\frac{a}{c}\right)^2] \frac{1}{a^2} , \quad (3.62)$$

whereby d_{hkl} represents the d-spacing on the hkl plane. a , b and c represent the lattice parameters. (hkl) represents the Miller indices of the diffraction peaks.

The observed peak positions on the 2-theta (2θ) scale can be converted into d_{hkl} values using Bragg’s Law as follows;

$$d_{hkl} = \frac{\lambda}{2 d \sin \theta} , \quad (3.63)$$

where λ represents the X-ray wavelength, d is the distance between lattice planes, θ is the angle of incidence with the lattice plane and n represents an integer [211, 212].

X-ray diffraction patterns are graphs of the intensity of X-rays scattered at different angles as beams of light are directed through a sample. The number of X-rays observed in a peak on the 2θ scale varies due to instrumental parameters. A phase represents a specific arrangement of atoms in a structure. These phases all put

together represent a fingerprint that can be used to identify a specific material of interest. To identify a phase, the position and intensity of the reference peaks are matched to existing data repositories from previous published XRD patterns that have been reported and verified [213].

The Reflex module embedded in the Materials Studio software package is used in this study to determine the XRD patterns of the bulk structures and the stable nanoclusters.

3.10. Binding energy and relative stability

The binding energy or sometimes referred to as the internal cohesive energy is defined as the energy required to disassemble or break apart a whole structure into separate individual parts. The more firmly bound the atoms are in a system, the stronger the forces that keep the structure intact [214]. The binding energy of nanostructures is reduced relative to the bulk counterparts because their large surface to volume ratio decreases with the number of nearest neighbour bonds. A bound system has a lower potential energy than its individual constituent parts.

The stability of a structure and binding energy are directly proportional to each other and clusters with more binding energy are more stable [215]. Previous studies have shown that the binding energy of clusters is inversely proportional to the particle size for low-aspect-ratio nanoparticles [216]. The binding energy for the pure and doped bulk structures will be calculated using the following formulas;

$$E_B = [E(Mn) + E(O) - E(MnO_2)] / 2 , \quad (3.64)$$

$$E_B = [E(Mn) + E(O) + E(x) - E(Mn/xO)] / 2 , \quad (3.65)$$

Equation (3.64) will be used to calculate the binding energy of the pure/undoped β -MnO₂ where E_B is the binding energy of the bulk structure. $E(Mn)$ is the total energy of the separate individual manganese atom, $E(O)$ is the total energy of the separate individual oxygen atom and $E(MnO_2)$ is the total energy of the optimised β -MnO₂ bulk structure.

Equation (3.65) will be used to calculate the binding energy of the doped bulk structure where $E(x)$ represent the total energy of the separate individual dopant elements i.e., iron, cobalt and nickel [217, 218]. Two techniques of doping will be employed to investigate the effect of adding other elements to the stability of the optimised bulk structure and generated nanoclusters. The Virtual Crystal Approximation (VCA) method will be applied first and followed by the Substitution method.

3.11. Doping of the bulk structure and the nanoclusters

This section focuses on the theoretical background of the techniques that will be employed in the doping of the optimised β -MnO₂ bulk structure and its generated stable nanoclusters. The importance and efficacy of doping has been reported on previously in section 2.5 of the literature review showing the successes and challenges from previous studies in this field of nanostructural materials science.

Two techniques will be used in this study to dope the selected structures; the Virtual Crystal Approximation (VCA) method and Atomistic substitution method. Simulated doping is important as it allows scientists to investigate the disorder that arises in crystal structures when atomic vibrations increase at higher temperatures creating some disorder. This study will use the 'mixture atoms' functionality of Material Studio

to simulate the scenario where one atomic site is randomly occupied by two or more different types of atoms from different elements with distinct concentrations.

3.11.1. Virtual crystal approximation method

The virtual crystal approximation (VCA) method is an approach that can readily be applied to most types of pseudopotentials and it has been shown to produce good estimates of the atomic forces that would arise if the real atoms were present. VCA gives insight into the expected displacements in the lattice structure of crystals and solid solutions in the context of DFT.

The VCA is a much simpler and computationally less expensive approach to use in studying band-structure calculations as opposed to the supercell approach and the Coherent Potential Approximation (CPA). Previous studies have reported on the good accuracy of VCA when employed in researching some common semiconductor systems [219].

VCA ignores possible short-range order and assumes that there is a virtual atom on each potentially disordered site which interpolates between the behaviour of the actual components. This approach overlooks local distortions around atoms and cannot fail to reproduce the finer details of the disordered structures. VCA has been successfully used to investigate and predict the effect of doping in solid solutions. Its calculations are based on a weighting of the pseudopotentials according to site occupancies [220]. The main statement for the implementation of VCA with ultrasoft potentials can be written as follows: -

$$V_{ext}(r, r') = \sum_I \sum_{\alpha} w_{\alpha}^I V_{pe}^{\alpha}(r - R_{I\alpha}, r' - R_{I\alpha}) , \quad (3.66)$$

where α represents the total external potential that is generated as the sum of the nonlocal potentials of each atomic species, w represents the weights of the component atoms in the mixture atom. All the key components of the ultrasoft potentials; the local part, V_{loc} and the D and Q matrices, are all weighted according to the site occupancies. This basic premise of a workable VCA implementation for DFT was studied by Bellaiche *et al.* [219]. The DFT-based code, CASTEP will be used initially to optimise the doped structures and the MD code; DMol³ will be used to calculate the binding energies, band structures and density of states of the optimised doped structures.

The VCA method of doping is limited to smaller concentrations and it is recommended that it must be performed at lower percentages, preferably 20 % or less because it produces unphysical results at larger concentrations and for bigger systems. With VCA, the doping is done automatically to all manganese atoms present in the structure irrespective of the different bonds and levels of coordination existing on those individual atoms.

A percentage of the dopant concentrations at 10 % and 20 % is systematically introduced across all manganese atoms to determine which percentage of doping produces the more stable bulk structure and nanocluster in this study. The relative concentrations can be set for any number of atoms, where the total concentrations must all add up to a total of 100% when all the dopants have been added to the original atom.

This study will investigate two varying concentrations of doping: 10 % and 20 % doping on both the manganese atoms in the bulk structure. The results obtained will

show the preferred concentration of doping and also reveal which dopant element is more compatible with the pyrolusite bulk structure.

3.11.2. Substitutional method of doping

In some cases, VCA has been shown to produce unphysical results due to the inability of the traditional VCA to represent different chemical bonding and ionicity. On its own VCA does not sufficiently describe the different local atomic environment in inhomogeneous materials hence the use of the substitutional to validate the results obtained by VCA [221].

The atomistic substitutional approach is used to investigate the doping of the β -MnO₂ structure with the selected dopants; iron (Fe), cobalt (Co) and nickel (Ni). The investigation begins with determining which of the two manganese sites is preferred in substitution to gain insight into the substitution energy cost and subsequent preferential sites for the dopants in the host lattice of the bulk structure. This study will focus on the direct substitution of a preferred manganese atom with the dopant unlike the vacancy occupation technique followed in other studies.

The atomistic study of dopant site-selectivity has been conducted previously and has been shown to improve the stability and conductivity in the doped complexes [222, 223]. Substitutional doping has been shown to be capable of reducing the volume of structures as opposed to interstitial bonding which can increase the size of a structure due to the increase in the atoms after doping [224, 225].

The advantages of using the dopants we have selected is that the dopants will not require any charge-compensation because we are focusing on neutral compounds and no spin polarisation is applied during the calculations as proven by the Hirshfeld

charges and the Mulliken atomic charges all adding up to zero for all the structures. The DFT based approach towards doping has been shown to be more efficient as opposed to the semi-empirical potentials method although the DFT approach requires more computational resources and it is limited to smaller systems which is well suited to this study as it is centred on the smaller MnO₂ nanocluster systems [226].

3.12. Charge density differences

The previous section focused on the effect that doping will have on the stability and conductivity of the nanoclusters without detailing exactly what happens to the atoms, specifically to the valence electrons that will result in them becoming better or worse conductors. This section will investigate the electronic transfer and localisations that occurs between the manganese and oxygen atoms which ultimately determines what type of material MnO₂ is. The focus will also be on determining how doping affects the hybridization of electrons when a new dopant element is inserted into the existing MnO₂ stable nanocluster and the bulk structure.

The electron energy levels in the bulk structure are continuous while they become discrete in nano crystals because of the confinement of the electron wave function to the physical dimensions of the particles. This phenomenon is referred to as quantum confinement [227]. This phenomenon causes the energy of the band-gap to increase due the smaller dimensions when the energy levels are quantified, these sometimes results in the energy band overlap which was present in metals to disappear and transform into a band-gap between the conduction band and the valence band. This explains why some metals transform to semiconductors as their size is decreased

during nanostructuring. Some nanomaterials exhibit exceptional electrical properties that are related to their unique size dependent structures [228].

Investigating the hybridization and redistribution of charges during doping is important in the quest towards understanding the electronic and electrical properties of the optimised β -MnO₂ bulk structure and the generated stabilised nanoclusters. The analysis of the charge density differences enables the researchers to observe and visualise the types of bonds that are formed i.e., Covalent bonding or ionic bonding. This type of bonding depends on the size and significance in the overlap of the electronic density clouds due to the hybridization and redistribution of valence electrons in the outer most orbitals of the concerned atomic elements as the bonds are reformed during crystallisation shapes [229].

Ionic bonds form when a non-metal element and metallic element exchange electrons to form a bond, ionic bonds occur via an electrostatic attraction between two oppositely charged ions, in this case this will be the positively charged manganese and the dopant elements, with the negatively charged oxygen. The manganese represents the cation while the oxygen represents the anion. Covalent bonds occur when two atoms share a pair of electrons to form a bond. Covalent bonding is preferable in this study because atoms that have bonded covalently are regarded as being more stable in multiple states and have definite shapes [230].

Two distinct measurements of importance in the analysis of electronic charge density differences are the Hirshfeld charges and the Mulliken atomic populations. These two relatable quantities divide the atomic structures into well-defined fragments or partitions, which are studied with emphasis placed upon the effect that each fragment has on the other and also on the whole nanocluster. In this study, two computational

software have the sufficient capabilities to calculate the Hirshfeld charges and the Milliken atomic populations in a single calculation thereby ensuring their mutual interdependence; CASTEP and DMol3. These two codes will be discussed in more detail later in section 3.12 below.

3.12.1. Hirshfeld charges

Hirshfeld charges are explained in relation to their deformation density, this deformation density refers to the difference between the molecular and the unrelaxed atomic charges [130, 231]. The Hirshfeld analysis defines atomic charges by dividing the deformation density between the individual atoms in the molecule. In a molecule, the total density is the sum of well-defined contributions from all the constituent atoms that make up the whole molecular structure. Dividing the molecular density among the atoms at each point of the molecule mimics the atomic compositions. Algebraically, the proportional molecular density at point r is defined as;

$$\rho^{pro}(r) = \sum_i \rho_i^{at}(r), \quad (3.67)$$

Where the functions ρ_i^{at} are spherically averaged ground-state atomic densities. For each atom, the sharing function is defined by

$$w_i(r) = \rho_i^{at}(r) / \rho^{pro}(r), \quad (3.68)$$

The several sharing functions are all positive and equal to one everywhere. The charge density of the bonded atom i is defined by

$$\rho_i^{b.a.}(r) = w_i(r) \rho^{mol}(r), \quad (3.69)$$

whereby ρ^{mol} is the actual molecular density. Subtracting the density of the free atom from the bonded atom gives the atomic deformation density as follows

$$\delta_{\rho_i}(r) = \rho_i^{b.a.}(r) - \rho_i^{ba}(r) , \quad (3.70)$$

The total electronic charge in the bonded atom is thus given by

$$Q_i = - \int \rho_i^{b.a.}(r) dv , \quad (3.71)$$

The negative sign illustrates the negative charge of the electrons. Adding the nuclear component to the total electronic gives the net atomic charge as follows below

$$q_i = Q_i + Z_i , \quad (3.72)$$

This net atomic charge is the quantity referred to as the Hirshfeld charge that will be calculated using the chosen computational software code. The original Hirshfeld charges have been continuously improved throughout the years to incorporate the new emerging technologies developed to improve the accuracies and efficacies of calculations.

Bultinck *et al.* [130] claimed in his study that using an alternative iterative version of the Hirshfeld partitioning procedure ensures a proper mathematical representation of the entropy which allows the Hirshfeld approach to be used for charged molecules with increased magnitudes. This approach was resulted in a positive correlation with the electrostatic potential that was derived from the atomic charges.

3.12.2. Analysis of the Mulliken atomic populations

Atomic charges are key in materials science because they are used routinely to analyse experimental data and they are a fundamental component in atomic

computational simulations using quantum molecular force fields and plane-wave basis. Atomic charges measure the electron population occupying a specific atom. Out of the many approaches developed to calculate these atomic charges, the Mulliken atomic population analysis has emerged as the preferred method due to its conceptual appeal and calculation simplicity [131].

Mulliken charges and bond populations are measured using the plane-wave formalism. Plane-Wave basis have been shown to be large in some scenarios however the use of optimised pseudopotentials has had considerable success in reducing the number of plane-waves necessary to properly represent the electronic states [232].

The Cambridge Serial Total Energy Package (CASTEP) is used in this study to calculate the Mulliken atomic populations. Population analysis with CASTEP is done using a projection of the localised plane-waves into the atomic orbitals. The quality of the projection can be assessed using the following spilling parameter;

$$\sigma = \frac{1}{N_\alpha} \sum_k w_k \sum_\alpha \langle \psi_\alpha(k) | 1 - \hat{p}(k) | \psi_\alpha(k) \rangle, \quad (3.73)$$

N_α is the number of plane-wave states, w_k is the associated weight using the selected k-points in the Brillouin zone. $\hat{p}(k)$ gives the projection operator of Bloch functions with a wave vector k generated by the atomic basis set which is given by ...

$$\hat{p}(k) = \sum_\mu | \emptyset_\mu(k) \rangle \langle \emptyset_\mu(k) |, \quad (3.74)$$

where $| \emptyset_\mu(k) \rangle$ are dualities of the linear combination of atomic orbitals (LCAO) basis such that;

$$\langle \emptyset_\mu(k) | \psi_\alpha(k) \rangle = \langle \emptyset^\mu(k) | \emptyset_\nu(k) \rangle = \delta_{\mu\nu} . \quad (3.75)$$

The density operator may be defined as

$$\hat{\rho}(k) = \sum_\alpha^{occ} n_\alpha |X_\alpha(k) \rangle \langle X^\alpha(k)| , \quad (3.76)$$

where n_α is the occupancy of the plane-wave states and $X_\alpha(k) \rangle$ is the projected plane-wave states. From this operator, the density matrix for the atomic states can be calculated as follows

$$P_{\mu\nu}(k) = \langle \emptyset^\mu(k) | \hat{\rho}(k) | \emptyset^\nu(k) \rangle . \quad (3.77)$$

The overlap matrix of the localised basis set is defined as

$$S_{\mu\nu}(k) = \langle \emptyset_\mu(k) | \emptyset_\nu(k) \rangle . \quad (3.78)$$

The density matrix and the overlap matrix make it possible to perform the population analysis whereby the charge associated with atom A is given by

$$Q(A) = \sum_k w_k \sum_\mu^{onA} \sum_\nu P_{\mu\nu}(k) S_{\nu\mu}(k) . \quad (3.79)$$

The overlap population between atom A and atom B is thus

$$n(AB) = \sum_k w_k \sum_\mu^{onA} \sum_\nu^{onB} 2 P_{\mu\nu}(k) S_{\mu\nu}(k) . \quad (3.80)$$

The weight of an α band on a μ orbital is given by

$$W_{\alpha\mu}(k) = \langle \psi_\alpha(k) | \emptyset_\mu(k) \rangle \langle \emptyset^\alpha(k) | \psi_\alpha(k) \rangle . \quad (3.81)$$

The above equations make it possible to calculate the charge accumulated on each atom and also the contributions of each band to the density of states. The basis set

that is applied on a specific atom is that of the orbitals in the closed valence shell of that species. These orbitals are determined by calculating for the lowest energy eigenstates of the applied pseudopotential.

Caution should be taken when increasing the basis sets because this can lead to inconsistencies with natural chemical intuition. The theory and techniques discussed here was successfully shown to produce reliable results on the nature of bonds from plane-wave pseudopotential calculations in the DFT paradigm [233, 234]. CASTEP incorporates the formalisms explained in section 3.11 to successfully produce the Hirshfeld charges and the Mulliken atomic populations which are essential in analysing the electronic charge density differences.

3.13. Implementation of computational software codes

This section discusses all the computational software codes implemented in this study. This section will also look into the interfaces that house a variety of stand-alone codes that can be aligned to function together towards a common purpose.

3.13.1. GULP

The General Utility Lattice Program (GULP) [141] is designed to perform varying calculations based on force field methods. The original code was developed to incorporate the fitting of interatomic potentials to both energy surfaces and empirical data. GULP supports geometry optimisation and molecular dynamics of molecules, clusters, 2D and 3D systems using a wide range of potential models that covers both the organic fields and inorganic fields.

The potentials include the shell model, embedded atoms (for metals) and bond order reactive force-fields. The potentials describing the interatomic interactions between two ions with formal charge Z separated by the distance r can be represented as:

$$U_{ij} = \frac{z_i z_j e^2}{r} + A e^{\left(-\frac{r}{\rho}\right)} - \frac{C}{r^6}, \quad (3.82)$$

where the first part is the long-range Coulomb term and the latter are the short-range terms, Pauli repulsion and the leading term of the dispersion energy. The A , ρ and C parameters are the adjustable potential parameters [49]. In this study, the GULP code was incorporated inside the knowledge-led master code and used to generate MnO₂ nanoclusters employing interatomic potential methods.

3.13.2. Knowledge-Led Master Code

The Knowledge Led Master Code (KLMC) was designed as a means to automate many singular tasks traditionally performed by a user employing other third-party computer simulation tools to construct complex calculations which used a lot of computer resources and demanded too much time, however, the KLMC code incorporates a multistage approach which uses the same third-party codes in a single calculation. KLMC learns on the fly and refines input files that are submitted for new calculations and it can be easily set up to exploit massive parallel computing platforms for a more general set of applications that may require statistical sampling over large landscapes.

KLMC can run on local machines and is also capable of transferring many other individual calculations, or tasks to other larger networked resources elsewhere on high computation platforms. KLMC applications include simple task farming (screening structures imported from the database of other third-party codes). They

include the structural prediction of nano-sized clusters, surfaces and bulk phases using a range of global optimisation techniques based on basin hopping and genetic algorithms. It also allows for the exploration of ergodic regions (application of the energy lid or threshold algorithm) and statistical sampling of solid solutions or multiple point defects in a crystalline solid [235].

KLMC makes it easier to submit calculations to third party codes, monitor the progress of these calculations, extract data from the output files of these third-party codes, edit the files as necessary to resubmit the uncompleted calculations and distribute the workload of these calculations on all available nodes to produce final results in a number of required formats. KLMC can therefore be seen as a tool that maximises chain optimisation calculations while still affording the control to the user.

In this study, the Genetic Algorithm (GA) module inside KLMC is used to generate a sample database of nanocluster structures, performing post-calculation analysis, generating, editing, reading of input and output files for use in third party codes; GULP [138, 43], FHI-aims [48, 49] and VASP [26, 47] for further calculations. KLMC is used to drive random and global optimisation routines. It can generate and update a structure's database and it links up with other computational software codes such as GULP to compute and minimise IP energies determined during the global optimisation calculations.

The structural database is then linked up with the FHI-aims code to compute and optimise the structures determined from GULP using interatomic potentials. In the final stages of the refinement of structures in the database, the generated nanoclusters are ranked according to their stabilities of $(\text{MnO}_2)_n$ for sizes $n = 2$ to 20.

3.13.3. FHI-aims

The Fritz Haber Institute ab initio molecular simulations (FHI-aims) package is an all-electron code for efficient high-accuracy DFT calculations with advanced exchange-correlation methods like the many-body perturbation theory. It can be used to perform efficient all-electron modelling of molecules, clusters, surfaces, interfaces and bulk materials. The FHI-aims code incorporates a number of default basis sets for each atom, with the accuracy increasing from “tier 1” to “tier 4” and further basis functions below -0.08 meV. However, due to the ionic nature of the Mn atoms. Only tier 1 basis sets proved necessary when ranking the nanoclusters together with the default “light” settings set for tolerances.

The PBEsol functional was chosen because it is not too computationally expensive and it is also unbiased when it comes to neutrally charged systems. The FHI-AIMS code will be used to optimise the generated nanoclusters as well as to perform doping using the substitution technique where a suitable manganese atom will be determined and replaced with the selected dopants. The FHI-AIMS code will also be used to measure the band-gaps between the Highest Occupied Molecular Orbitals and the Lowest Unoccupied Molecular Orbitals (HOMO-LUMO band-gaps)

3.13.4. Materials Studio

Accelrys Materials Studio is an inclusive computer software package that is designed to host vast computational nodules that can be used for research into chemicals and materials studies. The vast capabilities and functions of this software package includes analytical and crystallisation software that helps investigate, predict and modify the crystal structure and crystal growth. Materials Studio's visualisation and

statistical tools enable users to instantly view structures to obtain more data and greater insight about factors affecting the material's properties.

The Materials studio visualizer provides a broad range of support for the description of crystals and offers users the ability to change symmetry and periodicity of crystals. The specific codes used in this study are discussed below briefly. CASTEP will be used for the geometric optimisation of the bulk structure and the nanoclusters. Reflex will be used to study the X-Ray Diffraction spectroscopy. DMol3 will be used to investigate the effect of adding dopants on the stability of the bulk structure and the generated nanoclusters. DMol3 will also be used to calculate the bonding energies of the selected structures.

3.13.4.1 CASTEP

CASTEP (Cambridge Serial Total Energy Package) is a quantum mechanics-based scientific code designed for solid-state materials science and is embedded in Materials Studio software package. CASTEP employs density functional theory plane-wave pseudopotential method which enables users to perform scientific simulations and calculations that explore the various properties of crystalline structures based on first-principles quantum mechanics. It was originally developed by Payne *et al.* [168] and subsequent developments were added by a large number of collaborators and researchers [236].

In CASTEP, the solution to a set of one-electron Schrodinger (Kohn-Sham) equations is executed using the plane-wave pseudopotential approach. The wavefunctions are expanded in a plane wave basis set that is defined using simple periodic boundary conditions and Bloch's Theorem. Direct energy minimisation schemes are used to

obtain the electronic wavefunctions and the corresponding charge density. Although the total energy is the central quantity in CASTEP, that total energy is measured in response to external influences that are also vital in an effort to compare with experimental data.

In this study, CASTEP is used to determine stability of the nanoclusters and calculate their structural, electronic and thermal properties [27]. All the DFT optimisations performed in this were done using CASTEP for both the bulk structures and the generated nanoclusters. The NVE molecular dynamics calculations presented in this study were also calculated using CASTEP, this includes the effects of temperature fluctuations on stability. The doping of the bulk structure and stable nanoclusters presented in this study using both the Virtual Approximation Method and the atomistic substitution method were also conducted using the CASTEP code

3.13.4.2 Reflex code

The Reflex module is a computer software tool that simulates and analyses X-ray diffraction data. The reflex module is also embedded in the Material Studio software package. It extracts vast amounts of data from diffraction patterns of organic, inorganic, organometallic and biological crystals [237]. Reflex monitors the effects of structural changes on the diffraction patterns by providing graphical representations of the simulated data to display X-ray diffraction patterns. Analysis of the diffraction patterns reveals interesting aspects of the atomic structure and energy of the crystal.

The Reflex module is used in this study to calculate XRD patterns for the bulk structures and stable nanoclusters. All the XRD pattern in this study were developed using the Bragg-Brentano geometry with no peak shifts selected to display the

intensities clearly, copper was the selected source and the polarisation was set to 0.50. The Pseudo-Voigt function was used and atomic temperature factors were used. A 0.05 step size on a 5.00 to 40.00 range on the 2θ positional scale was set. A d-spacing ($1/d_{hkl}$) of 0.056628 and a separation ($1/\text{\AA}$) of 0.44402 were used to generate all the XRD patterns in this study.

3.13.4.3 DMol³ code

The DFT-based code DMol³ was employed to investigate the electronic properties of the bulk β -MnO₂ structure and the generated nanoclusters. The basic DMol³ methodology uses a three-dimensional numerical integration for the matrix elements which only makes minimal assumptions about the form of the basis functions and molecular orbitals [238]. The local functionals used in DMol³ are the Perdew-Wang generalised-gradient approximation (PW91) [239].

DMol³ combines computational speed with the accuracy of quantum mechanical methods and first principle methods to predict the properties of materials reliably and quickly. Furthermore, the localised numerical orbitals used as basis sets for DMol³ are designed to offer maximum accuracy for a given basis set. Recent advances in DMol³ have made it a band structure method capable of computing the SCF with general k-points. These upgrades have also introduced Hard-core semi-local pseudo-potentials which help to reduce the size of the matrices. The pseudo-potentials give a favourable means to introduce scalar relativistic effects into a formerly non-relativistic approach thereby speeding up the calculations and reducing the computational costs [51].

In this study, DMol³ was used to determine the electronic properties of the bulk β -MnO₂ and the generated nanoclusters. In particular, the density of states, the Fermi energy and the band-gap energy were calculated. Furthermore, the binding energy is also calculated as way to determine the effect of doping on the stability of the bulk structure and the nanoclusters using this code.

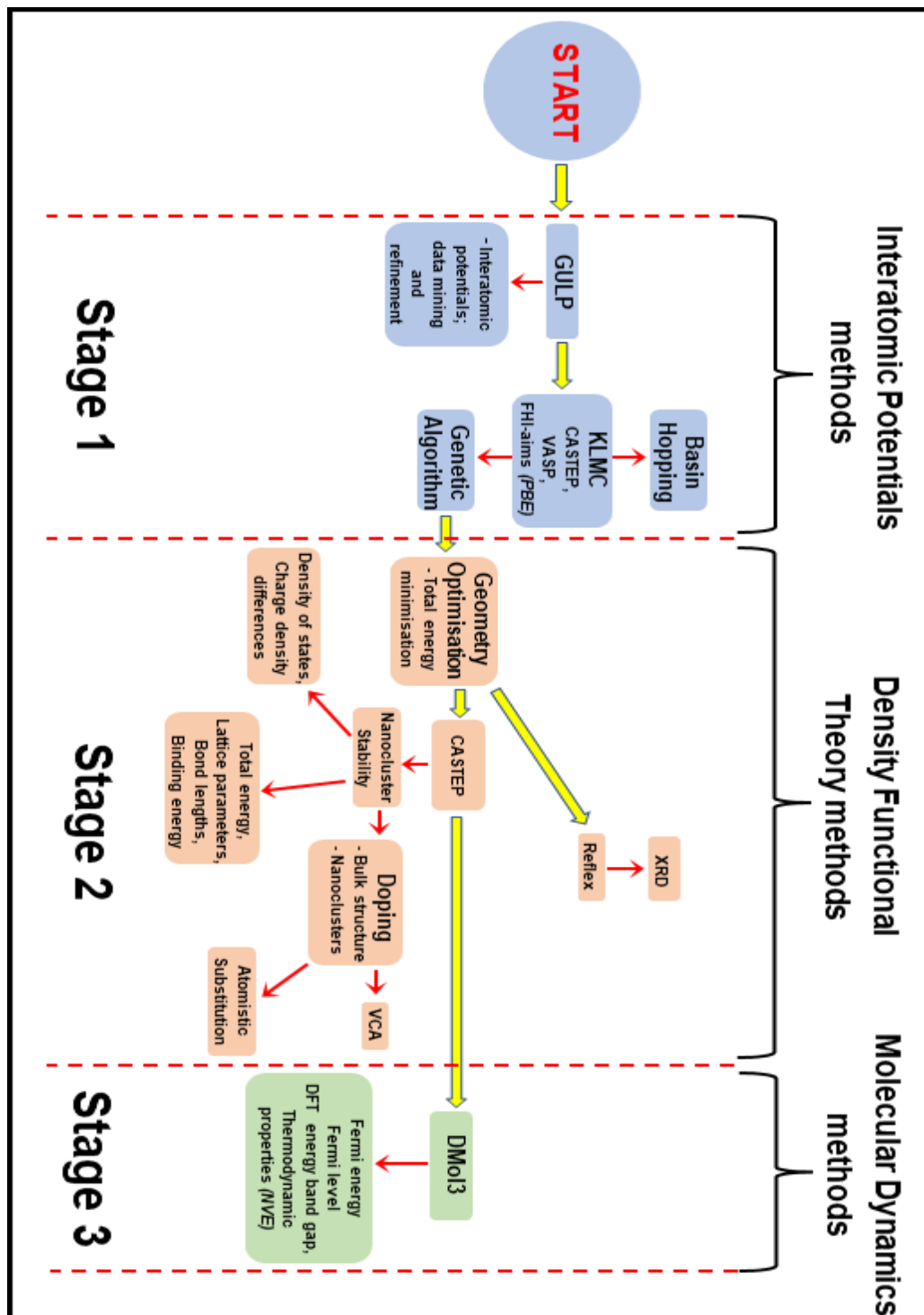


Figure 9: Flow chart of the computational codes used and the properties measured

Figure 9 displays the sequence of calculations employed through the evolutionary algorithm sequence used to generate the nanoclusters. The figure also shows all the codes used and the properties that were measured using those codes.

Chapter 4: β -MnO₂ bulk Structure

This chapter gives analysis on the β -MnO₂ bulk structure and nanoclusters. In particular, the structural properties of the bulk structure such as the lattice parameters and the bond lengths. The stability of the β -MnO₂ bulk structure at varied temperatures is also discussed. Furthermore, the XRD patterns and the effect of doping the bulk structure with different transition metals as dopants is discussed.

4.1. Convergence tests: cut-off energy and k-points

The convergence tests for both the cut-off energy and k-point mesh are of particular importance in DFT calculations. They ensure that the accurate ground state equilibrium parameters of the β -MnO₂ bulk system is realised. The β -MnO₂ bulk structure was subjected to a full geometry optimisation and energy minimisation procedure using DFT techniques. The energy cut-off is an important parameter in PWP calculations because it determines the number of plane waves required in a minimisation process.

The geometry optimisation calculations were performed by allowing the lattice parameters and cell volume to relax using the Broyden-Fletcher-Goldfarb-Shano (BFGS) minimisation method employing the determined stable cut-off energy and suitable k-point mesh. Electronic minimisation was performed using the band-by-band conjugate gradient (CG) method. The DFT-based planewave CASTEP code using the GGA-PBE functionality was used to perform the convergence tests for the stable cut-off energy and suitable k-point mesh.

4.1.1. Cut-off energy

Calculations based on different values of the cut-off energy ranging from 250 eV to 900 eV were performed in order to achieve minimisation of the total energy. The convergence tests for the varying cut-off energies were determined by performing a series of single-point calculations at a constant default k-point set. Figure 10 illustrates the convergence of the total energy as a function of the cut-off energy.

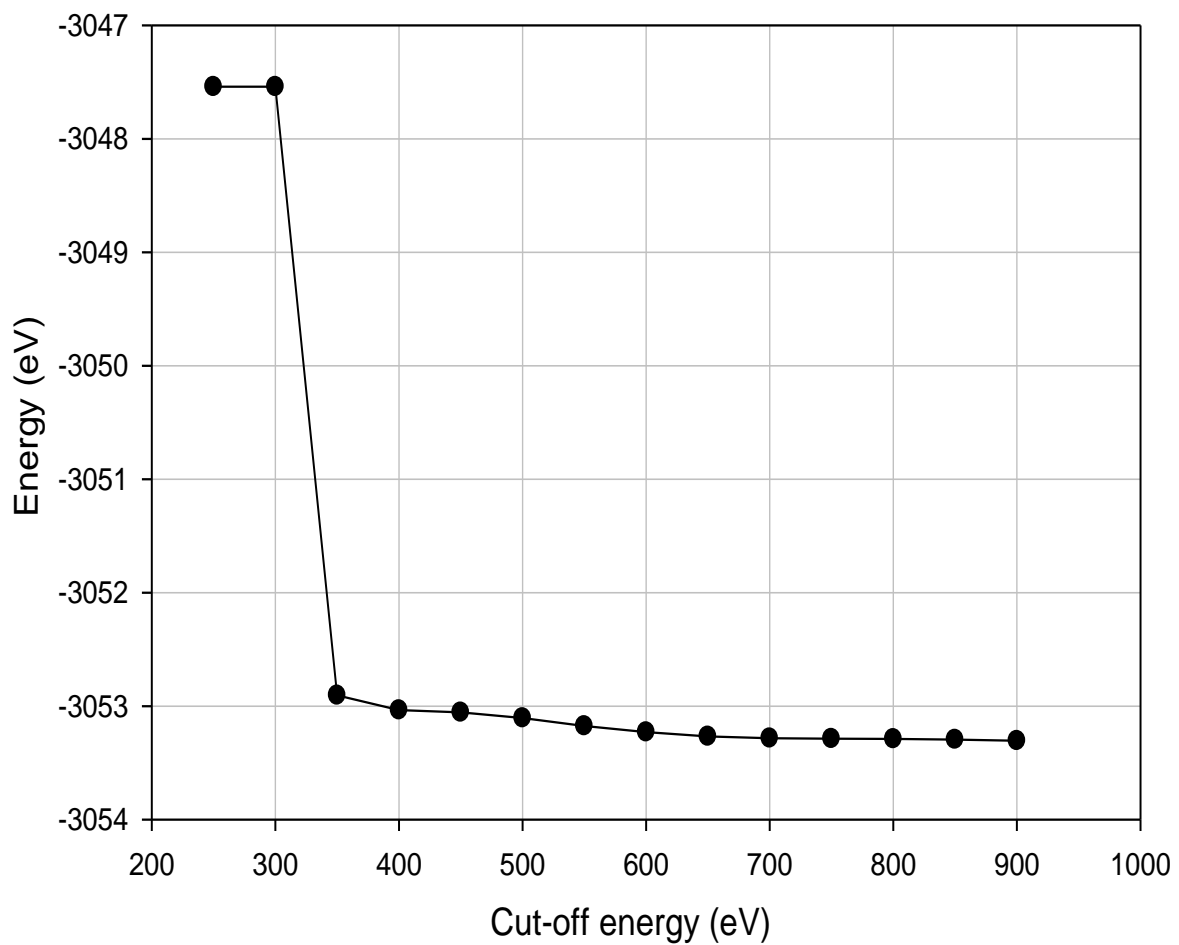


Figure 10: The plot for the total energy versus energy cut-off of the β -MnO₂ bulk structure.

Figure 10 displays the total energies measured at varying temperatures from 250 eV to 900 eV varied with a 50-eV difference for every calculation. From the plot in figure 10, it is observed that the total energy decreases and becomes more stable as the

energy cut-off is increased. There is a steep decrease in the total energy from 300 eV corresponding to a total energy of -3047.5409 eV to a cut-off energy of -3053.0354 at a cut-off energy of 400 eV. From the cut-off energy of 450 eV, the graph stabilises and its energy difference decreases very slightly to 500 eV.

The cut-off energy of 500 eV with a total energy of -3053.1054 eV is identified as the most stable cut-off energy. It is at this point where the total energy is relatively constant with a negligible variation in the energy difference of less than 1 meV/atom and a marginal gradient in the slope. This cut-off energy of 500 eV is then used to determine the suitable k-point mesh. This cut-off energy will also be used to calculate all the DFT and molecular dynamics calculations for the MnO₂ nanoclusters in the latter chapters of this study.

4.1.2. k-point mesh

The convergence test for the total energies was performed using the constant cut-off energy of 500 eV to determine a suitable k-point set for the β -MnO₂ bulk structure. The Monkhorst-Pack scheme was used to select an optimal set of a special k-point sample size integrated on the Brillouin zone such that the greatest possible accuracy is achieved from the number of k-points used. The number of k-points is determined by running self-consistent field (SCF) calculations for different k-point sets ranging from 1x1x2 to 10x10x20, these k-point sets are chosen based on them befitting the tetragonal crystal structure of pyrolusite.

Table 1 gives the single-point energy results determined from calculating the total energy at different k-point sets with the cut-off energy of 500eV until minimisation is achieved as shown in figure 11.

Table 1: k-points at 500eV cut-off energy of the β -MnO₂

k-points	x-axis	Total energy (eV) y-axis
1x1x2	1	-3046.7399
2x2x4	2	-3053.1054
3x3x6	3	-3052.7629
4x4x8	4	-3052.8505
5x5x10	5	-3052.7973
6x6x12	6	-3052.8075
7x7x14	7	-3052.8046
8x8x16	8	-3052.8003
9x9x18	9	-3052.7982
10x10x20	10	-3052.7975

Figure 11 displays the plot for total energy measured at varying k-points corresponding to the rutile tetragonal crystal space group of β -MnO₂ given in table 1.

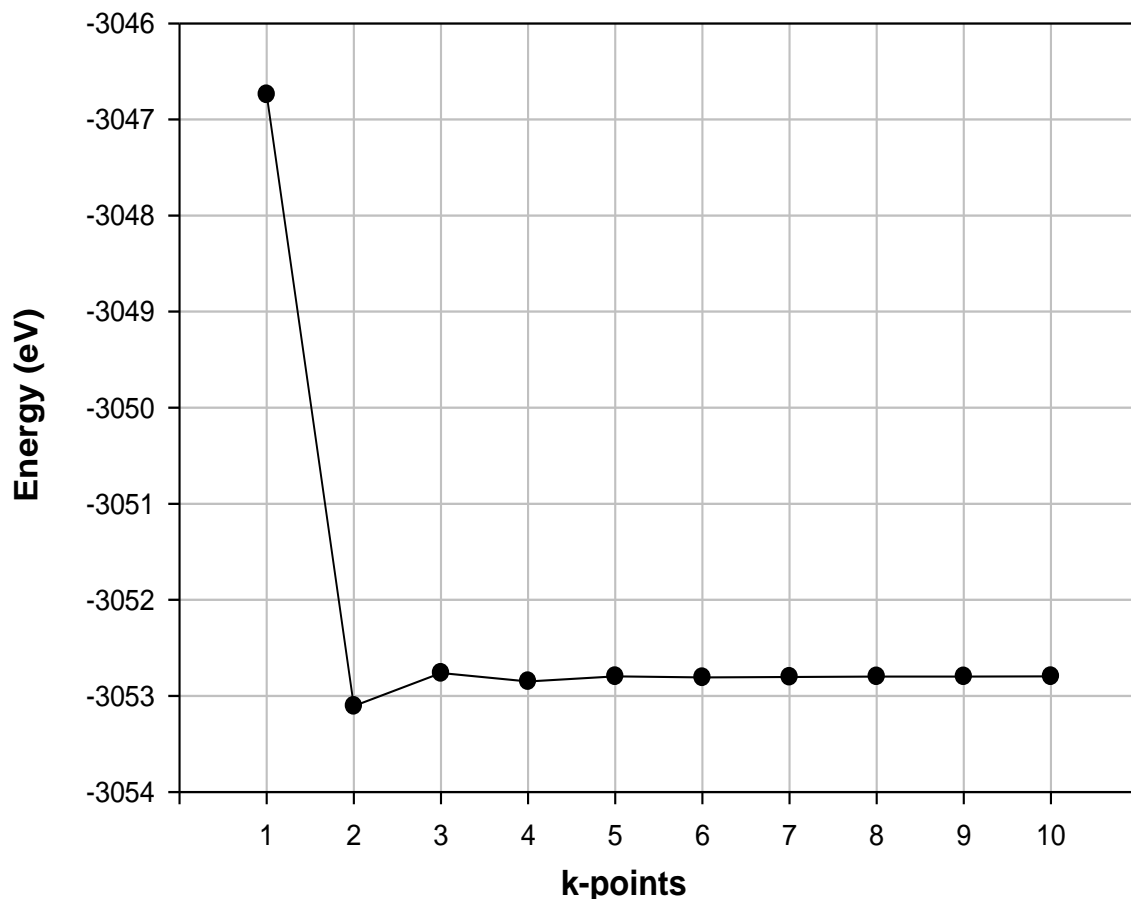


Figure 11: Plot for total energy vs k-points of the β -MnO₂ bulk structure

From figure 11, a steep decrease in the total energy occurs from the 1x1x2 k-point set to the lowest point at a k-point set of 2x2x4. From this point, the plot fluctuates upwards momentarily and begins to stabilise. Therefore, the k-point set of 2x2x4 which has the lowest total energy of -3053.105 eV is identified as the most suitable to accurately converge the bulk structure to its stable ground state.

From this 2x2x4 k-point set there is an energy difference of less than 1 meV/atom as the k-point set is increased sequentially which reinforces the choice of this k-point mesh to perform all the DFT and molecular dynamics calculations in this study. Furthermore, a geometry optimisation calculation was performed on the bulk β -MnO₂ structure using these derived parameters.

4.1.3. Optimisation of the β -MnO₂ bulk structure

A geometry optimisation calculation was performed using the 500-eV cut-off energy and the 2x2x4 k-point mesh. The Pulay correction was applied to the forces in order to compensate for the selected energy cut-off. The tolerance in the total energy and the pressure change before self-consistency was 1×10^{-5} eV/atom with a 0.05 GPa. The root mean square (RMS) tolerance for the atoms' maximum displacement was restricted to 0.001 Å with two hundred maximum iterations and five hundred SCF cycles used to achieve the required minimisation. These parameters were successfully used to optimise the β -MnO₂ bulk structure and the results are presented in table 2 with reference to results from previous similar parameters.

The percentage difference values presented in table 2 were calculated using the calculated parameters from the DFT-optimised β -MnO₂ bulk structure compared against parameters derived from a previous study employing IP techniques. The equation used to calculate the percentage difference is given as follows;

$$\% \text{ Difference} = \frac{|E_1 - E_2|}{(E_1 + E_2) / 2} \times 100 \% \quad (4.1)$$

where E_1 is the experimental value of the bulk structure from this study and E_2 is the value of the optimised bulk structure from a previous IP study. For example, the percentage difference for the cell volume was calculated as follows;

$$\% \text{ Difference} = \frac{|53.98 - 64.21|}{(53.98 + 64.21) / 2} \times 100 \% = 17.31 \% .$$

This percentage difference calculations serve to compare the results of this study employing DFT techniques with another study employing IP techniques in order to determine which method is best suitable for optimising the bulk β -MnO₂ structure to

its most accurate and stable ground state configuration. Results from other experimental and computer simulation studies are also included as a reference point in table 2.

Table 2: Comparison of the lattice parameters (Å), cell volume (Å³), bond length (Å) and density (g/cm³) of the bulk β-MnO₂ Structure

Parameters	Calculated (DFT-CASTEP)	Experimental [26]	IP [163]	Other works
a = b (Å) (% diff.)	4.395 (0.43 %)	4.414	4.462	4.404 [21] (exp.) 4.459 [21] (GGA) 4.398 [42] (exp.)
c (Å) (% diff.)	2.795 (14.32 %)	2.860	3.226	2.876 [21] (exp.) 2.906 [21] (GGA) 2.873 [42] (exp.)
Cell volume (Å ³) (% diff.)	53.98 (17.31 %)	55.56	64.21	55.78 [21] (exp.) 57.78 [21] (GGA) 55.58 [42] (exp.)
Density (g/cm ³)	4.99	5.20	4.50	5.19 [42] (exp.)
Bond length (Å)				
(Mn-O1)	1.898	1.891	1.965	1.884 [21] (exp.)
(Mn-O2)	1.823	1.886	1.783	1.904 [21] (GGA)
Total length	3.721	3.777	3.748	3.788

Table 2 compares the calculated bulk β -MnO₂ structure which was optimised using the DFT-based CASTEP code with the bulk structure optimised by interatomic potentials techniques in a previous study by Maphanga *et al.* [163]. The results are also compared with a DFT based study using the GGA functional by Balachandran *et al.* [21] and an experimental study of a rutile type MnO₂ by Baur *et al.* [42]. The bulk structure maintains its crystal structure with a space group of P42/MNM (D4H–14). The optimised β -MnO₂ bulk structure with parameters displayed in column 2, i.e., calculated (DFT-CASTEP) is displayed in figure 12 with bond lengths of interest labelled within.

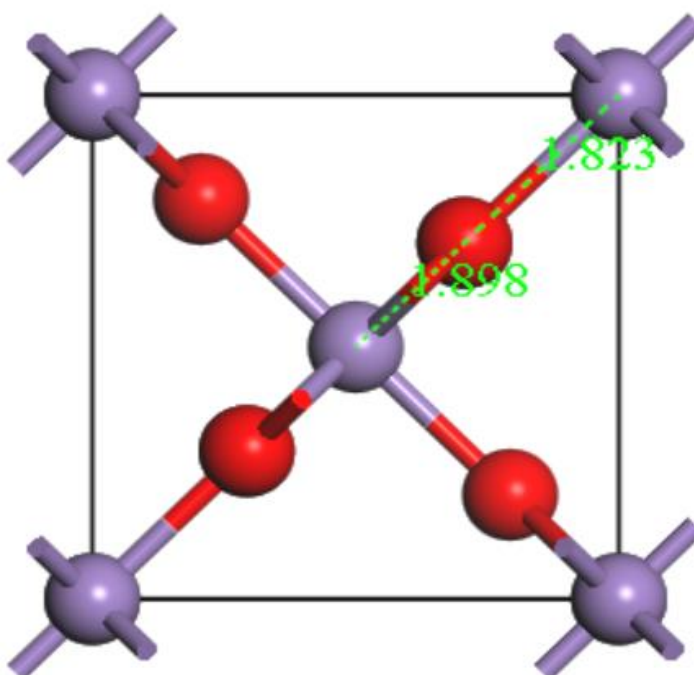


Figure 12: Atomic arrangement of the DFT optimised β -MnO₂ bulk structure displaying the Mn (purple) and O (red) atoms

The analysis in this section focuses on the structural properties, i.e., the lattice parameters, cell volume, density and the bond length between similar manganese to oxygen bonds [240]. It is observed that the DFT CASTEP results are in better

accordance with the experimental data [42] and other previous studies [21]. The DFT calculated lattice parameters agree to within 5 % of the experimental data, however there is a significant deviation when compared to the IP results as proven by the percentage difference in the “c” lattice parameter and the cell volume being greater than 14 % [163].

Moreover, this shows that the IP calculations still require further refinement before they can be applied on larger scale for this type of calculations. It is observed from figure 12 that the calculated parameters from the DFT optimised bulk β -MnO₂ structure indicates a decrease in the lattice parameters and bond lengths as compared with the parameters from the IP optimised bulk structure. This is in accordance with the objectives of the study to decrease the size of the structures while improving their structural stability and electrochemical performance.

This shows that optimisation with DFT is the preferred method of minimising the bulk structure for the purpose of this study. In the next chapter, the DFT optimised results for the generated nanoclusters is presented.

4.2. X-Ray diffraction patterns for the bulk β -MnO₂ structure

This section focuses on the X-ray diffraction patterns of the optimised bulk β -MnO₂ bulk structure. The XRD patterns were extracted using the Reflex module and these are compared with previous experimental studies to validate the current results. Figure 13 (a) and (b) shows the XRD patterns of the simulated bulk β -MnO₂ structure compared to the XRD patterns from a previous experimental study by Zheng *et al.* [241].

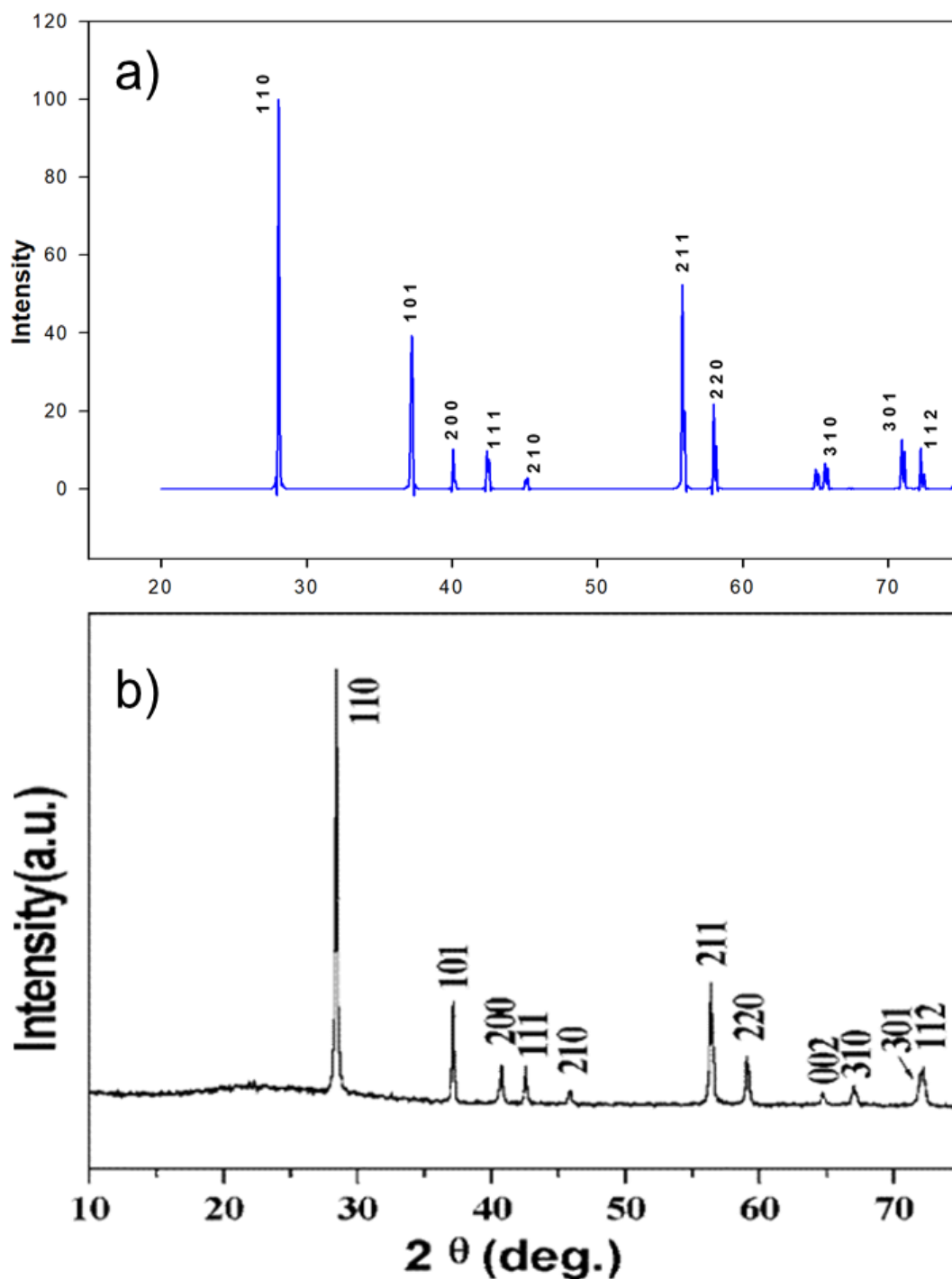


Figure 13: XRD patterns comparing (a) simulated XRD patterns of the bulk β -MnO₂ structure generated using the Reflex module and (b) an experimental study [241].

From figure 13 (a) and (b), the simulated and experimental XRD peaks appear to be similar. It can be clearly seen that all the dominant peaks are observed on both the

simulated and experimental XRD patterns. There are three dominant peaks observed at 28°, 37° and 58° corresponding to (110), (101) and (211) respectively. Furthermore, it is observed that the indexed X-ray diffraction peaks from our current study confirm the tetragonal phase of the β -MnO₂ structure. This is confirmed by the similarity with the XRD pattern from a previous experimental study as displayed in figure 13 (b) [242] of a tetragonal phase of MnO₂.

Minor differences are observed in the size of the peak widths and intensities. Specifically, these differences are brought about by the presence and quantities of impurities or foreign elements in the samples of experimental studies as compared to the purity of simulated studies. The peak width gives insight into the size of the crystallite as well as the significance of the deformations found in the crystallite [243]. Moreover, the width of the peaks on the XRD patterns of the optimised β -MnO₂ bulk structure is very narrow and of roughly equal size for all the peaks. Note that XRD peaks can be broadened by crystal defects [244]. There are no peaks observed for other types MnO₂ phases indicating high purity and crystallinity. All the major distinguishable peak positions are similar on both the previous study and the current study but differ slightly in the intensities.

The (211) peak displays the greater intensity on the XRD pattern of the optimised β -MnO₂ structure which can be attributed to the absence of impurities and other defects in this simulated bulk structure. Their absence removes adverse sound that limits the detection of dominant phases. This intensity differences are also observed for the (101) and (220) peaks. The (301) and (112) peaks are clearly separated on the simulated XRD patterns in contrast with those merged together as observed on the XRD pattern from the experimental study by Zheng *et al.* [241]. These differences show that this simulated study produces better quality results focusing solely on the

target elements while disregarding imperfections brought by impurities and foreign elements present in experimental studies.

It is encouraged to undertake more computer simulation studies because they are shown to produce results that are consistent with experimental studies and sometimes even indicating improvements. The XRD patterns show that similar phases were discovered in the simulated patterns with those from the experimental and naturally occurring minerals however the real minerals are saved and used for the actual use that will benefit humanity.

4.3. Effect of temperature on the stability of the bulk β -MnO₂ structure

This section focuses on the effect that changes in temperature affect the stability of the bulk β -MnO₂ structure. In order to explore the effect of temperature on the stability of the bulk β -MnO₂ structure, a molecular dynamics (MD) calculation was conducted with the CASTEP code using the NVE ensemble with the GGA-PBE functionality. In these calculations the temperature is changed while the number of atoms and volume are kept constant. At each and every iteration, the temperature is set and the corresponding energy is recorded.

The analysis of the results in this section will help determine the effect that fluctuating temperatures has on the bulk structure's stability. This will aid to also determine ways of maintaining the bulk structure's integrity with respect to the natural temperature changes in the environment. The results for the total energy versus the temperature is displayed in figure 14. This is done because first-principles total-energy

calculations have been shown to be of significant importance when examining the properties of materials and their interactions [245].

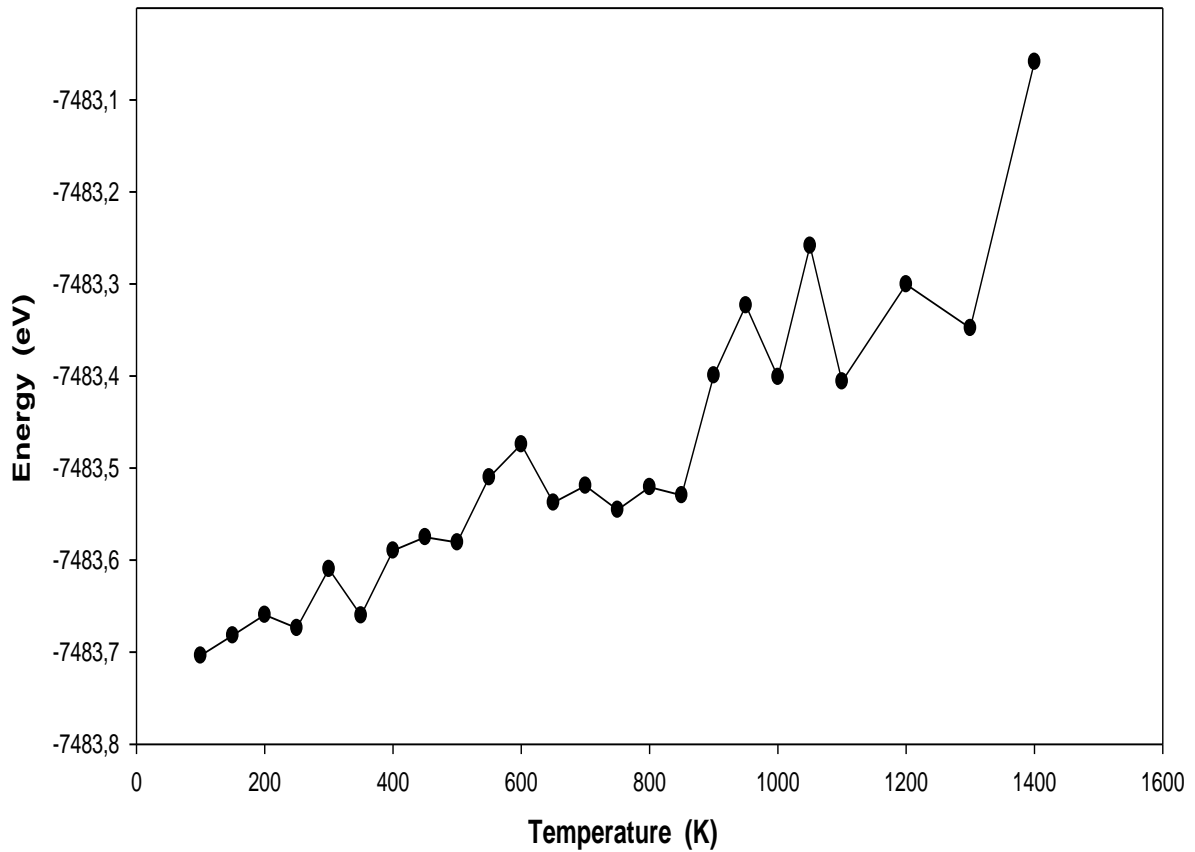


Figure 14: Plot illustrating the behaviour of the bulk structure with respect to increasing temperatures.

Figure 14 indicates the total energy of the bulk β -MnO₂ structure against the increasing temperature (ranging from 100 K to 1500 K). This temperature was selected to observe the behaviour of the bulk structure and the nanoclusters at the various melting points of the main polymorphs of manganese dioxide and also at extremely higher temperatures for use in aeronautical applications.

- At lower temperatures up to 200 K, the β -MnO₂ bulk structure is still crystallised. However, beyond this temperature a minor fluctuation is observed.

- Another fluctuation is observed between 400 K and 600 K, where the plot appears stable from 600 K to 800 K.
- Above 800 K, the structure appears to have lost shape due to the large fluctuation observed. This implies that there is a possible phase change occurring at this temperature. This behaviour is in line with the experimental observations that the bulk β -MnO₂ melts at 808K (535 °C) where MnO₂ possibly decomposes and transitions into other polymorphs of manganese dioxide that may differ from the original rutile structure of the bulk pyrolusite [246]. This phenomenon will be investigated further when studying XRD patterns of the doped nanoclusters.

This sharp increases in the plot have been shown to be indicative of phase transitions in previous studies as reported by Jassem *et al.* [128]. It was reported that manganese oxide nanoparticles were successfully synthesised at 600 °C (873 K) then transformed to the tetragonal MnO₂ at 800 °C (1073 K) which is consistent with observations from this current study. The plot shows that the structure's stability decreases with increasing temperatures.

Another study by Antoniammal *et al.* [247] accounted for the variations of the locations of these peaks in the current study as they concluded that the melting point of spherical cylindrical nanostructures decreased with the decrease in the size of the particle radius. These observations show the success of the potentials used in this simulated study to create plausible stable structures as the results match those observed in other experimental studies.

In thermodynamics, an increase in the temperature of a system causes a rapid movement of atoms in the system thereby increasing the disorder which may result

in crystallographic defects [16]. The dominant defect species in the β -MnO₂ structure are cation vacancies at high oxygen activities (elevated temperatures) and manganese interstitials at low oxygen activities (low temperatures). These defects have been shown to contribute much to the structural deficiencies and deterioration of MnO₂ when used as cathode materials in Lithium-ion rechargeable batteries because of the higher temperatures reached during the charging-discharging cycle [18]. Table 3 reports on the electronic properties of the β -MnO₂ bulk structure as temperature is increased from 100K to 1500K.

Table 3: Binding Energy and Fermi Energy of the β -MnO₂ Bulk structure ranging from 100 K to 1500 K

100 K		
Total Energy	-7483.706 eV	
Binding Energy	-5.148 eV/atom	
Fermi Energy:	-7.393 eV	
DFT energy gap:	0.047 eV	
valence band edge:	-7.399 eV	
conduction band edge:	-7.352 eV	
Bond Length (Å) centre Mn – O	1.899	3.736
corner Mn – O	1.837	
500 K		
Total Energy	-7483.535 eV	
Binding Energy	-5.143 eV/atom	
Fermi Energy:	-7.321 eV	
DFT energy gap:	0.040 eV	
valence band edge:	-7.324 eV	
conduction band edge:	-7.284 eV	
Bond Length (Å) centre Mn – O	1.946	

corner Mn – O	1.919	3.865
1000 K		
Total Energy	-7483.415 eV	
Binding Energy	-5.093 eV/atom	
Fermi Energy:	-7.249 eV	
DFT energy gap:	0.049 eV	
valence band edge:	-7.257 eV	
conduction band edge:	-7.208 eV	
Bond Length (Å) centre Mn – O	1.812	3.591
corner Mn – O	1.779	
1500 K		
Total Energy	-7483.116 eV	
Binding Energy	-5.084 eV/atom	
Fermi Energy:	-7.220 eV	
DFT energy gap:	0.107 eV	
valence band edge:	-7.304 eV	
conduction band edge:	-7.196 eV	
Bond Length (Å) centre Mn – O	2.050	3.896
corner Mn – O	1.846	

Table 3 reports on the binding energies and Fermi energies of the bulk structure as a means to build onto the information that was discussed from Figure 14 pertaining to the effect of increasing temperatures on the stability of the Bulk structure. The data from the table above was calculated using the DMol³ code and CASTEP code from the Materials Studio software suit.

Based on the Fermi Energy results in table 3, the structural optimisation that occurred at a temperature of 100 K recorded the lowest Fermi energy of -7.393 eV. The Fermi energy shows an increase to -7.321 eV when the calculations were performed at a

temperature of 500 K. This increment of the Fermi energy continues when the temperature is increased to the maximum temperature of 1500 K. These results show that the structure optimised at 100 K is more stable and is the better electrical conductor as compared with all the other bulk structures optimised at higher temperatures.

Looking at the total energies, it is observed that the most stable structure is optimised at the lowest temperature of 100 K with a total energy of -7483.706 eV. The total energies increase from there on as the temperature increases. This increase in the temperature also causes an increase in the bond lengths between the manganese atoms and the oxygen atoms as displayed in figure 15. This increase causes a direct increase in the cell volume and the lattice parameters of the structure going against the aim of this study to determine compact stable structures.

The structure optimised at 100 K has the most stable binding energy which is the lowest at -5.148 eV/atom. It is observed that the energies increase directly with the temperature. It can thus be deduced that the increasing temperatures cause a destabilisation of the atomic structure in the bulk structure, specifically after the melting point temperature. This is in line with the results from the study by Grundy *et al.* [248], where it was stated that pyrolusite was stable below 300 K. Figure 15 displays the bond lengths of the DFT optimised bulk β -MnO₂ structure as the temperature is varied from 200 K to 1400 K to further observe the changes occurring to this bulk structure due to temperature variations.

From figure 15, it is observed that the bond length is showing a gradual direct linear increment from 200 K to 600 K where a sharp spike occurs to 800 K at the peak of

the plot which has already been mentioned to be the melting point for pyrolusite at 808K.

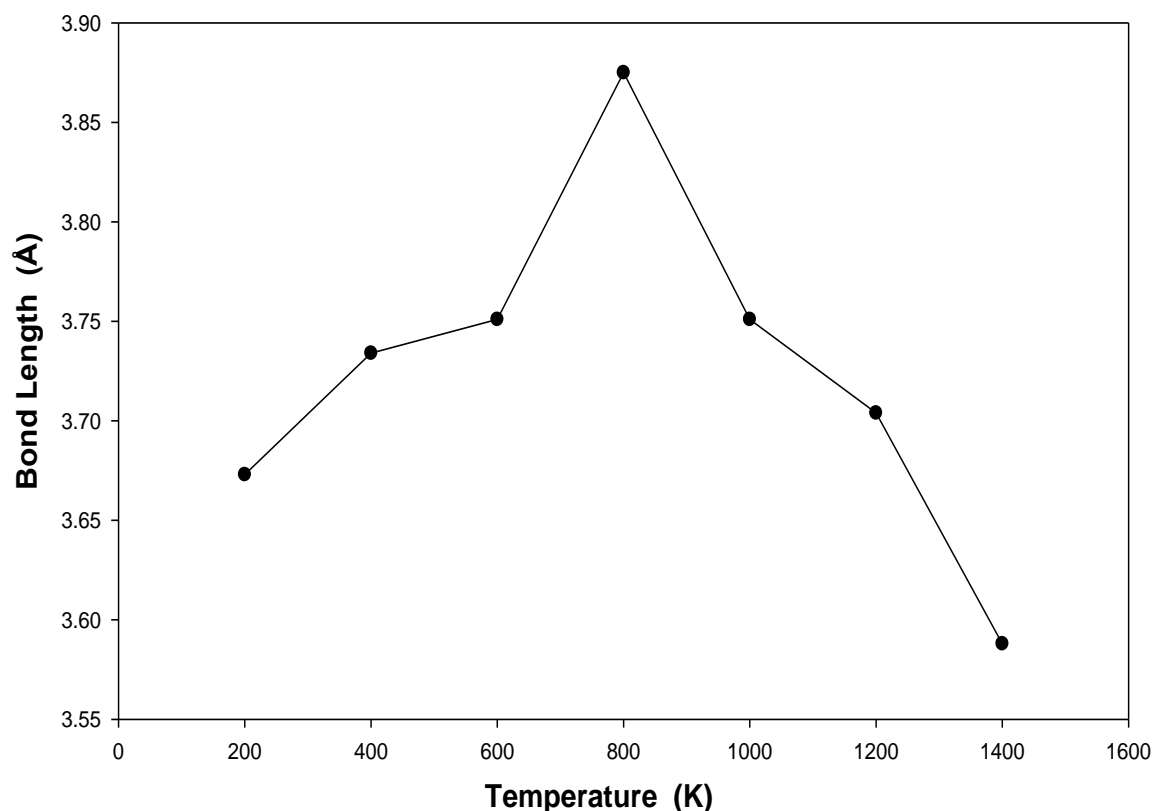


Figure 15: Bond length from the central Mn atom to the exterior corner Mn atom of the β -MnO₂ bulk structure drawn against temperature from 200 K to 1400 K

From the peak around 800 K, a gradual decrease in the bond lengths occurs until the maximum temperature recorded at 1400 K. It is known that when a material melts, it changes from a solid phase to a liquid phase. Therefore, it can be deduced from this plot that the change from a solid phase to a liquid phase causes the bond length between cations to decrease as seen with the bond length between the central manganese atom and exterior manganese atom situated on the corner of the crystal box to decrease from 3.67 Å at 200K to 3.59 Å at 1400K.

This is in line with observations by Tompsett *et al.* [16] and Kwon *et al.* [18] showing that bonds are weakened at higher temperatures. Some studies have even shown that nanostructures containing oxygen tend to record lower melting points than their bulk counterparts [249]. This shows that measures must be put in place to keep temperatures exceptionally low in order to maintain the compactness and rigidity of β -MnO₂ when used as a component in secondary rechargeable batteries.

MnO₂ is well known for its high activity and thermal stability as reported by Jideh *et al.* [250]. However, this stability degrades at higher temperatures above the melting region of pyrolusite as observed from these results in this subsection. These deficiencies in the bulk structure are further indications that new innovative ways should be researched to improve the stability of the rechargeable battery components. One of them is nanostructuring which is investigated from chapter 5 and another is doping which is investigated in the next subsection.

4.4. Doping of the β -MnO₂ bulk structure

This section focuses on the effect of doping the bulk β -MnO₂ structure with the selected dopant elements, i.e., nickel, cobalt and iron. These dopants have been shown to exhibit favourable results in previous studies [251]. Two methods of doping have been employed, that is the virtual crystal approximation (VCA) method [219] and the substitutional method [223]. These approaches have been discussed in the methodology chapter 3. The analysis conducted in this section will clarify which of the two doping techniques is preferred for this study and also to establish which of the dopant elements is more preferable.

4.4.1. Virtual crystal approximation method

The VCA approach allows the substitution of small compositions into a simple unit cell, however for the purpose of this study, two different percentages were considered i.e., 10 % and 20 % for all the dopants. Similar percentile doping was done in previous studies focused on similar compounds [252]. The effect of this doping is discussed focusing on the structural properties, specifically the lattice parameters, bond lengths, densities and the cell volume, as displayed in table 4. The analysis of the changes occurring to these properties will aid in determining the effectiveness of doping using the VCA technique for the bulk β -MnO₂ structure.

Table 4: Structural properties of the doped bulk β -MnO₂ structures

	Symmetry (Space group)	Binding Energy (eV/atom)	Total Energy (eV)	Cell Volume (Å ³)	Density (g/cm ³)	Lattice Parameters (Å)		Bond Lengths (Å)	
						a = b	c	centre Mn/x-O	corner Mn/x-O
Pure bulk	P42/MNM (D4H-14)	-5.082	-7483.734	53.980	4.99	4.395	2.795	1.898	1.823
20% Fe		-5.074	-6480.269	54.204	8.748	4.493	2.685	1.856	1.895
10% Fe		-5.045	-6973.646	53.454	8.871	4.459	2.687	1.880	1.838

20% Co		-5.086	-6628.364	55.508	8.727	4.525	2.712	1.878	1.900
10% Co		-5.090	-7052.618	54.555	8.879	4.449	2.756	1.882	1.864
20% Ni		-5.089	-6790.226	57.115	8.468	4.566	2.739	1.899	1.914
10% Ni		-5.106	-7137.298	55.388	8.733	4.454	2.791	1.888	1.878

From table 4; firstly, consider the doping with Fe on the Mn sub-lattice positions by both 10% and 20%. It is observed that 20% doping of all the manganese atoms in the optimised bulk structure with the first dopant material, iron (Fe) results in the cell volume increasing from 53.98 \AA^3 (as reported in table 2) to 54.20 \AA^3 . This implies that with 20% VCA doping the bond lengths and the lattice parameters have increased (see table 4) in comparison with the pure (undoped) bulk $\beta\text{-MnO}_2$ structure (see table 2). This shows that there is more atomic repulsion between the positively charged iron and manganese atoms, which causes these atoms to move further apart resulting in the larger lattice parameters and effectively a larger bulk structure which is less tightly held together, hence less stable.

However, 10% doping has the desired effect of actually decreasing the cell volume from 53.98 \AA^3 to 53.45 \AA^3 . This indicates a decrease in the bond lengths and the lattice parameters which is the desired result as envisioned in the objectives of this study. This shows that doping with 10% offers the better results as compared with

20% as far as Fe is concerned. Similar trends are observed when evaluating the doping with Co and Ni whereby inserting a concentration of 10 % respectively produces doped bulk structures that have a smaller cell volume than those observed with 20 % of VCA doping.

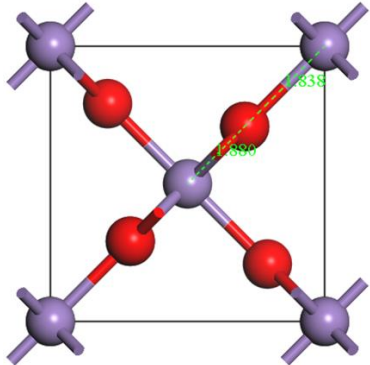
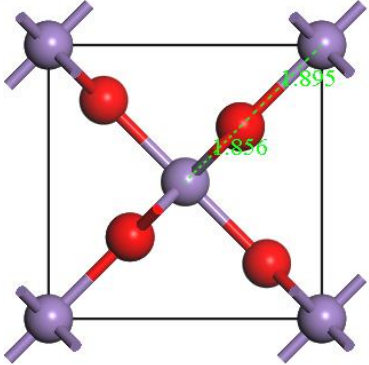
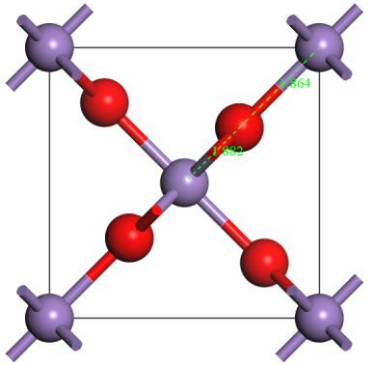
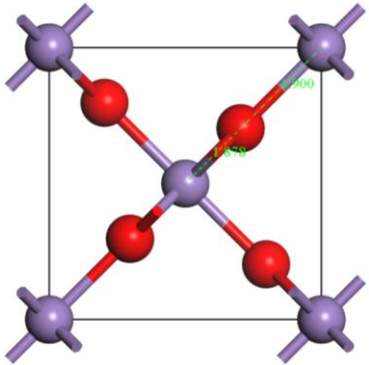
Secondly, the external manganese-oxygen bonds have a longer bond length for 20 % bonding as opposed to 10 % concentration. For example, doping with 20 % nickel has a bond length of 1.914 Å which is longer than doping with 10 % nickel which has an external manganese to oxygen bond length of 1.878 Å. A similar trend is observed for the bond lengths of the other doping concentrations with 20 % always having longer bond lengths than 10 %.

Lastly, comparing the binding energies of all the dopants at all the concentrations and also with the pure bulk β -MnO₂ structure, shows that 10% of Ni-doping produces the most stable and most tightly bonded doped structures. This is because 10 % Ni-doping has the lowest binding energy of -5.106 eV/atom. 10% Fe-doping produces the least stable doped bulk structure with the highest binding energy of -5.045 eV/atom. This indicates that Ni is the most favoured dopant for the bulk β -MnO₂ structure and Fe is the least favoured. It should be stated that the doped bulk structures have not necessarily improved the on all the properties of the pure bulk structure.

These observations further reinforce the choice of doping with smaller concentrations of the dopant element when using VCA. This agrees well with the study's objectives of discovering smaller compact structures while still trying to improve their stability and electrochemical performance. It is hoped that these positive attributes achieved with the bulk structure can be implemented to the new nanoclusters that will be

generated and investigated in the next chapter. The table below visualises the bond length measurements discussed above. It is important to investigate how the concentration of the dopants affects the size of the β -MnO₂ bulk structure by specifically focusing on the bond lengths of specific atoms as shown in table 5.

Table 5: Depicted below in the table are the bulk structures doped with 10 % and 20 % of the dopants; iron, cobalt and nickel

10 % concentration doping	20 % concentration doping
<p data-bbox="204 770 392 801">0.9Mn-0.1Fe</p> 	<p data-bbox="798 770 986 801">0.8Mn-0.2Fe</p> 
<p data-bbox="204 1252 392 1283">0.9Mn-0.1Co</p> 	<p data-bbox="798 1252 986 1283">0.8Mn-0.2Co</p> 

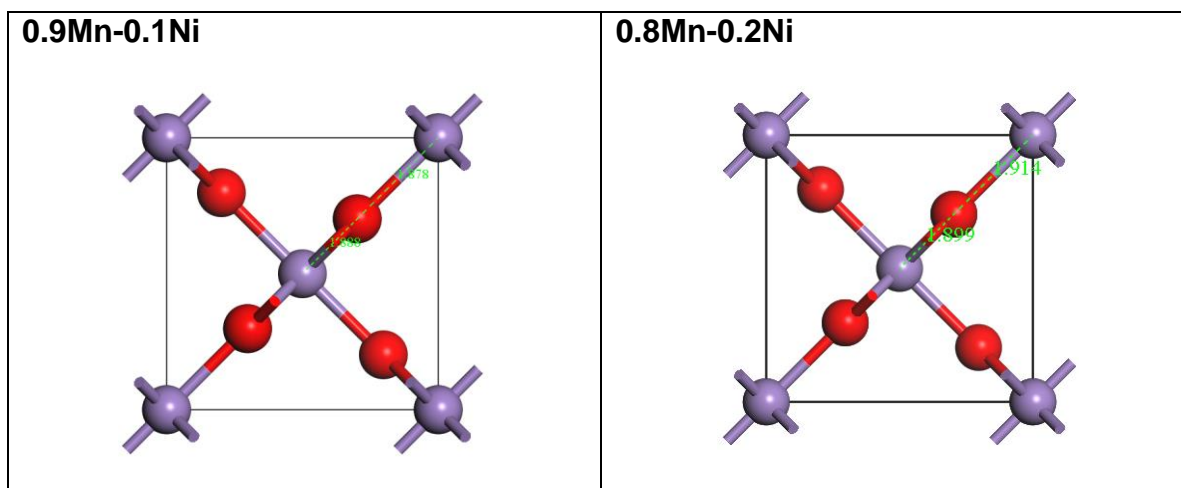


Table 5 displays the optimised bulk structures that have been doped with a concentration of 10% and 20% respectively on all the manganese atoms with Fe, Co and Ni using the VCA method. The bond lengths from the central manganese atom to exterior manganese atom are indicated on the bulk structures in the table. Based on the indicated bond lengths, it is observed that doping with 10% Nickel produces the most stable structure as it has the lowest binding energy of -5.106 eV/atom. All the doped bulk structures maintained their original symmetry and space group; P42/MNM (D4H-14).

The cell volume is highest for the bulk structure doped with 20 % nickel. This result is expected because an increase in the number of electrons coincides with an increase in the nuclear size [253], hence nickel with the most electrons occupying the valence shell in the d orbital will have largest cell volume as observed in the table. This effectively means that the nuclear size of the transition metals used in this study is Mn > Fe > Co > Ni. However, it is the intention of this study to show that an increase in the nuclear size of one component does not effectively expand the whole structure.

An interesting observation occurs with the densities whereby they are all relatively equal ranging between 8.47 g/cm³ to 8.88 g/cm³, showing that the doped structures are maintaining their rigidity even when the size of the crystal box containing the doped structures is changing. This is a positive result and bodes well for the study. Interestingly, doping with 10 % Fe produced the bulk structure with lowest cell volume of 53.45 Å³ although that bulk structure is energetically less stable than the bulk structure doped with 10 % Ni.

From this section, it can be concluded that nickel is the preferred dopant for the β -MnO₂ bulk structure. Furthermore, VCA is more efficient at lower concentrations because 10 % was shown to produce the more stable bulk structure. It is important to note that the pure un-doped bulk structure of β -MnO₂ is energetically more stable than all doped bulk structures and has the lowest cell volume in comparison. The next section will investigate another method of doping in order to verify and validate the results from this section due to the inaccuracies of VCA as discussed in section 3.10.1 of the Methodology chapter.

4.4.2. Substitutional method of doping

The substitutional method of doping involves the replacement of a specific atom in a structure by the selected dopants. The theoretical background of this technique was discussed in section 3.10.2 of the methodology chapter. The pyrolusite bulk structure has two manganese atoms, so a determination was initially done to show that the selected atom was contributing to the instability of the structure.

To determine this level of instability; the focus is on the binding energies and total energies of the optimised bulk structures after the substitutions have been made and

optimised using DFT. The bond lengths, the densities, the cell volumes and the lattice parameters are also analysed and discussed to determine the atomic position that is most suitable to perform doping. The discussions focus on both the substitutional positions in order to declare definitively which doping position is most preferable. The analysis also sheds light on which dopant element produces the most stable doped complex. Comparisons are made with the VCA results to determine the suitable doping technique and the most suitable dopant element.

These results from the doped structures will be compared with the pure un-doped bulk structure. Particularly, this is done to determine the overall efficacy of doping on the stability of the bulk systems and whether those trends carry over to the nanoclusters. To achieve this, the structural properties of the doped bulk structures were calculated and given in table 6 where the β -MnO₂ bulk structure was doped on the central manganese atom.

Table 6: Substitutional doping of the β -MnO₂ bulk structure on the central manganese atom

	Symmetry (Space group)	E _B (eV/atom)	E _T (eV)	Cell Volume (Å ³)	Density (g/cm ³)	Lattice Parameters (Å)		Bond Lengths (Å)	
						a = b	C	centre Mn/x- O	corner Mn/x- O
Pure bulk		-5.082	-7483.73	53.980	4.99	4.395	2.795	1.898	1.823

Mn/Fe	CMMM (D2H-19)	-5.170	-5483.29	53.833	5.391	4.356	2.837	1.863	1.855
Mn/Co		-5.185	-5719.47	53.619	5.508	4.334	2.859	1.874	1.829
Mn/Ni		-5.231	-5994.86	54.706	5.392	4.332	2.915	1.903	1.824

Table 6 reports on the structural properties determined when doping was done on the central manganese atoms with the greater coordination. The Ni-doped bulk β -MnO₂ structure is the most stable because it has the lowest, most negative binding energy of -5.231 eV/atom while the Fe-doped bulk β -MnO₂ structure is the least stable with a binding energy of -5.170 eV/atom.

These results are compared with those when doping was performed on the outer (the exterior, less coordinated manganese atoms positioned on the corners of the crystal box) manganese atoms as shown in table 7. Table 7 displays results of the optimised bulk structures that were substitutionally doped with iron, cobalt and nickel on the exterior manganese atoms that are visualised on the corners of the crystal box. The bond length from the central manganese atom to its neighbouring oxygen atom and another bond length from the corner manganese atom to its neighbouring oxygen atom are also measured.

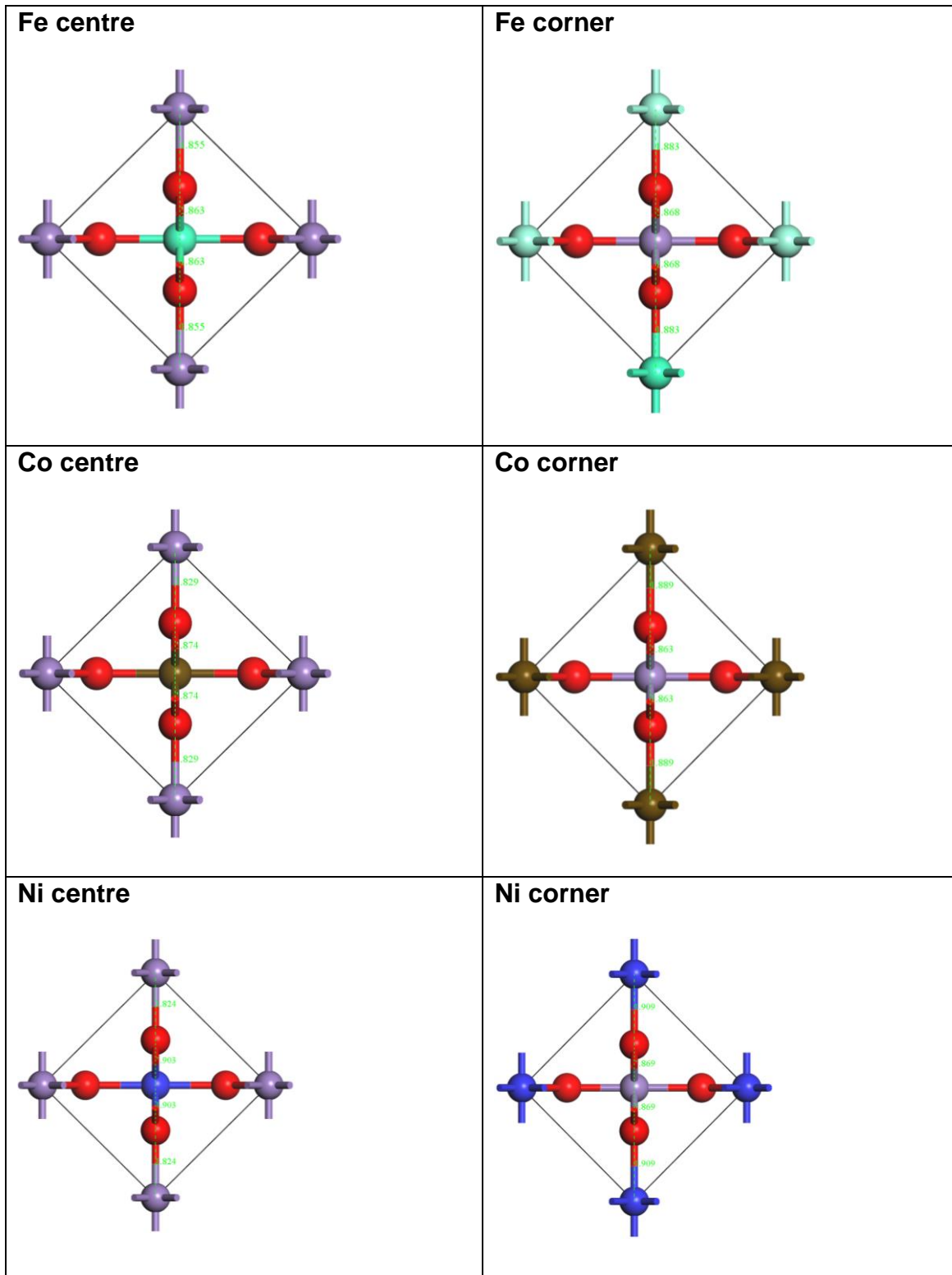
These bond length comparisons aid in determining which doping position and which dopant element produces the most stable and most compact doped bulk structure. Comparisons are also made between these stable, doped bulk structures with the pure undoped β -MnO₂ bulk structure to gauge the overall impact of doping.

Table 7: Atomistic substitutional doping of the β -MnO₂ bulk structure on the corner manganese atoms, 25 % of each making one whole atom

	Symmetry (Space group)	E _B (eV)	E _T (eV)	Cell Volume (Å ³)	Density (g/cm ³)	Lattice Parameters (Å)		Bond Lengths (Å)	
						a = b	C	centre Mn/x- O	corner Mn/x- O
Pure bulk		-5.082	-7483.734	53.980	4.99	4.395	2.795	1.898	1.823
Mn/Fe	CMMM (D2H-19)	-5.112	-5483.296	53.834	5.391	4.336	2.838	1.868	1.883
Mn/Co		-5.170	-5719.472	53.624	5.508	4.330	2.859	1.863	1.889
Mn/Ni		-5.211	-5994.861	54.706	5.392	4.332	2.915	1.869	1.909

Similar to table 6, the Ni-doped bulk β -MnO₂ structure is the most stable because it has the lowest, most negative binding energy of -5.211 eV/atom while the Fe-doped bulk β -MnO₂ structure is the least stable with a binding energy of -5.112 eV/atom. However, the centrally Ni-doped bulk β -MnO₂ structure is the most stable as it has lowest binding energy in comparison with all other structures in both table 6 and 7.

Table 8: Central and corner atomic substitutional doping of the manganese atoms displayed side-by-side for iron, cobalt and nickel dopants.



Tables 6 – 8 shows that the Fe-doped bulk structure and the nickel doped bulk structure both have the equal lowest densities at 5.39 g/cm^3 , furthermore the nickel-doped bulk structure has the lowest total energy of -5994.86 eV when doping was performed on the central manganese atom. The nickel-doped bulk structure also has the shortest lattice parameters for the $a=b$ parameters at 4.332 \AA . The binding energy is lowest for nickel at -5.231 eV/atom . Some properties favour the other dopant elements such as the c parameter which favours iron. The cell volume is the smallest favouring cobalt with 53.619 \AA^3 although the cobalt density is the highest at 5.508 g/cm^3 .

Based on these results and preliminary analysis, nickel is outperforming the other dopants when it comes to improving the properties of the bulk $\beta\text{-MnO}_2$ structure. However, it cannot yet be stated categorically which dopant element is the best because the other dopants display some desirable qualities. But, so far nickel produces the most stable complex energetically due to it having the lowest total energy and binding energy. Cobalt produces the most compact structure due to it having the lowest cell volume and the shortest bond length from the central manganese atom to the outermost exterior manganese atom with 3.703 \AA . Even though it seems nickel is the better dopant for now, we shall avoid the biasness of choosing nickel at this moment to be the best dopant element from these observations hence the investigations will continue in order to better explain and conclude on this topic using the nanoclusters.

Table 7 reports on the doping of the bulk structure on the outer manganese atom. An interesting observation is that the total energies, densities and the cell volume are exactly identical as when the doping was performed on the central manganese atom,

meaning nickel still has lowest and most stable total energy. The fermi energies, binding energies are also identical at both atomic positions. Due to the study's objectives of determining the most stable structure on the energy landscape, it can be claimed that nickel is the favoured dopant element, this reinforces the observations from VCA which also had nickel as the better dopant element, but a more definitive declaration will follow in Chapter 8 after the analysis for doping of the nanoclusters.

The bond length between the central nickel atom and the neighbouring oxygen atom (centre Ni-O) is 1,903 Å which is shorter than the bond length between the external manganese atom located at the corner of the crystal box and its neighbouring oxygen atom which is 1.909 Å. This measurement shows that doping at the central manganese atom produces the smallest and most compact bulk structure which agrees sufficiently with the objectives of the study to maintain structural stability at reduced bond lengths.

Another fascinating observation is that the atomistic substitution of manganese with all the chosen elements changes the symmetry and space groups of the optimised doped bulk structures from P42/MNM (D4H-14) to CMMM (D2H-19). Future studies will further investigate this migration of the space group and its effect on the structural stability of nanostructures as this lies outside the scope of this current study.

Chapter 5: Generation and stability of β -MnO₂ nanoclusters

This chapter focuses on the stability of the β -MnO₂ nanoclusters generated with the interatomic potentials' technique employing the KLMC code. The nanoclusters were generated using the lattice constants that were parametrised from the optimised bulk β -MnO₂ system in chapter 4.

The nanoclusters are ranked and comparisons are made between the IP method and the DFT method. The optimised nanoclusters are then doped with Fe, Co and Ni. The 10 most stable nanoclusters are ranked from $n=2$ to $n = 20$ and are all displayed in the appendices section B at the end of this thesis.

5.1. Generation of the MnO₂ nanoclusters

The evolutionary algorithm method as employed within the KLMC software code was used to generate the manganese dioxide nanoclusters. The methodology and procedure within the code was discussed in chapter 3.

In order to establish the reliability of the simulation codes and techniques used, the total energies from the three interatomic potential methods; GULP, Basin Hopping [254] and Genetic Algorithm [255] were plotted together with the DFT-based code CASTEP. The total energies were obtained from a randomly selected atomic size to determine the local minima and global minima structures of the nanoclusters. The order of stability is determined according to the lowest energies in order to determine the most efficient approach to optimising the nanoclusters.

5.1.1. Energy landscape

The total energies of the most stable nanoclusters for each atomic size were plotted in order to determine which optimisation technique was best suited to stabilising the nanocluster to their lowest possible energies as illustrated in figure16.

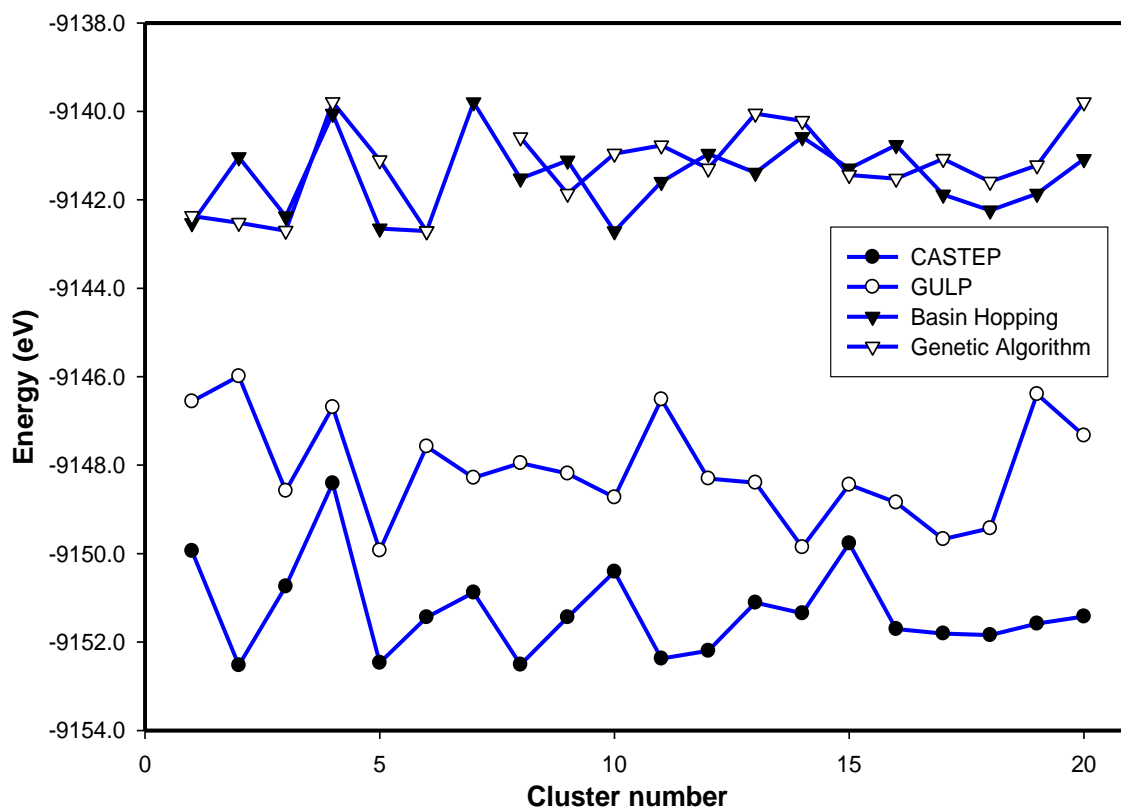


Figure 16: Comparison of energy landscape as determined by the Basin Hopping, Genetic Algorithm, CASTEP and GULP codes for the 20 most stable $(\text{MnO}_2)_n=6$ nanoclusters

Figure 16 shows the comparison of the energy landscape of four different codes to establish the preferred approach. The two approaches; Basin Hopping and Genetic Algorithm predict almost similar energies, which are higher than those predicted by GULP and CASTEP. The graph shows that the nanoclusters optimised with the DFT based CASTEP code produced the lowest energies as compared to the other techniques.

These results further ascertain that DFT-based approaches are capable of refining the structures obtained using interatomic potential techniques, in terms of the order of stability and reactivity. CASTEP will be used to optimise the nanoclusters the nanoclusters and other DFT based techniques such as DMol3 and Reflex will be employed to calculate properties of the nanoclusters that will be presented in the subsequent chapters. These observations reinforce findings from chapter 4 that showed that DFT-based techniques produced more energetically stable bulk structures.

5.1.2. Convergence parameters for the k-point mesh

In order to accurately evaluate the stability of the nanoclusters, a k-point set was determined by optimising the nanoclusters at a 500-eV cut-off energy. This cut-off energy was determined in the previous chapter and it is adopted to optimise the nanoclusters to maintain continuity in the calculations undertaken.

The nanoclusters adopt a P1 (C1) cubic symmetry during calculations with CASTEP. This is migrating from the P42/MNM symmetry group of the ditetragonal dipyramidal class corresponding to the rutile type bulk β -MnO₂ structure. A new k-point separation was determined in order to accommodate the new cubic system of these nanoclusters. A random stable configuration was selected and used to determine the new optimal k-point separations using the n4-01 nanocluster was chosen. Table 9 presents total energies and the energy differences between successive k-point separations.

Table 9: Total Energies of the randomly selected nanocluster with varying k-point separations

K-point Separations (1/Å)	Total energy (eV)	Total energy difference ΔE
0.05	-14962.6809	-
0.10	-14963.4804	0.7995
0.20	-14963.5020	0.0216
0.30	-14963.5039	0.0019
0.40	-14963.5043	0.0004
0.50	-14963.5033	0.001
0.60	-14963.5036	0.0003
0.70	-14963.5038	0.0002
0.80	-14963.5043	0.0005
0.90	-14963.5038	0.0005
1.10	-14963.5038	0

The values in table 9 were used to plot the total energy against the k-point separations in figure 17. This serves to determine the optimal k-point separation that accurately minimises the total energy of the nanocluster to its most stable ground state. The total energy was considered converged when the energy change per atom between successive readings was within 1 meV.

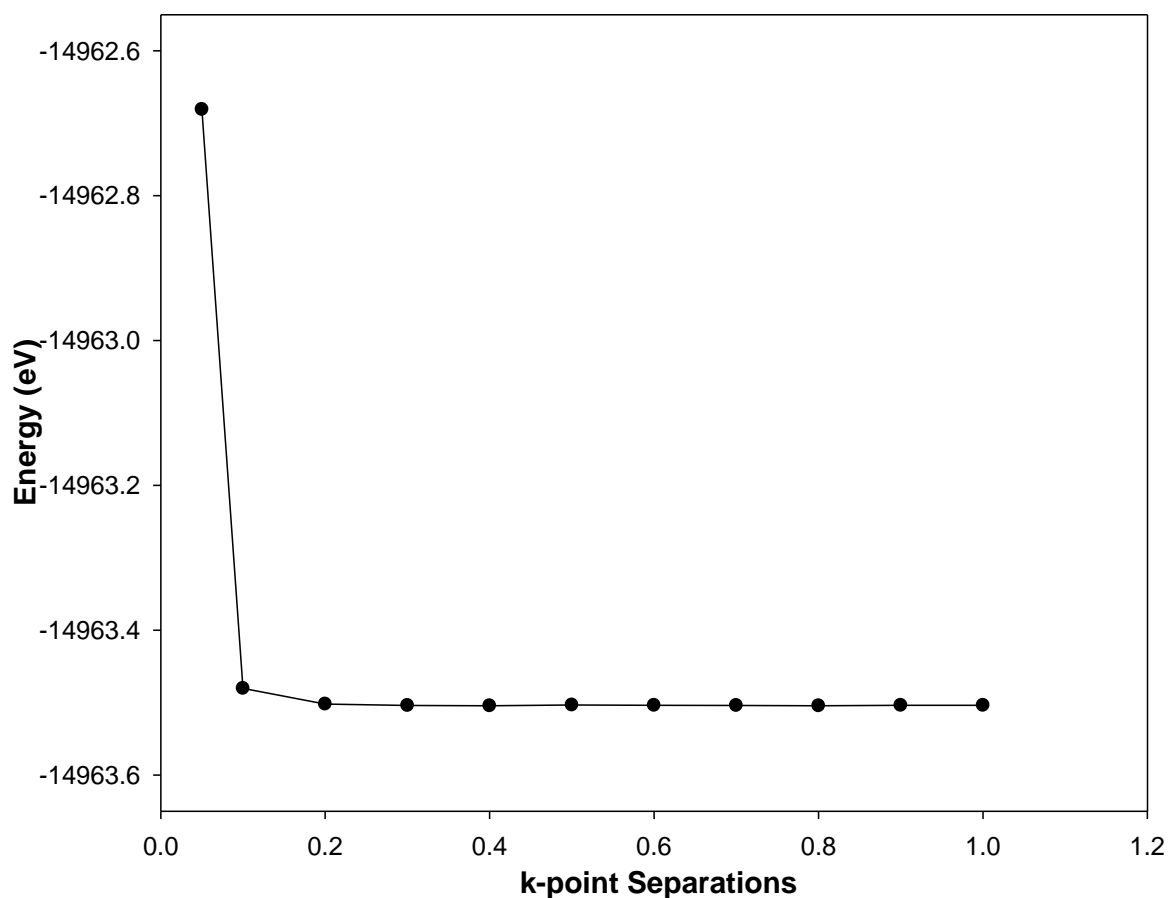


Figure 17: Plot depicting the total energy of the increasing k-point separations

Figure 17 depicts the convergence of the total energies for the k-point separations varied from 0.05 Å to 1.0 Å at 500 eV cut-off energy. It is observed that the graph undergoes a steep and sudden decrease from a separation of 0.05 Å to 0.1 Å where it begins to stabilise until its minimal fluctuation at 0.4 Å separation. The k-point separation of 0.4 Å is thus chosen as a suitable k-point separation to optimise all the generated nanoclusters using DFT techniques. The separation will be increased gradually as the nanocluster size increases to ensure minimisation is achieved even for the largest nanocluster size in this study, i.e., n=20 atoms.

The nanoclusters were initially placed in crystal cell with dimensions of 10 Å x 10 Å x 10 Å (x, y, z) for atomic sizes smaller than n=10. This cell volume became insufficient to accurately optimise the larger nanoclusters to their ground state. A search for the most suitable cell volume was thus conducted and the results are given in table 10.

Table 10: Suitable cell volumes determined to accurately minimise the nanoclusters to their most accurate ground state

Number of atoms	n=14	n=15	n=16	n=17	n=18	n=19	n=20
Suitable Cell volume	16 Å ³	18 Å ³	16 Å ³	19 Å ³	23 Å ³	25 Å ³	25 Å ³


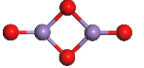
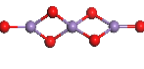
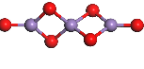
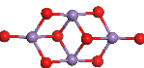
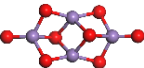
All the other parameters that were determined in the previous chapter for optimising the bulk β -MnO₂ structure were adopted for the nanoclusters. The maximum iterations and SCF cycles were increased to 500 and 1000 respectively to ensure that convergence was achieved. This is done in concert with the increasing crystal box size for the growing atomic numbers ranging upwards to the n=20 atomic number. The DFT optimised nanoclusters are displayed in Appendices B1- B19 at the end of the thesis.

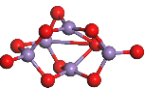
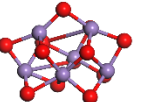
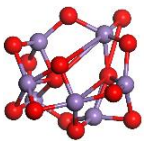
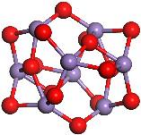
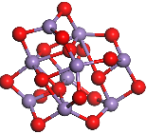
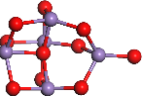
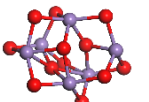
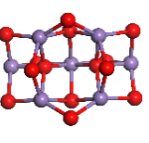
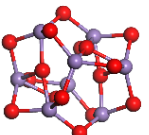
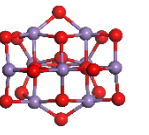
5.2. Stability of the nanoclusters

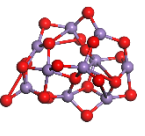
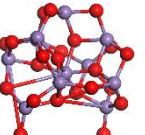
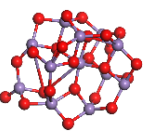
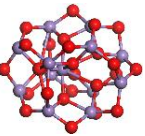
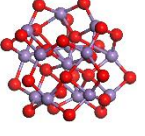
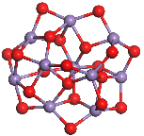
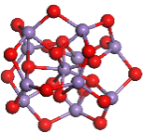
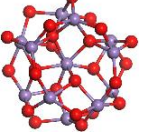
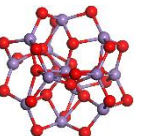

A lot of significance and emphasis cannot be placed solely on the total energy values to determine the structural stabilities and electrochemical activities. To remedy the situation and overcome this obstacle; the binding energy, Fermi energy and band-gap energies were calculated and tabulated.

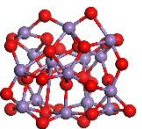
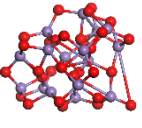
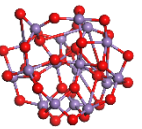
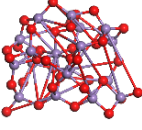
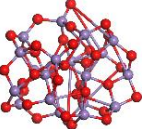
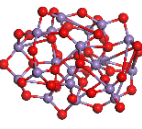
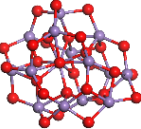
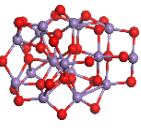
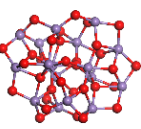
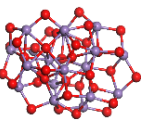
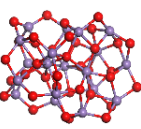
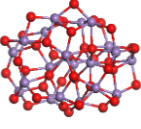
Table 11 illustrates the most stable nanocluster for each atomic size ranging from $n=2$ increasing to $n=20$. The table gives the single-point energy of the nanoclusters and the total energy after DFT optimisation with CASTEP. The densities, binding energies, Fermi energies and energy band-gaps of the optimised nanoclusters are also reported.

Table 11: A display of the most stable nanoclusters ($n = 2 - 20$) generated by the IP-based KLMC and optimised by the DFT-based CASTEP.

N	IP	DFT	Single-point Energy (eV)	Total Energy (eV)	Density g/cm ³	Binding Energy (eV/atom)	Fermi Energy (eV)	DFT Energy band gap (eV)
2			- 7472.836	- 7479.495	0.289	- 4.075	- 6.163	0.000
3			- 11211.247	- 11220.719	0.128	- 4.174	- 6.486	0.496
4			- 14951.443	- 14961.735	0.103	- 4.283	- 6.268	0.397

DFT Energy band gap (eV)	0.473	0.439	0.412	0.405	0.386
Fermi Energy (eV)	- 6.606	- 6.565	- 6.346	- 6.220	- 6.021
Binding Energy (eV/atom)	- 4.371	- 4.509	- 4.643	- 4.702	- 4.786
Density g/cm ³	0.214	0.257	0.585	0.668	0.752
Total Energy (eV)	- 18704.111	- 22442.251	- 26184.250	- 29921.671	- 33665.357
Single-point Energy (eV)	- 18691.104	- 22429.390	- 26169.323	- 29908.632	- 33649.257
DFT					
IP					
N	5	6	7	8	9

DFT Energy band gap (eV)	0.365	0.338	0.309	0.282	0.255
Fermi Energy (eV)	- 6.270	- 6.108	- 6.030	- 5.726	- 5.966
Binding Energy (eV/atom)	- 4.799	- 4.863	- 4.879	- 4.885	- 4.897
Density g/cm ³	0.657	0.723	0.789	0.684	0.736
Total Energy (eV)	- 37408.503	- 41149.409	- 44891.684	- 48629.875	- 52371.922
Single-point Energy (eV)	- 37387.184	- 41127.946	- 44870.406	- 48609.009	- 52350.146
DFT					
IP					
N	10	11	12	13	14

	DFT Energy band gap (eV)	0.225	0.213	0.196	0.173	0.143	0.113
	Fermi Energy (eV)	- 6.291	- 6.418	- 5.903	- 6.572	- 6.364	- 5.608
	Binding Energy (eV/atom)	- 4.903	- 4.921	- 4.947	- 4.953	- 4.972	- 4.994
	Density g/cm³	0.371	0.564	0.358	0.214	0.176	0.185
	Total Energy (eV)	- 56111.156	- 59856.9398	- 63597.316	- 67344.290	- 71083.591	- 74824.237
	Single-point Energy (eV)	- 56088.645	- 59828.5586	- 63570.502	- 67304.002	- 71048.718	- 74789.039
	DFT						
N	IP						
		15	16	17	18	19	20

Firstly, it is observed from table 11 that the total energy of the nanoclusters is lower after DFT optimisation by CASTEP. This shows that optimising the nanoclusters using DFT techniques is effective because it produces more stable nanoclusters as proven by their lower total energies, this was also observed with the bulk β -MnO₂ structure. It is also observed that the binding energy is increasing from n=2 atoms with -4.075 eV/atom to n=20 atoms with a binding energy of -4.994 eV/atom. This increment indicates that stability increases with nanocluster size as reported by Zhai *et al.* [256] for (TiO₂)_n; (n=1–10).

5.3. Band-gap energy and Fermi energy

The band-gap energy and Fermi energy were calculated using molecular dynamics techniques with the CASTEP code. The same parameters and settings used to optimise the bulk β -MnO₂ structure and the nanoclusters were employed for these calculations.

The band-gap energy was measured to be zero for the smallest atomic size; n=2. This indicates that this optimised nanocluster is an excellent conductor because of the overlap between the valence band and the conduction band as proven by the 0.0 eV band-gap energy. The band-gap energy is 0.496 eV for the Mn₃O₆ and subsequently decreases gradually as the nanoclusters are growing in size until the n=20 atomic size. This Mn₂₀O₄₀ nanocluster had the smallest band-gap energy of 0.113 eV (disregarding the n=2 nanocluster as an outlier). It can thus be construed that the conductivity of the nanoclusters is increasing as the nanoclusters grow larger until n=20.

It is observed that the Fermi energies do not follow a specific trend in terms of increments and decrements with the growing nanoclusters. This is because the values increase and decrease randomly as the nanoclusters grow in size. Therefore, no conclusive relationships can be derived about their impact on the stability of the nanoclusters.

The lack of a definitive relationship or trend between the band-gap energy, fermi energy and the increasing number of atoms in the nanoclusters might be because of the increasing k-point separations when the nanoclusters were growing larger. The cell volume was also increased in concert with the increasing number of atoms. This changes in the lattice constants may have affected the density of the nanoclusters, band-gap energy and Fermi energy such that they adversely affect their dependence on each other.

The Fermi energies have a negative non-zero value indicating that the nanoclusters are conductors as the graph is continuous at the fermi level. The band-gap energy between the valence band and the conduction band fluctuates between 0.000 eV and 0.496 eV which indicates the good conductive properties of the nanoclusters.

5.4. Density and binding energy

The density and binding energy of the optimised nanoclusters were calculated using the CASTEP code employing the parameters already determined in the previous sections. The relationship between the density of the nanoclusters against the increasing number of atoms in the growing nanoclusters from $n=2$ to $n=20$ is illustrated in figure 18.

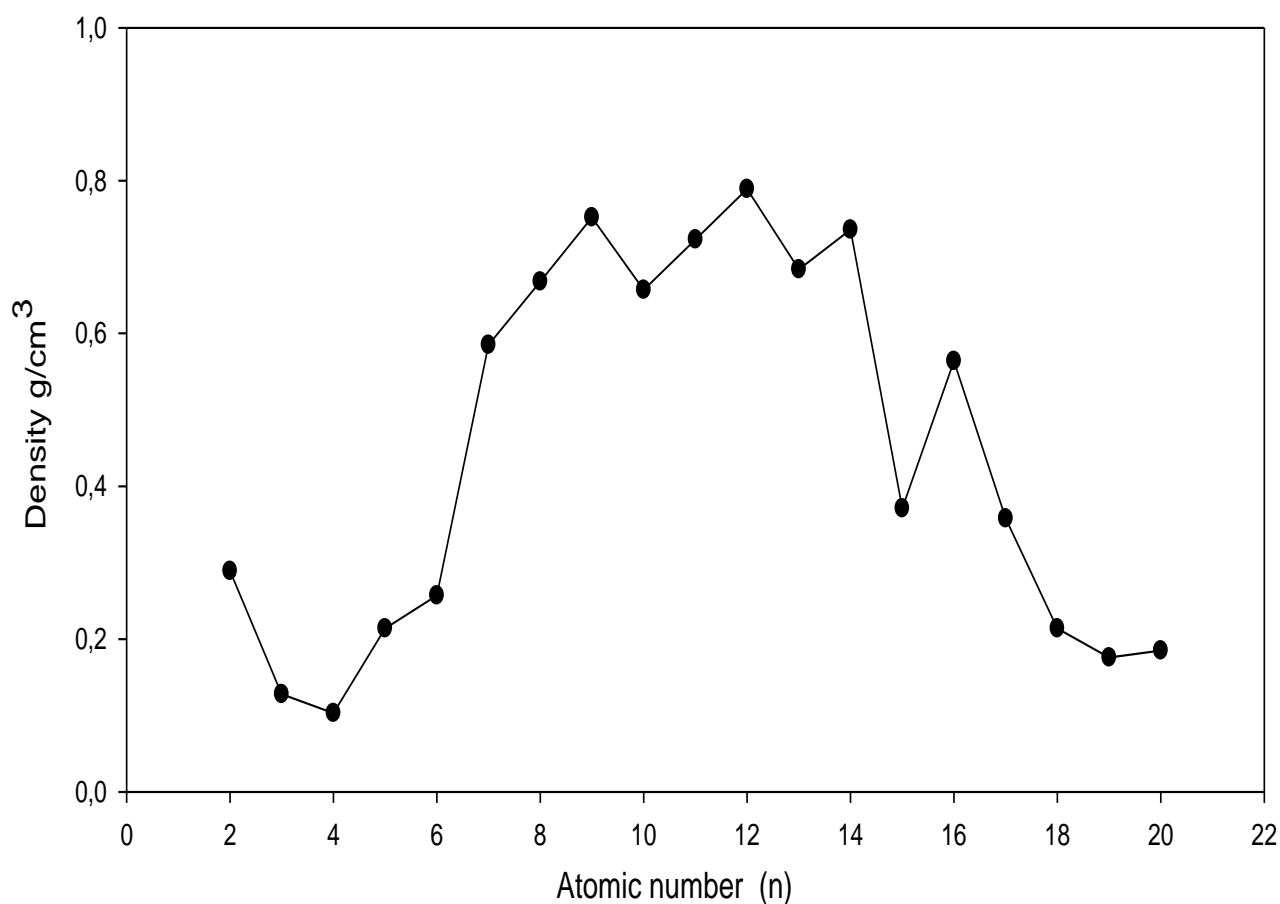


Figure 18: A plot of the Density against the atomic number for all the generated nanoclusters (n = 2 - 20)

From figure 18, it is observed that the density does not display a definitive trend in its values when measured against the increasing nanoclusters. This is possible considering that the size of the crystal box containing the nanoclusters was systematically increased to tolerate the growing size of the nanoclusters. Figure 19 illustrates the relationship of the nanoclusters with the total energy of the optimised nanoclusters using the DFT-based CASTEP code.

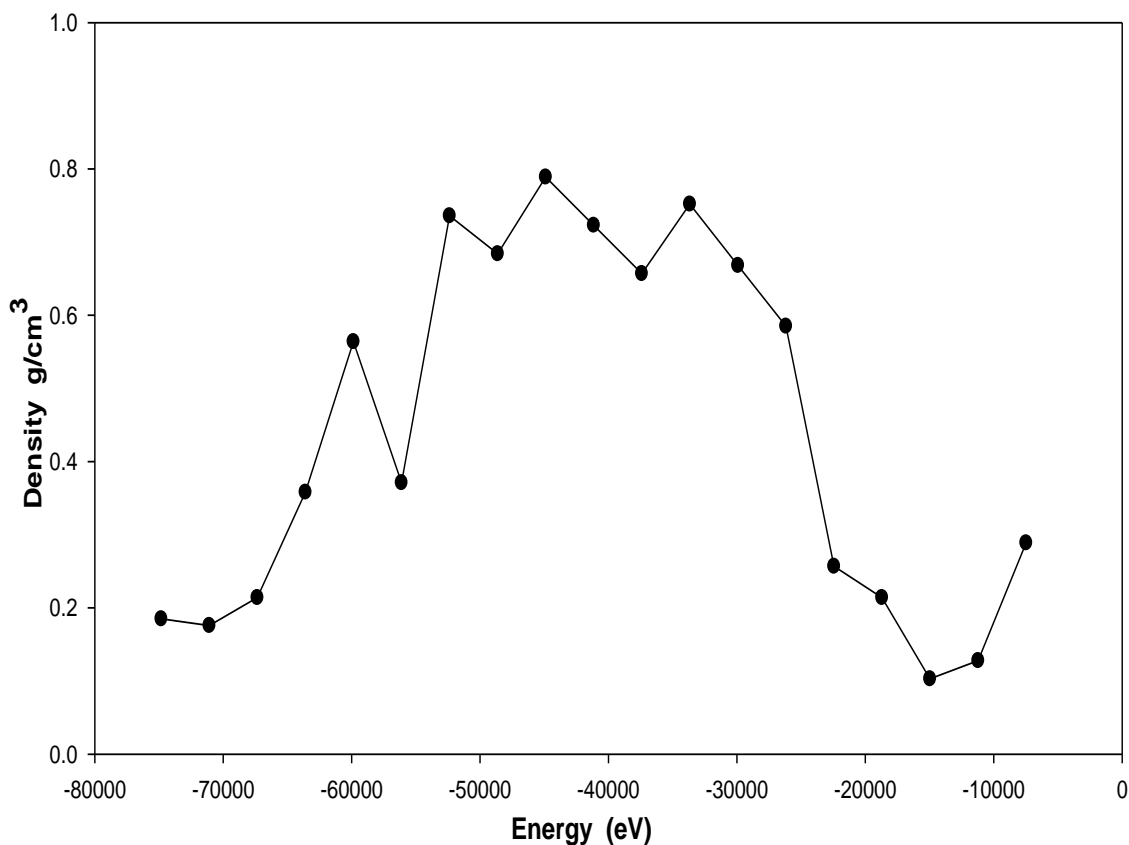


Figure 19: A plot for the Density against the total energy for all the generated nanoclusters

Figure 19 shows the density of nanoclusters against the total energies of the DFT optimised nanoclusters. It is observed that the densities are fluctuating constantly, hence a definitive relationship cannot be surmised from this plot. This eliminates the possibility of making any conclusive trends regarding the dependence of the stability on the density of the nanoclusters. This agrees well with the notion that an increase in the number of atoms results in the increased complexity of the structures as reported previously by Pan *et al.* for SnO₂ [104].

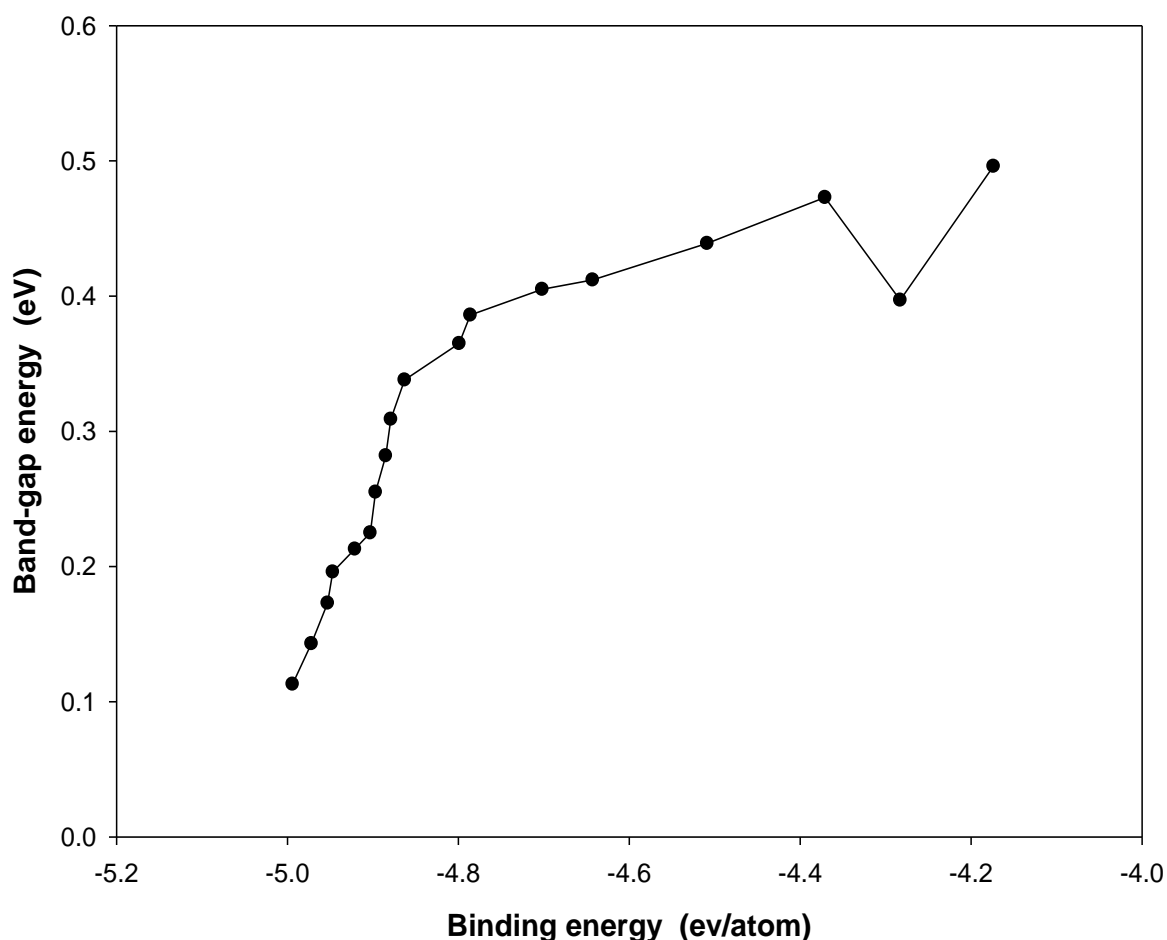


Figure 20: Band-gap energy plotted against the binding energy of the DFT optimised nanoclusters; n=2-20

Figure 20 indicates the band-gap energy of the n3-01 nanocluster measured against the binding energy using molecular dynamics techniques. An outlier reading for the band-gap energy of 0.000 eV for the smallest nanocluster size (n=2) was excluded from the results in order to display a more plausible plot. From figure 20, it is observed that the band-gap is getting broader as the binding energy increasing. This shows that the smaller band-gap energy is aligned to a more stable, more intact nanocluster. This also means the conductivity of the nanocluster increases with stability. The n3-01 nanocluster can thus be classified as semi-conductor due to the range of the band-gap energies [195, 196].

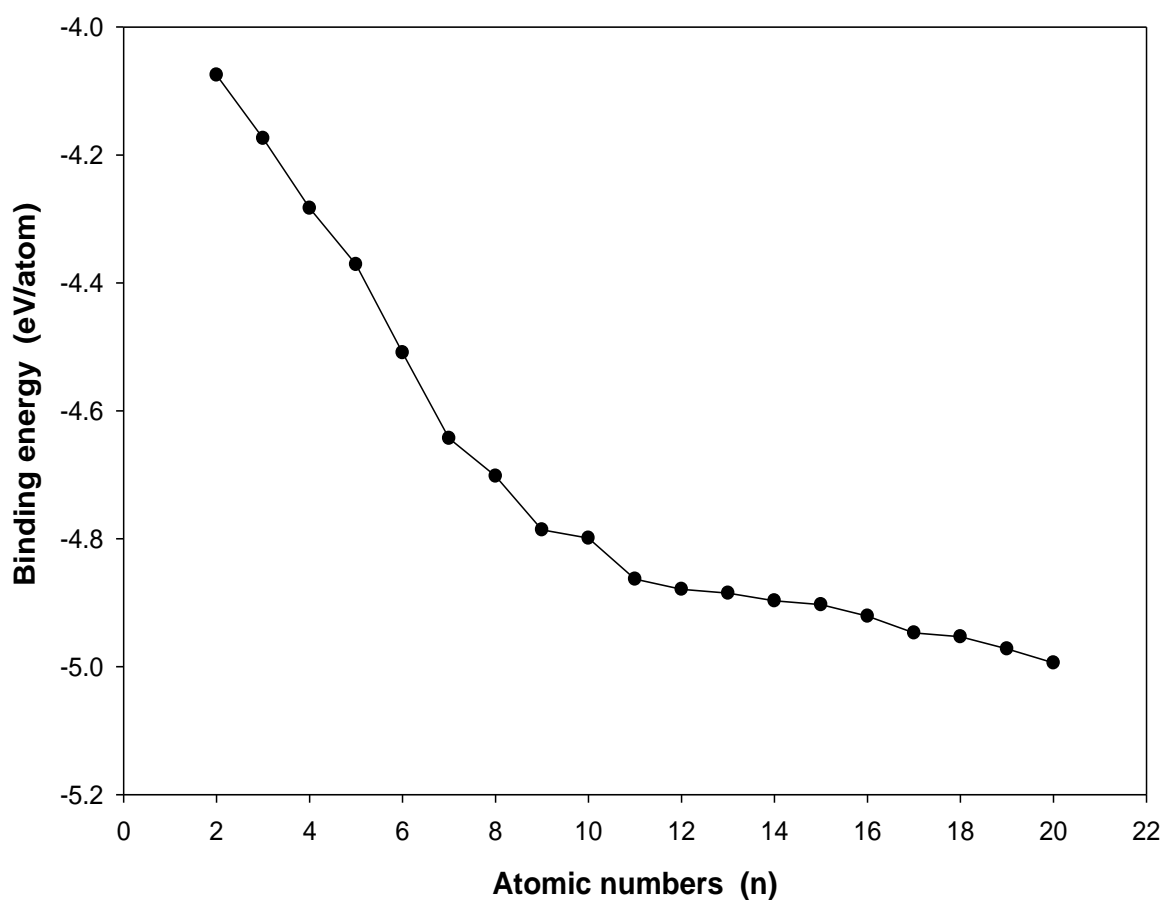


Figure 21: A plot of the binding energies drawn against the atomic number

Figure 21 is plot of the binding energy against the increasing atomic size of the DFT optimised nanoclusters. The graph is plotted from the smallest nanocluster denoted by Mn_2O_4 to the largest nanocluster denoted by $Mn_{20}O_{40}$. The graph illustrates a direct linear relationship between the binding energies and the atomic numbers of the nanoclusters. This linear relationship shows the increasing stability as the number of atoms in the nanoclusters are increasing. These observations correlate well with results from the previous study as reported by Zhai *et al.* [256]. The decreasing binding energies are proof that the stability of the nanoclusters is improving with the increasing number of atoms.

From this chapter, it was definitively determined that DFT is indeed capable of improving the nanoclusters that were originally generated with IP techniques as employed with the KLMC code. The DFT-based CASTEP code was shown to be successful in optimising and enhancing the structural and electronic properties of the nanoclusters. A new k-point separation of 0.2 Å was necessary to perform DFT calculations on the nanoclusters due to the cubic crystal system of the nanoclusters which is a divergence from the tetragonal crystal system of the bulk β -MnO₂ structure.

The total energy of the nanoclusters is lower after DFT optimisation by CASTEP and that the binding energy is decreasing from n=2 atoms to n=20 atoms indicating that stability increases with nanocluster size. The nanocluster's Fermi energy and band-gap energy indicate the semi-conductive nature of the nanoclusters. The smaller band-gap energy is aligned to a more stable, more intact nanocluster also showing that the conductivity of the nanoclusters increases with stability. The density values of the nanoclusters are not definitive as there is no observable trend in their values with regards to the nanocluster size. This agrees well with the notion that an increase in the number of atoms results in the increased complexity of the structures as reported by Pan *et al.* for SnO₂ [104].

Chapter 6: Effect of temperature on the stability of the MnO₂ nanoclusters

This chapter focuses on the effect of temperature on the stability of the n3-01 nanocluster. The stability is evaluated as the temperature is increased from 100 K to 1500 K. This stability was determined by calculating the binding energy of the nanocluster at each temperature. The NVE ensemble was utilised to perform molecular dynamics calculations to determine the effect of temperature on the stability of this nanocluster.

The (MnO₂); n=3 nanocluster was selected for further investigation because it showed a remarkable stability in previous cluster studies of manganese oxides [257]. Furthermore, this nanocluster represents the sequential growth of the nanocluster as the number of atoms are increased from the size of the unit bulk β-MnO₂ structure. The number of atoms in the bulk β-MnO₂ structure (as displayed in figure 2, Chapter 1) has two manganese atoms and four oxygen atoms arrayed in a distorted hexagonal configuration.

The generated nanoclusters formed four-coordinated tetrahedral networks with a high structural complexity similar to a previous study focusing on an iso-structural SiO₂ cluster consisting of chains with two-rings, terminated at either end by a silanone group. The tetrahedral bonding networks were found to be inherent in the most stable structures of (SiO₂)_n up to n=6 atoms [113].

6.1. Bonding patterns

Figure 22 depicts the n3-01 nanocluster displaying the various bonds occurring in the system. The particular bonds are indicated by means of labels showing the bond lengths between the atoms of interest. The measurements focused on the bond lengths and the bond angles between specified atoms in order to observe all the changes as the temperature is increased in this chapter. This displayed nanocluster will continue to serve as a reference for the subsequent chapters in this study.

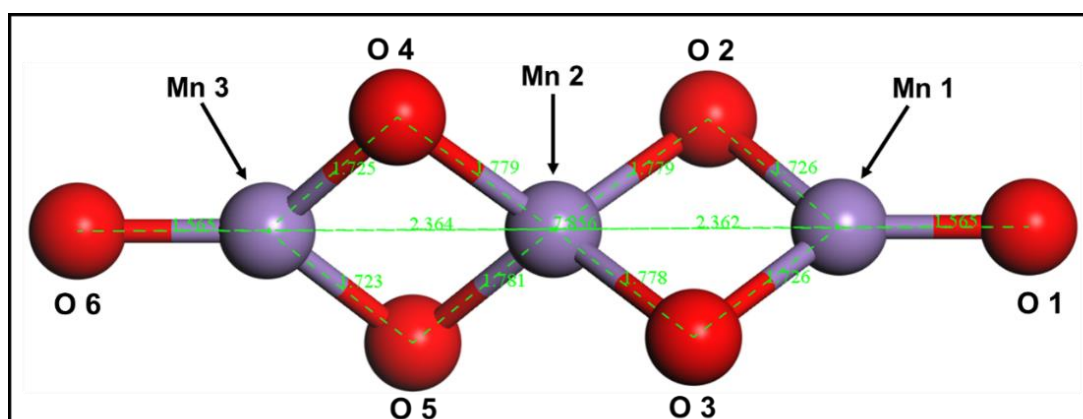


Figure 22: Illustration of the numberings of the atoms in the n3-01 manganese dioxide nanocluster after optimisation with DFT optimisation

The indicated bond lengths and bond angles in figure 22 will be used as a reference to observe and compare the occurring changes as this nanocluster is exposed to increasing temperatures. Table 12 gives the bond lengths, bond angles and displays the atomic configurations of the n3-01 nanocluster as the temperature is increased from 100 K to 1500 K.

Table 12: Structural properties of the most stable nanocluster composed of 3 manganese atoms and 6 oxygen atoms focusing on the Binding and Fermi energies

Temp. (K)	Atomic configurations Bond lengths and bond angles	Terminal bond length (Å)	Terminal bond angle (°)
IP		9.933	180.00
DFT		7.856	179.898
100		7.416	156.812

200		7.205	153.908
300		7.228	152.800
400		7.245	163.209
500		7.418	158.306

1000		7.452	172.847
1100		7.388	151.915
1200		shortest 7.013	152.496
1300		7.378	148.935

1400		7.439	147.910
1500		7.784	162.661

From table 12, the structural changes occurring to the n3-01 nanocluster as the temperature is increased from 100 K to 1500 K are observed. The bonding distance between the dangling terminal oxygen atoms is measured in order to show the overall size of the nanocluster as the temperature is increased. The bond angle between some specified atoms is also displayed to show the changes occurring to the atomic configuration and orientation due to the increasing temperatures. The results are extracted and tabulated in the following subsections for a more detailed analysis.

6.1.1. Bond lengths

This section investigates the changes occurring to the bond length in the n3-01 nanocluster as convergence was achieved at temperatures ranging from 100 K to 1500 K. In particular, the O1-Mn1, Mn1-O2, O2-O4, Mn1-Mn2 and O1-O6 bonds were specifically targeted for analysis because they represented the most influential

atomic interactions in the n3-01 nanocluster. It must be noted that a bond limit of 3.0 Å was instituted to all the DFT and MD calculations to ensure reliability and efficacy in the calculations.

Table 13: Comparison of the bond lengths in the n3-01 nanocluster calculated by IP and DFT techniques at varied temperatures ranging from 200 K to 1400 K.

	Bonds (Å)				
	O ₁ -O ₆	O ₁ -Mn ₁	Mn ₁ -O ₂	O ₂ -O ₄	Mn ₁ -Mn ₂
IP	9.933	1.926	1.997	3.562	3.040
DFT	7.856	1.565	1.726	3.048	2.362
200 K	7.205	1.566	1.741	3.124	2.298
400 K	7.245	1.528	1.781	3.192	2.286
600 K	7.461	1.628	1.731	3.157	2.392
800 K	7.664	1.547	1.740	3.301	2.344
1000 K	7.452	1.602	1.741	3.136	2.314
1200 K	7.013	1.602	1.767	3.088	2.259
1400 K	7.439	1.624	1.682	3.081	2.435

Table 13 compares the bond lengths of the n3-01 nanocluster. These comparisons are shown for IP and DFT calculations to determine which technique is more suitable for this material. The DFT measurements were shown to have shorter bond lengths as compared with the IP results. All the specified bond lengths have decreased after DFT optimisation. This shows that DFT is the preferred method for optimising the MnO₂ nanoclusters because shorter bond lengths imply more compact structures

which are associated with increased stabilities as mentioned in previous studies [22, 256, 70].

The calculations were also performed in order to investigate the behaviour of the atoms after DFT optimisation as the temperature was varied from 100 K to 1500 K. The extremely high temperatures above the melting point are considered in order to observe the changes occurring to the atomic configurations as was done in previous studies [258]. The analysis of the length is mainly focused on the terminal oxygen atoms, which is believed to sufficiently reflect on the stability and compactness of the n3-01 nanocluster because it measures the total length of this nanocluster.

It was found that the longest bond length between the terminal oxygen bonds is recorded at 800 K which coincidentally correlates with the melting point of pyrolusite at 808 K [246]. Tetragonal MnO₂ nanostructures have been shown to be stable 873 K and 1073 K, whereby phase transitions occur as temperatures are increased. Various polymorphs of manganese dioxide have been previously studied and shown to be stable at different temperatures. These polymorphs are hollandite (α -MnO₂), pyrolusite (β -MnO₂), nsutite (γ -MnO₂) and Akhtenskite (ϵ -MnO₂) [11].

Above the melting point, the terminal bond lengths rapidly decrease to 7.013 Å at 1200 K and again increases to 7.439 Å at 1400 K. This rapid changes in the bonding patterns might indicate the loss of stability and shape as a phase change occurs from a solid structure to a liquid phase after melting. Other bonds in the n3-01 nanocluster show similar trends occurring at the higher temperatures beyond the melting point.

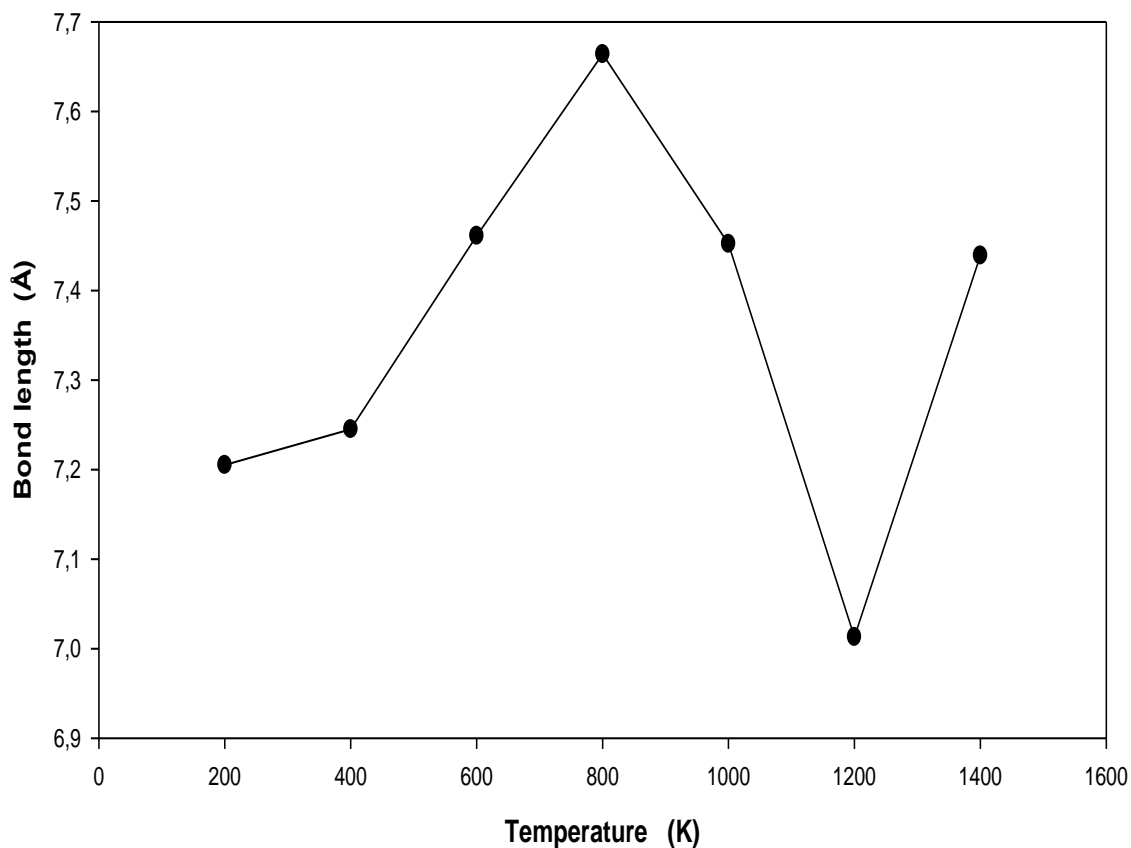


Figure 23: Bond length measurements of the n3-01 nanocluster as the temperatures was varied from 200 K to 1400 K

The high temperatures cause the exterior terminal oxygen atoms to lose their linear configuration and form compact circular configurations. Initially, a bond length of 9.933 Å for the IP nanocluster generated by KLMC was measured. This measurement decreased to 7.856 Å after optimisation with the DFT-based CASTEP code. This proves the capability of DFT techniques in optimising manganese dioxide nanoclusters and decreasing their bond lengths essentially making them more compact and smaller. This shows that the DFT optimised n3-01 nanocluster is structurally more stable and its atoms are more tightly bonded to each other as proven by their smaller bond lengths as measured in table 13.

The increasing temperatures are shown to cause an increase in the bond lengths as seen with the bond length between the two exterior terminal oxygen atoms. The bond

length was initially. 7.416 Å at 100 K and it increased to 7.784 Å for 1500 K. These observations are not encouraging as they display negative aspect of the nanoclusters. This result show that the nanoclusters are losing their shape and rigidity when temperatures rise which is a common occurrence in nature. These leads to the determination of other strategies to keep the bond distances smaller even when temperatures are rising. One of these strategies is doping which is investigated further in the next chapter.

6.1.2. Bond angles

This section reports on the changes occurring to the bond angles. The results compare the IP and DFT calculations. Furthermore, the DFT calculations were calculated for varying temperatures from 200 K to 1400 K to determine the effect of increasing temperatures on the orientation and coordination of the n3-01 nanocluster as their convergence was achieved. This specific bond angles were targeted for analysis because they represented the most influential atomic interactions in the n3-01 nanocluster.

Table 14 shows the bond angles between the bonds that have been deemed significant to sufficiently discuss changes occurring to the configuration and compactness of the nanocluster as the temperature is increased. Investigating this changes aids in determining the defects caused by high oxygen activities and erratic movements of other atoms caused by the increased disorder due to the higher temperatures [16].

Table 14: Comparison of the bond angles in the n3-01 nanocluster optimised by IP and DFT techniques and calculated at varied temperatures from 200 K to 400 K.

	Angles (degrees; °)		
	O₁-Mn₂-O₆	O₂-Mn₂-O₄	Mn₁-O₃-Mn₂
IP	180.00	125.37	98.88
DFT	179.90	117.92	84.76
200 K	153.91	125.22	80.11
400 K	163.21	126.54	81.57
600 K	157.95	123.41	84.21
800 K	169.30	136.95	87.64
1000 K	172.85	121.35	83.61
1200 K	152.50	116.52	79.03
1400 K	147.91	118.25	86.06

The angle between the exterior terminal oxygen atoms decreased from a linear 180° to 169.3° at the melting region of pyrolusite near 800 K. Furthermore, the angle continued to decrease to 147.9° at 1400 K. This shows that the nanoclusters adopt a more compact circular bonding pattern as the temperature was increased which is a significant positive attribute because that the nanocluster has actually decreased in size at higher temperatures which is a positive departure from the observations seen with the bulk structure. Smaller compact structures have been shown to be more stable and preferable for use in rechargeable batteries [22, 70, 256].

6.2. Binding energy

The binding energy was calculated using the molecular dynamics code DMol3. The binding energy can be defined as the energy required to disassemble the whole atomic structure into its constituent atoms [259]. The more tightly bound an atomic system is, the stronger the interatomic forces that adhere the whole atoms together. The binding energy is a convenient way to determine how well the nucleus of an element is intact. This measure is particularly important in evaluating the stability of the generated nanoclusters when temperature is varied. An increase in temperature is commonly associated with the constant charge and discharge occurring with rechargeable batteries [260].

The relationship between the binding energy, Fermi energies and the band-gap energy is tabulated in table 15 with plots discussed subsequently. Table 15 presents the binding energy, band-gap energy and Fermi energy values for the n3-01 nanocluster as the temperature was varied from 100 K to 1500 K.

This section reports on the binding energy results calculated for the n3-01 nanocluster as temperature was varied from 100 K to 1500 K. The binding energy fortifies the information derived from ranking the nanoclusters according to the total energies. These results are compared with those from the bulk structure to ascertain the structural changes that occur due to temperature changes.

Table 15: Total energies, binding energies, Fermi energies and the energy band-gap between the valence band edge and the conduction band edge with respect to the increasing temperature from 100 K to 1500 K.

Temp. (K)	Total energy (eV)	Binding energy (eV/atom)	Fermi energy (eV)	Band-gap energy (eV)
100	-11220.728	-4.439	-6.415	0.444
200	-11220.673	-4.490	-6.545	0.870
300	-11220.647	-4.474	-6.588	0.786
400	-11220.517	-4.486	-6.505	0.922
500	-11220.477	-4.423	-6.540	0.673
600	-11220.518	-4.482	-6.530	0.429
700	-11220.550	-4.435	-6.460	0.572
800	-11220.314	-4.439	-6.338	0.265
900	-11220.363	-4.413	-6.282	0.319
1000	-11220.547	-4.429	-6.604	0.650
1100	-11220.437	-4.405	-6.667	0.641
1200	-11220.102	-4.390	-6.697	0.725
1300	-11220.150	-4.416	-6.618	0.678
1400	-11220.156	-4.387	-6.283	0.475
1500	-11220.041	-4.401	-6.538	0.646

It is observed that the binding energy decreases from -3.969 eV/atom for the IP generated nanocluster to -4.441 eV for the DFT optimised nanocluster. The lowest total energy is recorded at 100 K and the highest total energy is recorded at 1500 K showing that the higher temperatures reduce the stability in the nanoclusters.

An increase in the bond lengths is associated with the weakening of the bonds as it implies that there is an increased repulsion between the atoms in the nanocluster. As the bond lengths increase this will result in the deformation of the crystal and loss of the structural integrity [18]. The inverse also applies, such that a decrease in the bond lengths implies stronger bonds. These observations agree well the results of this study because the nanocluster optimised by DFT shows a decrease in the bond lengths as compared to the nanoclusters optimised by IP techniques.

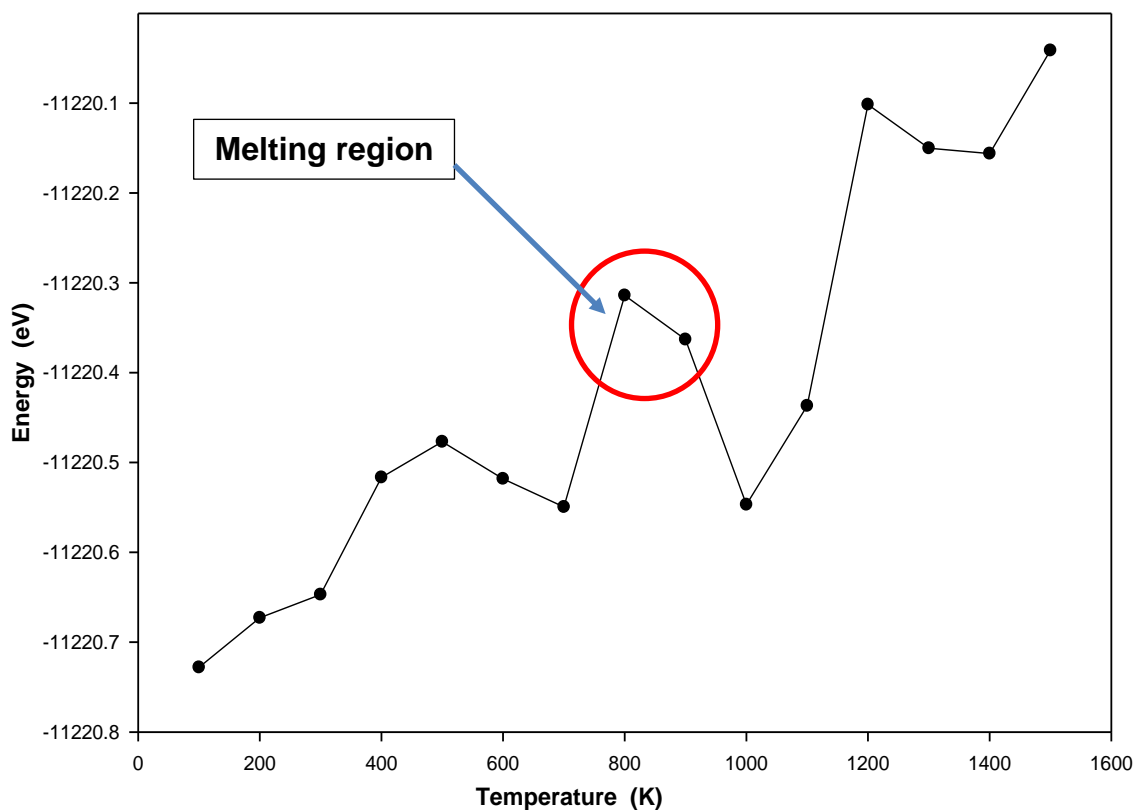


Figure 24: Total Energies of the n3-01 nanocluster drawn against the temperature ranging from 100 K to 1500 K.

Figure 24 measures the total energy of the nanoclusters as the temperature is varied from 100 K to 1500 K. Recall from chapter 4.3, that first-principles total-energy calculations have been shown to be of significant importance on examining the properties of materials and their interactions with dopant impurities and native defects existing in natural compounds [245], hence their continued discussions in the thesis.

Figure 24 shows the direct relationship whereby the total energy is increasing with the increasing temperatures. This trend was also observed with the bulk structure as reported in chapter 4. An interesting observation is noted around the 800 K temperature where the total energy shows a sudden spike from 700 K to 900 K then decreases sharply at 1000 K. This sudden increase occurs at the exact region reported to be the melting point of pyrolusite which is synonymous with phase changes to other polymorphs of manganese dioxide.

The melting points of nanostructures containing oxygen have been shown to decrease to lower temperatures as compared to the bulk structure [249]. This could explain why this plot decreases immediately after 800 K as opposed to the bulk structure which showed the decrease only after 900 K. The decrease continues on this plot sharply until it bottoms out at 1000 K where it starts another gradual increase in the total energy showing instability as the temperature continues to increase.

The binding energy, Fermi energy and the band-gap energy give further insight about the electronic properties of the n3-01 nanocluster as the temperature is increased. The binding energy was calculated one at a time at the indicated temperatures and the results are plotted below.

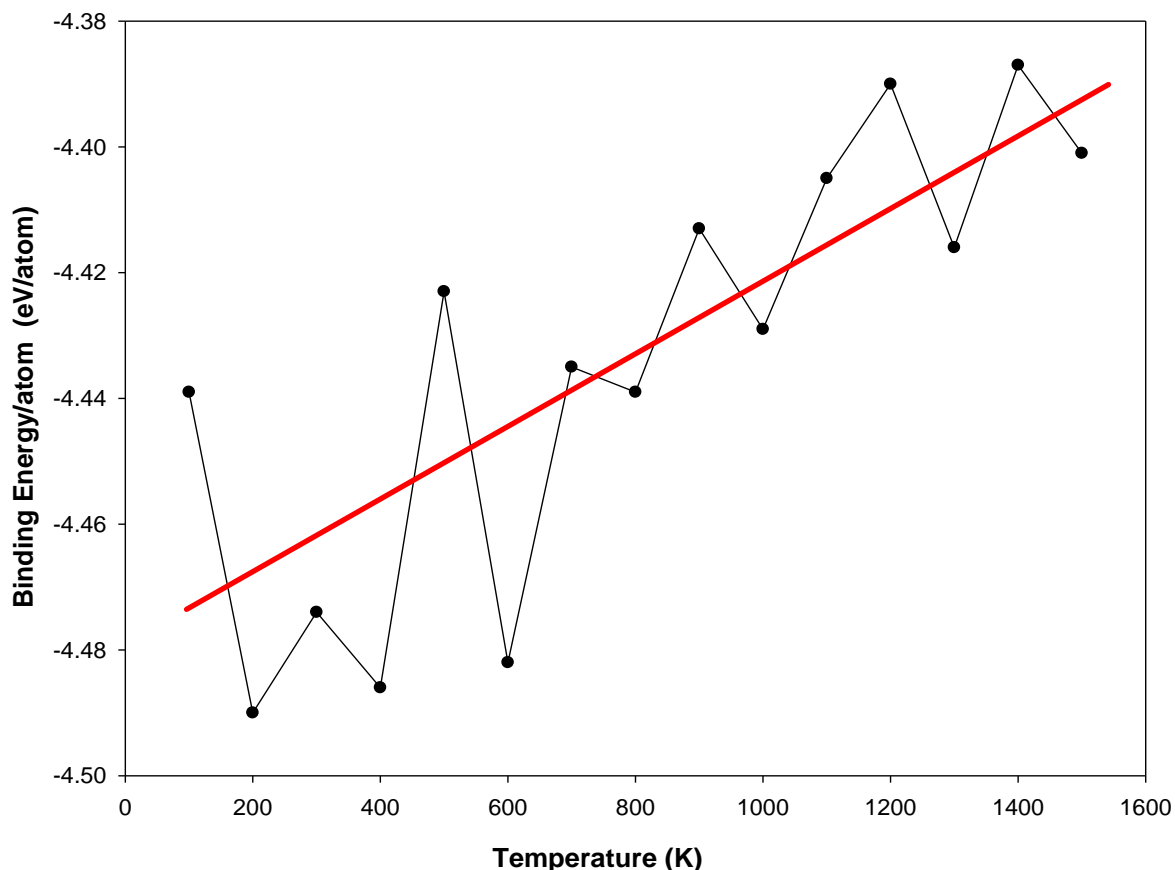


Figure 25: Plot depicting the Binding energy vs Temperature of the most stable nanocluster consisting of 3 manganese atoms and 6 oxygen atoms ranging from 100 K to 1500 K.

Figure 25 displays the binding energy of the atoms in the n3-01 nanocluster as the temperature was increased from 100 K to 1500 K at a rate of 100 K. It is observed from the graph and the line of best fit that the binding energy is decreasing as the temperature is being increased at a 100 K interval. The graphs show an indirect relationship where the binding energy decreases with increasing temperature showing that high temperatures weaken the bonds in the nanocluster. This is in line with observations by Tompsett et al. [16] and Kwon et al. [18] showing that bonds are weakened at higher temperatures. It is thus imperative to explore new innovative ways to keep the nanoclusters intact even when temperature is increasing, one of the methods is doping which is discussed in the next chapter.

The least negative readings of the binding energy are recorded at the lower temperatures and the highest negative readings are recorded at the higher temperatures showing that the structure is most stable when kept cool and begins to disintegrate and deteriorate as the temperature increases. The most stable binding energy of -4.490 eV/atom is recorded at 200 K and the least stable energy of -4.387 eV/atom is recorded at 1400 K show that increased temperatures cause the atoms in the structure to be less tightly bound together.

6.3. Fermi energy

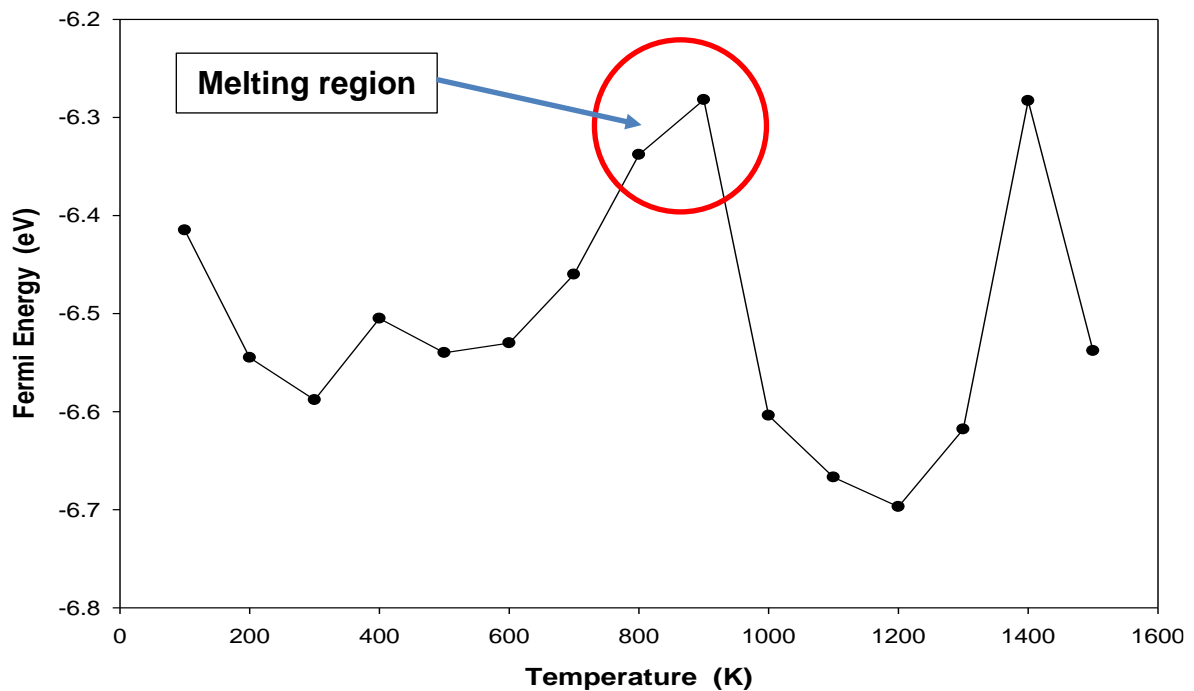


Figure 26: Plot depicting the Fermi Energy vs Temperature of the most stable nanocluster consisting of 3 manganese atoms and 6 oxygen atoms ranging from 100 K to 1500 K.

Figure 26 is plot of the Fermi energy drawn against the increasing temperature from 100 K to 1500 K. It is observed that the initial fermi energy of -6.415 eV was recorded at 100 K and then decreased from 100 K to 300 K. After 300 K, the Fermi energy

increased gradually until the plot plateaued near the melting region of pyrolusite around 800 K, the actual melting point of pyrolusite is reported to be 808 K [246]. An interesting observation is made around this melting region from 800 K – 900 K where the plot reaches its highest Fermi energy reading at 900 K and immediately drops drastically until it reaches its lowest point at 1200 K.

The negative sign of the Fermi energies indicates that the Fermi is located below the conduction band edge implying a good conductive nature. An increase in temperature is associated with a decrease in conductivity because free electrons vibrate due to excitation and they do not flow easily due their increased motion and entropy. This decreases the conductivity in metallic conductors [194, 195].

6.4. Band-gap energy

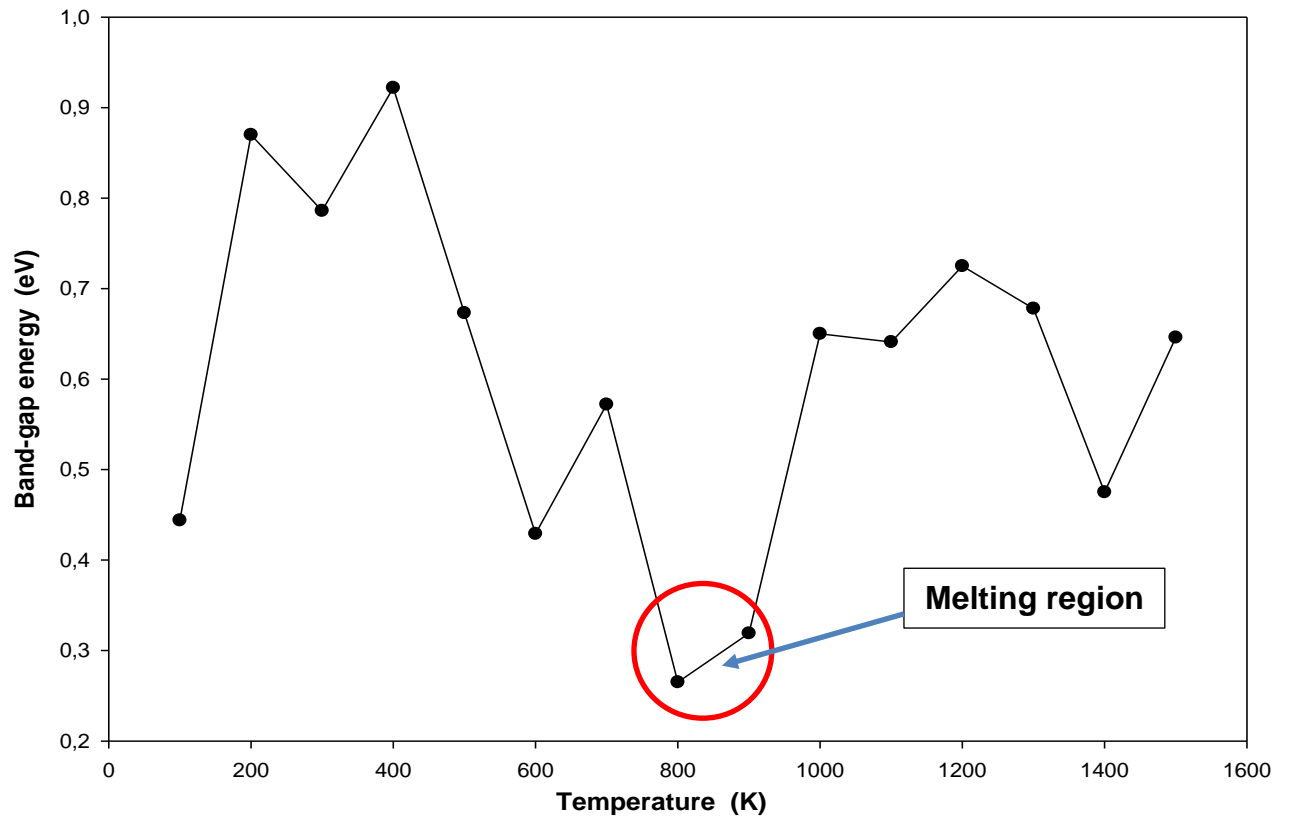


Figure 27: Plot depicting the band-gap energy of the n3-01 nanocluster measured against increasing temperatures from 100 K to 1500 K.

Figure 27 displays the relationship between the band-gap energy and the temperature as it is increased from 100 K to 1500 K. The band-gap energy measures the energy difference between the valence band edge and the conduction band edge. The band-gap energy gives information on the electrical conductivity of the nanocluster structures in question. It details whether a material is a semiconductor, insulator or a conductor [195, 196]. For this study, the quest is on determining the structure with the smallest band-gap energy. This is of interest because of the MnO₂ nanoclusters intended use as a cathode material that can efficiently conduct electricity to facilitate a speedy charge/discharge cycle in secondary batteries [261].

From figure 27, it is observed that the highest band-gap of 0.922 eV was recorded at 400 K and the lowest band-gap of 0.265 eV was recorded at 800 K. This lowest band-gap is recorded near the melting region of pyrolusite in the region of 800 K - 900 K as reported in previous literature [246]. This indicates that MnO₂ nanoclusters become better electrical conductors in their liquid form which occur at the melting region where it has been shown that some phase transitions do occur to other phases of manganese dioxide.

The analysis and discussions carried out in this chapter show that DFT is the preferred method for optimising the MnO₂ nanoclusters because of the measured shorter bond lengths. The longest bond length between the terminal oxygen bonds is recorded at 800 K which is the melting point of pyrolusite [246]. The nanoclusters display a loss in their structural integrity and rigidity when temperatures reach extreme high levels.

The angle between the exterior terminal oxygen atoms decreased from a linear 180° to 147.9° at 1400 K. This shows that the nanoclusters favour more compact circular bonding patterns at higher temperatures which is a significant positive attribute. The implications are that circular compact structures are associated with the increased stabilities which correlates well with previous studies [22, 256, 70].

The binding energy is shown to decrease with increasing temperature showing that high temperatures weaken the bonds in the nanocluster. The negative sign of the Fermi energies indicates that the Fermi is located below the conduction band edge implying a good conductive nature. This lowest band-gap is recorded near the melting region of pyrolusite in the region of 800 K - 900 K as reported in previous literature

[246]. This indicates that MnO_2 nanoclusters become better electrical conductors in their liquid form which occur at the melting region.

This results also indicate that although pyrolusite has been reported to be the most stable polymorph, it might not be the best electrical conductor which is one of the requirements for its use as a cathode material in secondary batteries. The loss of stability at a higher temperature is a concern for pyrolusite however other phases of MnO_2 have been shown to be stable upon heating [128, 262]. Other avenues such as doping have been shown to improve the stability of pyrolusite and this will be investigated in more detail in the latter chapters.

Chapter 7: X-Ray diffraction

This chapter presents the X-ray diffraction (XRD) patterns of the undoped and doped n3-01 nanoclusters. The XRD patterns have been developed using the Reflex code embedded as part of the Material Studio software package. A brief methodology of this code is given in the methodology chapter 3. In particular, these XRD patterns were determined in order to check for the possible structural and phase changes occurring to the nanoclusters after doping with Fe, Co and Ni. Recall from chapter 4 that these dopants were chosen due to their effectiveness in other previous studies [68, 123, 126].

Furthermore, the XRD patterns are used to investigate the effect of the varied temperatures on the structural morphology, phase changes as well as the behaviour of the nanoclusters as they approach their melting temperatures. The temperature was varied from 100 K to 1000 K. Initial calculations showed that the XRD patterns did not produce any peaks beyond the 40 2θ region hence the scale of all the XRD patterns ranged from 0 to 40 2θ on the horizontal scale.

7.1.1. X-Ray diffraction of the undoped n3 nanoclusters

This section reports on the XRD patterns of the three most stable nanocluster systems from the n=3 local minima nanoclusters; n3-01, n3-02 and n3-03. The XRD patterns displayed in figure 28 were of the nanoclusters that were generated using IP techniques with KLMC (before they were subjected to optimisation by DFT techniques with CASTEP).

Figure 28 (a, b, c) shows the calculated XRD pattern of the three most stable nanoclusters composed of 3 manganese atoms and 6 oxygen atoms without the rutile space group limitation as was done with the β - MnO_2 bulk structure.

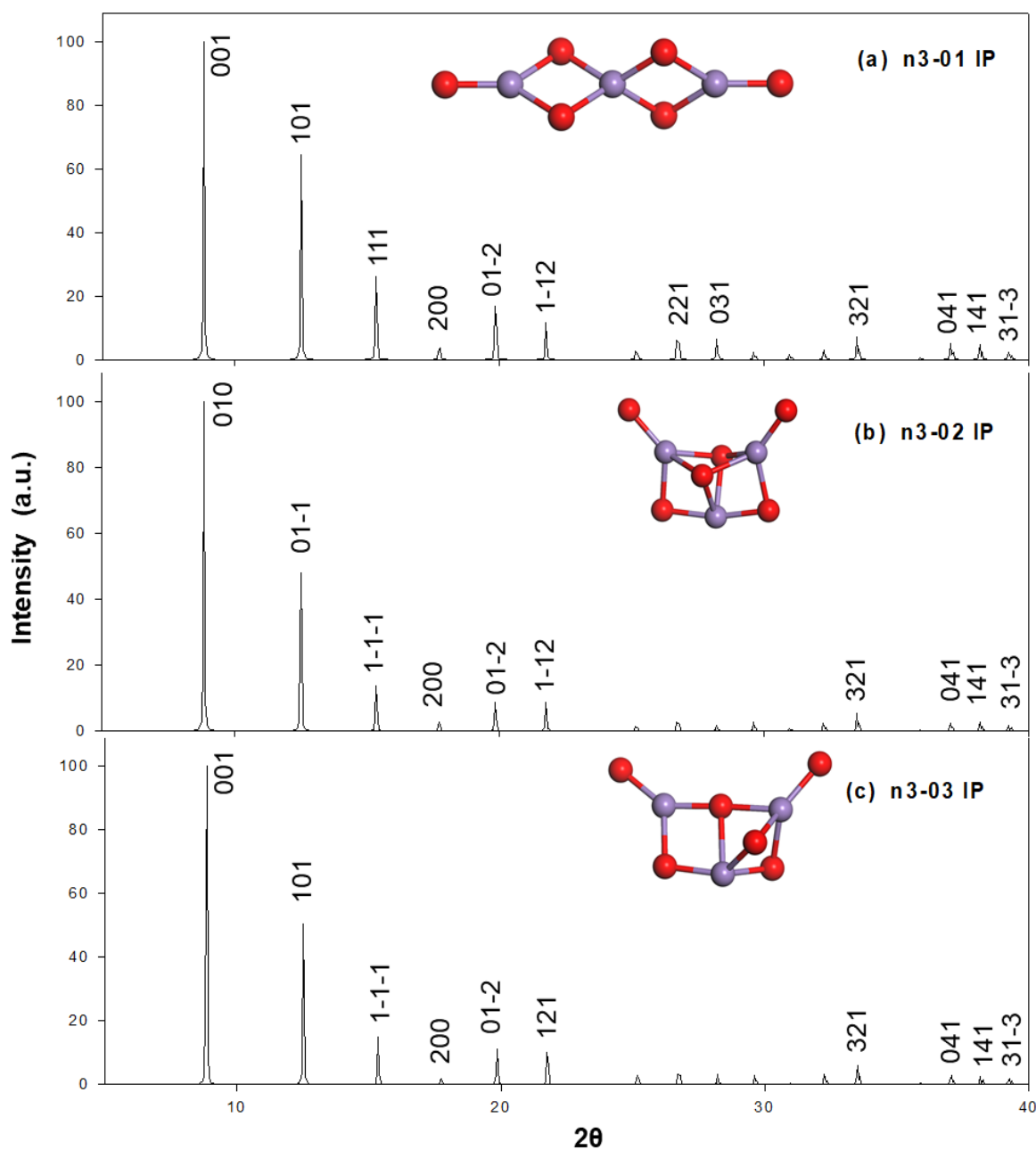


Figure 28: XRD patterns for the three most stable (MnO_2) $n=3$ nanoclusters developed using IP techniques.

From figure 28, it is observed that the most stable nanocluster i.e., n3-01 and the lesser stable nanocluster, the n3-03 contain similar peaks with miller indices such as

the (001), (101), (01-2), (321), (041), (141) and (31-3) respectively. These identically Miller indexed peaks are all situated on the same 2θ positions indicate the presence of similar phases such as the tetragonal dipyramidal class indicative of the rutile phase in both the nanoclusters. It is noted that the (001) peak is the first and most dominant peak across the two XRD patterns due to its highest intensity of 100 arbitrary units (a.u.) occurring at approximately $8.9^\circ 2\theta$. A similar behaviour was observed in a previous study by Augustin *et al.* [244] as displayed in figure 29 containing MnO_2 with a dominant (001) peak near the $10^\circ 2\theta$ region.

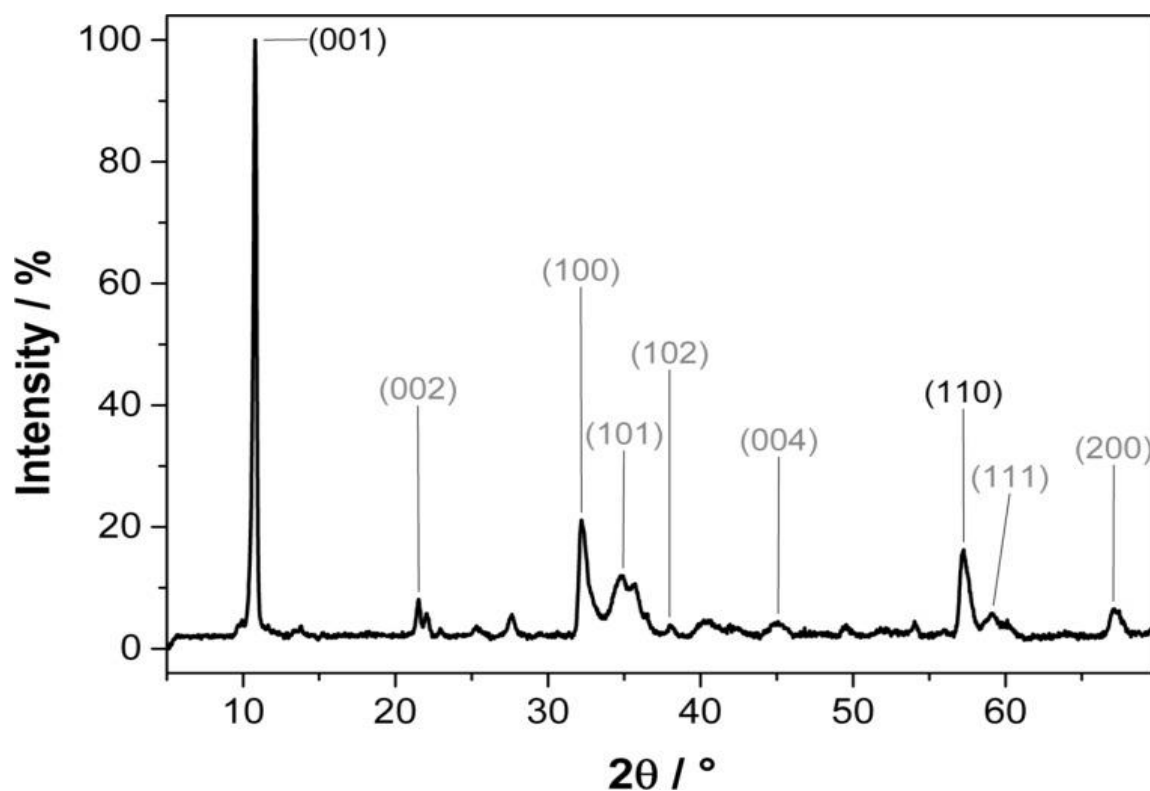


Figure 29: XRD pattern from a previous study by Augustine *et al.* [244] depicting different MnO_x species

Comparing figure 28 (a) and (c) with figure 29, it is observed that the n3-01 and n3-03 nanoclusters have the (001), (101) and (200) peaks which are also present on the previous study in figure 29. Furthermore, a peak indexed (010) for the (b) n3-02

nanocluster in figure 28 has similar attributes to the (001) peak due to its intensity and 2θ positioning. Hence, it is inferred that they all indicate the presence of the same stable rutile phase as shown in figure 30 displaying some similar peaks from a previous study by McLeod *et al.* [263].

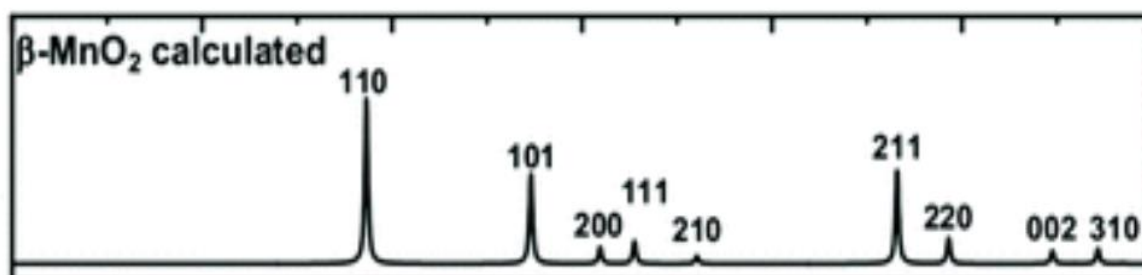


Figure 30: XRD patterns of a rutile-type pyrolusite product synthesised from mixed manganese dioxide mixtures crystallised under acidic hydrothermal conditions [263].

From figure 30, we observe that the illustrated XRD patterns display some similar Miller indexed peaks to figure 28 showing that these simulated nanoclusters contain some traits and phases that are available in the naturally occurring manganese dioxide structures that have been studied experimentally [263]. The (101), (111) and (200) Miller indexed peaks observed at the 2θ position of 12.5, 15.3 and 17.7 respectively are all indicative of the presence of the tetragonal phase signifying the stable rutile $\beta\text{-MnO}_2$. This is in good agreement with a previous study by Hassan *et al.* [212] which indicated a similar peak with the Miller d_{hkl} index of (200) at a 2θ position of 18.9° and this correlates agreeably.

The similarities in the location of the peaks and the Miller indexes can be attributed to the identical bonding patterns of some atoms in all the three nanoclusters. For example, 1) all the structural configurations have a central manganese atom that is bonded to 4 oxygen atoms, 2) they all have exterior terminal oxygen atoms that are

bonded singularly to a manganese atom, 3) the internal arrangement of the atoms is dominated by diamond or cubic like structure consisting of two manganese atoms and two oxygen atoms. These similar characteristics in the atomic configurations explain the similar attributes in the XRD patterns and the presence of common phases. Inversely, all the other differences observed in the positions of the peaks, their intensities and their Miller indexes can be attributed to their differences in the atomic configurations.

It is especially encouraging that both the simulated nanoclusters and the experimental XRD patterns displays some similar peaks representing the stable pyrolusite polymorph such as the (001), (101), (111) and the (200) peaks. Recall that the nanoclusters adopt a cubic crystal system during DFT calculations whereas the bulk β -MnO₂ structure belongs to the tetragonal crystal system. These differences in the crystal models of the bulk pyrolusite and the generated stable nanoclusters has an effect on their XRD patterns. For example, peaks such as (01-2) and (031) on figure 28 (a) are not present on both the previous XRD patterns displayed in figure 29 and 30. However, it is envisaged that some of these observed differences are indicative of some improvements in the structural integrity of the nanoclusters.

Peaks associated with other MnO₂ phases such as the Anatase and Brookite phases that have dominant high intensity peaks occurring near 25 2 θ and 48 2 θ are not observed in figure 28 [264, 265]. Hence, no other phases except the stable rutile phase have been detected in the n3 nanoclusters. From these discussions, the peaks in figure 28 can be associated and attributed to phases correlating to the most stable and abundant polymorph of MnO₂, i.e., pyrolusite [12] as shown in figure 30.

7.1.2. XRD patterns of the n3-01 nanocluster at varying temperatures

This section investigates the impact of increasing temperatures of the phase changes present in the most stable nanocluster with three manganese and 6 oxygen atoms, i.e., n3-01. Figure 31 presents the XRD patterns of the n3-01 nanocluster calculated at increasing temperatures ranging from 200 K to 1000 K. These temperatures are selected to observe the behaviour of the nanoclusters at lower temperatures and even at temperatures above the melting point of 808 K to check for any phase changes. The intensities are displayed from zero until a maximum 2θ range of 40° .

From figure 31, it is observed that the XRD landscapes of all the XRD patterns are mostly indistinguishable with noticeable similarities in their 2θ positions, Miller indexes and intensities. The miller indexes were checked and they all reported identical indexes across the temperature range of 200 K to 1000 K measured (only 200 K is displayed). This similarity shows that these nanoclusters have maintained their structural integrity and phases even when temperatures are increasing beyond the melting point at 808 K for the β -MnO₂ bulk structure. Furthermore, this encouraging result shows a significant improvement from the observations seen with the β -MnO₂ bulk structure which showed significant deterioration at higher temperatures in section 4.3.

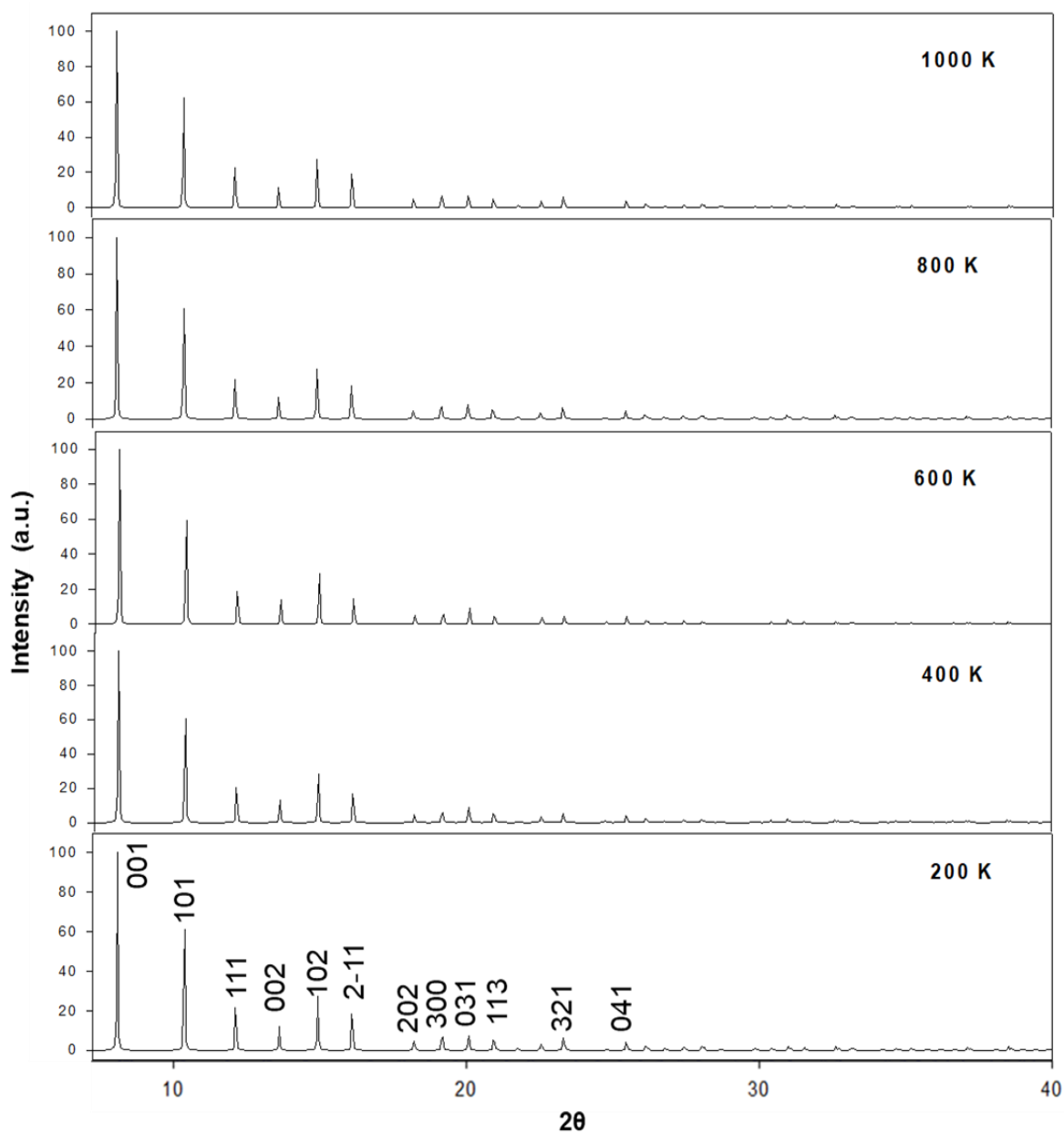


Figure 31: XRD patterns of the n3-01 nanocluster optimised at varying temperatures from 200 K to 1400 K.

The (001) which was shown to be dominant due to its high intensity in the undoped nanocluster generated using IP techniques (as shown in figure 28 a) is also observed in the XRD patterns on figure 31. Furthermore, other peaks such as the (101), (111) and (031) are also available on both XRD patterns, this indicative of similar phases of pyrolusite detected in both nanoclusters. This is proven by the (001), (101), (002),

(102) peaks being present on the previous XRD patterns by Augustine *et al.* [244] (see figure 29).

These results are promising and positive, considering that cathodes in rechargeable batteries reach higher temperatures during the repeated charge-discharge cycles. This shows that the operating temperature of manganese dioxide materials can be improved by nanostructuring. A similar XRD landscape was observed from a previous study where similar XRD patterns were plotted as depicted in figure 32 [243].

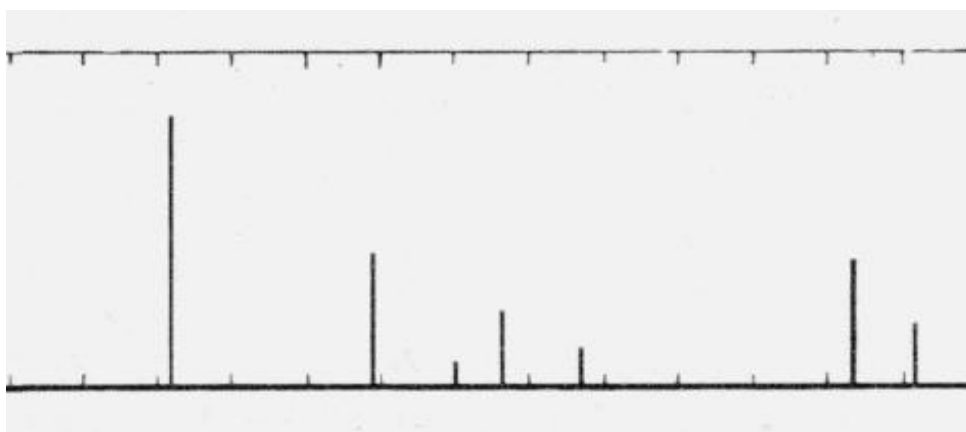


Figure 32: Extract from a study by McMurdie *et al.* [243] indicating the XRD pattern of an ore containing pyrolusite.

From figure 32, we observe an XRD pattern from a study by McMurdie *et al.* [243] illustrating a similar plot to those depicted in figure 31, in order to show the good correlation between these studies. It is observed that the peaks in figure 31 and figure 32 are consistent in their 2θ positioning and intensities, however no significant analysis can be made at this stage based on the peak sizes and peak widths due to the type of calculations and plots done. Broader peak widths are usually associated with a larger nanocrystallite [266], this aspect will be investigated further in future studies.

7.1.3. XRD spectroscopy of the doped n3-01 nanoclusters

This subsection focuses on the XRD analysis of the n3-01 doped on the central cation position denoted by Mn²⁺. Again, Fe, Co and Ni are used as the dopants of interest as was done in the previous chapters. The initial discussions carried out compare the XRD patterns from the bulk β -MnO₂ structure with the XRD patterns from the pure un-doped n3-01 nanocluster. Lastly, the comparisons are made with the XRD patterns from the doped n3-01 nanocluster optimised by the DFT based code CASTEP and illustrated using the Reflex code. Both these codes are found in the Materials studio software package as mentioned previously in this study.

The XRD patterns presented in chapter 4 (figure 13) were prepared using the 2015 version of Materials Studio, while the patterns illustrated in this section were prepared using the 2019 version of Materials Studio. This might lead to some discrepancies and/or mismatch in the comparisons of their XRD patterns. Speakman [213] stated that XRD intensities and their 2θ positions are dependent on the specific instrumental characteristics of that certain tool utilised. There is limited knowledge available on existing XRD patterns of manganese dioxide nanoclusters hence there is a shortage of previous studies that can be used to compare with the current study adding to the novelty of this study.

To verify the findings from the previous chapter concerning the effect of doping on the nanocluster's structural phase changes, The XRD patterns of the doped nanoclusters are illustrated in figure 34. The displayed patterns are for the n3-01 nanocluster doped by Fe, Co and Ni on the central manganese atom denoted by Mn²⁺. This position is selected because it was shown to be the most preferable atomic site to perform the substitutional doping on.

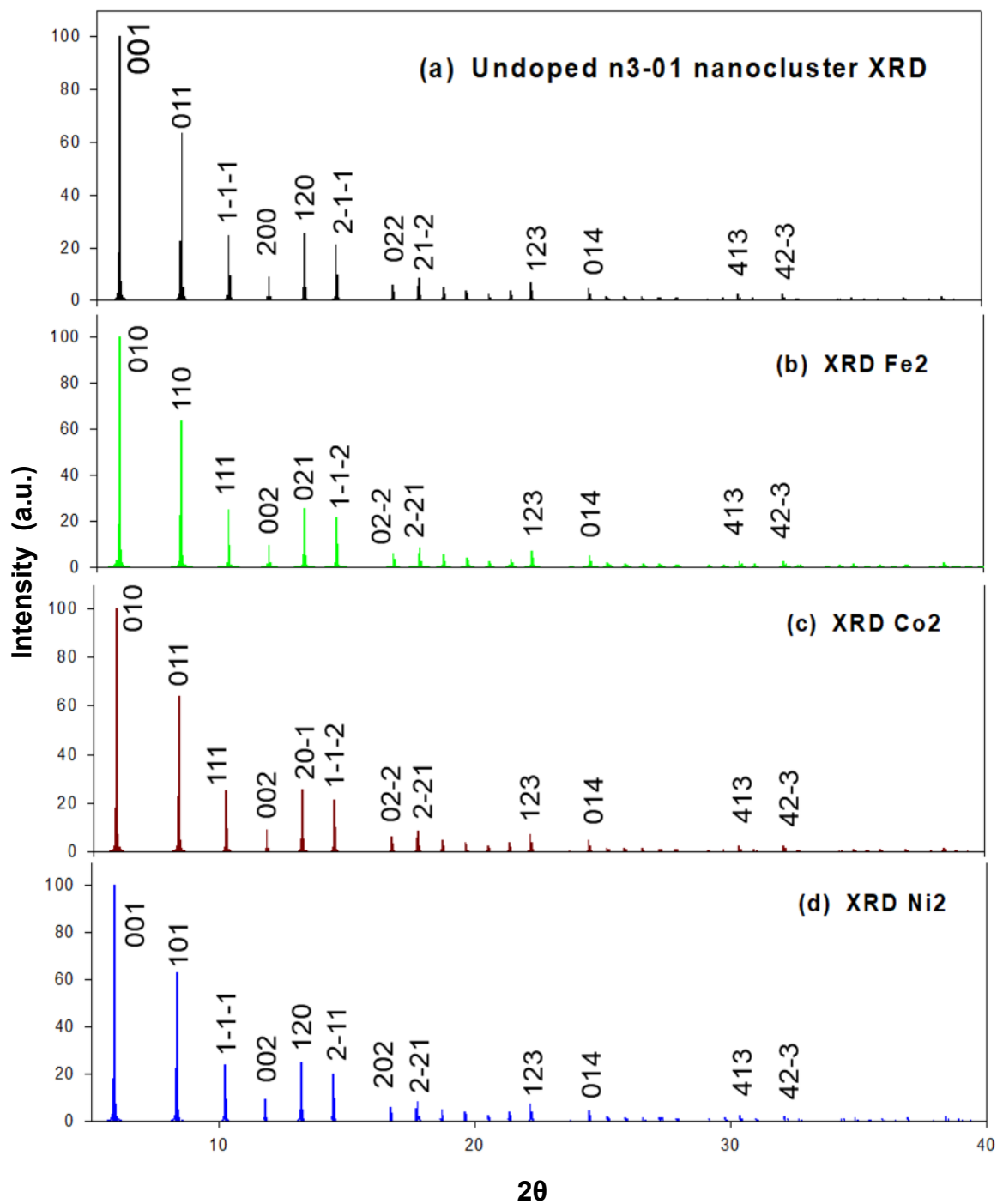


Figure 33: A comparison of the XRD patterns of the (a) undoped n3-01 nanocluster with XRD patterns of the n3-01 nanoclusters doped with (a) Fe, (b) Co and (d) Ni on the Mn₂ atomic position.

From the XRD patterns displayed in figure 33 of the doped n3-01 nanoclusters, it is observed that the (001) peak for the (a) undoped and (d) Ni-doped n3-01 nanocluster have the same highest intensity and 2θ positioning. Additionally, the (010) peak for

(b) Fe-doped and (c) Co-doped n3-01 nanocluster at the same position also has the highest intensities. These peaks with intensities of 100 a.u. are indicative of the stable rutile phase in the nanoclusters as discussed in the previous section and in previous literature [212, 241, 243, 263]. More detailed discussion about these phases was carried out in section 7.1.1. This observation is crucial as the study aims to improve the structural properties and stability of pyrolusite hence proof that there is actual presence of pyrolusite in this computer simulated nanoclusters is very encouraging [242, 263].

Comparing the XRD patterns in figure 32 (a), (b), (c) and (d) with figure 33 shows a remarkably similar landscape in the peaks from the previous study with the current study in terms of peak positioning and intensity. The minor positional differences of the peaks on the horizontal 2θ scale are inconsequential due to the mismatch in the instrumental settings however the succession and intensities of the peaks correlates well. Similar XRD landscapes were observed on similar previous studies [212, 263]. There are minor peaks beyond the 33 2θ position which are deemed insignificant due to their exceptionally low intensities as such they resemble noise [213] on the current study.

The presence of the rutile phase as shown by the (001), (002), (200) and (111) peaks indicates that the growing nanoclusters are mutating from the cubic crystal system towards the rutile tetragonal crystal system originally observed with the β -MnO₂ bulk structure [12]. This mutation is important because it shows that the growing nanoclusters are naturally conforming to structures that are prevalent in the naturally occurring manganese dioxide which are known to be stable [11].

Recall, from chapter 1 that the various polymorphs of manganese dioxide differed mainly in the distribution of manganese atoms in the octahedral sites. Now, looking at the different indexes of the peaks between the bulk structure and these nanoclusters, it is evident that there are new atomic orientations occurring in the doped nanoclusters. It is our goal to eventually show that these new phases indicate the improved stability of the new nanoclusters. Furthermore, this stability is again observed in the Ni-doped n3-01 nanocluster due to the first two peaks having highest intensities. From these discussions, it is evident that the growing nanoclusters indeed display different properties from the bulk pyrolusite. The XRD analysis from this chapter shows the sensitivity of the nanoclusters to their composition and size, which will lead to new and interesting properties improving those of the bulk material [20].

There are also some substantial differences in the intensities and positions of the other peaks showing that this nanocluster has undergone considerable changes during this process. It is envisaged that all these differences indicate an improvement in the structural stability, electrochemical activity and conductivity of these newly generated nanoclusters. Comparing the XRD patterns of this optimised nanocluster with the original nanocluster in figure 26 shows that indeed optimisation succeeds in altering the orientation and bonding lengths in the nanoclusters.

It is encouraging to observe that the XRD patterns discussed in this chapter show some similarity in the positioning and intensities of the peaks with the XRD pattern from the experimental study by Zheng *et al.* [241] for the β -MnO₂ nanotube bulk structure. This indicates that there are still some positive attributes maintained by these DFT optimised nanoclusters as discussed in section 4.2 focusing on XRD spectroscopy of the β -MnO₂ bulk structure.

Chapter 8: The effect of doping on the electronic properties of MnO₂ nanoclusters

This chapter focuses on the effect of doping on the electronic properties and stability of the MnO₂ nanoclusters, specifically the stable n3-01 nanocluster. The dopants of interest are Fe, Co and Ni. Additionally, the density of states (DOS), the band-gap energy between the valence band and conduction band at the Fermi level will also be discussed. Furthermore, the band structure is used to determine what type of material the nanoclusters are i.e., insulator or semi-conductor or conductor. A shorter band-gap indicates the material has a higher intrinsic conduction [197, 240].

The stability of the doped nanoclusters is investigated by focusing on the binding energies of the doped nanoclusters and the bond lengths between some respective atoms of interest. In particular, the bond lengths were measured to determine the impact of doping on the growth of the nanoclusters. The information gathered from this chapter is compared with that from the analysis of the bulk β -MnO₂ structure as discussed in chapter 4.

8.1. Doping of the n3-01 nanocluster

From this section, we focus on the substitutional of doping of the n3-01 nanocluster. Specifically, on determining the preferred cation position to perform the doping process. The atomic substitutional method was employed instead of the interstitial doping where a Mn atom is replaced by either Fe, Co or Ni. This choice of doping technique is preferred due to interstitial doping adding an extra atom to the existing nanocluster structure, thereby increasing its volume and size. Whereas this study

aims to decrease the size of the structures while increasing their stability doping, hence the choice of substitutional doping [224, 225].

The preferred doping position is determined by replacing the cations systematically on all the atomic positions initially occupied by manganese on the most stable nanocluster consisting of 3 manganese and 6 oxygen atoms (n3-01). This is done to specify whether the Mn1 (least coordinated cation) or Mn2 (highest coordinated cation) is more preferable to perform the substitutional doping procedure.

8.1.1. Preferred doping position

The doping process is performed by firstly determining the preferred doping site from among all the atomic sites initially occupied by the manganese atoms. The three dopants (Fe, Co and Ni) were substituted on the indicated atomic sites i.e., Mn1 and Mn2 of figure 35. The discussions from this subsection will seek to validate the selection of the specific dopant impurity as determined in chapter 4. Comparisons between the results from the earlier chapters are made in order to make certain conclusions and definitive recommendations for future studies.

The DFT-based CASTEP code is used to optimise the doped n3-01 nanoclusters. Subsequently, the molecular dynamics DMol³ code is used to measure the Fermi energy, band-gap energy, valence band and conduction band edges using the Material Studio software suit. Furthermore, figure 35 displays the bond lengths and all the labelled atomic positions occupied by all the manganese and oxygen atoms in the pure DFT-optimised n3-01 nanocluster. These measurements will serve to compare with the results after doping in an attempt to determine the impact of doping on the stability and electronic properties of the nanoclusters.

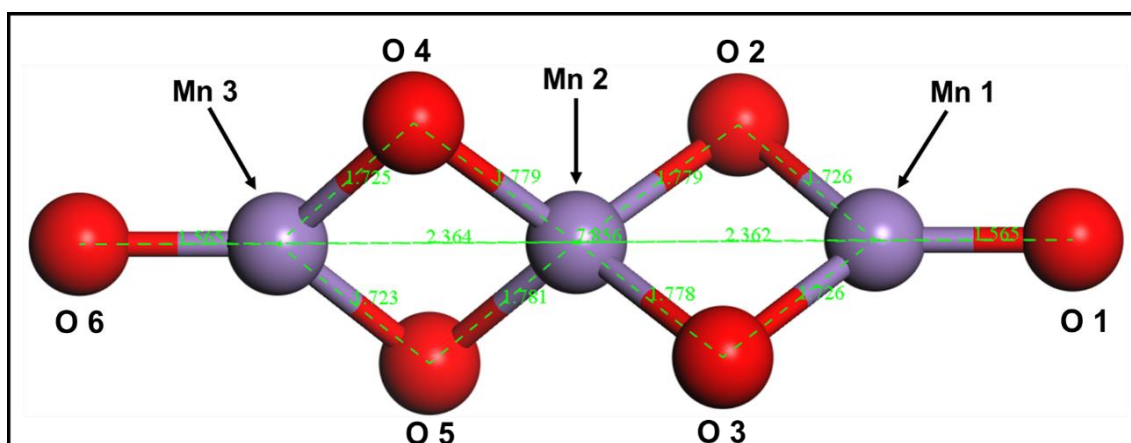


Figure 34: The n3-01 nanocluster indicating the labelled atomic positions before doping

From figure 34, it can be construed that the atomic positions labelled as Mn1 and Mn3 are symmetrically identical. This symmetry is attributed to the similarity of the left and right fragments of this nanocluster. The bond lengths on the left side are almost identical to the bond lengths on the right side of the central manganese atom.

This symmetry in the n3-01 nanocluster allows for the calculations and analysis to be performed on only one side of the fragment, i.e., on Mn1 and Mn2 only. Furthermore, the Mn1 and Mn3 atoms have equal Hirshfeld charges of 0.39e as further evidence of this similarity.

8.2.1. Iron doping of the n3-01 nanocluster

In this subsection, we focus on the Fe-doping of the n3-01 nanocluster. Table 16 presents the Fermi energy, band-gap energy and binding energy of the undoped and Fe-doped n3-01 nanocluster. In particular, these calculations are carried out in an effort towards determining the impact of Fe-doping on the n3-01 nanocluster.

Table 16: Electronic properties of the pure and Fe-doped n3-01 nanocluster showing their Fermi energies, band-gap energies and binding energies.

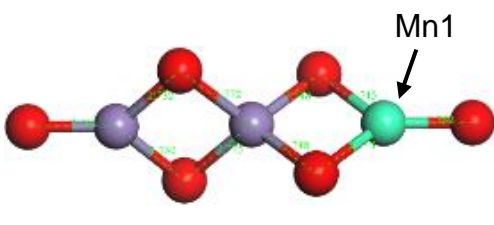
		
	Undoped n3-01	Fe-doped n3-01 nanocluster
Fermi energy (eV)	- 6.486	- 6.304
DFT energy gap (eV)	0.416	0.651
valence band (eV)	- 6.486	- 6.304
conduction band (eV)	- 6.071	- 5.653
binding energy (eV)	- 4.441	- 4.124
(eV/atom)		
Total energy (eV)	- 11220.719	- 9220.026

Table 16 presents the Fe-doping results when substitutional doping was performed on the Mn1 atomic position and comparing this with the pure undoped n3-01 nanocluster. The Mn2 position was unstable and failed to converge hence it is excluded from the analysis.

The Fe-doped nanocluster is less stable with a higher Fermi energy of -6.304 eV after DFT optimisation with the CASTEP code. This is a deterioration from the Fermi energy of -6.486 eV of the pure undoped n3-01 nanocluster. Consequently, the band-

gap energy of 0.416 eV and the binding energy of -4.441 eV/atom are lower and favour the undoped n3-01 nanocluster. In comparison, the Fe-doped n3-01 nanocluster recorded a larger band-gap energy of 0.714 eV and a less stable binding energy of -4.124 eV/atom.

Analysis of the results show that the pure undoped n3-01 nanocluster is a better conductor due to the lower Fermi energy and shorter band gap. Particularly, this is due to manganese having 5 electrons in its 3d valence orbital as opposed to the 6 electrons for iron. This shows that manganese can accommodate more electrons from the oxygen atoms during hybridisation and bonding due to its half-filled 3d orbital for the Mn^{2+} ion. Furthermore, the higher electron affinity of the iron dopant is shown to be negatively affecting the stability of the Fe-doped n3-01 nanocluster as shown by the decreased binding energy and lower Fermi energy.

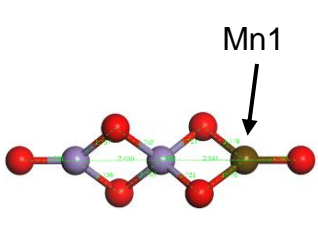
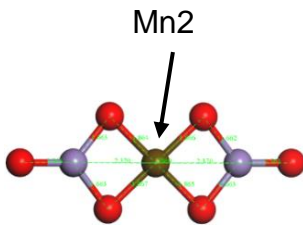
Consequently, this failure in enhancing the electronic properties and stability of the nanocluster indicates that iron cannot be recommended as a potential dopant in this study. This observation correlates well with discussions from chapter 4 pertaining to doping of the β - MnO_2 bulk structure. In addition to some calculations failing to converge when the n3-01 nanocluster was doped on the central Mn2 atom using the same parameters that were successful in optimising all the other structures in this study, points to the failure of iron as a potential dopant for manganese dioxide.

8.2.2. Cobalt doping of the n3-01 nanocluster

This section focuses on the Co-doping of the n3-01 nanocluster. Similar to Fe-doping, the Fermi energy, band-gap energy and binding energy are calculated in order to determine the influence of doping with cobalt on the n3-01 nanocluster. The

substitutional doping is performed on the two atomic positions denoted by Mn1 (exterior cation position on the right fragment) and Mn2 (central cation position with the higher coordination). Mn1 denotes the exterior manganese atom on the right fragment of the n3-01 nanocluster with the lower coordination having a 0.39e Hirshfeld charge. Mn2 is the interior central manganese atom with the higher coordination having a 0.32e Hirshfeld charge.

Table 17: Electronic properties of the Co-doped n3-01 nanocluster

			
	Undoped n3-01	Co1-doped n3-01 nanocluster	Co2-doped n3-01 nanocluster
Fermi Energy	- 6.486 eV	- 6.565 eV	- 6.795
DFT energy gap	0.416 eV	0.312 eV	0.116
valence band	- 6.486 eV	- 6.565 eV	- 6.795
conduction band	- 6.071 eV	- 6.253 eV	- 6.679
binding energy (eV/atom)	- 4.441	- 4.531	- 4.654
Total energy (eV)	- 11220.719	- 9220.030	- 9456.080

From table 17, we observe that the shortest band-gap energy of 0.116 eV is measured for the Co-doped n3-01 nanocluster on the central Mn2 atomic position. This Mn2 atomic position has the highest coordination because it is tetrahedrally bonded to its 4 neighbouring oxygen atoms that contribute positively to its stability and preferability as the doping position. Furthermore, the Co-doped n3-01 nanocluster on the Mn2 atomic position has the lowest Fermi energy of -6.795 eV, the lowest binding energy of -4.654 eV/atom.

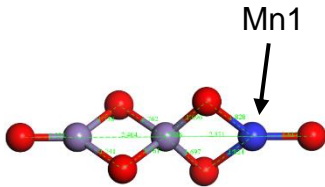
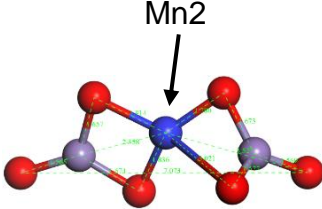
These results illustrate the overwhelming preference for cobalt doping to be targeted on the most coordinated cation positions. Co-doping shows some commendable success towards improving the electronic properties and stability of the n3-01 nanocluster hence it is recommended that cobalt can be used as a potential dopant for these systems.

8.2.3. Nickel doping of the n3-01 nanocluster

This section focuses on the Co-doping of the n3-01 nanocluster. Similar to Fe-doping and Co-doping; the Fermi energy, band-gap energy and binding energy are calculated in order to determine the efficacy of doping with nickel on the n3-01 nanocluster on the Mn1 and Mn2 atomic positions. Recall, that Mn1 refers to the exterior manganese atom on the right fragment of the n3-01 nanocluster with the lower coordination having a 0.39e Hirshfeld charge. Mn2 refers to the interior central manganese atom with the higher coordination having a 0.32e Hirshfeld charge.

Table 18 presents the results obtained when nickel was used to dope the n3-01 nanocluster on the two atomic sites denoted as Mn1 and Mn2.

Table 18: Electronic properties of the Ni-doped n3-01 nanocluster

			
		Ni1-doped n3-01 nanocluster	Ni2-doped n3-01 nanocluster
Fermi Energy	- 6.486 eV	- 6.667 eV	- 6.962
DFT energy gap	0.416 eV	0.220 eV	0.346
valence band	- 6.486 eV	- 6.667 eV	- 6.962
conduction band	- 6.071 eV	- 6.447 eV	- 6.616
binding energy (eV/atom)	- 4.441	- 4.516	- 4.674
Total energy (eV)	- 11220.719	- 9731.633	- 9732.794

The Ni-doped nanocluster on the highest coordinated atomic position (Mn2) improved the binding energy from -4.441 eV/atom to -4.674 eV/atom after DFT optimisation. More importantly, this is the lowest and most stable binding energy recorded for all the nanoclusters before and after doping with either Fe, Co or Ni across all the doping positions. In particular, this shows the stability of the Ni-doped nanoclusters.

Furthermore, the lowest Fermi energy and total energy of -6.962 eV and -9732.794 eV respectively are recorded for the Ni-doped nanocluster at the central cation position (Mn²⁺) with highest coordination. However, the band-gap energy of 0.346 eV for the Ni-doped n3-01 nanocluster is larger than the shortest band-gap energy of 0.116 eV recorded for the Co-doped n3-01 nanocluster substituted on Mn²⁺ also. Particularly, this shows that Co-doping succeeded in decreasing the energy difference between the valence band and the conduction band, thereby making it easier for an excited electron to move freely between the valence band and the conduction band, thereby effectively improving the electrical conductivity of the material.

The Fermi energy has negative values that are very close to the conduction band values. Furthermore, all the band-gap energies ranged between 0.116 eV to 0.651 eV showing that all the dopants produced nanoclusters which are good semi-conductors. This indicates the good metallic nature of all these nanoclusters [195]. The valence band energy for the Ni-doped nanocluster on the Mn²⁺ atomic position is -6.962 eV and the conduction band energy is -6.616 eV.

The valence band energies and the conduction band energies are very close to each other enabling easier flow of electrons between the bands. The conduction band is partly filled with electrons contributing electrical charges to the nanoclusters thus making them good conductors. [194]. Meaning that the average HOMO-LUMO band-gap is very small enabling free movement of excited electrons between these bands.

It is evident that the dopant elements prefer substitution on the Mn²⁺ atomic position with the higher number of bonds, having a greater coordination. Recall from section 4.4 that nickel was the best dopant for the bulk β -MnO₂ structure. However, cobalt is

now also emerging as a promising dopant due to its capability in refining the Co-doped nanoclusters to have the shortest band-gap energy. These results agree well with a previous experimental study that shown improved conductive properties of manganese dioxide nanostructures doped with cobalt [126].

The Ni-doped nanoclusters displayed the most structural stability after optimisation when compared with all the other doped nanoclusters because they had lowest binding energy of -4.674 eV/atom and the lowest Fermi energy of -6.962 eV. Furthermore, this nanocluster displayed an evolution from an elongated linear atomic configuration towards a more compact circular configuration. This is shown particularly by the angles between the two exterior terminal oxygen atoms decreasing from a linear 180° bond angle to a more compact and spherical 143.46° bond angle. In addition, the bond length decreased from 7.856 Å to 7.073 Å. The highest binding (least stable) is recorded for Fe-doping on the exterior manganese atom (Mn1) with a lesser coordination.

Moreover, the lowest binding energy (most stable) is recorded for Ni-doping on the central manganese atom (Mn2) with the higher coordination. Hence nickel is shown to be the preferable dopant element and the cation position with the higher coordination (greater number of bonds) is more suitable to perform the doping on. These observations are very encouraging and positive. The results agree very well with previous studies showing that stable nanostructures preferred shorter average bond distances and they evolved to adopt compact ring structures [22, 267]. Taking into consideration that both dopants offer some considerable qualities, it is worth investigating the dual doping of the nanoclusters using two dopants simultaneously. This approach is intended to take advantage of the good conductive qualities

observed with Co-doping, the stability and compactness observed with Ni-doping. This dual doping is explored in the next section.

8.3. Dual doping of the n3-01 nanocluster

In this chapter, we report on the simultaneous substitutional doping of the n3-01 nanoclusters using either Co or Ni dopants used in this study. Recall from the previous chapter that Ni was favoured as the preferred dopant due to its ability to form stable compact ring nanoclusters and Co also displayed some essential electrically conductive qualities. Primarily, both the structural stability and good electrical conduction are imperative to create the next generation of suitable cathode materials for rechargeable batteries. Hence, it is thus crucial to attempt the simultaneous doping using both Ni and Co in an attempt to take advantage of their positive attributes as observed in the previous section.

As shown in the previous chapter, both Ni and Co are best singularly utilised when doped on the central Mn2 atomic site with the higher coordination. Now, It must be newly determined which dopant must be substituted on the central Mn2 position and which dopant must be substituted on the right fragment's Mn1 atomic position. This determination is achieved firstly by substituting on the Mn2 atomic position with nickel and then doping the Mn1 atomic position with cobalt. Secondly, the doping is performed with cobalt substituting Mn2 and nickel substituting Mn1 on the n3-01 nanocluster.

Studying the nanoclusters binding energies, Fermi energies and their band-gap energies aids in determining the impact of dual doping in comparison with the singularly doped nanoclusters and the undoped nanocluster. Figure 35 displays the

dual doped n3-01 nanoclusters showing the different ways of arranging the dopant atoms on the two cation sites of the nanocluster, i.e., Mn1 and Mn2 (as listed in the previous chapter).

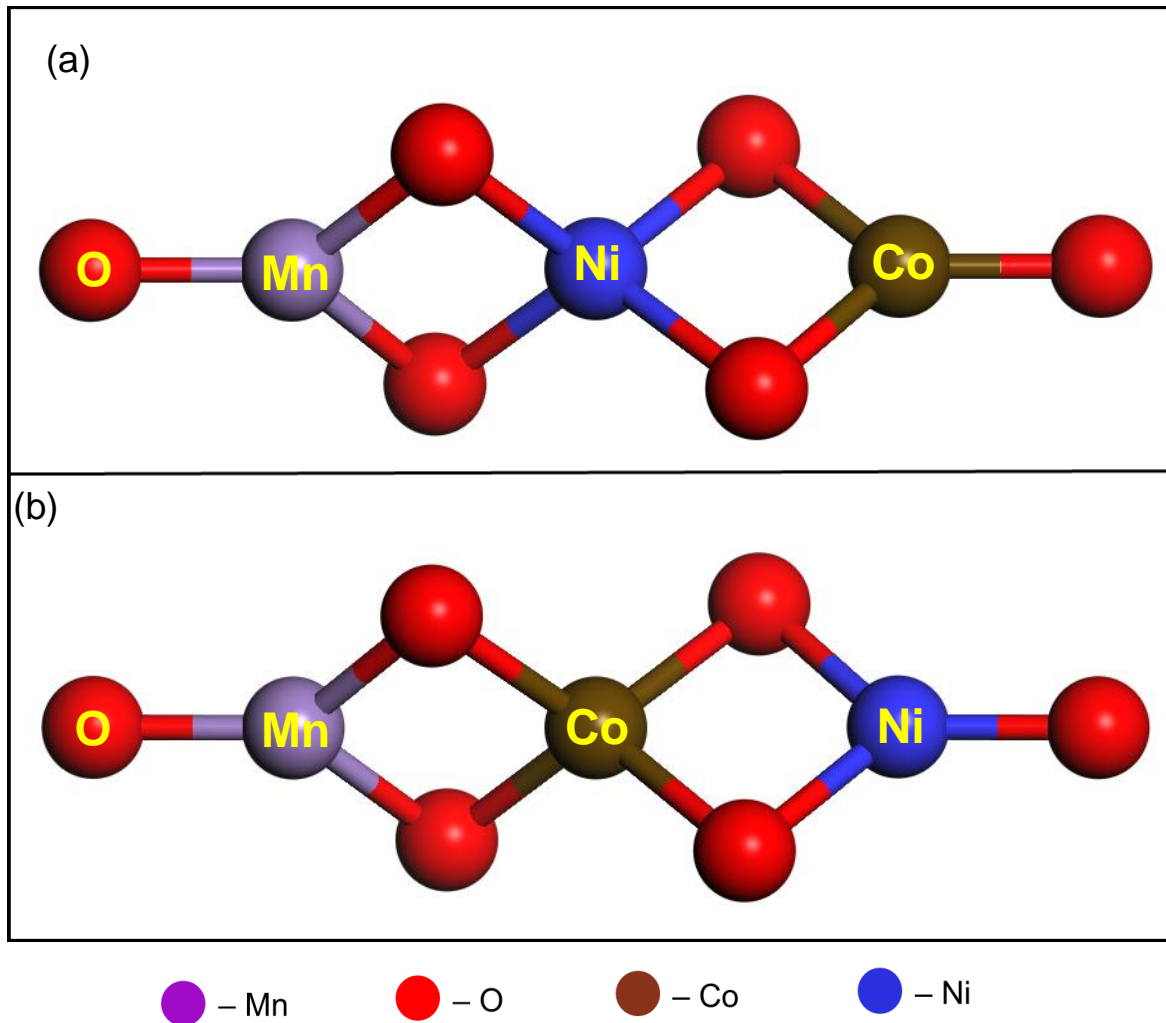


Figure 35: (a) The dual doped n3-01 nanocluster with Ni substituted on the Mn2 atomic position and Co substituted on the Mn1 atomic position, (b) The dual doped n3-01 nanocluster with Co substituted on the Mn2 atomic position and Ni substituted on the Mn1 atomic position. In-text labels distinguish the position of the atoms.

Figures 35 (a) and 35 (b) displays the two respective arrangements of doping the n3-01 nanocluster with both Ni and Co. The binding energies, total energies, Fermi energies and band-gap energies of the dual doped nanoclusters were measured and

compared pre and post doping with the DFT-based CASTEP code. These properties are presented in Table 19.

Table 19: Electronic properties of the dual-doped n3-01 nanocluster using the Ni- and Co- dopants.

Property	n3-01 Undoped	(a) n3-01 Ni-Co	(b) n3-01 Co-Ni
Fermi Energy (eV)	- 6.486	-6.911	-7.167
Band-gap energy (eV)	0.416	0.316	0.253
Valence band edge (eV)	- 6.486	-6.911	-7.167
Conduction band edge (eV)	- 6.071	-6.594	-6.914
Binding energy (eV/atom)	- 4.441	-4.404	-4.459

From table 19, the Fermi energy of the n3-01 nanocluster doped with Co substituted on the Mn2 atomic position and Ni substituted on the Mn1 position has the lowest and most stable energy at -7.167 eV, this shows that this nanocluster is the most structurally stable and this is reinforced by the binding energy being the most stable and lowest at -4.459 eV/atom. Furthermore, this Co-doped n3-01 nanocluster at the

Mn2 atomic position has shortest band gap of 0.253 eV, making it the better electrical conductor.

Recall from table 17, that the shortest band-gap energy of 0.116 eV/atom was recorded for the singularly Co-doped n3-01 nanocluster on the Mn2 atomic position with the highest coordination. This shows that dual doping has effectively failed in improving the conductivity of the n3-01 nanocluster, because the shortest dual doped n3-01 nanocluster has a larger band-gap energy of 0.253 eV/atom recorded for the n3-01 nanocluster doped with Ni on the Mn1 atomic position and Co on the Mn2 position.

Furthermore, the most stable binding energy from the singular doping results was recorded when Ni was doped on the Mn2 atomic position with a value of -4.674 eV/atom, it is important to note that this value is more stable than all the values recorded with the dual doping procedure. Consequently, this also shows that dual doping has failed to improve the structural stability of the nanocluster. The failure in enhancing the conductivity and stability shows that dual doping may not be recommended for the smaller nanoclusters based on these results.

It will be interesting to observe what happens when dual doping is performed on two centrally located cation atomic positions with a higher coordination in larger nanoclusters above $n = 10$, this aspect will be investigated further in future studies.

8.4. Density of states of the doped n3-01 nanocluster

The Density of States (DOS) were calculated for the pure and doped n3-01 nanoclusters to investigate their behaviour at the Fermi level. These calculations

were carried-out to discuss more insights on the conductivity and stability of the doped MnO₂ nanoclusters.

8.4.1. TDOS of the IP and DFT n3-01 nanocluster

Figure 36 depicts the Total Density of States (TDOS) plots comparing the IP generated n3-01 nanocluster in (A) and the DFT optimised n3-01 nanocluster in (B).

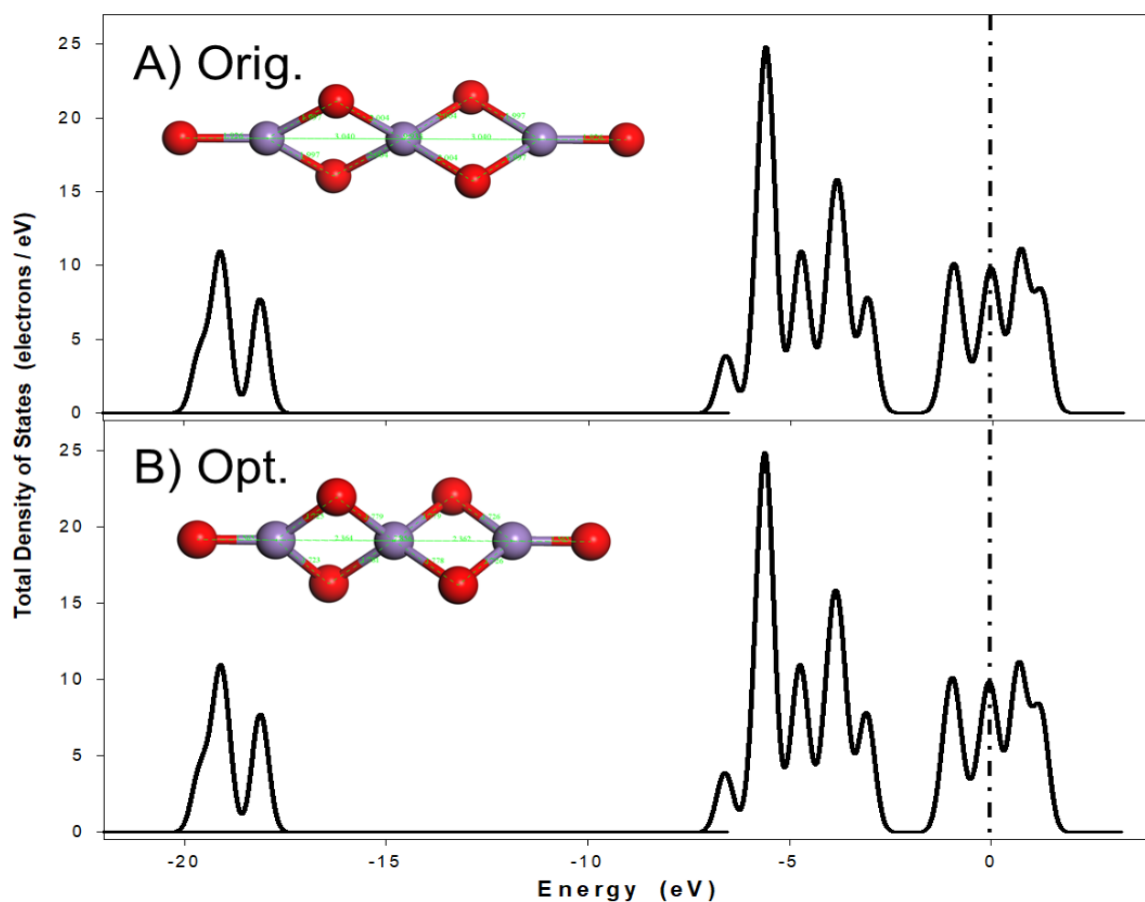


Figure 36: The Total Density of States (TDOS) plot of A) The original n3-01 nanocluster generated by KLMC and B) The optimised n3-01 nanocluster by CASTEP.

From figure 36, we observe that the plots have peaks on identical positions have identical intensities. This shows the presence of similar phases and similar bonds in both the nanoclusters which is expected considering the nanoclusters look the same,

differing only by some minor bond lengths. Furthermore, the identical plots show that there is a continuous non-zero peak on the Fermi level indicating the flow of electrons between the valence and the conduction band, this illustrates that both the nanoclusters depicted in figure 36 have a good capability of electrical conduction which is a required aspect of cathode materials for modern rechargeable batteries.

8.4.2. TDOS of the Fe-doped n3-01 nanocluster

This density of states plots presented in this subsection were calculated for the three dopant elements when substituted on the 2 atomic positions as discussed previously. Position Mn1 is labelled as A) and position Mn2 is labelled as B) in all the TDOS plots. The CASTEP code was used to determine these TDOS plots using the same parameters that were found to be optimal to optimise all the other nanoclusters from n=2 to n=20.

Figure 37 displays the TDOS of the DFT optimised nanocluster doped on the external manganese atom denoted by Mn1 (A) and the central manganese atom denoted by Mn2 (B) doped with iron.

From figure 37, we observe that the centrally doped n3-01 nanocluster has a lower DOS at the Fermi level than the externally doped nanocluster. This indicates that the centrally doped nanocluster is more stable and this is the preferred position for doping with iron. These preliminary results concur with those observed from the β -MnO₂ nanocluster showing that doping was preferable on atomic positions with the higher coordination.

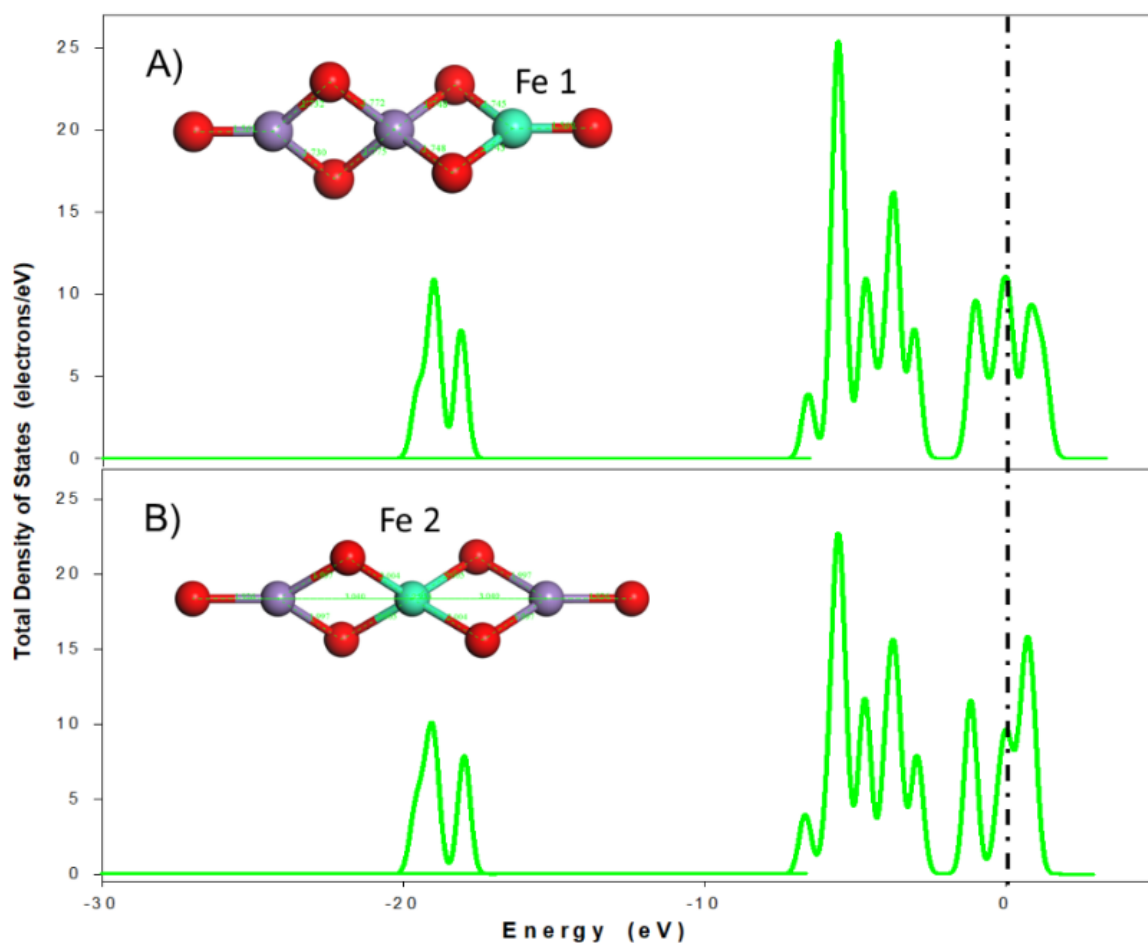


Figure 37: The Total Density of States (TDOS) plot of the Fe-doped n3-01 nanocluster substituted at A) The Mn1 atomic position and B) The Mn2 atomic position.

8.4.3. TDOS of the Co-doped n3-01 nanocluster

Figure 38 displays the total density of states for the n3-01 nanocluster doped on the external manganese atom denoted by Mn1 (A) and the central manganese atom denoted by Mn2 (B) doped with cobalt using the DFT-based CASTEP code.

The highest peaks on the TDOS of the centrally doped n3-01 nanocluster are lower than those on the exterior doped nanocluster. This indicates that the nanocluster displayed in B) is more stable than that in A). This shows that doping is more preferable when it is performed on the higher coordinated atomic positions.

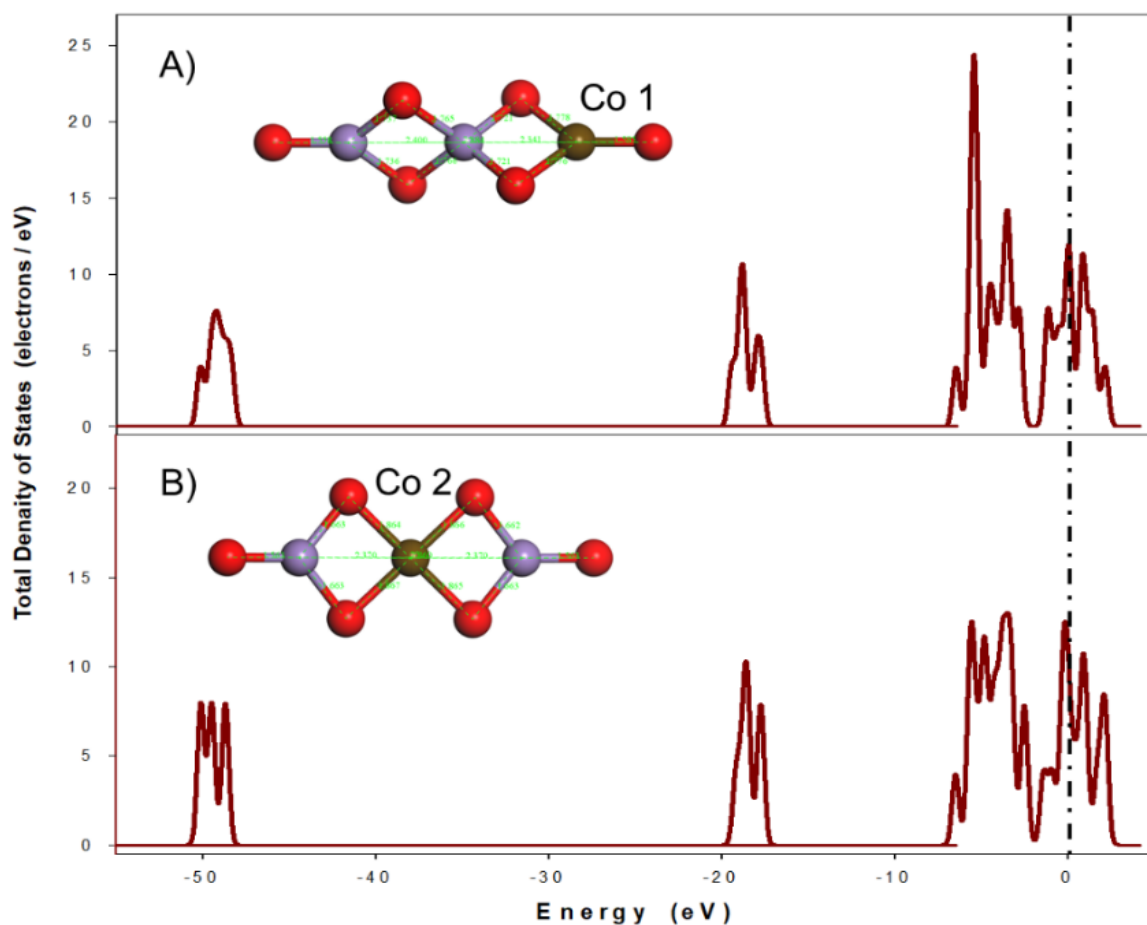


Figure 38: The Total Density of States (TDOS) plot of the Co-doped n3-01 nanocluster substituted at A) The Mn1 atomic position and B) The Mn2 atomic position.

8.4.4. TDOS of the Ni-doped n3-01 nanocluster

Figure 39 displays the total density of states for the n3-01 nanocluster doped on the external manganese atom denoted by Mn1 (A) and the central manganese atom denoted by Mn2 (B) doped with nickel using the DFT-based CASTEP code.

From figure 39, we observe that the Ni-doped n3-01 nanocluster on the lesser coordinated Mn1 position has peaks with higher intensities than those observed on TDOS of the centrally Ni-doped nanocluster on Mn2.

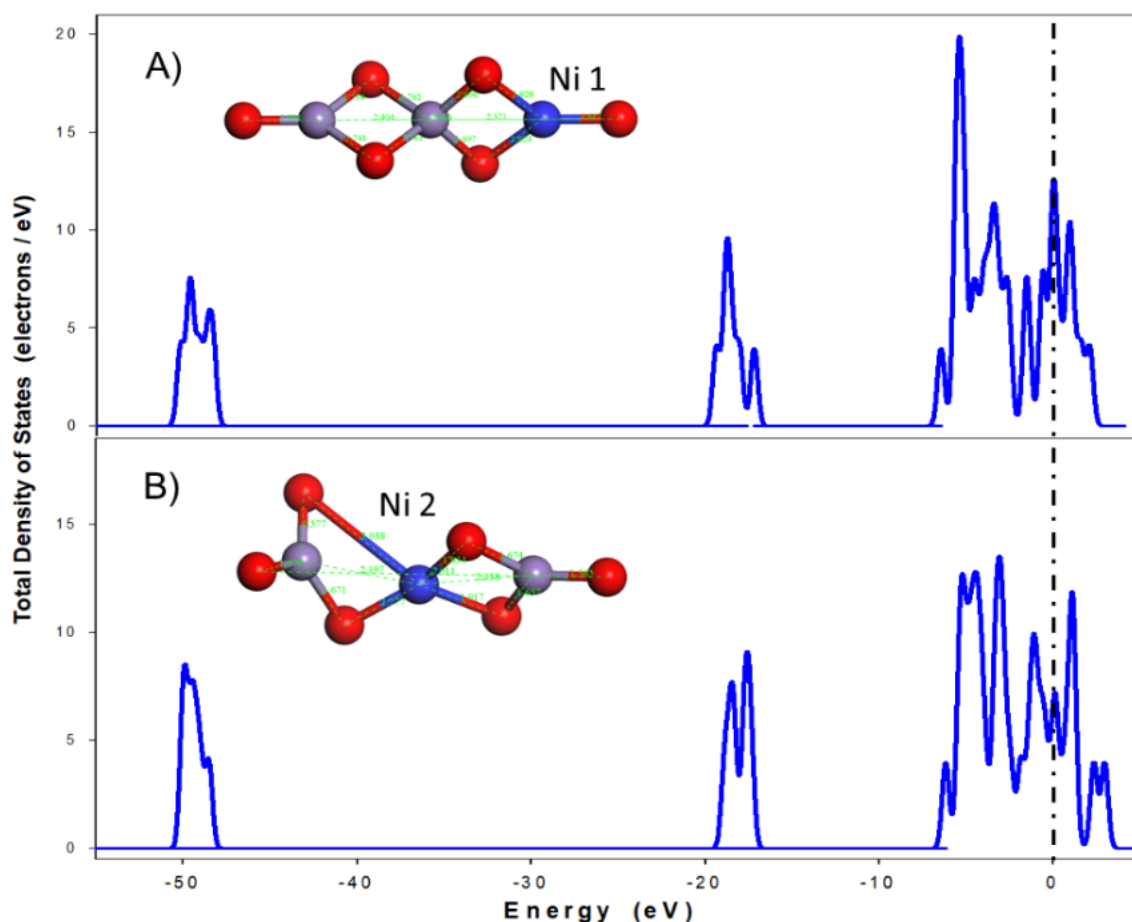


Figure 39: The Total Density of States (TDOS) plot of the Ni-doped n3-01 nanocluster substituted at A) The Mn1 atomic position and B) The Mn2 atomic position

It is observed that the centrally Ni-doped nanocluster at the Mn2 atomic position has a lower energy at the Fermi level as compared to the Ni-doped nanocluster as the atomic position with a lower coordination. This indicates that the centrally doped nanocluster is more stable and that the nanoclusters display a preference for doping at atomic positions with a higher coordination.

Another important property related to the Fermi energy worth investigating is the behaviour of all the doped nanoclusters at the Fermi Level. This is done to observe which doped nanocluster is the most stable and which is the better conductor of electricity to support the assertions made when analysing the Fermi energy values.

Table 20 gives the DOS of the pure and the doped nanoclusters at the Fermi level.

The table also gives the positions and values of the highest peaks to add onto the qualitative analysis to determine the conductivity of these nanoclusters.

Table 20: Table indicating the values of the Density of States at Fermi level for the pure n3-01 nanocluster and the doped n3-01 nanoclusters

	IP n3-01	DFT n3-01	Fe1	Fe2	Co1	Co2	Ni1	Ni2
DOS @ Fermi level	9.70	9.70	10.85	9.63	11.89	10.91	12.59	6.73
Highest Peak X : Y	-5.61 : 24.85	-5.61 : 24.85	-5.53 : 25.40	-5.57 : 22.80	-5.48 : 24.40	-3.50 : 13.01	-5.41 : 19.9	-3.09 : 13.50

From Table 19, it is observed that the Ni-doped n3-01 nanocluster on the central atomic position originally occupied by manganese (Mn2) produces the least conductive nanocluster. It is worth noting that all the doped nanoclusters have good conductive qualities due to their very small band-gap energy that is well below the 2eV limit for semiconductors. These doped nanoclusters also produced peaks with lower intensities indicative of the stability of the doped nanoclusters.

Furthermore, the nanoclusters doped on the external manganese atom produce better conductors which is expected because the central atoms use more of their valence electrons to bond with the oxygen atoms around them. This shows an indirect relationship between stability and conductivity. Nickel is more electron rich due to it having more unpaired electrons in its outermost shell hence the nanocluster doped

with nickel has the highest DOS of 12.59 eV meaning it is the best overall electrical conductor on the external atomic position even though it is not the most stable.

8.4.5. Fermi energy

This subsection focuses on the analysis of the Fermi energies of the top five most stable nanoclusters per atomic size, i.e., $n=1, 2, 3, 4$ and 5 . Figure 40 shows the TDOS of the five smallest and most stable nanoclusters. Each stable nanocluster is indicated by a different colour; namely light green (solid line) for $n2-01$, blue (long dash) for $n3-01$, purple (medium dash) for $n4-01$, brown (short dash) for $n5-01$ and dark green (dash-dot-dash) for $n6-01$

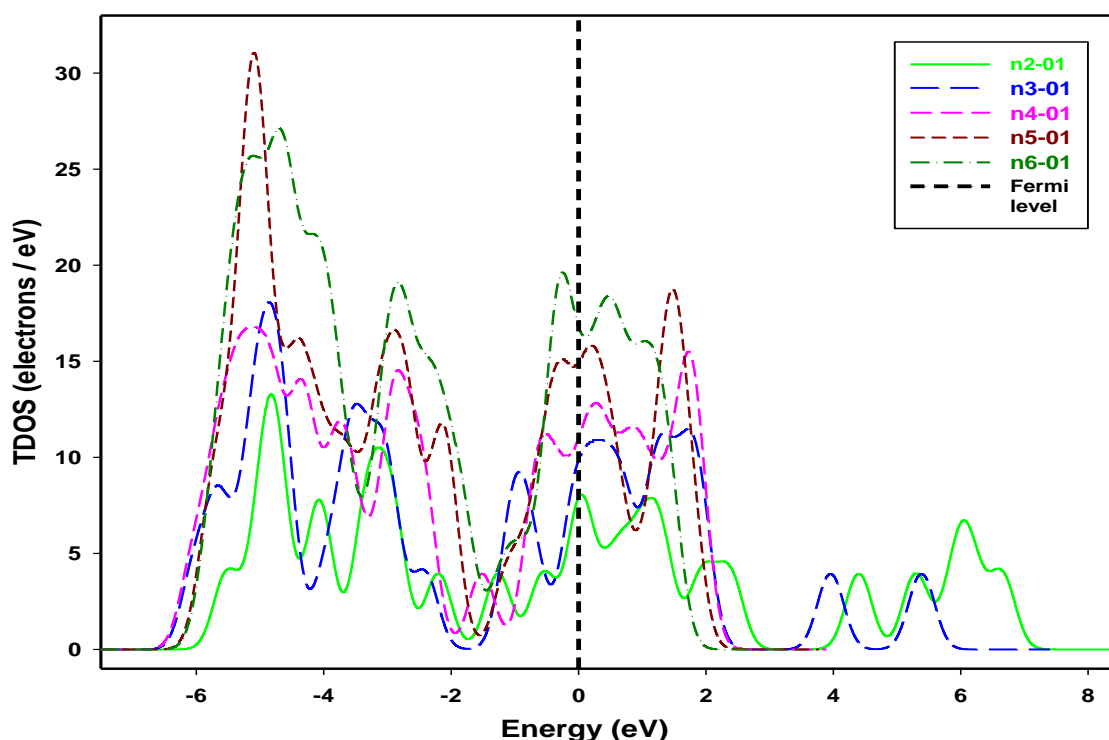


Figure 40: Total Density Of States (TDOS) of the most stable nanoclusters, (MnO_2); $n = 2$ atoms to $n = 6$ atoms

From the plots in figure 40, we observe that as the size of the cluster is increasing, contributions at the Fermi level are also increasing. Thus, the nanocluster systems

are becoming better electrical conductors and more stable as they grow in size. Similar behaviour was observed on the DOS plots of a study by Mishra *et al.* [268].

It is also observed that the highest peaks on both sides of the Fermi level are moving further away from the Fermi level as the cluster size increases, this is indicative of the varying metallic behaviour of the nanoclusters. The presence of peaks on both sides of the Fermi level is a good indicator that all the nanoclusters are good conductors.

The hybridisation of the protruding peaks from the individual atoms leads to the presence of the high peaks on the total DOS. The hybridisation of the Mn 3d orbital and the O 2p orbital forming a covalent bond, is mainly due to manganese contributing the majority DOS as it is more reactive and less stable. The highest peak on the valence band corresponds to the n5-01 nanocluster's contributions and is also referred to as the valence band maximum. The Ni-doped nanoclusters were shown to be the most structurally stable and that doping was preferential on the atom with the highest coordination to neighbouring oxygen atoms (the metallic atom with the greatest number of bonds). These higher coordinated atoms were also shown to be usually located internally towards the centre of the structure.

Cobalt was shown to produce the most conductive nanocluster although all the dopants were also shown to form good conductors as seen by their short band-gap energies. This shows that both nickel and cobalt can be recommended as suitable dopants considering the specific need of the material to be a good electrical conductor that maintains its structurally intact stability under stress. It is recommended that dual doping be performed with nickel being granted the higher concentration than cobalt.

Iron was shown to be a less suitable dopant in comparison and can be excluded from selection altogether.

It is thus discovered that the pure undoped nanoclusters are shown to be more stable than their doped counterparts, however 100% pure compounds do not exist in nature because all naturally occurring elements contain impurities or other foreign elements hence the importance to investigate this doping. To further investigate the impact of doping on the electronic properties of the nanoclusters, charge density differences were shown to provide vital information about the stability and conductivity of materials [229], hence they are studied in the next section.

Chapter 9: Charge density differences

This chapter focuses on the charge density differences of the stable n3-01 nanocluster. The analysis compares the charge density difference of the undoped and doped n3-01 nanocluster with the Fe, Co and Ni dopants. In particular, the effect of doping on the electronic charge density difference is explored to understand the nature of bonding within the system. The calculations were performed using the CASTEP code [27].

9.1. Undoped n3-01 nanocluster

This section discusses the electronic charge density differences of the n3-01 nanocluster in order to gain knowledge on the bond formations and their directional bonding patterns. In particular, the electronic charge density difference is calculated to visualise the charge transfer occurring between the Mn and O atoms. The Hirshfeld charges [130] and the Mulliken atomic populations [131], will be analysed in an effort to explain the distinct changes occurring in the coloured regions engulfing the atoms as displayed in figure 41. Note that, the Hirshfeld analysis defines atomic charges by dividing the deformation density between the individual atoms in the molecules and Mulliken atomic analysis measures the electron population occupying a specific atom.

In order to fully visualise the electronic charge density difference profiles, an iso-surface value of (+/-) 0.05 eV was implemented. Note that the individual atomic densities functionality was implemented in order to compute the charge density difference with respect to the individual atoms instead of the symmetric fragments of the nanocluster structure.

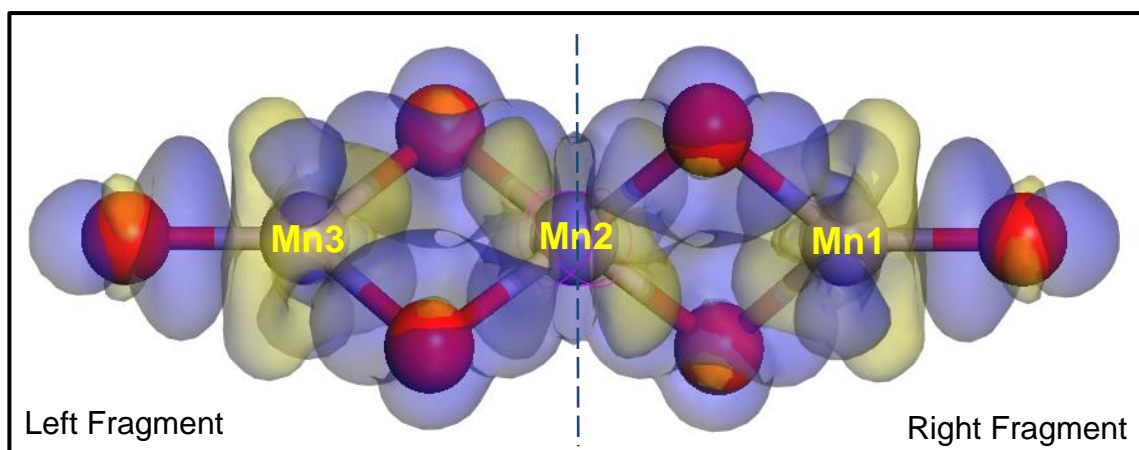


Figure 41: Charge density differences depiction of an undoped n3-01 nanocluster indicating the gain (blue) and loss (yellow) of electrons. The Mn1, Mn2 and Mn3 cations are labelled accordingly.

The (+/−) displays two iso-surface regions (see figure 41). The blue iso-surface at +0.05 eV represents the gain of electronic charge and the yellow iso-surface at −0.05 eV represents charge depletion. A higher transparency was used in order to show the position of the atoms responsible for creating the displayed charge densities.

From figure 41, it is observed that there are multiple occurrences of overlapping between the blue and yellow electronic charge density differences regions. The overlap is indicative of the prevalence of covalent bonds between the Mn and O atoms, similar observations were found by Menendez *et al.* [229]. This covalence shows a stronger rigid bond between the respective neighbouring atoms of the n3-01 nanocluster. Furthermore, we observe the square planar configuration consisting of two Mn atoms and two O atoms. This configuration is mostly observed in the centre of the nanocluster and it has been shown to be stable in other metallic oxide nanostructure studies [269].

All the oxygen atoms are engulfed by the blue charge density cloud and the manganese atoms are covered by the yellow charge density cloud. This indicates that manganese has donated electrons and oxygen has gained those electrons to form a strong covalent bond. This behaviour is confirmed by the overlap between the red and blue coloured charge density clouds.

It can be clearly seen that figure 41 is symmetrical, forming two identical fragments with reference to the central Mn₂ atom. The left and right fragments of the structure have identical charged density clouds indicating the high symmetry existing in this optimised nanocluster. The yellow-coloured region appears to occupy a larger surface area as compared to the blue region. This is due to the electrons in the valence 3d orbitals experiencing a greater mutual repulsion.

The 3d valence electrons form a larger electron density cloud than that formed by the electrons in the valence 2p orbital of the oxygen atoms. The Mn atom has a larger charge density region than the oxygen atom because the charge density near the nucleus is much lower for oxygen. Similar observations were reported previously by Helmenstine *et al.* [270].

9.2. Doped n3-01 nanocluster

This section focuses on the impact of doping the n3-01 nanocluster using Fe, Co and Ni. Recall that, the atomic substitutional method was employed instead of the interstitial doping where a Mn atom is replaced by either Fe, Co or Ni. This choice of doping technique is due to the fact that interstitial doping adds an atom to the structure which increases the volume whereas this study aims to decrease the size of structures while increasing their stability [224]. In particular, the focus is on the

differences between the 2-dimensional charge density profiles of the nanoclusters after doping. This is done to assess which of the dopants produces a better charge density for use as cathode materials in rechargeable batteries.

Note that, doping was performed on the two manganese atomic positions, i.e., Mn1 and Mn2. Where Mn1 represents the manganese atom on the right fragment of the n3-01 nanocluster while Mn2 is the central manganese atom (see figure 41). Note that, Mn1 and Mn3 are identical due to the symmetric nature of the n3-01 nanocluster and will give similar results. The similarity bond lengths, bond angles and overall appearance.

Firstly, the Fe-doping will be discussed in the next section, followed by Co-doping and lastly Ni-doping. The analysis focuses on the overlap of the electronic charge density difference regions to evaluate the covalency or ionic bonding occurring in the doped n3-01 nanocluster. Furthermore, the effect of the charge re-distribution and localisation of charges on the bond lengths, Hirshfeld charges and Mulliken atomic populations were investigated and reported in the following sections.

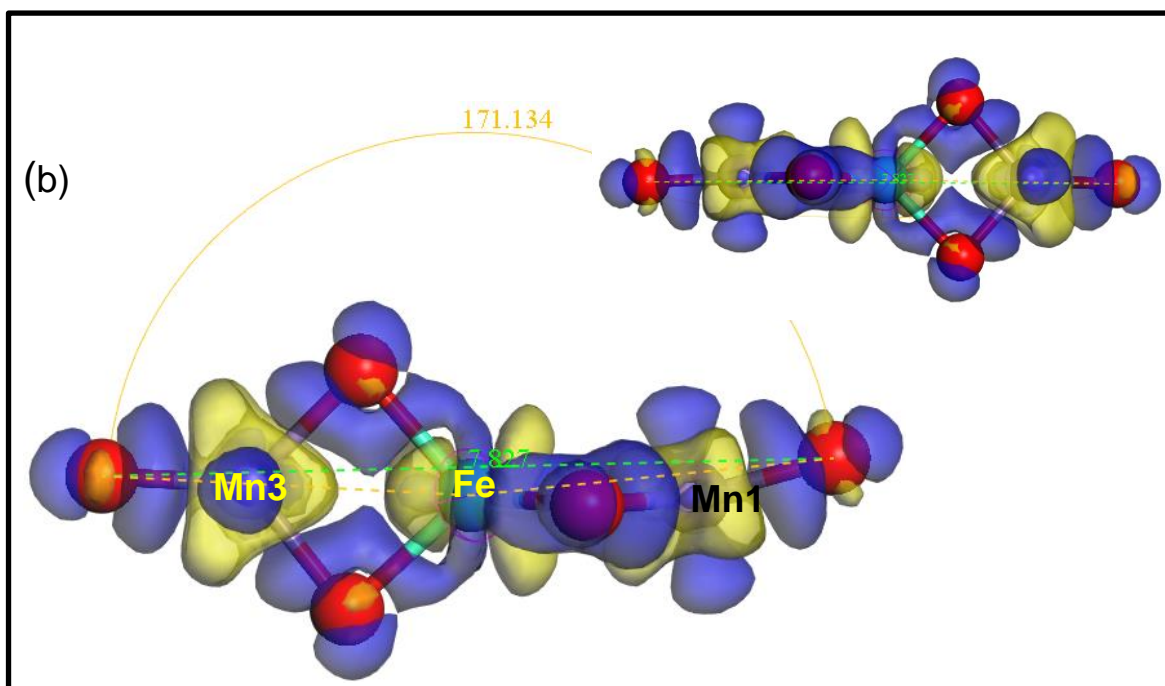
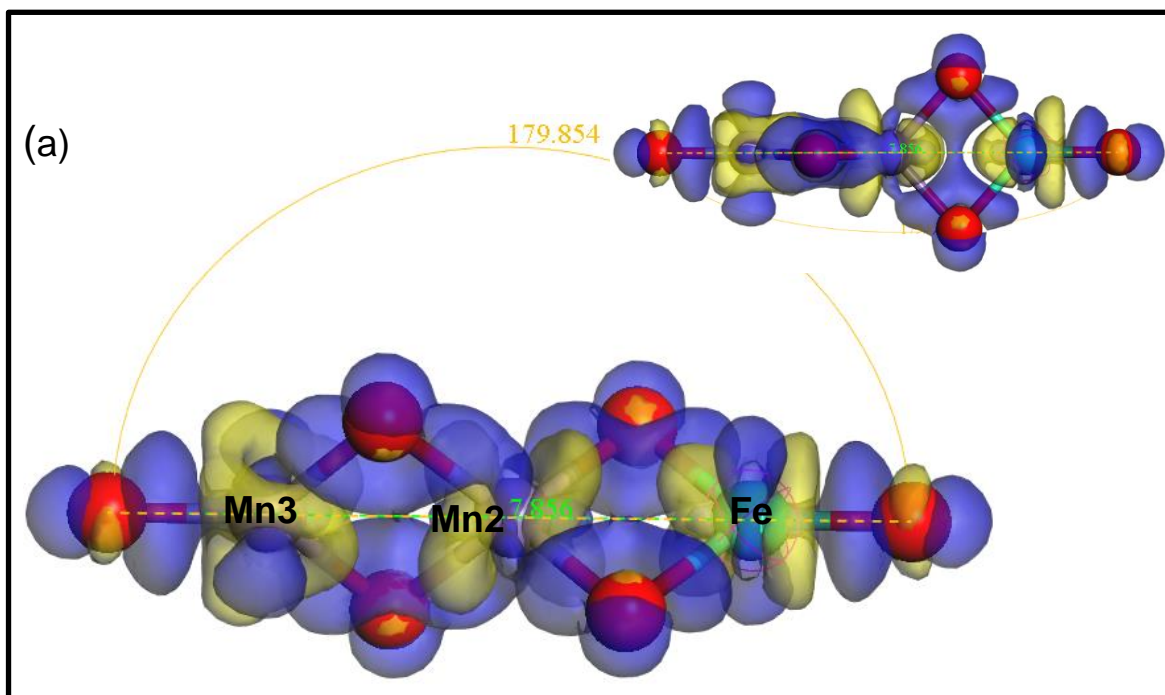
9.2.1. Fe-doping

Now, we consider the case of Fe-doping at both Mn1 and Mn2. Firstly, we explore the Fe-doping at the Mn1 position (see figure 42 (a), followed by Fe-doping at the Mn2 position (see figure 42 (b).) Varying views at different angles of the charge density difference profiles are shown to fully display the interactions. This is done to determine the nature of bonding (covalent or ionic) in the Fe-doped n3-01 nanocluster.

Secondly, a direct comparison is done between the charge density differences of the nanocluster doped on Mn1 and Mn2 in an effort to display the preferred doping position (see figure 42). The cation positions are labelled to show their positions.

From figure 42 (a) and (b), varying views of the substitutional doping performed on the Mn1 and Mn2 cation positions are displayed to better visualise the charge density difference in an effort to determine whether covalent bonding or ionic bonding is prevalent. Recall that, the overlap of charge density clouds is indicative of the prevalence of covalent bonds between the respective Mn and O atoms. Furthermore, a separation between the regions signifies an ionic bonding. Covalency is the preferred type of bonding because it shows stability of the nanocluster as reported previously by Menendez *et al.* [229].

Moreover, it is observed that there is a clear detachment between the yellow charge density cloud around the Fe atom and its neighbouring O atoms in figure 42 (a). This reveals the loss of electronic charge density at that region. However, there is an overlap of charge densities between Mn3 and its neighbouring O atoms. This shows that the Mn-O bond is covalent and more stable than the Fe-O ionic bond. The charge density map for ionic bonding is known to demonstrate a charge density difference that is localised on a single atom as observed with the Fe atom [271]. Furthermore, the detachment of density clouds is observed on figure 42 (b) on both fragments when Fe is doped on the central cation position denoted by Mn2. These observations show that Fe-doping destabilises the n3-01 nanocluster irrespective of the doping position.



● – Mn
 ● – O
 ● – Fe

Figure 42: Charge density differences of the Fe-doped n3-01 nanocluster at (a) On the right fragment Mn1 and (b) The Central manganese position Mn2. Different angles are displayed to fully show the charge density difference regions.

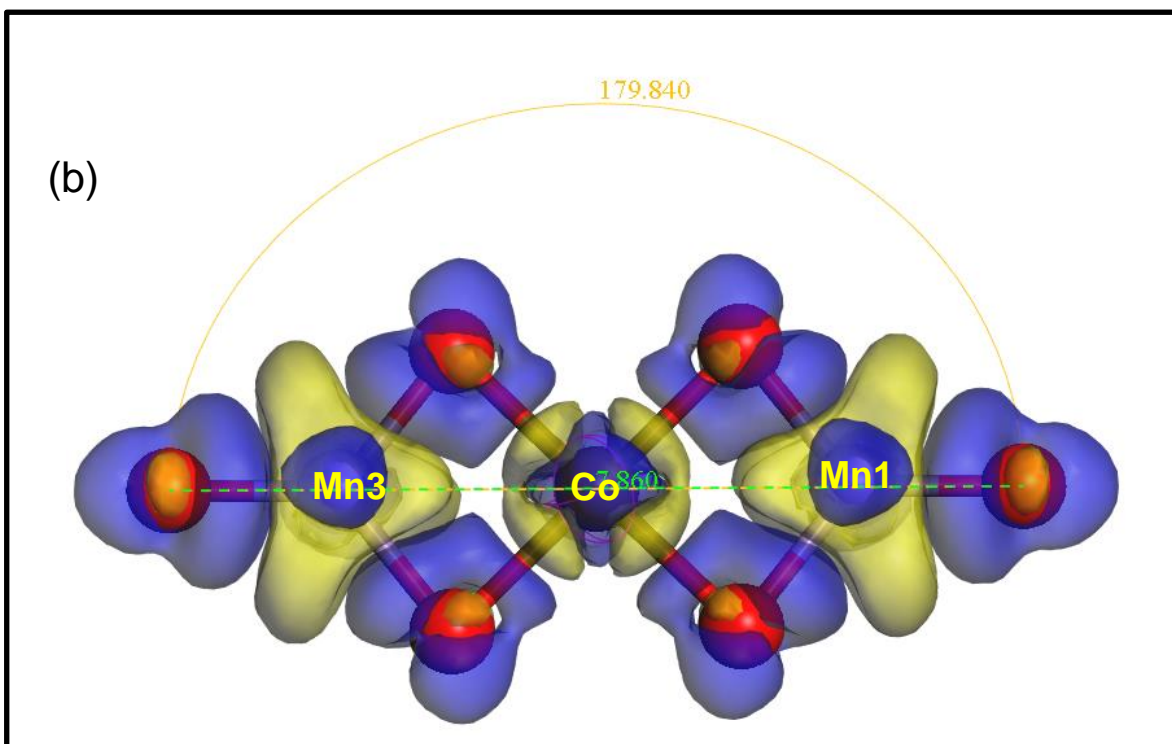
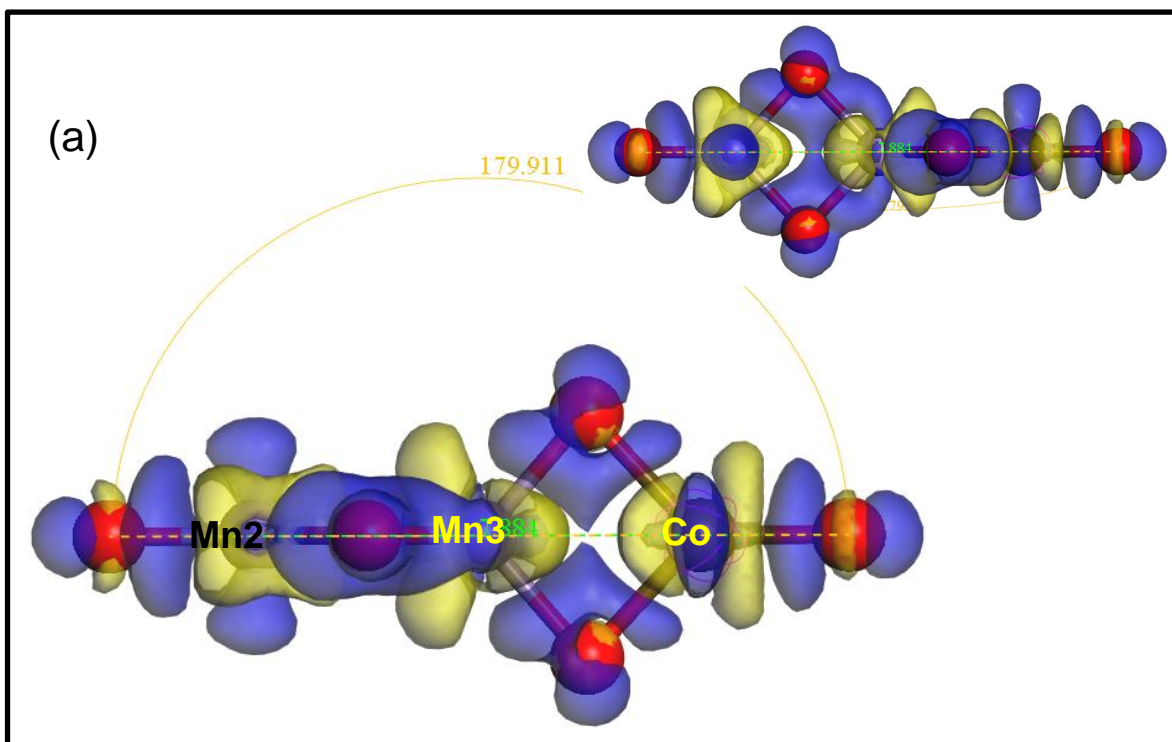
There is no distinguishable boundary between the manganese atom (denoted by Mn3) on the left fragment of the n3-01 nanocluster and the neighbouring oxygen atoms. This indicates a stronger covalent bond between the Mn-O atoms. The chemical bond formed by ions with metallic atoms is typically covalent in nature or an intermediate between the ionic and covalent bonding [272].

These bonding patterns show that the Mn-O bond is more stable and stronger than the Fe-O bond. This ionic bond existing between the Fe-O bonds confirms the weaknesses of iron doping as reported in the previous chapters. However, it should be noted that the Mn2 doping produces a more compact nanocluster as seen by the bond distance between the terminal oxygen atoms decreasing from 7.856 Å to 7.827 Å and the bond angle decreasing from 180° to 171.134°. This shows the preference of doping on the tetrahedral central Mn2 site with the higher coordination.

9.2.3. Co-doping

This section explores the charge redistribution occurring in the n3-01 nanocluster after Co-doping. The charge density differences are directly compared when the nanocluster is doped on Mn1 and Mn2 in an effort to display the preferred doping position. Furthermore, the nature of bonding (covalent or ionic) is discussed to determine the preferable doping position when Co is used as the dopant and its effect on the nanocluster's stability.

Figure 43 (a) and (b) displays the charge density differences of the n3-01 nanocluster after Co-doping by cobalt at Mn1 and Mn2. The charge density difference is again depicted in terms of the electron rich, blue (gain) regions and the electron depleted (loss), yellow-coloured regions.



● – Mn

● – Co

● – O

Figure 43: Charge density differences of the Co-doped n3-01 nanocluster at (a) Mn1 and (b) Mn2

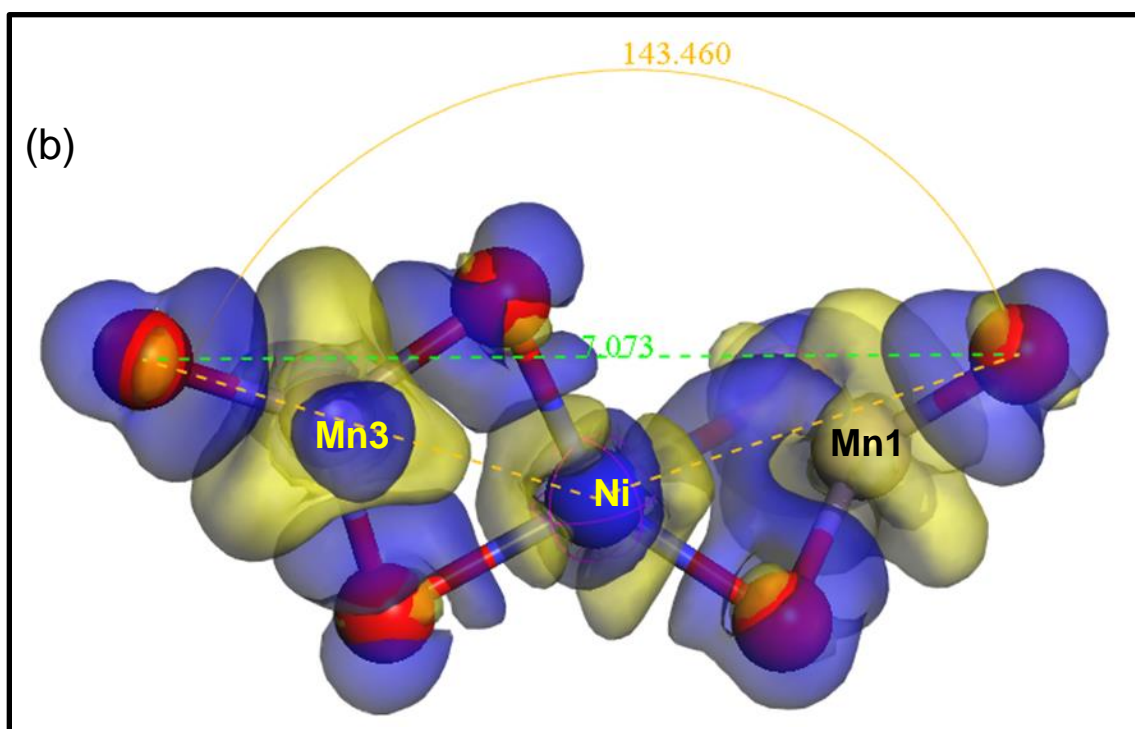
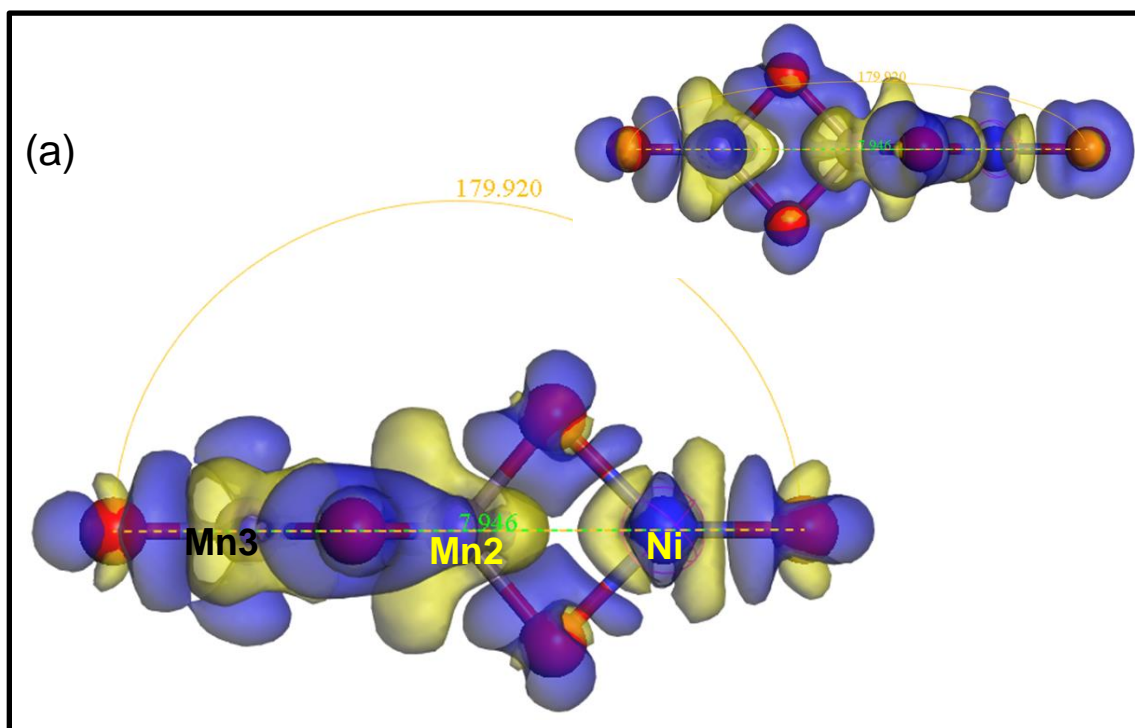
From figure 43 (a), ionic bonding patterns are observed when Co-doping was performed on the Mn1 atomic position and even more so on the Mn2 position on figure 43 (b). This is indicative of the instability that is caused by doping with cobalt. It is observed that an almost perfect symmetrical nanocluster is formed when cobalt was used to dope the n3-01 nanocluster on the central atomic Mn2 atom. However, there are multiple clearly distinguishable separations between the various yellow and blue charge density regions. These colour separations are due to the ionic bonding prevalent in the nanocluster and this indicates the lack of stability in this nanocluster.

This undesired outcome shows that cobalt is also not producing stable compact nanoclusters, similar to Fe-doping. However, the high level of symmetry is a positive aspect that bodes well for Co-doping. Furthermore, doping on Mn2 produces the more compact nanocluster illustrating the preference for doping on the central atomic position with a higher coordination, similar to Fe-doping.

9.2.4. Ni-doping

This section explores the charge density redistribution occurring in the n3-01 nanocluster after Ni-doping. The charge density differences are compared when the nanocluster is doped on Mn1 and Mn2 in an effort to display the preferred doping position. Particularly, the nature of bonding (covalent or ionic) is discussed to determine the preferable doping position when Ni is used as the dopant.

Figure 44 (a) and (b) depicts the electronic charge density differences of the substitutionally doped n3-01 nanoclusters at Mn1 and Mn2, respectively. The ionic or covalent bonding nature of the atomic bonds in the Ni-doped n3-01 nanocluster is investigated to determine the stability of these nanoclusters.



● – Mn ● – O ● – Ni

Figure 44: Charge density differences of the Ni-doped n3-01 nanocluster at (a) Mn1 and (b) Mn2

Figure 44 (a) shows the charge density differences profile of the Ni-doped n3-01 nanocluster on right fragment denoted by Mn1. It is observed that Ni-doping creates separations between the charge density clouds engulfing Ni and its surrounding oxygen atoms indicative of the ionicity of the formed bonds. However, there are overlaps occurring between the charge density clouds of the atom at Mn3 and its surrounding oxygen atoms indicative of the covalent nature of that bond. Covalent bonding is preferred over ionic bonding as covalency is associated with stability [230]

From figure 44 (b), it is observed that the structure displays a loss of symmetry after doping with nickel on the central Mn2 site. However, there are overlapping charge density clouds indicating the prevalence of covalent bonding in the Ni-doped n3-01 nanocluster doped on Mn2. This covalency is only observed in this nanocluster hence it can be alluded that nickel is the most preferred dopant in comparison with iron and cobalt.

9.3. Bond lengths

This section focuses on the bond lengths of the doped n3-01 nanocluster to investigate how the charge re-distribution during doping affects the length of bonds in the doped nanoclusters. This analysis is carried-out in conjunction with the Mulliken atomic populations as they report on the changes occurring in the bond lengths as a result of doping with Fe, Co and Ni on Mn1 and Mn2.

The localisation and re-distribution of charges during bond formation after doping has an effect on other properties of the nanoclusters. The properties of interest in this study are bond lengths, atomic orbital contributions, Mulliken atomic populations and Hirshfeld charges. These properties are discussed in the next sections.

9.3.1. Effect of Fe-doping on bond lengths

Figure 45 illustrates the bond lengths after Fe-doping on Mn1 and Mn2 to compare and determine which doping position creates the most stable and most compact nanocluster.

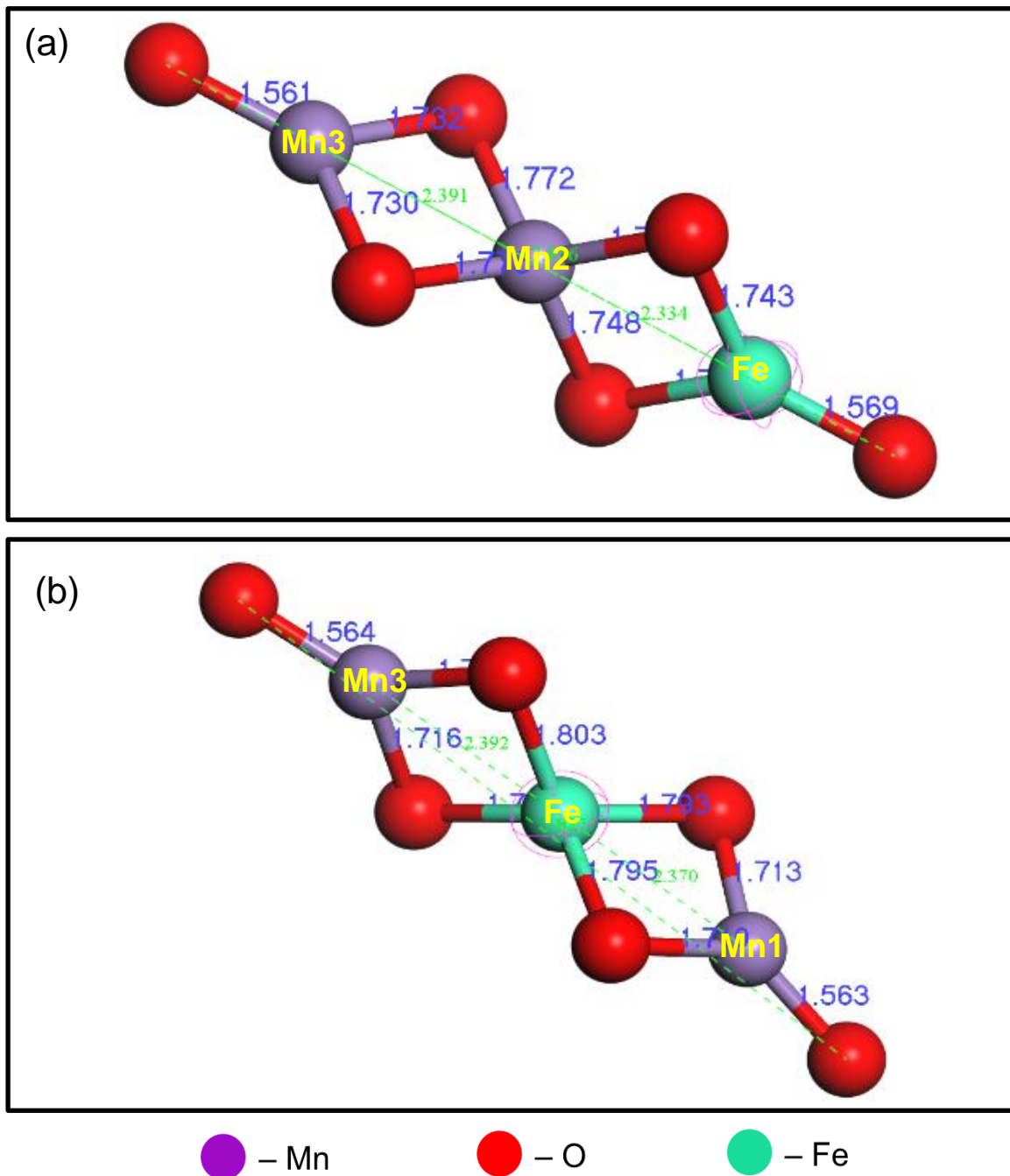


Figure 45: Depiction of the Fe-doped n3-01 nanocluster showing bond lengths doped at (a) Mn1 and (b) Mn2

From figure 45 (a), it is observed that the bond length between the two terminal exterior oxygen atoms has remained constant at 7.856 Å before and after Fe-doping on the Mn1 site. This shows that Fe-doping does not decrease the bond lengths, hence it does not enhance the structural compactness of the nanocluster as envisaged on Mn1.

Fe-doping on the centrally located Mn2 position having a higher coordination has marginally succeeded in decreasing the bond length from 7.856 Å before doping to 7.827 Å after Fe-doping. This continued trend shows the preference of doping on the higher coordinated manganese atom that is centrally positioned on the n3-01 nanocluster surrounded by oxygen atoms.

Mulliken atomic bond populations

The Mulliken population data presented in this section focuses on the charge distribution amongst the specific bonds in the Fe-doped n3-01 nanocluster. These charge distributions show the bonds that have accumulated the most electronic charge. This aids in selecting atomic sites for doping or adsorption in future studies.

The Mulliken overlap population analysis is an important tool proven to capably investigate the covalent and ionic nature of the formed bonds between respective atoms. A high value of the bond population indicates a covalent bond, whereas a low value represents an ionic bond. A zero value indicates a perfectly ionic bond and the values greater than zero indicate an increasing level of covalency [233].

Table 21: Bond lengths of the atomic interactions present in the Fe-doped n3-01 nanocluster

Mn1				Mn2		
Bond	Population	Length		Bond	Population	Length
O 6 -- Mn 2	0.24	1.5613		O 5 -- Mn 1	0.24	1.5635
O 5 -- Fe 1	0.63	1.5693		O 6 -- Mn 2	0.24	1.5643
O 4 -- Mn 2	0.10	1.7300		O 2 -- Mn 2	0.14	1.7096
O 2 -- Mn 2	0.10	1.7322		O 3 -- Mn 1	0.14	1.7100
O 3 -- Fe 1	0.37	1.7432		O 1 -- Mn 1	0.13	1.7135
O 1 -- Fe 1	0.37	1.7446		O 4 -- Mn 2	0.14	1.7156
O 3 -- Mn 1	0.12	1.7478		O 4 -- Fe 1	0.32	1.7861
O 1 -- Mn 1	0.12	1.7483		O 1 -- Fe 1	0.31	1.7931
O 2 -- Mn 1	0.10	1.7716		O 3 -- Fe 1	0.31	1.7949
O 4 -- Mn 1	0.10	1.7754		O 2 -- Fe 1	0.30	1.8026
Mn 1 - Fe 1	-0.04	2.3341		Mn 1 - Fe 1	-0.07	2.3699
Mn 1 - Mn 2	0.00	2.3913		Mn 2 - Fe 1	-0.08	2.3916
O 2 -- O 4	0.05	2.5617		O 2 -- O 4	0.02	2.5629
O 1 -- O 3	0.02	2.5972		O 1 -- O 3	0.02	2.5734
				O 3 -- O 5	0.03	2.9670
				O 1 -- O 5	0.03	2.9799
				O 2 -- O 6	0.03	2.9819
				O 4 -- O 6	0.03	2.9955

Table 21 reports on the atomic populations of all the bonds that make-up the Fe-doped n3-01 nanocluster. It is observed that the highest atomic population of 0.63 is recorded for the exterior Fe1-O5 bond. This bond length has increased marginally

from 1.56 Å to 1.57 Å as compared to the similar bonding in figure 29 before doping. This further shows the inability of iron to reduce the size of this n3-01 nanocluster after doping.

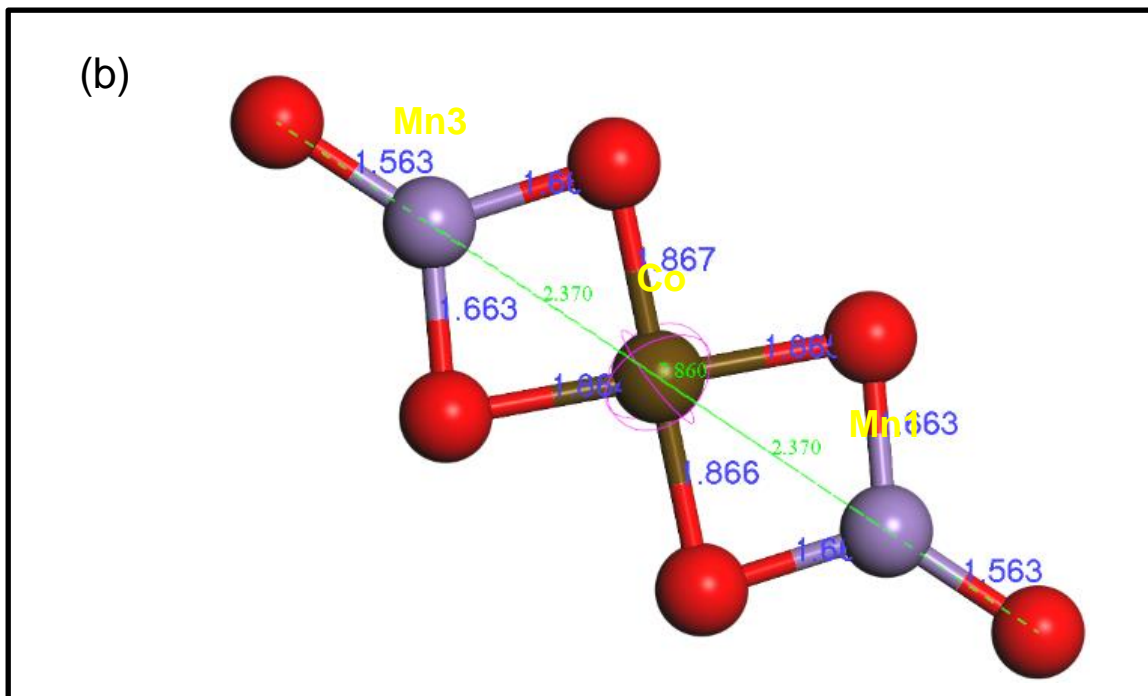
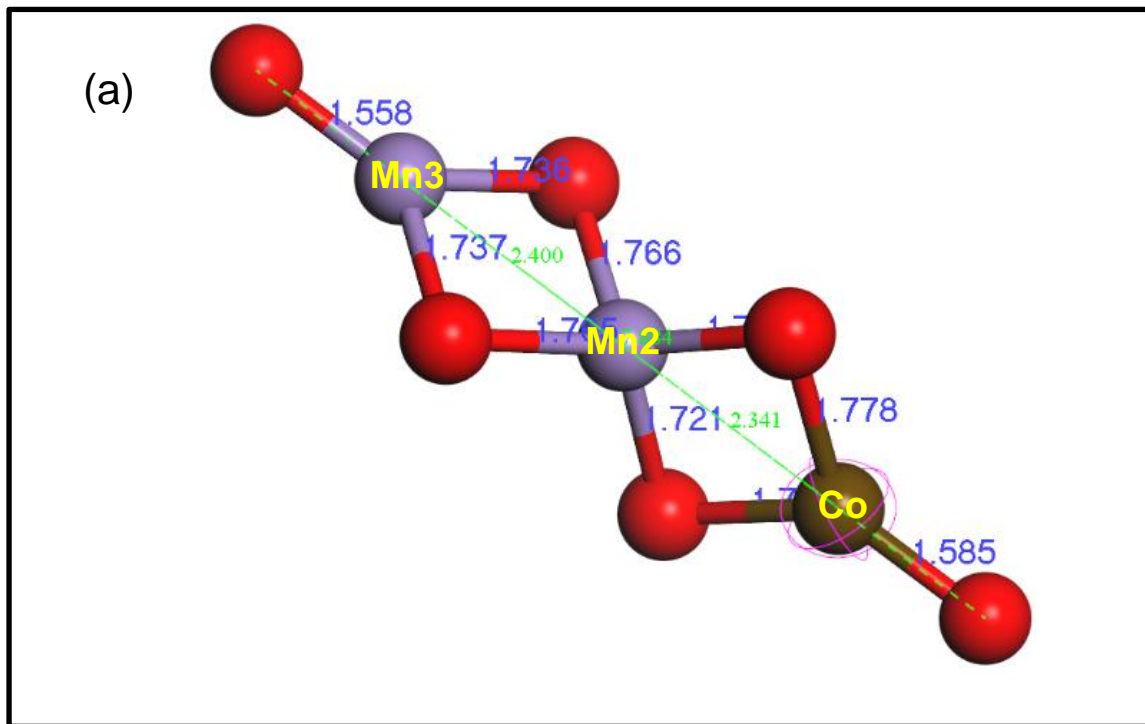
The Mn-Fe bond has a negative bond population showing the strong ionic nature of that bond. The shortest bond length is measured on both the terminal Mn-O bonds, with a bond length of 1.56 Å. This indicates the strong attractive force that exist between these oppositely charged atoms. Inversely, the longest bond of 2.99 Å is recorded between the like-charged oxygen atoms which have a strong repulsive force between them.

9.3.2. Effect of Co-doping on bond lengths

This section focuses on the substitutional doping performed on Mn1 and Mn2, with cobalt replacing the manganese atoms that originally occupied those atomic sites on the undoped optimised n3-01 nanocluster.

Figure 46 depicts the bond lengths in the n3-01 nanocluster that is substitutionally doped by cobalt at Mn1 and Mn2, respectively. Furthermore, the indicated bond lengths correspond to the bond populations reported on in table 22.

From figure 46, it is observed that the bond distance between the two terminal oxygen atoms has increased from 7.856 Å before doping to 7.884 Å after Co-doping on Mn1. The doping on Mn2 shows a decreased bond distance between the two-terminal oxygen of 7.860 Å which is a shorter bond than that of doping on Mn1.



● – Mn

● – Co

● – O

Figure 46: Depiction of the Co-doped n3-01 nanocluster with labelled bond lengths at (a) Mn1 and (b) Mn2

However, this bond length is still longer than that of the undoped n3-01 nanocluster. Similar to Fe-doping, this shows that cobalt doping also does not achieve the desired effect of decreasing the size of the nanocluster as a whole. Therefore, it can be inferred that cobalt does not improve the structural stability and compactness of the nanocluster since smaller compact structures are associated with increased stability for metallic oxide nanostructures [22, 267].

Mulliken atomic bond populations

The data presented in table 21 gives the bond lengths and Mulliken atomic populations of all the admissible bonds in the co-doped n3-01 nanocluster doped on the two sites: Mn1 and Mn2, respectively. The respective bonds are displayed side by side to enable a more direct comparison.

Table 22: Bond lengths of the atomic interactions present in the Co-doped n3-01 nanocluster

Mn1			Mn2		
Bond	Population	Length	Bond	Population	Length
O 6 - Mn 2	0.25	1.5575	O 5 - Mn 1	0.24	1.5632
O 5 - Co 1	0.57	1.5853	O 6 - Mn 2	0.24	1.5632
O 3 - Mn 1	0.13	1.7210	O 1 - Mn 1	0.17	1.6623
O 1 - Mn 1	0.14	1.7210	O 4 - Mn 2	0.17	1.6628
O 4 - Mn 2	0.10	1.7365	O 3 - Mn 1	0.17	1.6629
O 2 - Mn 2	0.10	1.7370	O 2 - Mn 2	0.17	1.6632
O 2 - Mn 1	0.11	1.7649	O 4 - Co 1	0.26	1.8643
O 4 - Mn 1	0.11	1.7664	O 3 - Co 1	0.26	1.8653
O 3 - Co 1	0.31	1.7760	O 1 - Co 1	0.26	1.8661

O 1 - Co 1	0.31	1.7779		O 2 - Co 1	0.27	1.8667
Mn 1 - Co 1	-0.04	2.3407		Mn 2 - Co 1	-0.09	2.3695
Mn 1 - Mn 2	-0.00	2.4004		Mn 1 - Co 1	-0.09	2.3699
O 2 - O 4	0.04	2.5503		O 1 - O 3	0.02	2.6014
O 1 - O 3	0.02	2.5986		O 2 - O 4	0.02	2.6023
O 2 - O 3	0.01	2.9671		O 1 - O 4	-0.01	2.6722
O 1 - O 2	0.01	2.9720		O 2 - O 3	-0.01	2.6764
O 3 - O 4	0.01	2.9726		O 4 - O 6	0.04	2.9030
O 1 - O 4	0.04	2.9783		O 3 - O 5	0.04	2.9051
				O 1 - O 5	0.04	2.9070
				O 2 - O 6	0.04	2.9095

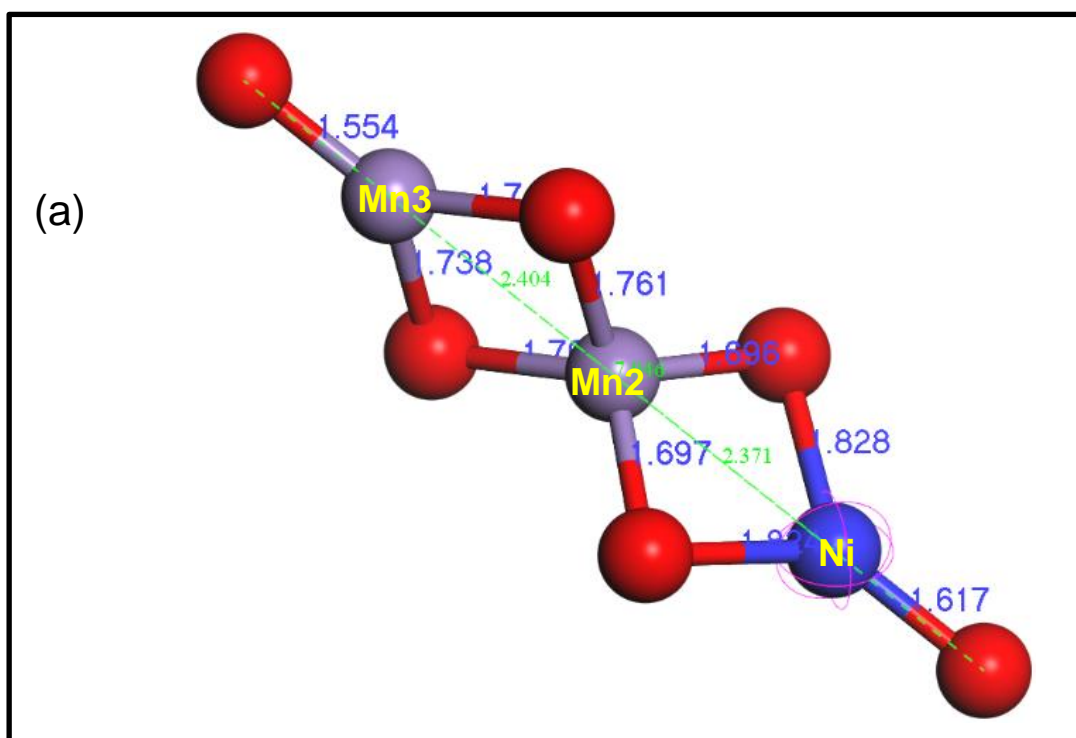
From table 22, it is observed that the shortest bond length of 1.557 Å is measured for the O6-Mn2 bond. This indirectly corresponds to the highest atomic population of 0.25 in comparison to all other manganese-oxygen bonds in when doping was performed on Mn1 or Mn2. Interestingly, this shows that a decrease in the bond length leads to an increase in the bond population.

The oxygen-oxygen bonds are the longest, indicative of the strong repulsion existing between the negatively charged electron rich atoms. The manganese-oxygen bonds are the shortest showing the strong attractive force between the atoms, also proof of the stability of that bond. The oxygen-cobalt bond with a population of 0.57 indicates a stable, covalent bond between those two atoms, however the lower populations on most of these bonds indicates the less desired ionic bonding nature.

9.3.3. Effect of Ni-doping on bond lengths

In this section, we focus on Ni-doping of the n3-01 nanocluster at the Mn1 and Mn2 sites as was done previously for Fe- and Co-doping. The results from this section are compared with those from the previous sections focusing on Fe-doping and Co-doping towards reaching a conclusion on which dopant is preferable for the MnO₂ nanoclusters.

Figure 47 depicts the bond lengths in the n3-01 nanocluster after substitutional doping by Ni at Mn1 and Mn2, respectively. Furthermore, the indicated bond lengths correspond to the bond populations reported on in table 23.



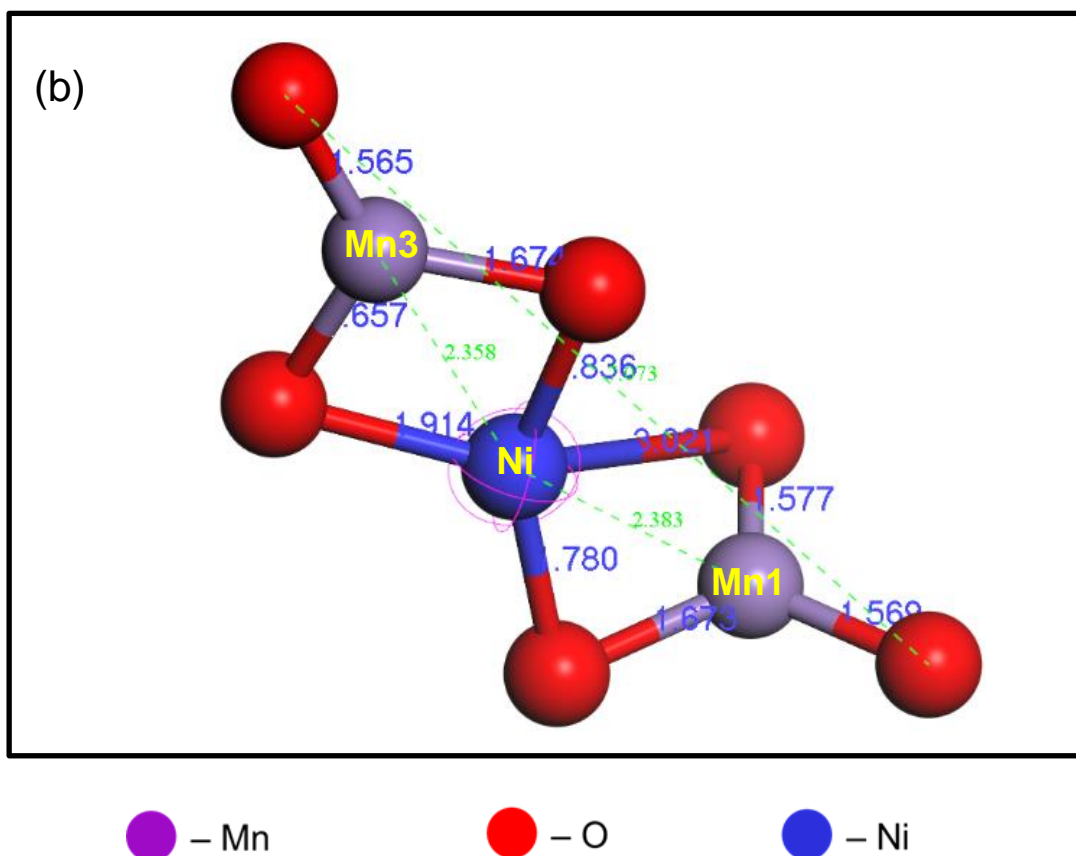


Figure 47: Depiction of the Ni-doped n3-01 nanocluster at (a) Mn1 and (b) Mn2 with labelled bond lengths

Mulliken atomic bond populations

Table 23 represents the Mulliken atomic populations of all the atomic bonds below the 3.0 Å threshold. These bond populations and bond lengths are together analysed with emphasis on the bonding patterns as observed in figure 47. Recall that, a high value of the bond populations indicates the presence of a covalent bond, whereas a low value represents an ionic bond. A zero value indicates a perfectly ionic bond and the values greater than zero indicate increasing levels of covalency [233].

Table 23: Bond lengths of the atomic interactions present in the Ni-doped n3-01 nanocluster

Mn1			Mn2		
Bond	Population	Length	Bond	Population	Length
O 6 - Mn 2	0.26	1.5543	O 6 - Mn 2	0.23	1.5646
O 5 -- Ni 1	0.52	1.6172	O 5 - Mn 1	0.24	1.5694
O 1 - Mn 1	0.15	1.6964	O 3 - Mn 1	0.24	1.5773
O 3 - Mn 1	0.15	1.6973	O 2 - Mn 2	0.18	1.6567
O 4 - Mn 2	0.10	1.7377	O 1 - Mn 1	0.16	1.6734
O 2 - Mn 2	0.10	1.7405	O 4 - Mn 2	0.16	1.6736
O 2 - Mn 1	0.12	1.7615	O 1 -- Ni 1	0.31	1.7796
O 4 - Mn 1	0.12	1.7620	O 4 -- Ni 1	0.31	1.8355
O 3 -- Ni 1	0.27	1.8238	O 2 -- Ni 1	0.24	1.9138
O 1 -- Ni 1	0.26	1.8279	Mn 2 - Ni 1	-0.09	2.3585
Mn 1 - Ni 1	-0.05	2.3711	Mn 1 - Ni 1	-0.01	2.3833
Mn 1- Mn 2	-0.01	2.4037	O 2 -- O 4	0.02	2.6289
O 2 -- O 4	0.03	2.5451	O 3 -- O 5	0.05	2.7421
O 1 -- O 3	0.02	2.6013	O 1 -- O 5	0.02	2.7913
O 3 -- O 4	0.01	2.9378	O 1 -- O 3	0.02	2.8131
O 1 -- O 2	0.01	2.9393	O 2 -- O 6	0.04	2.8842
O 2 -- O 3	0.01	2.9395	O 4 -- O 6	0.04	2.9175
O 1 -- O 4	0.01	2.9397			

From table 23, it is observed that the highest bond population of 0.52 is recorded for the Ni1-O5 bond with a bond length of 1.617 Å. This high value in the atomic population indicates the strong covalency occurring between these atoms as reported previously [233].

9.4. Electronic atomic orbital contributions

In this section, we report on the orbital contributions from the individual electronic orbitals of each atomic specie that constitutes the doped n3-01 nanocluster by Fe, Co and Ni.

9.4.1. Electronic atomic orbital contributions of the Fe-doped n3-01 nanocluster

The results discussed in this section emanate from the contributions to the Mulliken populations due to each electronic orbital. The partial charges attributed to each atomic specie are displayed in table 24. This is done in order to analyse the atomic contributions to the charge density differences as the charges are re-distributed and hybridised during bond formations and doping.

Table 24: Comparisons of the electronic contributions to the total atomic populations of the Fe-doped n3-01 nanocluster on site Mn1 and Mn2.

	Mn1					Mn2				
Specie	s	p	D	Total		Specie	s	p	D	Total
O1	1.94	4.71	0.00	6.65		O1	1.94	4.74	0.00	6.68
O2	1.97	4.81	0.00	6.79		O2	1.94	4.74	0.00	6.68
O3	1.94	4.71	0.00	6.65		O3	1.94	4.74	0.00	6.68

O4	1.97	4.81	0.00	6.79		O4	1.94	4.74	0.00	6.68
O5	1.94	4.49	0.00	6.43		O5	1.98	4.57	0.00	6.55
O6	1.98	4.56	0.00	6.55		O6	1.94	4.57	0.00	6.55
Mn1	2.00	6.00	5.48	13.48		Mn1	2.00	6.00	5.49	13.49
Mn2	2.00	6.00	5.57	13.57		Mn2	2.00	6.00	5.49	13.49
Fe1	0.39	0.23	6.48	7.10		Fe2	0.26	0.44	6.52	7.22

From table 24, it is observed that the highest charge contribution per orbital emanates from the Fe atom. This is because Fe has the higher number of electrons in its outer most shell; the 3d orbital as compared to Mn. Manganese has 5 electrons in its outer most shell 3d and iron has 6 electrons in its valence shell, also the 3d orbital. Hence Fe has the highest value in the d orbital when compared with oxygen and manganese.

It has been reported that 3d orbitals are higher in energy than the preceding orbitals [270]. However, Mn is more stable than Fe because it has a higher electronic contribution from the preceding orbitals as proven by the totals of the contributions being higher for both manganese atoms in the Fe-doped n3-01 nanocluster.

Table 25 reports the partial charges on the individual atoms as measured in terms of the Hirshfeld and Mulliken charges.

Table 25: Charge density differences of the Fe-doped n3-01 nanocluster substituted at the two atomic positions at Mn1 and Mn2 with their Hirshfeld and Mulliken charges

Doping site	Mn1			Mn2	
Specie	Mulliken	Hirshfeld		Mulliken	Hirshfeld
O1	-0.65	-0.17		-0.68	-0.17
O2	-0.79	-0.19		-0.68	-0.17
O3	-0.65	-0.17		-0.68	-0.17
O4	-0.79	-0.19		-0.68	-0.17
O5	-0.43	-0.16		-0.55	-0.19
O6	-0.55	-0.18		-0.55	-0.19
Mn1	1.52	0.34		1.51	0.37
Mn2	1.43	0.41		1.51	0.37
Fe1	0.90	0.30		0.78	0.30

From the data in table 25, the summation of both the Mulliken charges and Hirshfeld charges all add up to $-0,01 e$ representing the minimal negative charge of the nanocluster in its entirety which is indicative of the electrical conductivity of the n3-01 nanocluster. This summation is carried out as follows;

$$\begin{aligned} \sum_i H &= (-0.17 - 0.19 - 0.17 - 0.19 - 0.16 - 0.18) + (0.34 + 0.41 + 0.30) = 0 \\ &= -1.06 + 1.05 = -0,01 e \end{aligned}$$

$$\begin{aligned} \sum_i M &= (-0.65 - 0.79 - 0.65 - 0.79 - 0.43 - 0.55) + (1.52 + 1.43 + 0.90) = 0 \\ &= -3.86 + 3.85 = -0,01 e \end{aligned}$$

Similar discussions are carried out in the following sections focusing on the substitutional doping by Co and Ni cobalt and nickel on Mn1 and Mn2.

9.4.2. Electronic atomic orbital contributions of the Co-doped n3-01 nanocluster

Table 26 reports on the electronic charge contributions of each atomic orbital due to each atomic specie in the Co-doped n3-01 nanocluster. The atoms are labelled numerically to distinguish them which helps to specify Mulliken atomic populations.

Table 26: Electronic contributions to the total atomic populations of the Co-doped n3-01 nanocluster on Mn1 and Mn2.

	Mn1					Mn2			
Specie	S	p	D	Total		S	P	d	Total
O1	1.94	4.71	0.00	6.65		1.94	4.72	0.00	6.66
O2	1.97	4.81	0.00	6.78		1.94	4.72	0.00	6.66
O3	1.94	4.71	0.00	6.65		1.94	4.72	0.00	6.66
O4	1.97	4.81	0.00	6.78		1.94	4.72	0.00	6.65
O5	1.95	4.51	0.00	6.46		1.98	4.56	0.00	6.54
O6	1.98	4.55	0.00	6.53		1.98	4.56	0.00	6.54
Mn1	2.00	6.00	5.45	13.45		2.00	6.00	5.44	13.43
Mn2	2.00	6.00	5.58	13.58		2.00	6.00	5.44	13.43
Co1	0.40	0.25	7.46	8.11		0.41	0.43	7.60	8.43

From table 26, similar observations can be deduced to those observed in table 24 for Fe-doping. The Co dopant atom contributes fewer in the s and p orbitals but is the highest in the d orbital. The manganese atoms are more stable than the other atoms

because they have the highest total contributions. The cobalt dopant on the Mn2 site with the higher coordination has a higher total of 8.43 than the cobalt dopant on the Mn1 site with 8.11. This shows the preference of substitutional doping to be performed on atoms with a higher coordination that are also centrally positioned in the nanoclusters. The O5 atom has the lowest contribution of 6.46 to the electronic charge of the nanocluster for the doping performed on the Mn1 site.

Table 27 reports on the partial charges that have accumulated on the individual atoms in the Co-doped n3-01 nanocluster. The measurements are given in terms of the Hirshfeld and Mulliken charges.

Table 27: Charge density differences of the Co-doped n3-01 nanocluster substituted at the two atomic positions at Mn1 and Mn2 with their Hirshfeld and Mulliken charges

Doping site	Mn1			Mn2	
	Mulliken	Hirshfeld		Mulliken	Hirshfeld
O1	-0.65	-0.17		-0.66	-0.16
O2	-0.78	-0.19		-0.66	-0.16
O3	-0.65	-0.17		-0.66	-0.16
O4	-0.78	-0.19		-0.65	-0.16
O5	-0.46	-0.16		-0.54	-0.19
O6	-0.53	-0.18		-0.54	-0.19
Mn1	1.55	0.36		1.57	0.40
Mn2	1.42	0.42		1.57	0.40
Co1	0.89	0.26		0.57	0.19

The two manganese atoms have equal charges when the cobalt atomic substitution was performed on the Mn2 atomic site. This further illustrates the highly symmetric nature of the nanocluster, especially when doping is done on the central manganese site with the greater coordination. There are greater variations in the atomic charges when doping was done on Mn1 showing the lesser stability of this doped nanocluster.

9.4.3. Electronic atomic orbital contributions of the Ni-doped n3-01 nanocluster

This section reports on the individual orbital contributions from each atom in the n3-01 nanocluster doped with Ni. These contributions are compared when nickel is doped on the two metallic sites occupied by the manganese atoms at Mn1 and Mn2.

The data given in table 28 represents the electronic atomic orbital contributions derived from each electronic contribution of the different orbitals.

Table 28: Comparisons of the electronic contributions to the total atomic populations of the Ni-doped n3-01 nanocluster on the Mn1 and Mn2 sites.

	Mn1					Mn2			
Specie	s	p	D	Total		s	p	d	Total
O1	1.94	4.72	0.00	6.66		1.93	4.76	0.00	6.69
O2	1.97	4.80	0.00	6.77		1.94	4.73	0.00	6.67
O3	1.94	4.72	0.00	6.66		1.97	4.57	0.00	6.54
O4	1.97	4.80	0.00	6.77		1.94	4.73	0.00	6.67
O5	1.95	4.56	0.00	6.50		1.98	4.54	0.00	6.52
O6	1.98	4.54	0.00	6.52		1.98	4.55	0.00	6.53
Mn1	2.00	6.00	5.43	13.43		2.00	6.00	5.42	13.41

Mn2	2.00	6.00	5.58	13.58		2.00	6.00	5.45	13.44
Ni1	0.43	0.27	8.41	9.10		0.48	0.47	8.58	9.52

From table 28, it is observed that the highest orbital contribution emanates from the two manganese atoms in the n3-01 nanocluster. It is also observed that the central manganese atom denoted by Mn2 has the higher orbital contribution in comparison between the two cations. This goes a long way in explaining why the pure undoped nanocluster consisting only of manganese and oxygen atoms is more stable than all the other doped complexes. Comparing the two nickel dopants at Mn1 and Mn2, shows that the central atomic site with the greater coordination has the higher orbital contribution of 9.52 as compared with 9.10 for Mn1. This further shows the preference for the substitutional doping to be performed at the central Mn2 site.

Table 29 reports on the partial charges that have accumulated on the individual atoms in the Ni-doped n3-01 nanocluster. The measurements are given in terms of the Hirshfeld and Mulliken charges.

Table 29: Charge density differences of the Ni-doped n3-01 nanocluster substituted at the two atomic positions at Mn1 and Mn2 with their Hirshfeld and Mulliken charges

	Mn1			Mn2	
Specie	Mulliken	Hirshfeld		Mulliken	Hirshfeld
O1	-0.66	-0.18		-0.69	-0.19
O2	-0.77	-0.18		-0.67	-0.17
O3	-0.66	-0.18		-0.54	-0.18
O4	-0.77	-0.18		-0.67	-0.16

O5	-0.50	-0.19		-0.52	-0.18
O6	-0.52	-0.18		-0.53	-0.18
Mn1	1.57	0.38		1.59	0.42
Mn2	1.42	0.43		1.56	0.40
Ni1	0.90	0.26		0.48	0.22

From table 29, it is observed again that the summation of the total Hirshfeld is a negative value. This negativity in the total charge alludes to the nanocluster's ability to conduct electrical charges adding on to the positive results from charge density differences of the Ni-doped nanoclusters.

It is observed from the measurements in this chapter that the shortest bond length between the exterior terminal oxygen atoms is measured for the Ni-doped n3-01 nanocluster on the central atomic position denoted by Mn2 at 7.073 Å as shown in figure 48. This is the position with the highest level of coordination because the cation at this position is tetrahedrally bonded to 4 oxygen atoms whereas the other two cation sites are only bonded to 3 neighbouring oxygen atoms.

From figure 48, it is observed that shortest bond between the two exterior terminal oxygen atoms on the right left side and the right side is recorded when nickel was doped on the central atomic site with highest coordination denoted by Mn2. This shows that nickel is the preferred dopant and that this central metallic site is the best position to perform the doping process.

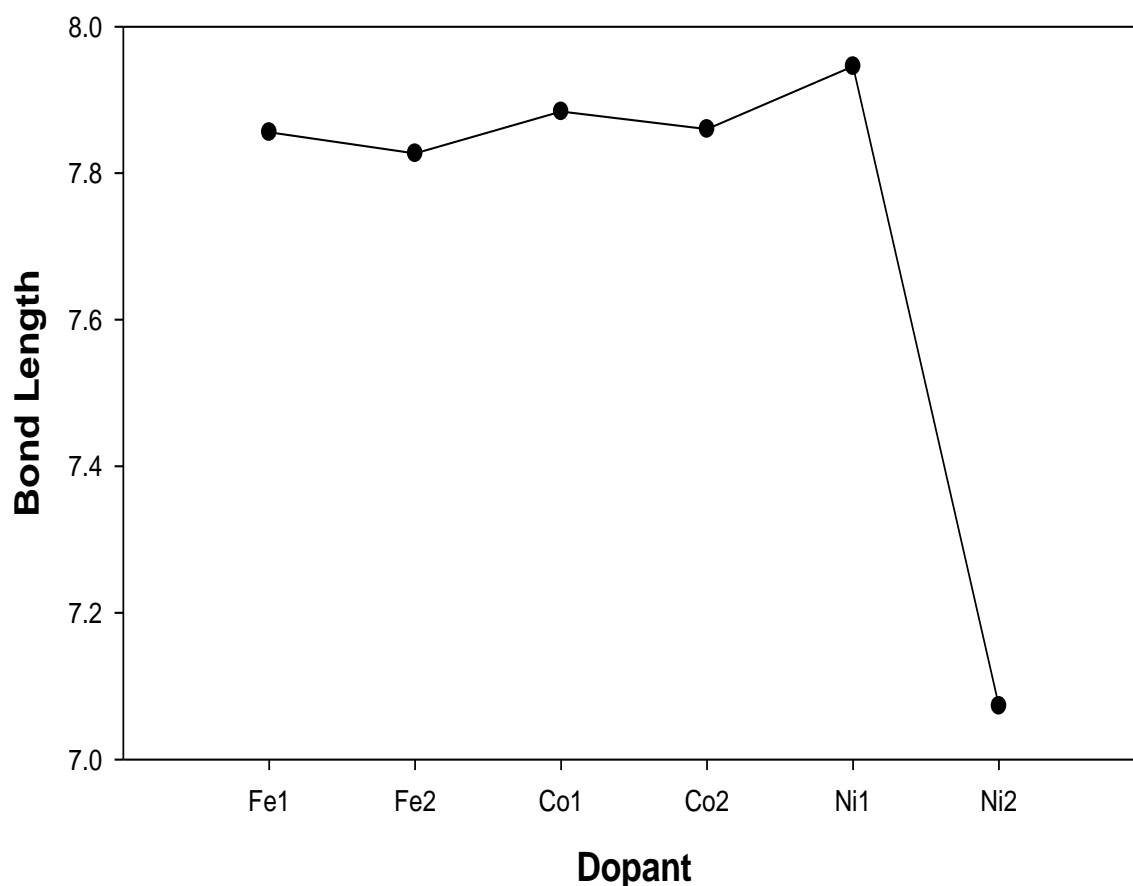


Figure 48: End to end bond length of the exterior terminal oxygen atoms from the doped n3-01 nanocluster

The Ni-doped n3-01 nanocluster shows a deviation from its linear atomic configuration towards a more compact circular configuration. This is proven by the angle between the exterior terminal oxygen atoms decreasing from 180° to 147° as shown in figure 45. This behaviour is similar to those predicted for isostructural ZrO_2 , SiO_2 and TiO_2 nanoclusters [22, 113]. The most stable structures were found to adopt compact ring configurations, suggesting that the nanoclusters preferred shorter average bond distances and a higher average coordination of the constituent atoms.

The centrally doped n3-01 nanocluster with cobalt shows that the yellow density cloud surrounding the cobalt atom has the biggest separation from the blue density of its neighbouring oxygen atoms bonded to it. This clear boundary indicates that cobalt

has bonded ionically to the oxygen atoms as compared to the figure showing the doping with nickel on the same atomic position.

A covalent bond is observed between the central nickel atom with its neighbouring oxygen atoms because of the overlap between the blue enriched density regions of the oxygen atoms and the yellow depleted electron density regions of the nickel atom. The manganese-oxygen bonds also show a considerable magnitude of covalency owing to the stability of the doped manganese dioxide nanoclusters. Figure 49 illustrates the atomic populations measured for all the dopant elements on their substituted positions on either the Mn1 or Mn2 atomic positions on the n3-01 nanocluster.

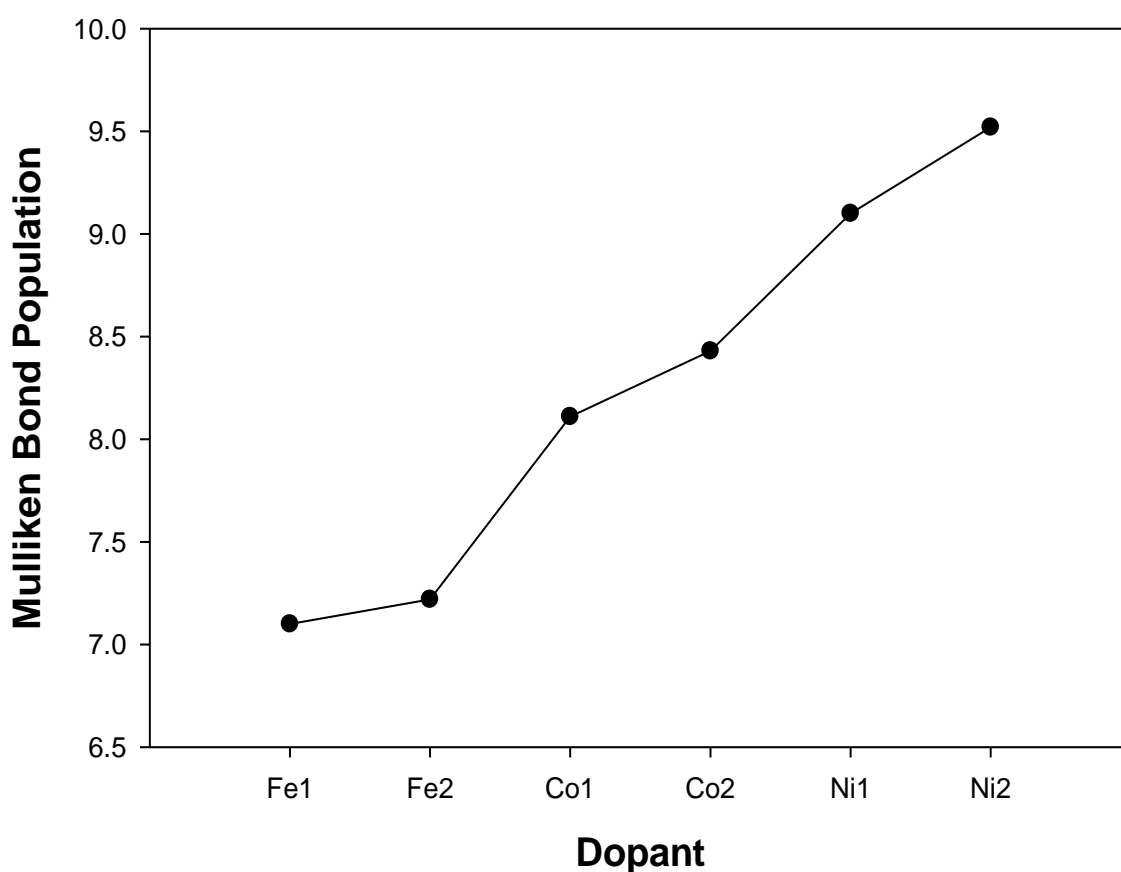


Figure 49: Mulliken bond populations of the dopants compared per doping site

Figure 49 shows that highest bond population was recorded when nickel is substituted on the central atomic site that was originally occupied by manganese with the highest coordination (number of bonds). Recall, that high population readings correlate with stability since a high value of the bond population indicates a covalent bond, whereas a low value represents an ionic bond [233]. It is thus further proven that nickel is the preferred dopant followed by cobalt and that the central cation site is the preferred site to perform the substitutional doping.

From this chapter, it was shown definitively that this manganese dioxide nanocluster prefers doping on the centrally located cation atoms with a higher coordination. This has been shown to contribute positively to the stability of structures in the earlier chapter of this study and in previous literature [21]. Hence the analysis in this chapter proves this assertion beyond certainty. Nickel has also been shown to be the preferable dopant element due to its positive contribution to the stability and compactness of the doped nanocluster. This is proven by the shorter bond lengths and evolution from a linear oriented structure to a more circular structure.

It is important to note that the higher atomic populations correspond with the shorter bonding lengths. For the centrally doped cobalt nanocluster, the shortest bond length of 1.563 Å corresponds to the highest atomic population of 0.24 between the O5-Mn1 bonds. All the Co-O bonds are relatively equal at 1.86 Å corresponding to a population of 0.26. The longest bond length of 2.91 Å is recorded for smallest population quantity of 0.04 indicative of the strong repulsive interaction between the negatively charged oxygen atoms.

The manganese-cobalt bond is also longer at 2.34 Å with a negative population of – 0.09. It is worthwhile to mention that the bonding cut-off length was set at 3 Å. This

was set at this cut-off because any atomic and electronic interactions beyond this point become inconsequential and irrelevant towards the broader scheme of the charge densities of the whole nanocluster. The metallic atoms such as cobalt and manganese have positive charges.

Manganese has the higher Hirshfeld charge at 0.40 |e| and cobalt has 0.19 |e|. The oxygen atoms have negative Hirshfeld charges of – 0.16 |e| indicative of their ability to accept electrons during bonding. The centrally nickel-doped n3-01 nanocluster is the most de-arranged. The manganese to nickel bond lengths in table 28 are 2.36 Å and 2.38 Å respectively which are the shortest when compared to any other doped nanocluster. Similar trends in the Hirshfeld and Mulliken charges are observed with the nickel doped nanoclusters as was seen with Fe and Co doping.

The oxygen-to-oxygen bonds are the longest while having the least atomic populations. The metallic ions are positively charged and the oxygen atoms are negatively charged which shows that the metallic atoms are contributing their electronic charge density to the oxygen atoms during bonding as shown by the yellow and blue charge densities. Both cobalt and nickel show positive attributes which explains why some previous studies have opted to use both of them in their doping investigations [53, 68].

From the analysis and discussions carried out in this chapter, doping offers a unique insight towards improving the stability and performance of manganese dioxide nanoclusters. Different types of bonding natures were observed which shows the qualities and disadvantages of the dopants used in this study. The Ni-doped nanoclusters are shown to be more stable due to their covalent bonding, shorter bonding lengths and lower binding energies, hence nickel is concluded to be the

better dopant material for the MnO₂ nanoclusters as was shown previously [64, 65, 66, 126].

9.5. Voltage profiles of the n3-01 nanocluster

In this section, we present the calculated voltage profiles of the undoped n3-01 nanocluster and the doped nanocluster. Fe, Co and Ni are studied further as the dopants of interest in this study. Analysis of voltage profiles are vital for the fabrication of new materials used as positive electrodes in rechargeable batteries. A high potential has been shown to increase the energy density of a material. However, a too high potential leads to electrolyte breakdown and too low potential leads to moisture sensitivity.

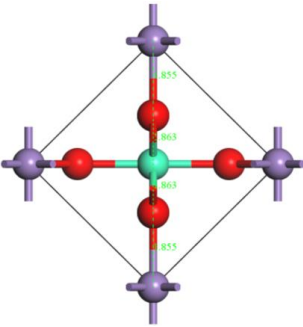
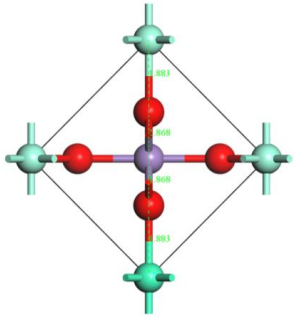
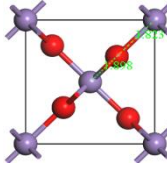

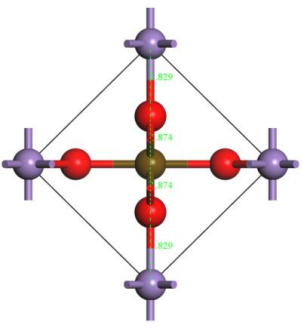
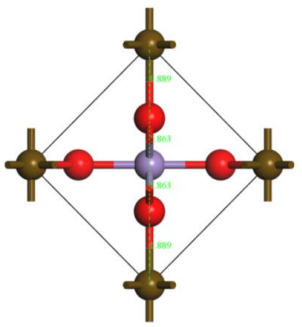
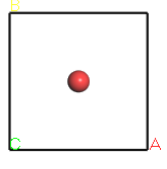
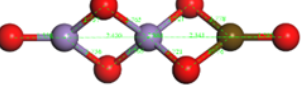
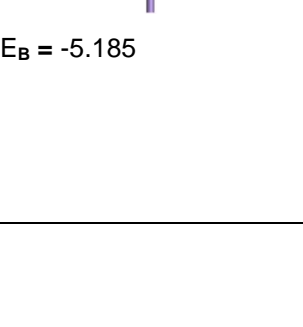
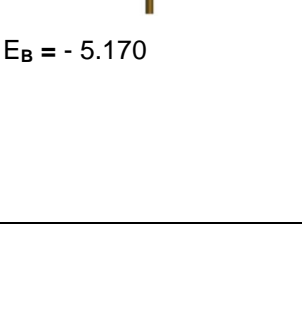
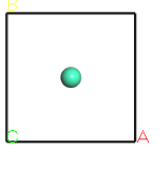
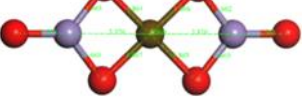


An understanding of the thermodynamic potential is of significant importance in creating the next generation of cathode materials in rechargeable batteries [273]. 2.7 V per cell and 3.9 V per cell have been reported as the predefined limits for charge and discharge when establishing these terminal cell voltages [274]. Hence these values are used as a reference for determining the effectiveness of these nanoclusters. Positive values of the calculated potentials indicate the stability and suitability of the electrode material for use in rechargeable batteries [275].

$$V = - \frac{E_{MnO_2} - E_{MnNiO_4}}{n e} \quad (9.1)$$

where E_{MnO_2} is the binding energy of the bulk β -MnO₂, E_{MnNiO_4} represents the doped n3-01 nanocluster. n represents the number of specie of the elements comprising the structure and e is the electric charge of an electron in electron-volts [276]. Substituting the binding energy values from table 6 in chapter 4 into equation 9.1

gives the results given in table 30. Also given in table 30, are the voltage profiles of the Fe-doped, Co-doped and Ni-doped bulk structures. Furthermore, the voltage profiles of the undoped n3-01 nanocluster are included, along with the Fe, Co and Ni-doped n3-01 nanocluster on the central Mn2 atomic site.

Table 30: Binding energies of all the structures

<p>Fe centre</p>  <p>$E_B = -5.170$</p>	<p>Fe corner</p>  <p>$E_B = -5.112$</p>	 <p>$E_B = -5.082$</p>	 <p>$E_B = -4.441$</p>
<p>Co centre</p>  <p>$E_B = -5.185$</p>	<p>Co corner</p>  <p>$E_B = -5.170$</p>	 <p>$E_B = -0.0737$</p>	 <p>$E_B = -4.524$</p>
<p>Co centre</p>  <p>$E_B = -5.185$</p>	<p>Co corner</p>  <p>$E_B = -5.170$</p>	 <p>$E_B = 0.0512$</p>	 <p>$E_B = -4.531$</p>
		 <p>$E_B = -1.1372$</p>	 <p>$E_B = -4.554$</p>

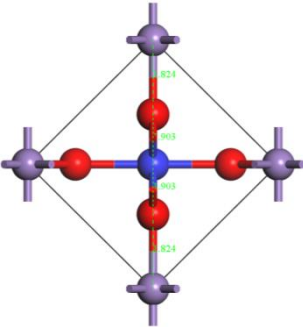
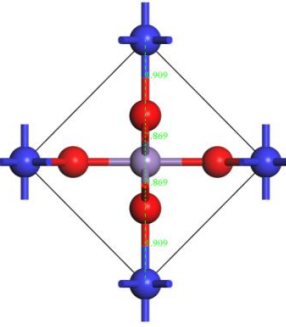
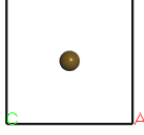
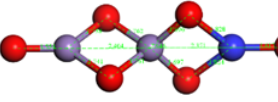
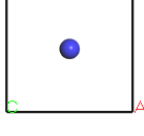
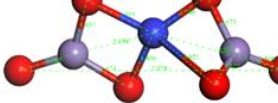
<p>Ni centre</p>  <p>$E_B = -5.231$</p>	<p>Ni corner</p>  <p>$E_B = -5.211$</p>	 <p>$E_B = -1.3181$</p>	 <p>$E_B = -4.516$</p>
		 <p>$E_B = -1.417$</p>	 <p>$E_B = -4.674$</p>

Table 30 gives the binding energy values that were initially reported in chapter 4 and chapter 8. These values are substituted into equation 9.1 to calculate the voltage profiles in order to further compare and highlight the electrical conductivity of the indicated structures.

$$\begin{aligned}
 V &= - \frac{E_{\beta-MnO_2} - nE_{Mn} - nE_O}{n e} \\
 &= - \frac{(-5.082 \text{ eV}) - 2(-0.0737 \text{ eV}) - 4(0.0512 \text{ eV})}{(2)(1 \text{ eV})} = 2.570 \text{ V}
 \end{aligned}$$

Equation 9.1 can also be re-arranged to calculate the voltage profiles of the nanoclusters. The results are given in table 31.

From table 31 focusing on the voltage profiles of the bulk structures, it is observed that the undoped bulk structure has the highest potential voltage in comparison to all the doped bulk structures. These results go against known trends where previous DFT-based calculations have shown that Co-based materials had a higher potential in comparison with Mn-based and Fe-based materials [273, 277].

Table 31: Voltage profiles of the undoped, the Fe-doped, Co-doped and Ni-doped β - Mn_2O_4 bulk structures.

Structure	Voltage Profile (V)
Bulk β - Mn_2O_4	2.570
Bulk β - $MnFeO_4$	1.388
Bulk β - $MnCoO_4$	1.333
Bulk β - $MnNiO_4$	1.308

Furthermore, none of the doped bulk structures have shown an improvement in the voltage. This is further proof of the inherent defects that limit the optimal use of the β - MnO_2 bulk structure as cathode materials for rechargeable batteries [16, 17].

Figure 50 is a plot of the voltage profile values given in table 31 comparing the undoped bulk β - MnO_2 with the bulk structure doped with Fe, Co and Ni. It must be noted that none of the voltage profile values depicted in figure 50 fall within the minimum and maximum operating limits set for charge and discharge in terminal cell voltages of 2.7 V and 3.9 V. This shows that these materials will suffer from moisture sensitivity and cause electrolyte breakdown if they are used in rechargeable batteries in their current condition.

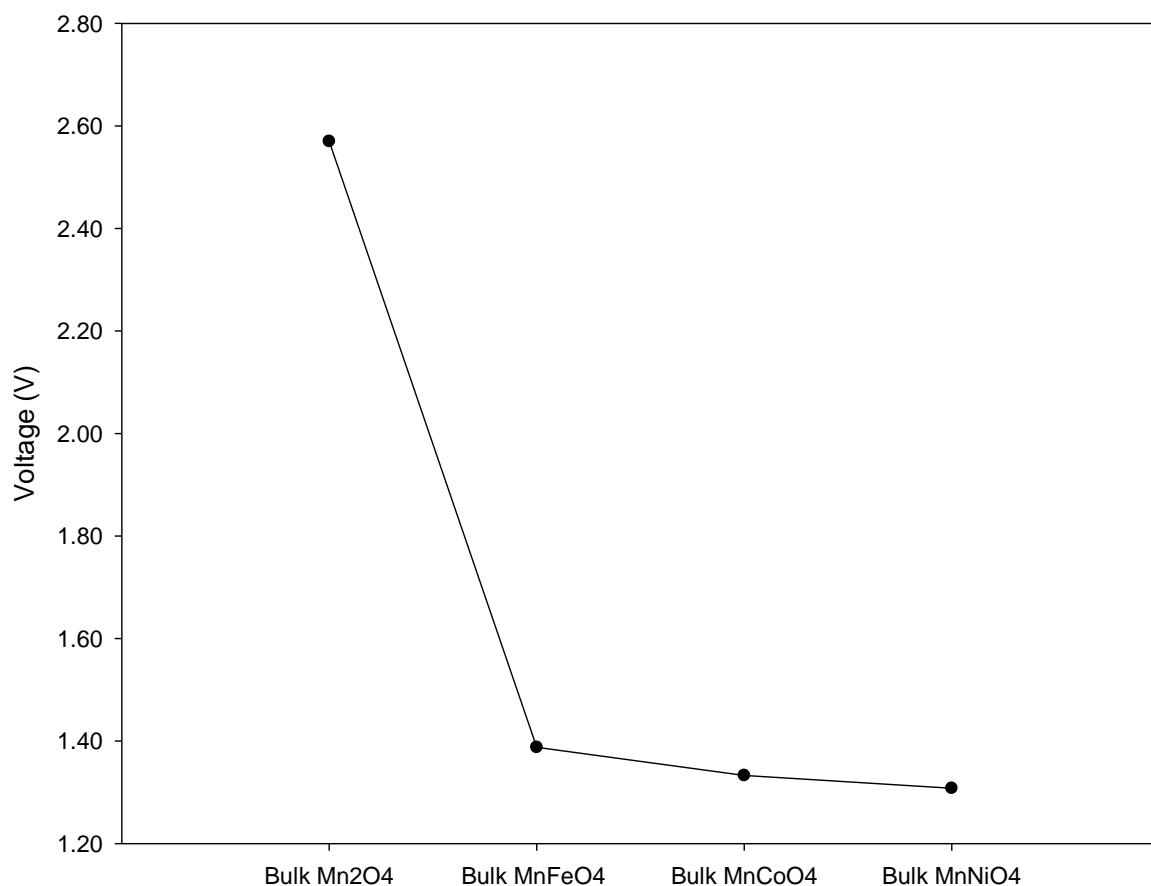


Figure 50: Plot depicting the voltage profiles of the undoped β -MnO₂, the Fe-doped, Co-doped and Ni-doped bulk β -Mn₂O₄ bulk structures.

A higher potential is required in cathode materials because it increases the energy density of the material [278]. Hence, the voltage profiles of the nanostructured materials are calculated and given in table 32.

Table 32: Voltage profiles of the undoped, the Fe-doped, Co-doped and Ni-doped n3-01 nanoclusters.

Structure	Voltage Profile
	(V)
n3-01	1.956

n3-01-Fe1	2.837
n3-01-Co1	2.991
n3-01-Co2	2.997
n3-01-Ni1	2.986
n3-01-Ni2	3.038

A plot of the voltage profiles given in table 32 is illustrated in figure 51. The plot compares the voltages of the n3-01 nanocluster doped at the Mn1 and Mn2 atomic positions with the Fe, Co and Ni dopants.

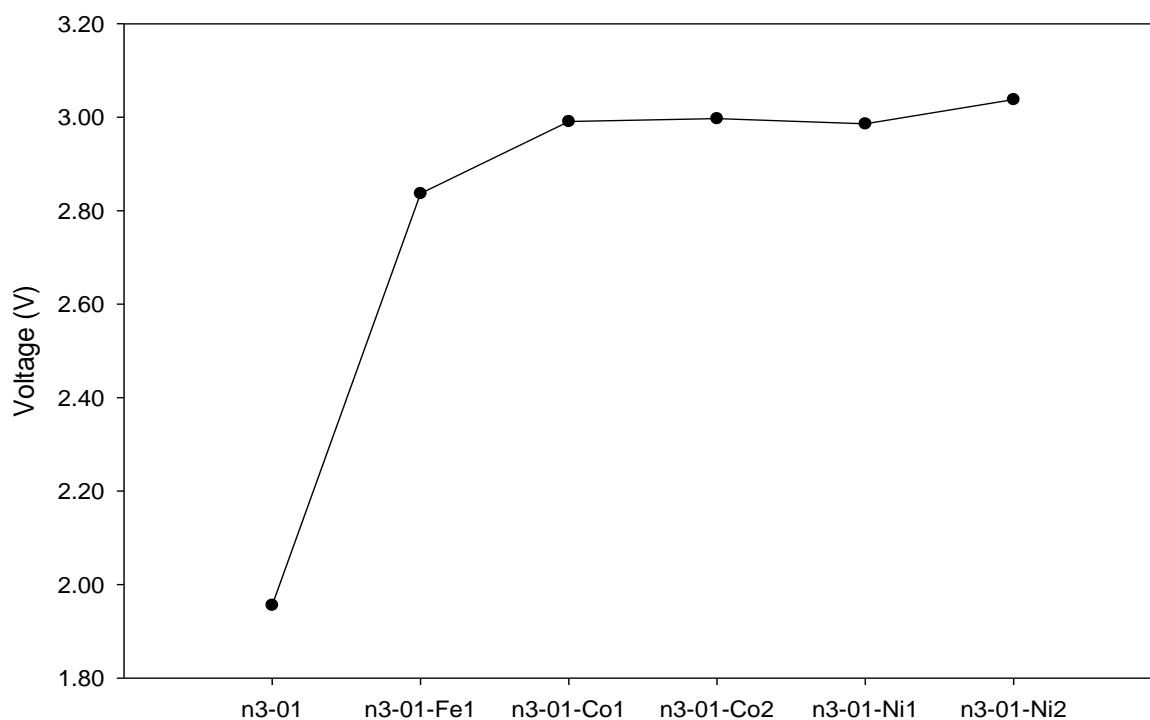


Figure 51: Plot depicting the voltage profiles of the undoped n3-01, the Fe-doped, Co-doped and the Ni-doped nanoclusters at the Mn1 and Mn2 atomic positions.

Due to the novelty of this work, experimental voltage profiles are not known hence a comparison can only be made amongst the nanoclusters in order to determine which dopant produces the electrical conducting material.

The undoped n3-01 nanocluster has the lowest voltage profile of 1.96 V which is also below the minimum limit of set operating terminal voltages. Hence the undoped nanocluster does not conduct electricity to the required standards in rechargeable batteries. Propitiously, all the doped nanoclusters have voltage profiles that fall within the minimum and maximum cut-off limits of 2.7 V and 3.9 V. These results are very positive as indicate that cathode materials composed of the structures will be safe from moisture sensitivity and will not result in electrolyte breakdown in the rechargeable battery [279].

Furthermore, the Ni-doped n3-01 nanocluster on the Mn₂ cation site has the highest voltage potential of 3.038 V, higher than all the other structures measured in this study but still stable enough to resist electrolyte breakdown. The Fe-doped n3-01 nanocluster on Mn₁ has the lowest voltage potential when compared with the other doped n3-01 nanoclusters. Hence nickel further shows that it is the most preferable dopant for manganese dioxide systems.

The Ni-doped MnO₂ electrode materials will have the highest energy density and the highest stability due to the high covalency as observed with the charge density differences. These results have shown the qualities of Ni-doping unreservedly.

9.6. Charge density differences of the dual doped n3-01 nanocluster

This subsection focuses on the electronic charge density differences of the dual doped n3-01 nanocluster. This is a continuation of the discussions about the electronic properties of the dual doped n3-01 nanocluster carried out in section 8.3. In particular, we will now investigate and compare the electronic charge density profiles of the dual doped n3-01 nanoclusters.

Firstly, the consideration is on the dual doping when Co is substituted on Mn1 and Ni is substituted on Mn2 simultaneously. Secondly, the discussions will focus on the Ni substitution of the Mn1 atomic position and when Co is substituted on the Mn2 atomic position. The analysis focuses solely on deciphering the bonding schemes formed by the dopant elements with their existing neighbouring atoms as viewed on the charge density differences as a way to determine whether ionic or covalent bonding dominates the newly formed atomic configurations.

Recall, from chapter 8 that Ni and Co were shown to be the most the most promising dopants hence their continued selection for dual doping. Moreover, Fe was shown to not improve the structural stability and electrical conductivity of the n3-01 nanocluster hence its exclusion from these calculations. Figure 52 displays the step-by-step process of the simultaneous dual doping with both the dopant impurities (Ni and Co) and analysing their charge density difference profiles.

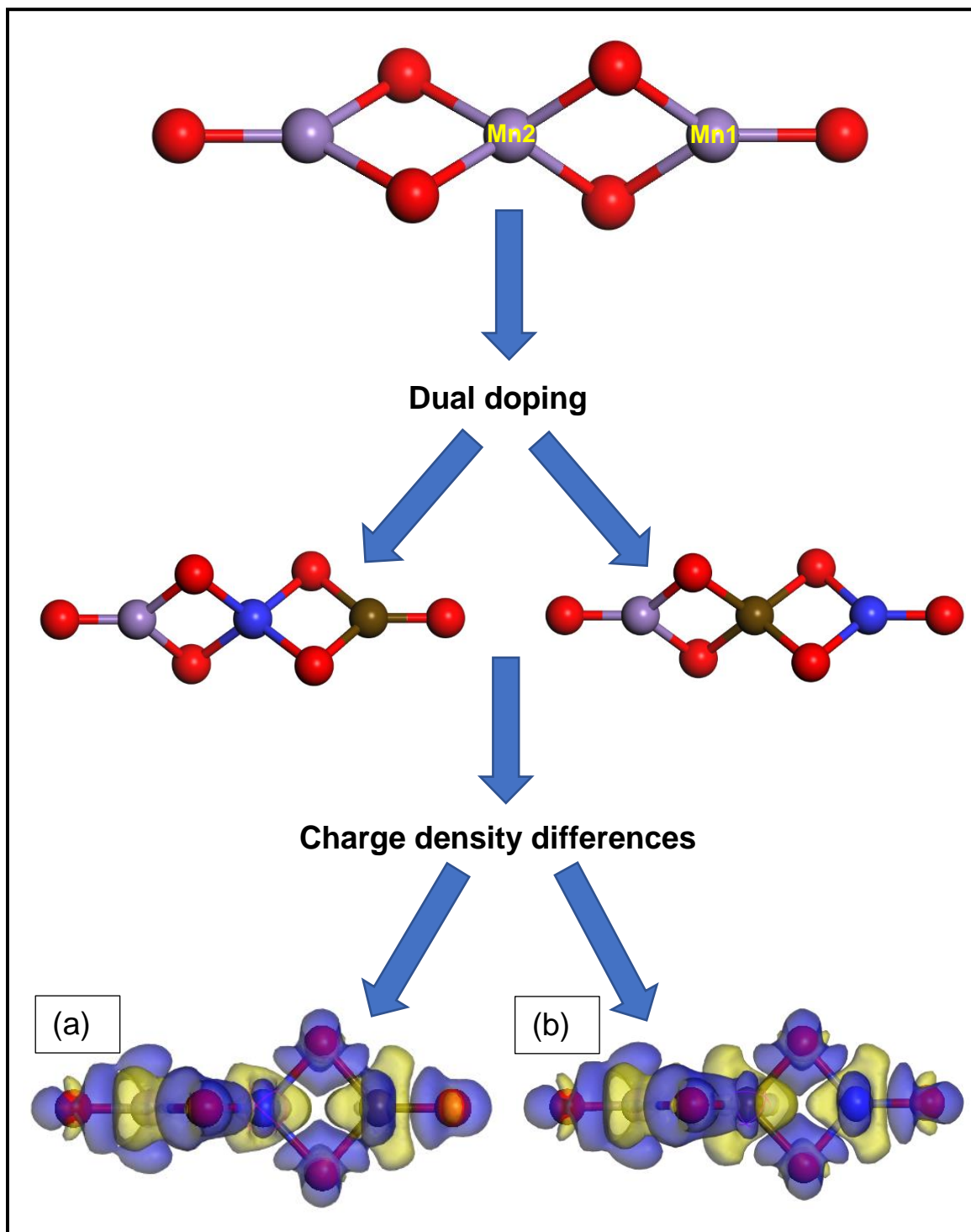


Figure 52: Charge density differences of the simultaneous dual doping of the n3-01 nanocluster with Ni and Co. (a) The n3-01 nanocluster doped with Ni on the Mn2 atomic position and Co on the Mn1 atomic position. (b) The n3-01 nanocluster doped with Co on the Mn2 atomic position and Ni on the Mn1 atomic position

In order to fully visualise the electronic charge density difference profiles, an iso-surface value of (+/-) 0.05 eV was implemented. Note that the individual atomic densities functionality was implemented in order to compute the charge density difference with respect to the individual atoms instead of the symmetric fragments of the nanocluster structure. The (+/-) displays two iso-surface regions (as was done for figure 41). The blue iso-surface at +0.05 eV represents the gain of electronic charge and the yellow iso-surface at -0.05 eV represents charge depletion. A higher transparency was used in order to show the position of the atoms responsible for creating the displayed charge densities.

A close up (zoomed-in) view of the bonding around the dopant elements is provided in figure 53 to aid the accurate analysis towards a determination about which dopant element best improves the stability of the bonds in the n3-01 nanocluster.

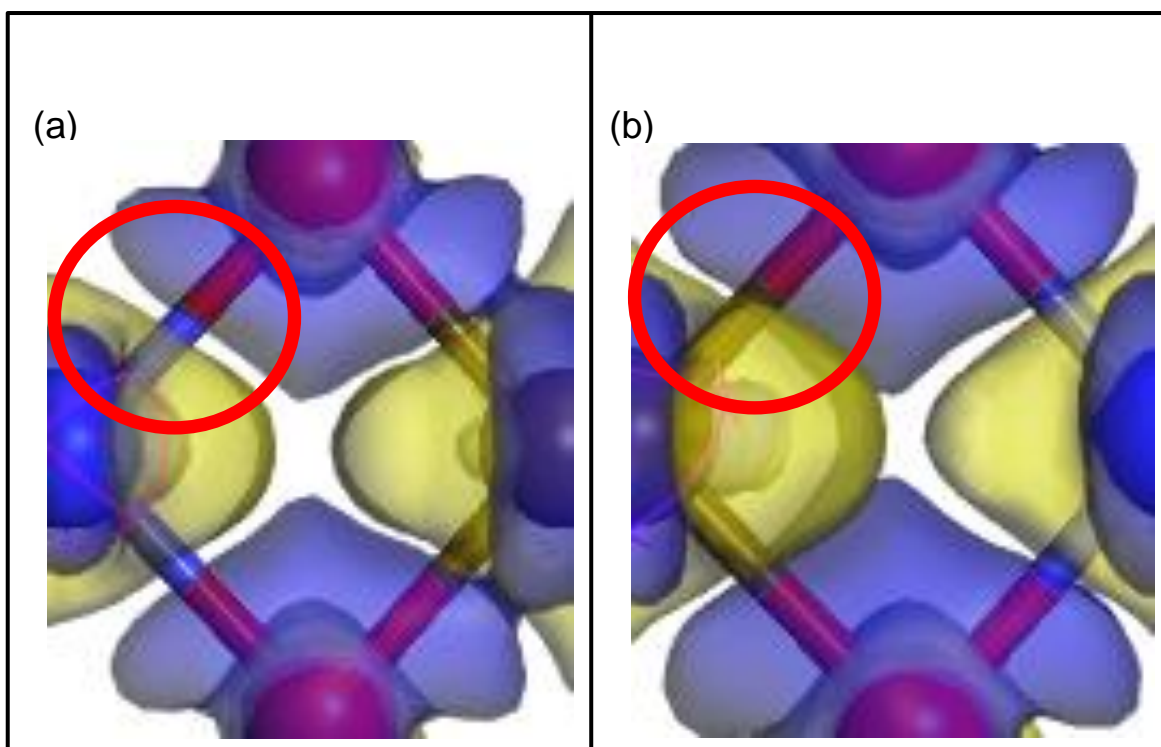


Figure 53: Close-up images of the interaction of the dopant impurities focusing on the type of bonds formed between oxygen with either Ni or Co

From figure 53 (a), it is observed that there is a visible detachment between the yellow charge density region around the nickel atom and the blue charge density region around the oxygen atoms (circled in red). This is indicative of the localisation of charges around individual atoms which signifies ionic bonding [229]. However, from figure 53 (b), there is an overlap between the yellow charge density region around the cobalt atom and the blue charge density region around the neighbouring oxygen atoms. In particular, this overlap of the charge density regions is indicative of the covalency, which in turn shows the stability of this bond.

Furthermore, it is observed that the charge density cloud surrounding the cobalt atom in (b) is substantially larger than the charge density cloud surrounding the nickel atom in (a), this shows that the cobalt atom contributes more to the stability and conductivity of this doped nanocluster than the nickel atom. These results reinforce the observations from table 19 in chapter 8 which showed that the dual doped n3-01 nanocluster with Co on the Mn2 atomic position and Ni on the Mn1 atomic position had the better binding energy and shorter band-gap energy. It can thus be concluded that dual doping favours Co doping on the higher coordinated atomic position.

Chapter 10

SUMMARY and CONCLUSIONS

This chapter gives the summary and conclusion of the study. The chapter is arranged as follows: firstly, a recap on the aim and objectives followed by the background on β -MnO₂ systems, then a brief outline on the literature and method (as discussed in chapter 1 to 3). Secondly, the summary and conclusion are given per chapter (chapter 4 to 9). Finally, recommendations for further research are provided based on the key outcomes of this study.

The main aim of the study was to investigate the structural, thermodynamic and electronic properties of the β -MnO₂ bulk structure. Additionally, the study investigated the evolution of the nanoclusters from $n=2-20$. Moreover, the study determined the effect of doping (with Fe, Co and Ni dopants) on the stability and conductivity of the β -MnO₂ nanoclusters. This is important to evaluate the potential use of this materials for future battery development. β -MnO₂ has been used successfully as cathode materials in lithium-ion rechargeable batteries. These systems are mostly used to power everyday items like cell phones, laptops, and other basic home appliances. Furthermore, these rechargeable batteries are capable of powering electricity vehicles and industrial electricity back-up generation units.

The study has used a combination of interatomic potentials (IP) and density functional theory (DFT) approaches to mimic the potential use of β -MnO₂ systems. More importantly, how IP and DFT can be applied to understand the properties of β -MnO₂ nanoclusters.

It was shown that a combination of the Buckingham potential and the 12-6 Lennard-Jones potential was able to predict the β -MnO₂ structural properties in good agreement to previous studies. These Interatomic Potentials were employed within the KLMC software code utilising an evolutionary algorithm (genetic algorithm) to generate a stable set of local minima nanoclusters. The GGA-PBE functional using the PBE regime was used within the DFT framework to optimise the generated nanoclusters to their stable ground state configurations.

In the following sections, a summary of the results per chapters is given.

- **Chapter 4**

The geometry optimisation results were calculated using the planewave pseudopotential CASTEP code. This was achieved by allowing the lattice parameters and cell volumes to relax using the BFGS minimisation method. The minimisation was attained by employing the cut-off energy of 500 eV and an optimal k-point set of 2x2x4 befitting the tetragonal crystal structure of pyrolusite (β -MnO₂) as discussed in chapter 4.

The calculated lattice parameters compared favourably with available experimental data. Moreover, optimisation with DFT was the preferred method for minimising the bulk structure for the purpose of this study. The lattice parameters were in good comparison with literature. An XRD pattern of the simulated β -MnO₂ bulk structure was generated using the Reflex code. The patterns exhibited a strong agreement with earlier experimental results, demonstrating the presence of the stable rutile phase of manganese dioxide. [241].

The effect of temperature fluctuations was also investigated and it was shown that the β -MnO₂ bulk structure was more stable and more compact at lower temperatures. Furthermore, there was a decrease in the band-gap energy which showed that the β -MnO₂ bulk structure was a better electrical conductor at lower temperatures. Additionally, the lattice parameters and bond lengths were shown to increase at higher temperatures.

A decrease in the conductivity of the β -MnO₂ bulk structure was observed as the temperature was increased. This became apparent at higher temperatures, when the density of states curves were greater at the Fermi level and the band-gap energies grew larger. At 600 K and 800 K, phase transitions were observed due to spikes in the energy graphs, alluding to a possible MnO₂ decomposition near the melting region of pyrolusite at 808 K.

The effect of doping the β -MnO₂ bulk structure using the metal impurities Fe, Co and Ni was investigated. The doping showed a preference on the central manganese atom with the higher coordination as compared to the manganese atom at the edge of the bulk structure. The atomistic substitutional method of doping was shown to produce the most stable and compact bulk structure in comparison to the virtual crystal approximation method.

Furthermore, nickel was found to be the most preferable dopant for β -MnO₂. Cobalt also showed some desirable properties, particularly on improving the electrical conductivity as observed by the shorter band-gap energy. This electrical conduction is important because it affects the speed of the charge-discharge cycle of the battery using MnO₂ as a cathode material. Fe doping was not favourable in improving the stability and conductivity of the β -MnO₂ bulk structure.

- **Chapter 5**

Chapter 5 reported on the generation and stabilities of the β -MnO₂ nanoclusters using the evolutionary algorithm sequence in the KLMC code. A subset of plausible stable nanoclusters known as local minimas were created using the same interatomic potentials used for the bulk β -MnO₂ structure. However, because the nanoclusters adhered to a cubic symmetry during DFT calculations, a different k-point separation of 0.20 Å was established.

The binding energy decreased from n=2 to n=20 atoms illustrating improved stability. The stability and complexity of the nanoclusters showed an increase directly proportional with nanocluster size which also correlates positively with previous literature [104]. The band-gap energy increases as the stability of the nanocluster systems declined. These phenomena demonstrates that the smaller band-gap energies are oriented towards the more intact and stable nanoclusters. In particular, this illustrates that conductivity of the nanocluster increases with stability. The stable n3-01 nanocluster is thus a good semi-conductor due to the band-gap energy below the 2-eV limit.

- **Chapter 6**

Chapter 6 investigated the effect of increasing temperatures on the stability of the β -MnO₂ nanoclusters. High temperatures caused a loss of stability, as seen by the atoms' growing bond lengths. Furthermore, some transitions to other phases of MnO₂ were observed as shown by significant spikes occurring near the reported melting point of pyrolusite. Future research will examine the stabilities and polymorphs of these phase transitions in greater depth.

The band-gap energy was calculated, and it was revealed to be the lowest near the pyrolusite melting point. In particular, this indicates that the conductivity was highest at the melting region where pyrolusite was decomposing from solid form to a liquid state. Moreover, transitions to other phases of manganese dioxide described in earlier experiments at comparable temperatures are also linked to this transformation [11, 18].

The Fermi energy results also supported these assertions because the plots were continuous at the Fermi level showing a flow of electrons between the valence band and the conduction band. The bond angle and the bond distance between the two exterior dangling oxygen atoms of the n3-01 nanocluster was shown to decrease from 180° to 147.9° and from 7.856 Å to 7.439 Å respectively, as the temperatures were methodically increased from 100 K to 1500 K.

These findings show that when temperature rose, the nanoclusters contracted in size. This is a very desirable result since it demonstrates that even at high temperatures, the nanoclusters can maintain their structural integrity and compactness better and more steadily than the bulk β -MnO₂ structure.

- **Chapter 7**

X-ray diffraction (XRD) patterns of the three most stable nanoclusters consisting of 3 manganese atoms and 6 oxygen atoms were generated via IP methodologies then optimised and ranked using DFT techniques. The analysis showed that all the three stable nanoclusters were symbolised by a cubic diamond like pattern consisting of two manganese and two dangling oxygen atoms. This particular configuration was shown to be stable in previous studies [12, 115].

The high intensity and similar miller indexes of the distinct peaks demonstrated the presence of rutile as the most dominant phase in the nanoclusters. The (010) and (110) indexed peaks had the highest intensities on the XRD patterns for the doped nanoclusters. Further analysis of the generated XRD patterns indicated the sensitivity of the nanoclusters to their doped composition and size which was proven by the differences in the positioning and height of the intensity peaks.

The n3-01 nanocluster showed a commendable stability and resilience even when temperatures were increased above the melting point. These differences will be investigated further in subsequent papers and it is hoped that they will lead to new and interesting properties improving those observed with the β -MnO₂ bulk structure.

NB: *Note that there are some discrepancies in the XRD patterns which may be due to equipment sensitivity because different versions of the software codes were used throughout the years to carry out the calculations in this study.*

- **Chapter 8**

Chapter 8 focused on the effect of doping on the stability and electronic properties of the MnO₂ nanoclusters. Nickel was shown to produce the most structurally stable doped nanocluster. In particular, doping preferred the central metallic sites which were originally occupied by the manganese atom with the highest coordination, denoted by Mn₂. Furthermore, the Ni-doped n3-01 nanocluster indicated a divergence from an elongated linear atomic configuration towards a more compact circular configuration. This was shown by the angles between the two terminal oxygen atoms decreasing from a linear 180° to 143.46° and a decrease of the bond distance from 7.856 Å to 7.073 Å.

Cobalt produced a lesser stable doped nanocluster which was however a better electrical conductor. Doping with iron at both the selected atomic positions was less stable than doping with cobalt and nickel. This shows that iron doping is the least stabilizer and less compatible with the MnO₂ nanoclusters. It is imperative to declare that the undoped nanoclusters are shown to be more stable than their doped counterparts. However, ideal 100% pure compounds do not occur naturally since all naturally existing materials contain impurities. Hence, the significance of exploring the effect of impurities on the stability of the MnO₂ nanoclusters [18].

- **Chapter 9**

This chapter focused on the charge density differences of the undoped and doped nanoclusters. The electronic charge density difference analysis showed that Ni-doping on the central cation position with a higher level of coordination produced the most stable doped nanocluster. In particular, the Ni-doped nanocluster was smaller and more compact than the pure undoped nanoclusters. Evidently, nickel improves the structural stability and succeeds in creating a smaller more compact MnO₂ nanocluster accomplishing the study's objectives [64, 65, 66].

Interestingly, cobalt has also shown some promise especially when it comes to the conductivity of the nanoclusters hence it should not be totally overlooked [126]. However, the charge density profile of the cobalt-doped nanocluster indicated that the structure had a prominence to ionic bonding which is indicative of some deficiencies in the structural stability of the nanocluster when doped with cobalt at both the Mn1 and Mn2 atomic positions.

The electronic charge density difference profiles displayed an ionic type of bonding when both iron and cobalt were used as the dopant elements. A covalent type of

bonding was observed when nickel was used to dope the n3-01 nanocluster on the tetrahedrally bonded Mn² position. Furthermore, similar charged atoms were shown to be strongly repulsive as indicated by the longer bond lengths between the oxygen atoms which corresponded lower atomic populations.

The charge density difference profile of the nickel-doped nanocluster had the shortest bond lengths and a prominence of covalent bonding. The bond angle between the two terminal oxygen atoms also decreases from a linear 180° to a more compact and spherical 143.5° when nickel was doped on the central Mn² atomic position. Similar observations were reported to be positive in other previous literature [64, 66]. These results further highlight the qualities of nickel. High Mulliken atomic populations readings were observed for both nickel and cobalt bonds with the neighbouring oxygen atoms showing the stability of those bonds.

Thus, it can be stated categorically that nickel is the most suitable dopant for singular doping investigations and for future computational modelling endeavours involving manganese dioxide nanostructures. Dual doping was also explored and the analysis showed that dual doping did not succeed in enhancing the stability and conductivity of the n3-01 nanocluster. The dual doped nanoclusters displayed larger band-gap energies and higher binding energies. It can thus be concluded that dual doping is not successful for the smaller nanoclusters. However, dual doping will be explored for larger nanoclusters in future studies as it was shown to be successful in previous literature.

Recommendations

- Evolutionary algorithms techniques and first principle density functional theory methodologies were shown to be successful in fulfilling the objectives of this study. Hence, they can be employed to predict, generate and investigate the properties of metallic oxide compounds such as pyrolusite. Their continued use is encouraged and championed for future studies.
- Doping has been shown to predominantly prefer cation sites that are centrally located and have a higher coordination due to the higher number of bonds occurring at those sites.
- The major key finding from the doping results is that nickel provided desirable qualities for the type of dopant envisaged for manganese dioxide nanoclusters. It is hoped that other metallic oxides with similar structural properties will show similar positive attributes.

Cobalt also showed some promise due to its favourable electrical conducting properties as it was also shown in previous studies [126]. This quality was observed with the Co-doped nanoclusters having the shortest band-gap energies. Hence, it is recommended that future investigations should attempt the simultaneous dual doping of the larger β -MnO₂ nanostructures with both nickel and cobalt. This is recommended in order to take full advantage of the positive attributes shown by both nickel and cobalt instead of limiting our options to just one dopant.

Furthermore, this dual doping must have a greater concentration of nickel than cobalt, because nickel was shown to be a better dopant overall. It is hoped that the doped complex should create the most stable nanoclusters that can maintain their structural

integrity and stability at different temperatures. Moreover, these dual doped nanoclusters should have a high level of electrical conductivity.

Future studies will explore the doping on larger nanoclusters which should enable the simultaneous doping on different cation sites of preferable coordination levels. Moreover, the effect of increasing nanocluster size will be investigated in greater detail, specifically on the electronic properties i.e., band-gap energy, stability and voltage profiles.

REFERENCES

- [1] Perera F., "Pollution from fossil-fuel combustion is the leading environmental threat to global pediatric health and equity: Solutions exist," *International Journal of Environmental Research and Public Health*, vol. 15, pp. 1-17, 2018.
- [2] Hook M. and Tang X, "Depletion of fossil fuels and anthropogenic climate change – A review," *Energy Policy*, vol. 52, pp. 797-809, 2012.
- [3] Sugantha M., Ramakrishnan P.A., Hermann A.M., Warmsingh C.P. and Ginley D.S., "Nanostructured MnO₂ for Li batteries," *International Journal of Hydrogen Energy*, vol. 28, pp. 597-600, 2003.
- [4] Yamada A., Chung S.C. and Hinokuma K., "Optimized LiFePO₄ for lithium battery cathodes," *Journal of the Electrochemical Society*, vol. 148, pp. 224-226, 2001.
- [5] Omarjee L., "SA still heavily reliant on coal for electricity - report," 05 April 2022. [Online]. Available: <https://www.news24.com/fin24/economy/sa-still-heavily-reliant-on-coal-for-electricity-report-20220405>.

- [6] Lawson B., "Electropaedia, battery and energy technologies," 2005. [Online]. Available: <http://www.mpoweruk.com/primary.htm>. [Accessed 23 February 2022].
- [7] Cho J., "VO_x-coated LiMn₂O₄ nanorod clusters for lithium battery cathode materials," *Journal of Materials Chemistry*, vol. 18, pp. 2257-2261, 2008.
- [8] Languang L., Xuebing, H., Jianqiu L., Jianfeng H. and Minggao O, "A review on the key issues for lithium-ion battery management in electric vehicles," *Journal of Power Sources*, vol. 226, pp. 272-288, 2013.
- [9] Fergus J.W., "Recent developments in cathode materials for lithium ion batteries," *Journal of Power Sources*, vol. 195, pp. 939-954, 2009.
- [10] Hu C.C. and Tsou T.W., "Capacitive and textural characteristics of hydrous manganese oxide prepared by anodic deposition," *Electrochimica Acta*, vol. 47, pp. 3523-3532, 2002.
- [11] Abou-El-Sherbini K.H.S., "Structure investigation and electrochemical behaviour of γ -MnO₂ synthesised from three-dimensional framework and layered structures," *Journal of Solid State Chemistry*, vol. 166, pp. 375-381, 2002.
- [12] Post J.E., "Manganese oxide minerals: Crystal structures, economic and environmental significance," *Proceedings of the National Academy of Sciences of the United States of America*, vol. 96, no. 7, pp. 3447-3454, 1999.

- [13] Harris M., Meyer D. and Auerswald K., "The production of electrolytic manganese in South Africa," *Journal of the South African Institute of Mining and Metallurgy*, vol. 77, pp. 137-142, 1977.
- [14] Palisade Research, "MINING.com," 24 March 2017. [Online]. Available: <http://www.mining.com/web/manganese-the-third-electric-vehicle-metal-no-one-is-talking-about-it-heres-how-to-take-advantage/>. [Accessed 24 February 2022].
- [15] Cannon W.F., Kimball B.E. and Corathers L.A., "Critical mineral resources of the United States-Manganese," Reston Publishing Service Centre, Reston, 2017.
- [16] Tompsett D.A., Parker S.C. and Islam M.S., "Rutile (β -) MnO₂ surfaces and vacancy formation for high electrochemical and catalytic performance," *Journal of the American Chemical Society*, vol. 136, pp. 1418-1426, 2014.
- [17] Benhaddad L., Makhouloufi L., Messaoudi B., Rahmouni K. and Takenouti H., "Reactivity of nanostructured MnO₂ in alkaline medium studied with a microcavity electrode: Effect of oxidizing agent," *Journal of Materials Science and Technology*, vol. 27, pp. 585-593, 2011.
- [18] Kwon K.D., Refson K. and Sposito G, "Ruetschi defects decrease the band gap energy in MnO₂ nanosheets," *Physical Review Letters*, vol. 100, p. 146601, 2008.

- [19] Hu C.C. and Wang C.C., "Nanostructures and capacitive characteristics of hydrous manganese oxide prepared by electrochemical deposition," *Journal of the Electrochemical Society*, vol. 150, pp. 1079-1084, 2003.
- [20] Bromley T.B., "Nanoclusters and nanostructured materials. Computational Materials Science Laboratory," 2006. [Online]. Available: <http://www.ub.edu/cmsl/cmsl/research/nanoclusters-and-nanostructured-materials.html>. [Accessed 8 March 2015].
- [21] Balachandran D., Morgan D. and Ceder G., "First principles study of H-insertion in MnO₂," *Journal of Solid State Chemistry*, vol. 166, pp. 91-103, 2002.
- [22] Hamad S., Catlow C.R.A., Woodley S.M., Lago S. and Mejias J.A., "Structure and stability of small TiO₂ nanoparticle," *The Journal of Physical Chemistry B*, vol. 109, pp. 15741-15748, 2005.
- [23] Sayle T. X. T, Maphanga R.R., Ngoepe P.E. and Sayle D.C., "Predicting the electrochemical properties of MnO₂ nanomaterials used in rechargeable Li batteries: simulating nanostructure at the atomistic level," *Journal of the American Chemical Society*, vol. 131, pp. 6161-6173, 2009.
- [24] Tompsett D.A. and Islam M.S., "Surfaces of rutile MnO₂ are electronically conducting, whereas the bulk material is insulating," *The Journal of Physical Chemistry C*, vol. 118, pp. 25009-25015, 2014.

- [25] Ralph J., "Pyrolusite," 2013. [Online]. Available: <http://www.mindat.org/min-3318.html>. [Accessed 24 February 2022].
- [26] Kresse G. and Furthmuller J., "Efficiency of ab-initio total energy calculations for metals and semiconductors using a plane-wave basis set," *Computational Materials Science*, vol. 6, pp. 15-50, 1996.
- [27] Clark, S.J., Segall, M.D., Pickard, C.J., Hasnip, P.J., Probert, M.I.J., Refson, K. and Payne, M.C., "First principles methods using CASTEP," *Zeitschrift für Kristallographie*, vol. 220, pp. 567-570, 2005.
- [28] Zheng-Jun P., "Evolutionary Algorithm," Tsinghua University Press, Beijing, 1998.
- [29] Holland J.H., "Genetic Algorithm," *Scientific American*, vol. 267, pp. 66-72, 1992.
- [30] Lian-Jun L., "Using evolutionary algorithm to calculate the ground-state energy of double-electron atoms in a uniform magnetic field ($B \leq 109\text{G}$)," *International Journal of Modern Physics C*, vol. 11, pp. 183-194, 2000.
- [31] Zhao J. and Jin R., "Heterogeneous catalysis by gold and gold-based bimetal nanoclusters," *Nano Today*, vol. 18, pp. 86-102, December 2018.
- [32] Liu X. and Astruc D., "Atomically precise copper nanoclusters and their applications," *Coordination Chemistry Reviews*, vol. 359, pp. 112-126, 2018.

- [33] Fahlman B.D, "Materials Chemistry," New York City, Salmon Tower, Springer, 2007, pp. 282-283.
- [34] Wang Z., Zhang G., Zhong Z., Lin Y. and Su Z., "In-situ synthesis of platinum nanoclusters in polyelectrolyte multilayer films," *Thin Solid Films*, vol. 660, pp. 59-64, 2018.
- [35] Said K., Qamhieh N. and Ayesh A.I., "Fabrication and characterization of size-selected Cu nanoclusters using a magnetron sputtering source," *Sensors and Actuators A: Physical*, vol. 277, pp. 112-116, 2018.
- [36] Ayesh A.I., "Size-selected fabrication of alloy nanoclusters by plasma-gas condensation," *Journal of Alloys and Compounds*, vol. 745, pp. 299 - 305, 2018.
- [37] Dagher S., Haik Y., Ayesh A.I. and Tit N., "Synthesis and optical properties of colloidal CuO nanoparticles," *Journal of Luminescence*, vol. 151, pp. 149 - 154, 2014.
- [38] Farrow M.R., Chow Y. and Woodley S.M., "Structure prediction of nanoclusters; a direct or a pre-screened search on the DFT energy landscape?," *Physical Chemistry Chemical Physics*, vol. 16, pp. 21119 - 21134, 2014.
- [39] Kalua A. and Jones J., "Epistemological Framework for Computer Simulations in Building Science Research: Insights from Theory and Practice," *Philosophies*, vol. 5, pp. 1-14, 2020.

- [40] Winsberg E., "Models of success versus the success of models: Reliability without truth," *Synthese*, vol. 152, pp. 1-19, 2006.
- [41] Humpheys P., *Extending Ourselves: Computational Science, Empiricism, and Scientific Method*, Oxford, UK.: Oxford University Press, 2004.
- [42] Baur W.H., "Rutile-Type Compounds. V. Refinement of MnO₂ and MgF₂," *Acta Crystallographica*, vol. 32, pp. 2200 - 2204, 1976.
- [43] Gale J.D. and Rohl A.L., "The General Utility Lattice Program (GULP)," *Molecular Simulation*, vol. 29, pp. 291-341, 2003.
- [44] Schon J.C, Putz H. and Jansen M., "Studying the energy hypersurface of continuous systems - The threshold algorithm.," *Journal of Physics: Condensed Matter*, vol. 8, pp. 143-156, 1996.
- [45] Woodley S.M. and Walker A.M., "New software for finding transition states by probing accessible, or ergodic regions," *Molecular Simulation*, vol. 33, pp. 1229-1231, 2007.
- [46] Zhang H. and Banfield J.F., "Aggregation, coarsening, and phase transformation in ZnS nanoparticles studied by molecular dynamics simulations," *Nano Letters*, vol. 4, pp. 713-718, 2004.
- [47] Kresse G., Marsman M. and Furthmüller J., "VASP the guide," [Online]. Available: <http://cms.mpi.univie.ac.at/vasp/vasp.pdf>. [Accessed 3 March 2015].

- [48] Havu V., Blum V, Havu P. and Scheffler M., "Efficient O(N) integration for all-electron electronic structure calculation using numeric basis functions.," *Journal of Computational Physics*, vol. 228, pp. 8367-8379, 2009.
- [49] Blum V., Gehrke R., Hanke F., Havu P., Havu V., Ren X., Reuter K. and Scheffler M., "ab initio molecular simulations with numeric atom-centered orbitals," *Computer Physics Communications*, vol. 180, no. 11, pp. 2175-2196, 2009.
- [50] Neumann M.A., "X-Cell: a novel indexing algorithm for routine tasks and difficult cases," *Journal of Applied Crystallography*, vol. 36, pp. 356-365, 2003.
- [51] Delley B., "DMol3 DFT studies: from molecules and molecular," *Computational Materials Science*, vol. 17, pp. 122-126, 2000.
- [52] Azam S., Abbas Z., Bilal Q., Irfan M., Khan M.A., Naqib S.H., Khenata R., Muhammad S., Algarni H., Al-Seheni A.G. and Wang X., "Effect of Fe doping on optoelectronic properties of CdS nanostructure: Insights from DFT calculations," *Physica B: Physics of Condensed Matter*, vol. 583, pp. 1-8, 2020.
- [53] Wen S., Yang T., Zhao N., Ma L. and Liu E., "Ni-Co-Mo-O nanosheets decorated with NiCo nanoparticles as advanced electrocatalysts for highly efficient hydrogen evolution," *Applied Catalysis B: Environmental*, vol. 258, pp. 1-7, 2019.

- [54] Dou R., Cheng H., Ma J. and Komarneni S., "Manganese doped magnetic cobalt ferrite nanoparticles for dye degradation via a novel heterogenous chemical catalysis," *Materials Chemistry and Physics*, vol. 240, pp. 1-9, 2020.
- [55] Phan H.T. and Haes A.J., "What does nanoparticle stability mean?," *The Journal of Physical Chemistry C: Nanomaterials Interfaces*, vol. 123, pp. 16495-16507, 2019.
- [56] Lee S., Jeong S. and Cho J., "Spinel $\text{LiCo}_0.7\text{Mn}_{1.3}\text{O}_4$ nanowire clusters as electrode materials," *ChemSusChem*, vol. 3, pp. 1260-1263, 2010.
- [57] Subramanian V., Zhu H.W., Vajtai R., Ajayan P.M. and Wei B.Q., "Hydrothermal synthesis and pseudocapacitance properties of MnO_2 nanostructures," *The Journal of Physical Chemistry B*, vol. 109, pp. 20207-20214, 2005.
- [58] Zhang H, Cao G.P., Wang Z.Y., Yang Y.S., Shi Z.J. and Gu Z.N., "Growth of manganese oxide nanoflowers on vertically-aligned carbon nanotube arrays for high-rate electrochemical capacitive energy storage," *Nano Letters*, vol. 8, pp. 2664-2668, 2008.
- [59] Andreatti R., Insola A., Caprio V., Marotta R. and Tufano V., "The use of manganese dioxides a heterogenous catalyst for oxalic acid ozonation in aqueous solution," *Applied Catalysis A*, vol. 138, pp. 75-81, 1996.

- [60] Jiao F. and Bruce P.G., "Mesoporous crystalline β -MnO₂ – A reversible positive electrode for rechargeable lithium batteries," *Advanced Materials*, vol. 19, pp. 657-660, 2007.
- [61] Sharma M.M., Krishnan B., Zachariah S. and Shah C.U., "Study to enhance the electrochemical activity of manganese dioxide by doping technique," *Journal of Power Sources*, vol. 79, pp. 69-74, 1999.
- [62] Lee C. and Aikens C.M., "Effects of Mn doping on (TiO₂)_n (n=2-5) complexes," *Computational and Theoretical Chemistry*, Vols. 1-13, pp. 32-45, 2013.
- [63] Sharma M. and Jeevanandam P., "Magnesium doping in hierarchical ZnO nanostructures and studies on optical properties," *Superlattices and Microstructures*, vol. 52, pp. 1083-1092, 2012.
- [64] Shan X., Guo F., Page K., Neufeind J.C., Ravel B., Abeykoon A.M.M., Kwon G., Olds D., Su D. and Teng X., "Framework doping of Ni enhances pseudocapacitive Na-ion storage of (Ni)MnO₂ layered birnessite," *Chemistry of Materials*, vol. 31, pp. 8774-8786, 2019.
- [65] Kim B.C., Raj C.J., Cho W., Lee W., Jeong H.T. and Yu K.H., "Enhanced electrochemical properties of cobalt doped manganese dioxide nanowires," *Journal of Alloys and Compounds*, vol. 617, pp. 491-497, 2014.

- [66] Marincas A. and Ilea P., "Enhancing lithium manganese oxide electrochemical behavior by doping and surface modifications," *Coatings*, vol. 11, pp. 1-32, 2021.
- [67] Thackeray M.M, Johnson C.S., Vaughey J.T., Li N. and Hackney S.A, "Advances in Manganese-Oxide "Composite" Electrodes for Lithium-Ion Batteries," *Journal of Materials Chemistry*, vol. 15, pp. 2257-2267, 2005.
- [68] Wang S., Mao M., Cao Y., Luo H., Wang H. and Guo D., "Novel cuboid-like cobalt nickel phosphate/manganese dioxide/multi-walled carbon nanotubes composites as binder-free electrodes for high-performance supercapacitors," *Inorganic Chemistry Communications*, vol. 114, pp. 1-9, 2020.
- [69] Adelkhani H., Ghaemi M. and Jafari S.M., "Novel nanostructured MnO₂ prepared by pulse electrodeposition: characterization and electrokinetics," *Journal of Materials Science and Technology*, vol. 25, pp. 857-862, 2008.
- [70] Yuan J.K., Li W.N., Gomez S. and Suib S.L., "Shape-controlled synthesis of manganese oxide octahedral molecular sieve three-dimensional nanostructures," *Journal of the American Chemical Society*, vol. 127, pp. 14184-14185, 2005.
- [71] Zhong X.H., Xie R.G., Sun L.T., Lieberwirth I. and Knoll W., "Synthesis of dumbbell-shaped manganese oxide nanocrystals," *The Journal of Physical Chemistry B*, vol. 110, pp. 2-4, 2006.

- [72] Li-Chun Z., Zong-Huai L., Hao L., Xiuhua T. and Kenta O., "Shape controllable synthesis and electrochemical properties of nanostructured manganese oxides," *The Journal of Physical Chemistry C*, vol. 111, pp. 8418-8423, 2007.
- [73] Wu M.S., Chiang P.C.J., Lee J.T. and Lin J.C., "Synthesis of manganese oxide electrodes with interconnected nanowire structure as an anode material for rechargeable lithium ion batteries," *The Journal of Physical Chemistry B*, vol. 109, pp. 23279-23284, 2005.
- [74] Cheng F.Y., Chen J., Gou X.L. and Shen P.W., "High-power alkaline Zn-MnO₂ batteries using gamma-MnO₂ nanowires/nanotubes and electrolytic zinc powder," *Advanced Materials*, vol. 17, no. 22, p. 2753, 2005.
- [75] Oaki Y. and Imai H., "One-pot synthesis of manganese oxide nanosheets in aqueous solution: Chelation-mediated parallel control of reaction and morphology," *Angewandte Chemie International Edition*, vol. 46, pp. 4951-4955, 2007.
- [76] Cheng F., Zhao J., Song W., Li C., Ma H., Chen J. and Shen P., "Facile controlled synthesis of MnO₂ nanostructures of novel shape and their application in batteries," *Inorganic Chemistry*, vol. 45, pp. 2038-2044, 2006.
- [77] Mathew V., Lim J., Kang J., Gim J., Rai A.K. and Kim J., "Self-assembled mesoporous manganese oxide with high surface area by ambient

- temperature synthesis and its enhanced electrochemical properties," *Electrochemistry Communications*, vol. 13, pp. 730-733, 2011.
- [78] Lee S., Choi B., Hamasuna N., Fushimi C. and Tsutsumi A., "Characterization of MnO₂ positive electrode for fuel cell/battery (FCB)," *Journal of Power Sources*, vol. 181, pp. 177-181, 2008.
- [79] Corpuz R. Juan-Corpuz L.M.Z. and Kheawhom S., "Manganese dioxide (MnO₂): A high-performance energy material for electrochemical energy storage applications," in *Metal and Metal oxides for energy and electronics*, New York City, Springer, 2020, pp. 91-119.
- [80] Snyder H., "Literature review as a research methodology: An overview and guidelines," *Journal of Business Research*, vol. 104, pp. 333-339, 2019.
- [81] Bonila L.E., "Archimedes archives. Alessandro Volta – Inventor of the battery," 27 February 2010. [Online]. Available: https://appel.nasa.gov/2010/02/27/ao_1-15_f_volta-html/. [Accessed 24 February 2022].
- [82] "Classification of Cells or Batteries," [Online]. Available: <http://depts.washington.edu/matseed/batteries/MSE/classification.html>. [Accessed 22 February 2022].
- [83] Dell R.M., "Batteries: fifty years of materials development," *Solid State Ionics*, vol. 134, pp. 139 - 158, 2000.

- [84] " American Institute of Physics," 2013. [Online]. Available: <http://www.rdmag.com/news/2013/11/enhancing-lithium-ion-battery-performance>. [Accessed 27 February 2014].
- [85] Armstrong A.R. and Bruce P.G., "Synthesis of layered LiMnO₂ as an electrode for rechargeable lithium batteries," *Nature*, vol. 381, pp. 499-500, 1996.
- [86] Hosono E., Kudo T., Honma I., Matsuda H. and Zhou H.S., "Synthesis of single crystalline spinel LiMn₂O₄ nanowires for a Lithium ion battery with high power density," *Nano Letters*, vol. 9, pp. 1045-1051, 2009.
- [87] Li J., Feng X., Nie Y., Chen S., Shi F., Xiong K., Ding W., Xueqiang Q., Hu J., Wei Z., Wan L and Xia M., "Insight into the effect of oxygen vacancy concentration on the catalytic performance of MnO₂," *ACS Catalysis*, vol. 5, pp. 4825-5832, 2015.
- [88] Karami H., Ramandi-Ghamoshi M., Moeini S. and Salehi F., "Low temperature hydrothermal synthesis of MnO₂ nanoclusters as positive material of RAM batteries," *Journal of Cluster Science*, vol. 21, no. 1, pp. 21-34, 2010.
- [89] Bruce P.G., Scrosati B. and Tarascon J., "Nanomaterials for rechargeable lithium batteries," *Angewandte Chemie International Edition*, vol. 47, pp. 2930-2946, 2008.

- [90] Tang W., Yang X., Liu Z. and Ooi K., "Preparation of β -MnO₂ nanocrystal/acetylene black composites for lithium batteries," *Journal of Materials Chemistry*, vol. 13, pp. 2989-2995, 2013.
- [91] Bach S., Pereira-Ramos J.P. and Willmann P.A., "Kinetic study of electrochemical lithium insertion in nanosized rutile β -MnO₂ by impedance spectroscopy," *Electrochimica Acta*, vol. 56, pp. 10016-10022, 2011.
- [92] Li S.M., Wang S.Y., Yang S.Y., Liu C.H., Chang K.H., Tien H.W., Wen N.T., Ma C.C.M. and Hu C.C., "Electrochemical deposition of nanostructured manganese oxide on hierarchically porous graphene carbon nanotube structure for ultrahigh-performance electrochemical capacitors," *Journal of Power Sources*, vol. 225, pp. 347-355, 2013.
- [93] Arico A.S., Bruce P.G., Scrosati B., Tarascon J.M. and Schalkwijk W.V., "Nanostructured materials for advanced energy conversion and storage devices," *Nature Materials*, vol. 4, pp. 366-377, 2005.
- [94] Yang Z.G., Choi D., Kerisit S., Rosso K.M., Wang D.H., Zhang J., Graff G. and Liu J., "Nanostructures and lithium electrochemical reactivity of lithium titanites and titanium oxides: A review," *Journal of Power Sources*, vol. 192, pp. 588-598, 2009.
- [95] Wang D.H., Choi D.W., Li J., Yang Z.G., Nie Z.M., Kou R., Hu D.H., Wang C.M., Saraf L.V., Zhang J.G., Aksay I.A. and Liu J., "Self-assembled TiO₂-graphene hybrid nanostructures for enhanced Li-Ion insertion," *ACS Nano*, vol. 3, pp. 907-914, 2009.

- [96] Huang S., Kavan L., Exnar I. and Grätzel M., "Rocking Chair lithium battery based on nanocrystalline TiO₂ (anatase)," *Journal of the Electrochemical Society*, vol. 142, pp. L142-L144, 1995.
- [97] Kavan L., Rathousky J., Grätzel M., Shklover V. and Zukal A., "Surfactant-templated TiO₂ (anatase): Characteristic features of lithium insertion electrochemistry in organized nanostructures," *The Journal of Physical Chemistry B*, vol. 104, pp. 12012-12020, 2002.
- [98] Feist T.P. and Davies P.K., "The soft chemical synthesis of TiO₂(B) form layered titanates," *Journal of Solid State Chemistry*, vol. 101, pp. 275-295, 1992.
- [99] Armstrong G., Armstrong A.R., Canales P.G. and Bruce P.G., "Lithium-ion intercalation into TiO₂-B nanowires," *Advanced Materials*, vol. 17, pp. 862-865, 2005.
- [100] Beuvier T., Richard-Plouet M., Mancini-Le Granvalet M., Brousse T, Crosnier O. and Brohan L., "TiO₂(B) nanoribbons as negative electrode material for lithium ion batteries with high rate performance," *Inorganic Chemistry*, vol. 49, pp. 8457-8464, 2010.
- [101] Moriguchi I., Hidaka R., Yamada H., Kudo T., Murakami H. and Nakashima N., "A mesoporous nanocomposite of TiO₂ and carbon nanotubes as a high-rate Li-intercalation electrode material," *Advanced Materials*, vol. 18, pp. 69-73, 2006.

- [102] Kubiak P., Geserick J., Hüsing N. and Wohlfahrt-Mehrens M., "Electrochemical performance of mesoporous TiO₂ anatase," *Journal of Power Sources*, vol. 175, pp. 510-516, 2007.
- [103] Park J., Belharouak I., Lee Y.J., Sun Y., "A carbon-free ruthenium oxide/mesoporous titanium dioxide electrode for lithium-oxygen batteries," *Journal of Power Sources*, vol. 295, pp. 299-304, 2015.
- [104] Pan J., Shen H. and Mathur S., "One-dimensional SnO₂ nanostructures: Synthesis and applications.," *Journal of Nanotechnology*, vol. 2012, pp. 1-12, 2012.
- [105] Chibisov A.N. and Chibisova M.A., "First-principle calculations of the structural and elastic properties of titanium nanowires," *Materials letters*, no. 141, pp. 333-335, 29 November 2014.
- [106] Lang X., Hirata A., Fujita T. and Chen M., "Nanoporous metal/oxide hybrid electrodes for electrochemical supercapacitors," *Nature Nanotechnology*, vol. 6, pp. 232-236, 2011.
- [107] Qiu G., Huang H., Dharmarathna S., Benbow E., Stafford L. and Suib S.L., "Hydrothermal synthesis of manganese oxide nanomaterials and their catalytic and electrochemical properties," *Chemistry of Materials*, vol. 23, pp. 3890-3901, 2011.

- [108] Kaluabarme R.S., Cho M.S., Yun K.S., Kim T.S. and Park C.J., "Catalytic characteristics of MnO₂ nanostructures for the O₂ reduction process," *Nanotechnology*, vol. 22, pp. 1-6, 2011.
- [109] Tang Y., Zheng S., Xu Y., Xiao X., Xue H. and Pang H., "Advanced batteries based on manganese dioxide and its composites," *Energy Storage Materials*, vol. 12, pp. 284-309, 2018.
- [110] Devaraj S. and Munichandraiah N., "Effect of crystallographic structure of MnO₂ on its electrochemical capacitance properties," *Journal of Physical Chemistry C*, vol. 112, pp. 4406-4417, 2008.
- [111] Zang J. and Li X., "in situ synthesis of ultrafine β -MnO₂/polypyrrole nanorod composites for high-performance supercapacitors," *J. Mater. Chem.*, vol. 21, pp. 10965-10969, 2011.
- [112] Kong F., Longo C., Zhang H., Liang H., Zheng Y. and Cho K., "Charge-transfer modified embedded-atom method for manganese oxides: Nanostructuring effects on MnO₂ nanorods," *Computational Materials Science*, vol. 121, pp. 191-203, 2016.
- [113] Catlow C.R.A., Bromley S.T., Hamad S., Mora-Fonz M., Sokol A.A. and Woodley S.M., "Modelling nano-clusters and nucleation," *Physical Chemistry Chemical Physics*, vol. 12, pp. 786-811, 2010.

- [114] Iwaszuk A., Mulheran P.A. and Nolan M., "TiO₂ nanocluster modified-rutile TiO₂ photocatalyst: a first principles investigation," *Journal of Materials Chemistry*, vol. 1A, pp. 2515 - 2525, 2013.
- [115] Nagarajan V., Saravanakannan V., Chandiramouli R., "Quantum chemical insights on structural and electronic properties of anionic, cationic and neutral ZrO₂ nanostructures," *International Journal of ChemTech Research*, vol. 6, pp. 2962-2970, 2014.
- [116] Gould A.L., Heard C.J. Logsdail A.J. and Catlow C.R.A., "Segregation effects on the properties of (AuAg)₁₄₇," *Physical Chemistry Chemical Physics*, vol. 16, pp. 21049-21061, 2014.
- [117] Rodriguez-Kessler P.L. and Rodriguez-Dominguez A.R., "Structures and electronic properties of TinV(n=1-16) clusters: First-principles calculations," *The Journal of Physical Chemistry A*, vol. 120, pp. 2401 - 2407, 2016.
- [118] Meng-Hsiung W., Chuan C. and Shin-Pon J., "A first-frinciple study on size-dependent thermodynamic properties of small TiO₂ nanoclusters," *Chinese Journal of Catalysis*, vol. 30, pp. 384 - 390, 2009.
- [119] Akbarzadeh H. and Abbaspour M., "Effect of pressure on some properties of Ag@Pd and Pd@Ag nanoclusters," *Jornal of Alloys and Compounds*, vol. 703, pp. 174 - 179, 30 January 2017.
- [120] Escher S.G.E.T., Lazauskas T., Zwijnenburg M.A. and Woodley S.M., "Structure prediction of (BaO)_n nanoclusters for n<24 using an evolutionary

- algorithm," *Computational and Theoretical Chemistry*, vol. 1107, pp. 74 - 81, 12 January 2017.
- [121] Lazauskas T., Sokol A.A., Buckeridge J., Catlow C.R.A, Escher S.G.E.T., Farrow M.R., Mora-Fonz D., Blum V.W., Phaahla T.M., Chauke H.R., Ngoepe P.E. and Woodley S.M., "Thermodynamically accessible titanium clusters," *Physical Chemistry Chemical Physics*, vol. 20, pp. 13962-13973, 2018.
- [122] Vilas Boas N., Batista Souza Junior J., Varanda L.C., Machado S.A.S. and Calegari M.L., "Bismuth and cerium doped cryptomelane-type manganese dioxide nanorods as bifunctional catalysts for rechargeable alkaline metal-air batteries," *Applied Catalysis B: Environmental*, vol. 118014, pp. 1-12, 2019.
- [123] Shalini S., Kumar T.S., Prasanna S. and Balasundaraprabhu R., "Investigations on the effect of co-doping in enhancing the performance of nanostructured TiO₂ based DSSC sensitized using extracts of Hibiscus Sabdariffa," *Optik - International Journal for Light and Electron Optics*, vol. 212, pp. 1-9, 2020.
- [124] Rudra K. and Prajapati Y.K., "Effect of Mn doping on defect-related photoluminescence and nanostructure of dense 3-D nano-root network of ZnO.," *Ceramics International*, vol. 46, pp. 10135-10141, 2020.

- [125] Liu F., Cao R., Rong S. and Zhang P., "Tungsten doped manganese dioxide for efficient removal of gaseous formaldehyde at ambient temperatures," *Materials and Design*, vol. 149, pp. 165-172, 2018.
- [126] Jadhav S.M., Kalubarme R.S., Suzuki N., Terashima C., Mun J., Kale B.B., Gosavi S.W. and Fujishima A., "Cobalt-Doped Manganese Dioxide Hierarchical Nanostructures for Enhancing Pseudocapacitive Properties," *ACS Omega*, vol. 6, pp. 5717-5729, 2021.
- [127] Shirako Y., Wang X., Tsujimoto Y., Tanaka K. Guo Y., Kojitani H. Yamaura K., Inaguma Y. and Akaogi M., "Synthesis, Crystal Structure, and Electronic Properties of High-Pressure PdF₂-Type Oxides MO₂ (M = Ru, Rh, Os, Ir, Pt)," *Inorganic Chemistry*, vol. 53, pp. 11616-11625, 2014.
- [128] Jassem E.K., Majeed A.M.A. and Umran N.M., "The effect of temperature on structural and optical properties of manganese oxide nanoparticles," in *First International Scientific conference Al-Ayen University, Al Nasiriya*, 2019.
- [129] Krawczuk A. and Macchi P., "Charge density analysis for crystal engineering," *Chemistry Central Journal*, vol. 8, no. 68, pp. 1-15, 2014.
- [130] Bultinick P., Alsenoy v. C., Ayers P. W. and Carbo-Dorca R., "Critical analysis and extension of the Hirshfeld atoms in molecules," *Journal of Chemical Physics*, vol. 126, pp. 1144111-1 - 144111-9, 2007.

- [131] Piela L., "Mulliken Population Analysis," in *Ideas of Quantum Chemistry*, Amsterdam, Elsevier, 2013, pp. e143-e147.
- [132] Peresypkina E.V. and Blatov V.A., "Topology of molecular packings in organic crystals," *Acta Crystallographica B*, vol. 56, pp. 1035-1045, 2000.
- [133] Ngoepe P.E., R.R. Maphanga and Sayle D.C., "Toward the nanoscale," in *Computational Approaches to Energy Materials*, John Wiley and Sons LTD, 2013.
- [134] Maphanga R. R., Ngoepe P. E., Catlow C. R. A. and Woodley S. M., "Structure prediction of manganese dioxide nanoclusters using computer simulation techniques. South African Institute of Physics (SAIP) Conference Proceedings," in *J. Phys.*, Port Elizabeth, 2015.
- [135] Iqbal M.A., Ashraf N., Shahid W. Afzal D., Idrees F. and Ahmad R., "Fundamentals of Density Functional Theory: Recent Developments, Challenges and Future Horizons," in *Density Functional Theory - Recent Advances, New Perspectives and Applications*, London, Intechopen, 2021.
- [136] Hine N.D.M., "Linear-scaling density functional theory using the projector augmented wave method," *Journal of Physics: Condensed Matter*, vol. 29, pp. 1-10, 2016.
- [137] Battle P.D., Gale J.D. and Catlow C.R.A., Woodley S.M., "Prediction of inorganic crystal framework structures, Part 1: Using a genetic algorithm

- and an indirect approach to exclusion zones," *Physical Chemistry Chemical Physics*, vol. 6, pp. 1815-1822, 2004.
- [138] Woodley S.M., Battle P.D., Gale J.D. and Catlow C.R.A., "The prediction of inorganic crystal structures using a genetic algorithm and energy minimisation," *Physical Chemistry Chemical Physics*, vol. 1, pp. 2535-2542, 1999.
- [139] Woodley S.M., Hamad S. and Catlow C.R.A., "Exploration of multiple energy landscapes for zirconia clusters," *Phys. Chem. Chem. Phys.* , vol. 12, pp. 8454-8465, 2010.
- [140] Walsh A. and Woodley S.M., "Evolutionary structure prediction and electronic properties of indium oxide nanoclusters," *Physical Chemistry Chemical Physics*, vol. 12, pp. 8446-8453, 2010.
- [141] Gale J.D., "Faraday Transactions, GULP: A computer program for the symmetry-adapted simulation of solids," *Journal of the Chemical Society*, vol. 93, pp. 629-637, 1997.
- [142] Coley D.A., *An Introduction to Genetic Algorithms for scientists and engineers*, London: World Scientific Publishing, 1999.
- [143] Woodley S.M., "Prediction of crystal structures using evolutionary algorithms and related techniques," *Structure and Bonding*, vol. 110, pp. 95 - 132, 2004.

- [144] Al-Sunaidi A., Sokol A., Catlow C.R.A. and Woodley S.M., "Structures of zinc oxide nanoclusters: As found by revolutionary algorithm techniques," *Journal of the Chemical Society C*, vol. 112, pp. 18860-18875, 2008.
- [145] Gale J.D., Catlow C.R.A. and Mackrodt W.C., "Periodic ab initio determination of interatomic potentials for alumina," *Modelling and Simulation in Materials Science and Engineering*, vol. 1, pp. 73-81, 1992.
- [146] Born M. and Huang K., *Dynamical Theory of Crystal Lattices*, London: Oxford University Press, 1954.
- [147] Gibbs J.W., *The collected works, Thermodynamics*, New York: Longman & Green, 1928.
- [148] Flikkema E. and Bromley S.T., "A new interatomic potential for nanoscale silica," *Chemical Physics Letters*, vol. 378, pp. 622-629, 2003.
- [149] Cichocki B., Felderhof B.U. and Hinsen K., "Electrostatic interactions in periodic Coulomb and dipolar systems," *Physical Review A*, vol. 39, pp. 5350-5358, 1989.
- [150] Pollock E.L. and Glosli J., "Comments on P 3M, FMM, and the Ewald method for large periodic Coulombic systems," *Computer Physics Communications*, vol. 95, no. 2, pp. 93-110, 1996.
- [151] Dick A.W. and Overhauser B.G., "Theory of dielectric constants of alkali halide crystals," *Physical Review*, vol. 112, pp. 90-103, 1958.

- [152] Lennard-Jones Potential, "CHEMISTRY LibreTexts," 15 August 2020. [Online]. Available: [https://chem.libretexts.org/Bookshelves/Physical_and_Theoretical_Chemistry_Textbook_Maps/Supplemental_Modules_\(Physical_and_Theoretical_Chemistry\)/Physical_Properties_of_Matter/Atomic_and_Molecular_Properties/Intermolecular_Forces/Specific_Interactions/Le](https://chem.libretexts.org/Bookshelves/Physical_and_Theoretical_Chemistry_Textbook_Maps/Supplemental_Modules_(Physical_and_Theoretical_Chemistry)/Physical_Properties_of_Matter/Atomic_and_Molecular_Properties/Intermolecular_Forces/Specific_Interactions/Le). [Accessed 23 February 2022].
- [153] Huang S., Mainardi D.S. and Balbuena P.B., "Structure and dynamics of graphite-supported bimetallic nanoclusters," *Surface Science*, vol. 545, pp. 163-179, 2003.
- [154] Mausbach P., Fingerhut R. and Vrabec J., "Structure and dynamics of the Lennard-Jones fcc-solid focusing on melting precursors," *Journal of Chemical Physics*, vol. 153, p. 104506, 2020.
- [155] Wang X., Ramirez-Hinestrosa S., Dobnkar J. and Frenkel D., "The Lennard-Jones potential: when (not) to use it," *Physical Chemistry Chemical Physics*, vol. 22, pp. 10624-10633, 2020.
- [156] Lim T., "Alignment of Buckingham parameters to generalized Lennard-Jones potential functions," *Zeitschrift für Naturforschung A*, vol. 64, pp. 200-204, 2009.
- [157] Raghvender, Bouzid A., Hamani D., Thomas P. and Masson O., "A Buckingham interatomic potential for thallium oxide (Ti₂O): Application to

- the case of thallium tellurite glasses," *Computational Materials Science*, vol. 201, p. 110891, 2022.
- [158] White D.N.J., "A computationally efficient alternative to the Buckingham potential for molecular mechanics calculations," *Journal of Computer-Aided Molecular Design*, vol. 11, pp. 517-521, 1997.
- [159] Buckingham R.A., "The classical equation of state of gaseous helium, neon and argon," *Proceedings of the Royal Society*, vol. 168, pp. 264-283, 1938.
- [160] Toure A.B.R., Mele E. and Christie J.K., "Atomic-scale clustering inhibits the bioactivity of fluoridated phosphate glasses," *Biomedical Glasses*, vol. 5, pp. 76-84, 2019.
- [161] Matsui A. and Akaogi M., "Molecular dynamics simulation of the structural and physical properties of the four polymorphs of TiO₂," *Molecular Simulation*, vol. 6, pp. 239-244, 1991.
- [162] Ammundsen B., Islam M.S., Jones D.J. and Rozière J., "Local structure and defect chemistry of substituted lithium manganate spinels: X-ray absorption and computer simulation studies," *Journal of Power Sources*, Vols. 81-82, pp. 500-504, 1999.
- [163] Maphanga R.R., Parker S.C. and Ngoepe P.E., "Atomistic simulation of the surface structure of electrolytic manganese dioxide," *Surface Science*, vol. 603, pp. 3184-3190, 2009.

- [164] Sayle T.X.T., Catlow C.R.A., Maphanga R.R., Ngoepe P.E. and Sayle D.C., "Modelling MnO₂ nanoparticles using simulated amorphisation and recrystallisation," *Journal of the American Chemical Society*, vol. 127, no. 37, pp. 12828-12837, 2005.
- [165] Hohenberg P. and Kohn W., "Inhomogeneous electron gas," *Physical Review*, vol. 136, pp. 864-871, 1964.
- [166] Kohn W. and Sham L.J., "Self-consistent equations including exchange and correlation effects," *Physical Review*, vol. 140, pp. 1133-1138, 1965.
- [167] Wolfenstine J., Lee U., Poesch B. and Allen J.L., "Effect of oxygen partial pressure on the discharge capacity of LiCoPO₄," *Journal of Power Sources*, vol. 144, pp. 226-230, 2005.
- [168] Payne M.C., Teter M.P., Allan D.C., Arias T.A. and Joannopoulos J.D., "Iterative-minimization techniques for ab initio total energy calculations: Molecular dynamics and conjugate gradients," *Reviews of Modern Physics*, vol. 64, pp. 1045-1097, 1992.
- [169] Vignale R.G., "DFT in magnetic fields," *Physical Review Letters*, vol. 59, pp. 2360-2363, 1979.
- [170] Roundy D., "Density Functional Theory - The plane wave pseudopotential method," 10 October 2005. [Online]. Available: https://itp.tugraz.at/LV/ewald/TFKP/Literatur_Pseudopotentiale/Roundy_05_DFT+PPsumm.pdf. [Accessed 23 February 2022].

- [171] Ceperley D.M. and Alder B.J., "Ground state of the electron gas by a stochastic method," *Physical Review Letters*, vol. 45, pp. 566-569, 1980.
- [172] Becke A.D., "Density-functional exchange-energy approximation with correct asymptotic behavior," *Physical Review A*, vol. 38, pp. 3098-3100, 1988.
- [173] Karasiev V.V., Sjoström T. and Trickey S.B., "Generalized-gradient-approximation noninteracting free-energy functionals for orbital-free density functional calculations," *Physical Review B*, vol. 86, pp. 115101-1151011, 2012.
- [174] Perdew J.P., "Density-functional approximation for the correlation energy of the inhomogeneous electron gas," *Physical Review B*, vol. 33, pp. 8822-8824, 1986.
- [175] Perdew J.P. and Wang Y., "Accurate and simple density functional for the electronic exchange energy: Generalized gradient approximation," *Physical Review B*, vol. 40, pp. 8800-8803, 1989.
- [176] Andzelm J. and Wimmer E., "Density functional Gaussian-type-orbital approach to molecular geometries, vibrations, and reaction energies," *Journal of Chemical Physics*, vol. 96, no. 2, p. 1280, 1992.
- [177] Perdew J.P., Burke K. and Ernzerhof M., "Generalized Gradient Approximation made simple," *Physical Review Letters*, vol. 77, pp. 3865-3868, 1996.

- [178] Tao J., Perdew J.P., Staroverov V.N. and Scuseria G.E., "Climbing the density functional ladder: nonempirical meta-generalized gradient approximation designed for molecules and solids," *Physical Review Letters*, vol. 91, pp. 146401-146405, 2003.
- [179] Mattsson A.E., Schultz P.A., Desjarlais M.P., Mattsson T.R. and Leung K., "Designing meaningful density functional theory calculations in materials science - a primer," *Modelling and Simulation in Materials Science and Engineering*, vol. 13, pp. 1-31, 2005.
- [180] Phillips J.C., "Energy-Band interpolation scheme based on a pseudopotential," *Physical Review*, vol. 112, no. 3, pp. 685-695, 1958.
- [181] Bockstedte M., Kley A., Neugebauer J. and Scheffler M., "Density-functional theory calculations for poly-atomic systems: electronic structure, static and elastic properties and ab initio molecular dynamics," *Computer Physics Communications*, vol. 107, no. 1-3, pp. 187-222, 1997.
- [182] Yin M.T. and Cohen M.L., "Theory of ab initio pseudopotential calculations," *Physical Review B*, vol. 25, no. 12, pp. 7403-7412, 1982.
- [183] Francis G.P. and Payne M.C., "Finite basis set corrections to total energy pseudopotential calculations," *Journal of Physics: Condensed Matter*, vol. 2, pp. 4395-4404, 1990.

- [184] Chelikowsky J.R., "The pseudopotential-density functional method applied to nanostructures," *Journal of Physics D: Applied Physics*, vol. 33, no. 8, pp. 33-50, 2000.
- [185] Catlow C.R.A., "Energy minimization techniques in materials modelling," in *Handbook of materials modelling*, New York City, Springer, 2005, pp. 547-564.
- [186] Shirley E.L., Allan D.C., Martins R.M. and Joannopoulos J.D., "Extended norm-conserving pseudopotentials," *Physical Review B*, vol. 40, no. 6, pp. 3652-3660, 1989.
- [187] Blochl P.E., "Projector Augmented-Wave Method," *Physical Review B*, vol. 50, no. 24, pp. 17953-17979, 1994.
- [188] Kresse G. and Joubert D., "From ultrasoft pseudopotentials to the projector augmented-wave method," *Physical Review B*, vol. 59, no. 3, pp. 1758-1775, 1999.
- [189] Blochl P.E., Forst C.J. and Schimpl J., "Projector augmented wave method: ab initio molecular dynamics with full wave functions," *Bulletin of Materials Science*, vol. 26, no. 1, pp. 33-41, 2003.
- [190] Blanc X., Cancès E. and Dupuy M.S., "Variational projector augmented-wavemethod: theoretical analysis and preliminary numerical results," *Numerische Mathematik*, vol. 144, pp. 271-321, 2020.

- [191] Monkhorst H.J. and Park J.D., "Special points for Brillouin-zone Integrations," *Physical Review B*, vol. 13, pp. 5188-5192, 1976.
- [192] Johansen L.G., "Energy bands in semiconductors," [Online]. Available: <http://web.ift.uib.no/AMOS/PHYS208/larsP-N/p-n-slide-lars.pdf>. [Accessed 29 June 2016].
- [193] Singleton J., *Band Theory and Electronic Properties of Solids*, New York: Oxford University Press, 2001.
- [194] "Band Gaps," 21 October 2020. [Online]. Available: [https://eng.libretexts.org/Bookshelves/Materials_Science/Supplemental_Modules_\(Materials_Science\)/Solar_Basics/C._Semiconductors_and_Solar_Interactions/I._Basic_Properties_of_Semiconductors/3._Band_Gaps](https://eng.libretexts.org/Bookshelves/Materials_Science/Supplemental_Modules_(Materials_Science)/Solar_Basics/C._Semiconductors_and_Solar_Interactions/I._Basic_Properties_of_Semiconductors/3._Band_Gaps). [Accessed 25 February 2022].
- [195] Hofmann P., *Solid State Physics: An Introduction*, New Jersey: Wiley-VCH, 2015.
- [196] Chattopadhyay D. and Rakshit P.C, *Basic Electronics*, New Delhi: New Age International (Pty) Ltd, 2002.
- [197] "Fermi Energy Levels," 21 October 2020. [Online]. Available: <https://eng.libretexts.org/@go/page/5952>. [Accessed 25 February 2022].
- [198] Cardona M., "Optical Properties and Electronic Density of States," *Journal of Research of the National Bureau of Standards-A. Physics and Chemistry*, vol. 74A, no. 2, pp. 1-13, 1970.

- [199] Schmitz K.S., *Physical Chemistry: Concepts and Theory*, Amsterdam: Elsevier, 2016.
- [200] Lang P.F., "Fermi energy, metals and the drift velocity of electrons," *Chemical Physics Letters*, vol. 770, pp. 138447-138452, 2021.
- [201] Arias T., Payne M.C. and Joannopoulos J.D., "Ab initio molecular dynamics: Analytically continued energy functionals and insights into iterative solutions," *Physical Review Letters*, vol. 69, pp. 1077-1080, 1992.
- [202] Alfe D., "Ab initio molecular dynamics, a simple algorithm for charge extrapolation," *Computer Physics Communications*, vol. 118, pp. 31-33, 1999.
- [203] Marx D. and Hutter J., "Ab initio molecular dynamics: Theory and implementation," *Modern Methods and Algorithms of Quantum Chemistry*, vol. 1, pp. 301-449, 2000.
- [204] Hartke B. and Carter E.A., "Spin eigenstate-dependent Hartree-Fock molecular dynamics," *Chemical Physics Letters*, vol. 189, pp. 358-362, 1992.
- [205] Schlegel H.B., "Ab initio molecular dynamics with Born-Oppenheimer and extended Lagrangian methods using atom centred basis functions," *Bulletin of the Korean Chemical Society*, vol. 24, no. 6, pp. 1-6, 2003.

- [206] Holender J.M., "Molecular-dynamics studies of the thermal properties of the solid and liquid FCC metals Ag, Au, Cu and Ni using many-body interactions," *Physical Review B*, vol. 41, pp. 8054-8061, 1990.
- [207] Springborg M., *Density-functional methods in chemistry and materials science*, New York: John Wiley & Sons, 1997.
- [208] "Classes of Materials," Chemistry LibreTexts, 18 June 2021. [Online]. Available: <https://chem.libretexts.org/@go/page/21777>. [Accessed 18 June 2021].
- [209] Doyle P.A. and Turner P.W., "Relativistic Hartree-Fock X-ray and electron scattering factors," *Acta Crystallographica*, vol. A24, pp. 390-397, 1968.
- [210] Rietveld H.M., "A profile refinement method for nuclear and magnetic structures," *Journal of Applied Crystallography*, vol. 2, pp. 65-71, 1968.
- [211] Mitchell S., Michels N., Kunze K. and Pérez-Ramirez J., "Visualization of hierarchically structured zeolite bodies from macro to nano length scales," *Nature Chemistry*, vol. 4, pp. 825-831, 2012.
- [212] Hassan M.F. and Sheng C.K., "X-ray diffraction characterization of crystallinity and phase composition in manganese oxides composite prepared by molten salts," *Scientific Research Journal*, vol. 16, pp. 13-27, 2019.
- [213] Speakman S.A., "Introduction to X-Ray Diffraction Data Analysis," Massachusetts Institute of Technology (MIT), Massachusetts.

- [214] "PHYISCS LibreTexts," 20 February 2022. [Online]. Available: [https://phys.libretexts.org/Bookshelves/College_Physics/Book%3A_College_Physics_\(OpenStax\)/31%3A_Radioactivity_and_Nuclear_Physics/31.06%3A_Binding_Energy](https://phys.libretexts.org/Bookshelves/College_Physics/Book%3A_College_Physics_(OpenStax)/31%3A_Radioactivity_and_Nuclear_Physics/31.06%3A_Binding_Energy). [Accessed 03 03 2022].
- [215] Parra R.D. and Farrell H.H., "Binding Energy of Metal Oxide Nanoparticles," *Journal of Physical Chemistry C*, vol. 113, pp. 4786-4791, 2009.
- [216] Vanithakumari S.C. and Nanda K.K., "Phenomenological predictions of cohesive energy and structural transition of nanoparticles," *Journal of Physical Chemistry B*, vol. 110, no. 2, pp. 1033-1037, 2006.
- [217] Aravindh S.A., "Studies of FemIrn ($2 < m+n < 4$) nano clusters using Density Functional Theory Techniques," *Applied Nanoscience*, vol. 4, pp. 593-600, 2014.
- [218] Wang J., Wang G. and Zhao J., "Density-functional study of Aun ($n=2-20$) clusters: Lowest energy structures and electronic properties," *Physical Review B*, vol. 66, pp. 1-6, 2002.
- [219] Bellaiche L. and Vanderbilt D., "Virtual crystal approximation revisited: Application to dielectric and piezoelectric properties of perovskites," *Physical Review B*, vol. 61, no. 12, pp. 7877-7882, 2000.
- [220] Wilson D.J., Winkler B., Juarez-Arellano E.A., Friedrich A., Knorr K., Pickard C.J. and Milman V., "Virtual crystal approximation study of

- nitridosilicates and oxonitridoaluminosilicates," *Journal of Physics and Chemistry of Solids*, vol. 69, pp. 1861-1868, 2008.
- [221] Ramer N.J. and Rappe A.M., "Virtual-crystal approximation that works: Locating a compositional phase boundary in $\text{Pb}(\text{Zr}_{1-x}\text{Ti}_x)\text{O}_3$," *Physical Review B*, vol. 62, no. 2, pp. 743-746, 2000.
- [222] Islam M.S. and Davies R.A., "Atomistic study of dopant site-selectivity and defect association in the lanthanum gallate perovskite," *Journal of Materials Chemistry*, vol. 14, pp. 86-93, 2004.
- [223] Kim B., Park I., Yoon G., Kim J.S., Kim H. and Kang K., "Atomistic Investigation of Doping Effects on Electrocatalytic Properties of Cobalt Oxides for Water Oxidation," *Advanced Science*, vol. 5, pp. 1-8, 2018.
- [224] Hirayama N., Iida T., Sakamoto M., Nishio K., and Hamada N., "Substitutional and interstitial impurity p-type doping of thermoelectric Mg_2Si : a theoretical study.," *Science and Technology of Advanced Materials*, vol. 20, pp. 160-172, 2019.
- [225] Khan S., Ruwer T.L., Khan N., Koche A., Lodge R.S., Coelho Junior H., Sommer R.L. Santos M.J.L., Malfatti C.F., Bergmann C.P. and Fernandes J.A., "Revealing the true impact of interstitial and substitutional nitrogen doping in TiO_2 on photoelectrochemical applications," *Journal of Materials Chemistry A*, vol. 9, pp. 12214-12224, 2021.

- [226] Wang Y.Z., Bevilhon E., Chesnaud A., Geneste G. and Dezanneau G., "Atomistic simulation of pure and doped BaSnO₃," *Journal of Physical Chemistry C*, vol. 113, pp. 20486-20492, 2009.
- [227] Cipriano L.A., Liberto G., Tosoni S. and Pacchioni G., "Quantum confinement in group III–V semiconductor 2D nanostructures," *Nanoscale*, vol. 12, pp. 17494-17501, 2020.
- [228] Emberly E.G. and Kircenow G., "Theoretical study of electrical conduction through a molecule connected to metallic nanocontacts," *Physical Review B*, vol. 58, no. 16, pp. 10911-10920, 1998.
- [229] Menendez M., Pendas A.M., Braida B. and Savin A., "A view of covalent and ionic bonding from maximum probability domains," *Computational and Theoretical Chemistry*, vol. 1053, pp. 142-149, 2015.
- [230] Puiu T., "ZME SCIENCE," 28 January 2021. [Online]. Available: <https://www.zmescience.com/other/feature-post/difference-ionic-covalent-bonds-0423/>. [Accessed 10 January 2022].
- [231] Hirshfeld F.L., "Bonded-Atom fragments for describing molecular charge densities," *Theoretica Chimica Acta*, vol. 44, pp. 129-138, 1977.
- [232] Sanchez-Portal D., Artacho E. and Soler J.M., "Projection of plane-wave calculations into atomic orbitals," *Solid State Communications*, vol. 95, no. 10, pp. 685-690, 1995.

- [233] Segall M.D., Shah R., Pickard C.J. and Payne M.C., "Population analysis of plane-wave electronic structure calculations of bulk materials," *Physical Review B*, vol. 54, no. 23, pp. 16317-16320, 1996.
- [234] Voityuk A. A., Stasyuk A. J. and Vyboishchikov S. F., "A simple model for calculating atomic charges in molecules," *Physical Chemistry Chemical Physics*, vol. 2018, pp. 23328-23337, 2018.
- [235] Woodley S.M. and Walker A.M., "New software for finding transition states by probing accessible, or ergodic, regions," *Molecular Simulations*, vol. 33, pp. 1229-1231, 2007.
- [236] "Material studio online help - CASTEP," 17 October 2019. [Online]. Available:
<http://www.tcm.phy.cam.ac.uk/castep/documentation/WebHelp/CASTEP.html>. [Accessed 25 February 2022].
- [237] "Material studio Online help – Reflex," [Online]. Available:
[file:///C:/Program%20Files%20\(x86\)/Accelrys/Materials%20Studio%207.0/share/doc/MaterialsStudio.htm#modules/reflex/abtreflex.htm%3FTocPath%3DReflex%7C_____0](file:///C:/Program%20Files%20(x86)/Accelrys/Materials%20Studio%207.0/share/doc/MaterialsStudio.htm#modules/reflex/abtreflex.htm%3FTocPath%3DReflex%7C_____0) . [Accessed 27 08 2016].
- [238] Delley B., "DMol, a Standard Tool for Density Functional Calculations: Review and advances," *Theoretical and Computational Chemistry*, vol. 2, pp. 221-254, 1995.

- [239] Perdew J.P. and Wang Y., "Accurate and simple analytic representation of the electron-gas correlation energy," *Physical Review B*, vol. 45, no. 23, pp. 13244-13250, 1992.
- [240] Pakiari A.H. and Salarhaji M., "Introducing nano-particle-type properties of Ti(n), (n=2-6) clusters," *Journal of Molecular Graphics and Modelling*, vol. 85, pp. 294-303, 2018.
- [241] Zheng D., Sun S., Fan W., Yu H., Fan C., Cao G., Yin Z. and Song X., "One-step preparation of single-crystalline β -MnO₂ nanotubes," *Journal Physical Chemistry B*, vol. 109, pp. 16439-16443, 2005.
- [242] Smith K.D. and Jenkins R., "The powder diffraction file: Past, present, and future," *Journal of Research of the National Institute of Standards and Technology*, vol. 101, no. 3, p. 259, 1996.
- [243] McMurdie H.F. and Golovato E., "Study of the Modifications of Manganese Dioxide," *Journal of Research of the National Bureau of Standards*, vol. 41, pp. 589-600, 1948.
- [244] Augustin M., Fenske D., Bardenhagen I., Westphal A., Knipper M., Plaggenborg T., Kolny-Olesiak J. and Parisi J., "Manganese oxide phases and morphologies: A study on calcination temperature and atmospheric dependence," *Beilstein Journal of Nanotechnology*, vol. 6, pp. 47-59, 2015.

- [245] Van De Walle C.G. and Neugebauer J., "First-principles calculations for defects and impurities: Applications to III-nitrides," *Journal of Applied Physics*, vol. 95, p. 3851, 2004.
- [246] Winter M., "WebElements," The University of Sheffield, [Online]. Available: https://www.webelements.com/compounds/manganese/manganese_dioxide.html. [Accessed 30 March 2021].
- [247] Antoniammal P. and Arivuoli D., "Size and shape dependence on melting temperature of Gallium Nitride nanoparticles.," *Journal of Nanomaterials*, vol. 5, pp. 1-11, 2012.
- [248] Grundy A.N., Hallstedt B. and Gauckler L.J., "Assessment of the Mn-O System," *Journal of Phase Equilibria*, vol. 24, pp. 21-39, 2003.
- [249] Sun J. and Simon S.L., "The melting behavior of aluminum nanoparticles," *Thermochimica Acta*, vol. 463, no. 2, pp. 32-40, 2007.
- [250] Jildeh Z.B., Oberlander J., Kirchner P., Wagner P.H. and Schoning M.J., "Thermocatalytic behavior of manganese (IV) oxide as nanoporous material on the dissociation of a gas mixture containing hydrogen peroxide," *Nanomaterials*, vol. 8, p. 262, 2018.
- [251] Ding F., Rosen A. and Bolton K., "Molecular dynamics study of the catalyst particle size dependence on carbon nanotube growth," *Journal of Chemical Physics*, vol. 121, p. 2775, 2004.

- [252] Kasinathan D., Lee K. and Pickett W. , "On heavy carbon doping of MbB_2 ," *Physica C*, vol. 424, pp. 116-224, 2005.
- [253] Piela L., *Ideas of Quantum Chemistry*, Amsterdam: Elsevier, 2007.
- [254] Wales D.J. and Doye J.P.K., "Global optimization by Basin-Hopping and the lowest energy structures of leonard-Jones clusters containing up to 110 atoms," *Journal of Physical Chemistry*, vol. 101, no. 28, pp. 5111-5116, 1997.
- [255] Zayed A.O.H., Mohammad N.D. and Zain S.M., "Global structural optimization and growth mechanism of cobalt oxide nanoclusters by genetic algorithm with spin-polarized DFT," *Journal of Alloys and Compounds*, vol. 695, pp. 2513-2518, 2016.
- [256] Zhai H. and Wang L., "Probing the electronic structure and band gap evolution of Titanium Oxide Clusters $(TiO_2)_n$ - ($n = 1-10$) using photoelectron spectroscopy," *Journal of the American Chemical Society*, vol. 129, pp. 3022-3026, 2007.
- [257] Nayak S.K. and Jena P., "Equilibrium geometry, stability and magnetic propoerties of small MnO clusters," *Journal of the American Chemical Society*, vol. 121, pp. 644-652, 1999.
- [258] Zhang N., Cheng F., Liu J., Wang L., Long X., Liu X., Li F. and Chen J., "Rechargeable aqueous zinc-manganese dioxide batteries with high energy and power densities," *Nature Communications*, vol. 8, 2017.

- [259] OpenStax, "BCCampus: College Physics," [Online]. Available: <https://pressbooks.bccampus.ca/collegephysics/chapter/binding-energy/>. [Accessed 12 April 2022].
- [260] "Nuclear Binding Energy and Mass Defect," [Online]. Available: <https://courses.lumenlearning.com/introchem/chapter/nuclear-binding-energy-and-mass-defect/>. [Accessed 12 April 2022].
- [261] Chen L. and Ruigang Z., "Manganese Dioxide As Rechargeable Magnesium Battery Cathode," *Frontiers in Energy Research*, vol. 5, 2017.
- [262] Ouassim G., Jean-Louis P., Fraisse B. and Favier F., "Structural in Situ Study of the Thermal Behavior of Manganese Dioxide Materials: Toward Selected Electrode Materials for Supercapacitors," *ACS applied materials and interfaces*, vol. 2, no. 12, pp. 3493-3505, 2010.
- [263] McLeod L.K., Spikes G.H., Kashtiban R.Z., Walker M., Chadwick A.V., Sharman J.D.B. and Richard I.W., "Structures of mixed manganese ruthenium oxides (Mn_{1-x}Ru_x)O₂ crystallised under acidic hydrothermal conditions," *Royal Society of Chemistry*, vol. 49, pp. 2661-2270, 2020.
- [264] Ijadpanah-Saravy H., Safari M., Khodadani-Darban A. and Rezaei A. , "Synthesis of titanium dioxide nanoparticles for photocatalytic degradation of cyanide in wastewater," *Analytical Letters*, vol. 47, pp. 1772-1782, 2014.
- [265] Kandiel T.A., Robben L., Alkaim A. and Bahnemann D., "Brookite versus anatase TiO₂ photocatalysts: Phase transformations and photocatalytic

- activities," *Photochemical and Photobiological Sciences*, vol. 12, pp. 602-609, 2013.
- [266] Sherin J.S., Thomas J.K. and Manoj S., "Facile Synthesis and Characterization of Pyrolusite, β -MnO₂, Nano Crystal with Magnetic Studies," *International Journal of Science and Engineering Applications*, vol. 4, no. 5, pp. 250-252, 2015.
- [267] Woodley S.M., "Atomistic and electronic structure of (X₂O₃)_n nanoclusters; n = 1 – 5, X = B, Al, Ga, In and Tl," *Proceedings of the Royal Society A*, pp. 1-24, 2011.
- [268] Mishra S.K. and Ceder G., "Structural stability of lithium manganese oxides," *Physical Review B*, vol. 59, pp. 6120-6130, 1998.
- [269] Farrell H.H. and Parra R.D., "Oxide nanotube analogues: CuO nanobarrels," *Journal of Vacuum Science and Technology B*, vol. 29, no. 1, pp. 061806-1 - 061806-5, 2011.
- [270] Helmenstine A.M., "S P D F Orbitals and Angular Momentum Quantum Numbers," ThoughtCo., 07 May 2019. [Online]. Available: <https://www.thoughtco.com/angular-momentum-quantum-numbers-606461>. [Accessed 21 April 2022].
- [271] Bader R.F.W. and Henneker W.H., "Molecular charge distributions and chemical Binding," *Journal of Chemical Physics*, vol. 46, pp. 3341-3349, 1967.

- [272] Migani A. and Illas F., "A systematic study of the structure and bonding of halogens on low-index transition metal surfaces," *Journal of Physical Chemistry B*, vol. 110, pp. 11894-11906, 2006.
- [273] Lethole N.L., Ngoepe P.E. and Chauke H.R., "First-principles study: Effect of lithium and sodium intercalation in transition metal phosphates, MPO_4 (M: Mn, Fe, Co)," *Computational Condensed Matter*, pp. e00437 1 - 11, 2020.
- [274] Ogasawara T., Debart A., Holzapfel M., Novak P. and Bruce P.G., "Rechargeable Li_2O_2 Electrode for Lithium Batteries," *Journal of the American Chemical Society*, vol. 131, pp. 1390-1393, 2006.
- [275] Mortazavi, B., Rahaman, O., Ahzi, S., and Rabczuk, T., "Flat borophene films as anode materials for Mg, Na or Li-ion batteries with ultra high capacities: A first-principles study," *Applied Materials Today*, vol. 8, pp. 60-67, 2017.
- [276] Wu X., Kang F., Duan W. and Li J., "Density functional theory calculations: A powerful tool to simulate and design high-performance energy storage and conversion materials," *Progress in Natural Science: Materials International*, vol. 29, pp. 247-255, 2019.
- [277] Zhou F., Cococcioni M., Kang K. and Ceder G., "The Li Intercalation Potential of $LiMPO_4$ and $LiMSiO_4$ Olivines with M = Fe, Mn, Co, Ni," *Electrochemistry Communications*, vol. 6, pp. 1144-1148, 2004.

- [278] Smith K. and Wang C.Y., "Power and Thermal Characterization of a Lithium-ion Battery Pack for Hybrid-Electric Vehicles," *Journal of Power Sources*, vol. 160, pp. 662-673, 2006.
- [279] Lethole N.L., Chauke H.R. and Ngoepe P.E., Computer Modelling Studies of MPO_4 , $LiMPO_4$ and $NaMPO_4$ (M: Fe, Co, Mn) Polymorphs, Polokwane: PhD Thesis from University of Limpopo, 2016.
- [280] Shan X., Guo F., Page K., Neufeind J.C., Ravel B., Abekoon A.M.M., Kwon G., Olds D., Su D. and Teng X., "Framework Doping of Ni Enhances Pseudocapacitive Na-Ion Storage of (Ni)MnO₂ Layered Birnessite," *Chemistry of Materials*, vol. 31, pp. 8774-8786, 2019.

Appendices

Appendix A

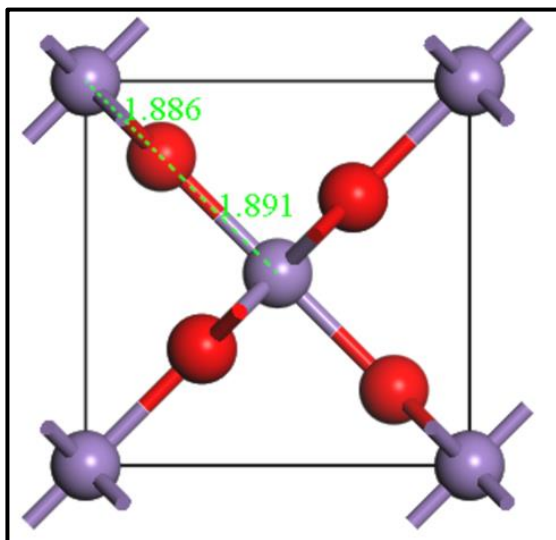


Figure 54: Original Bulk structure of β -MnO₂

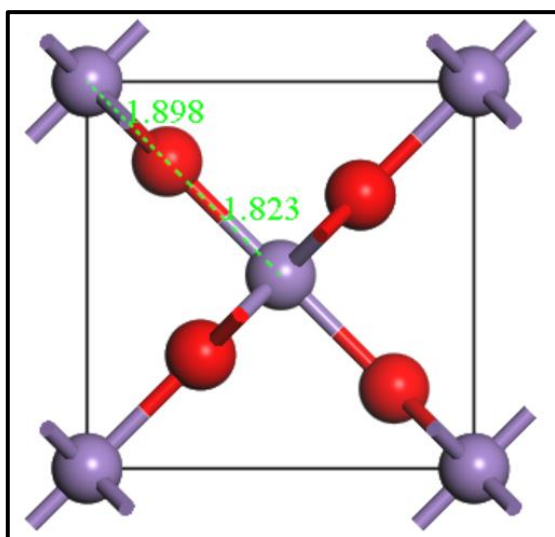
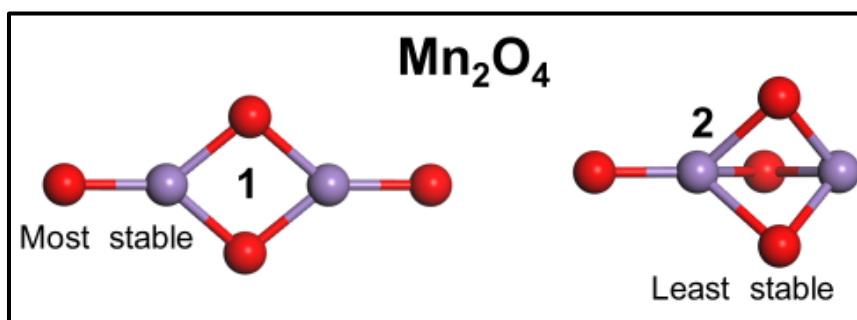
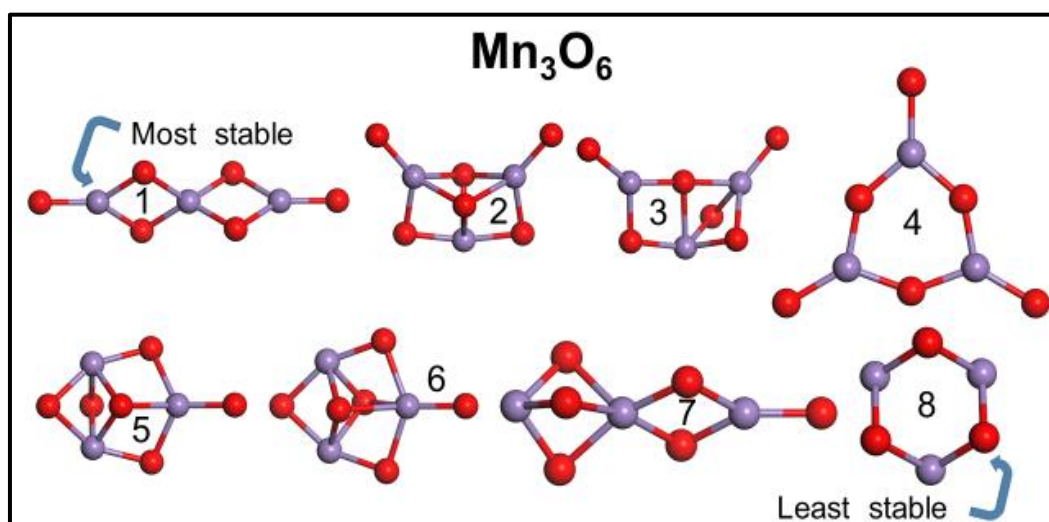


Figure 55: β -MnO₂ bulk structure after optimisation to the ground state

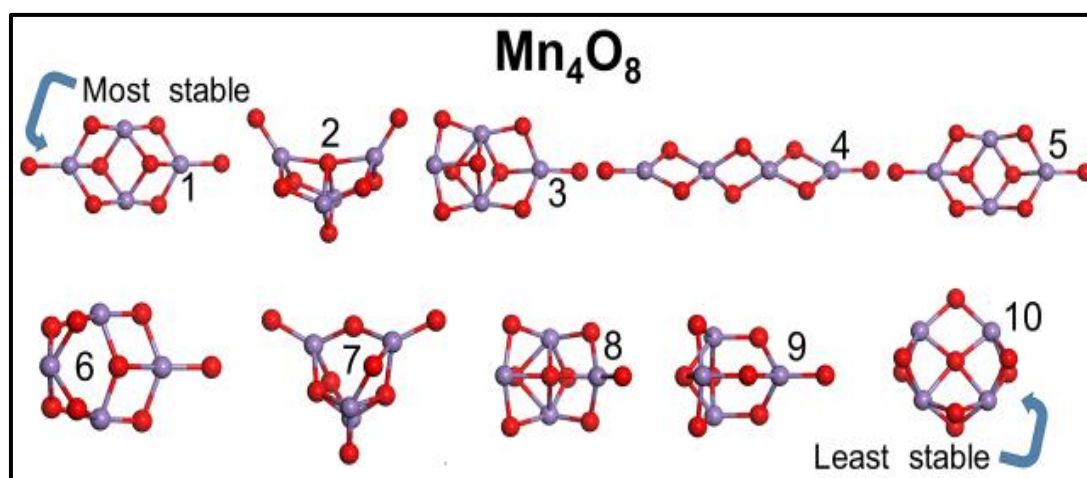
Appendix B1-1: Mn_2O_4



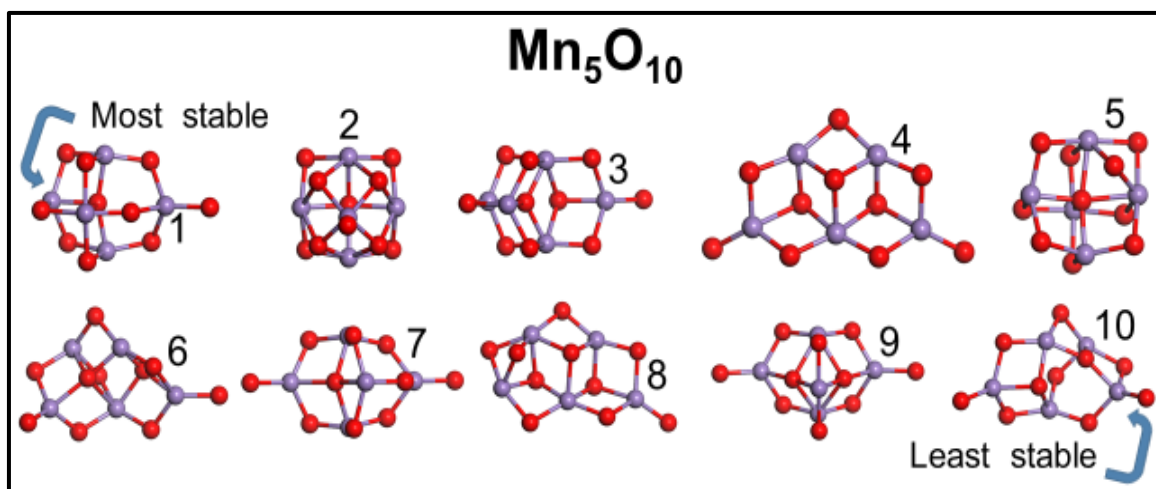
Appendix B1-2: Mn_3O_6



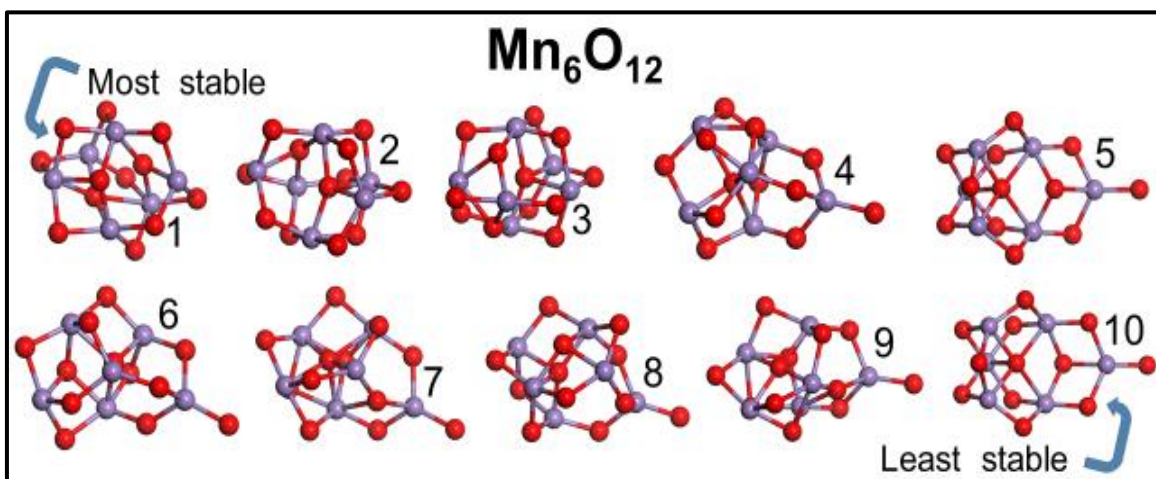
Appendix B1-3: Mn_4O_8



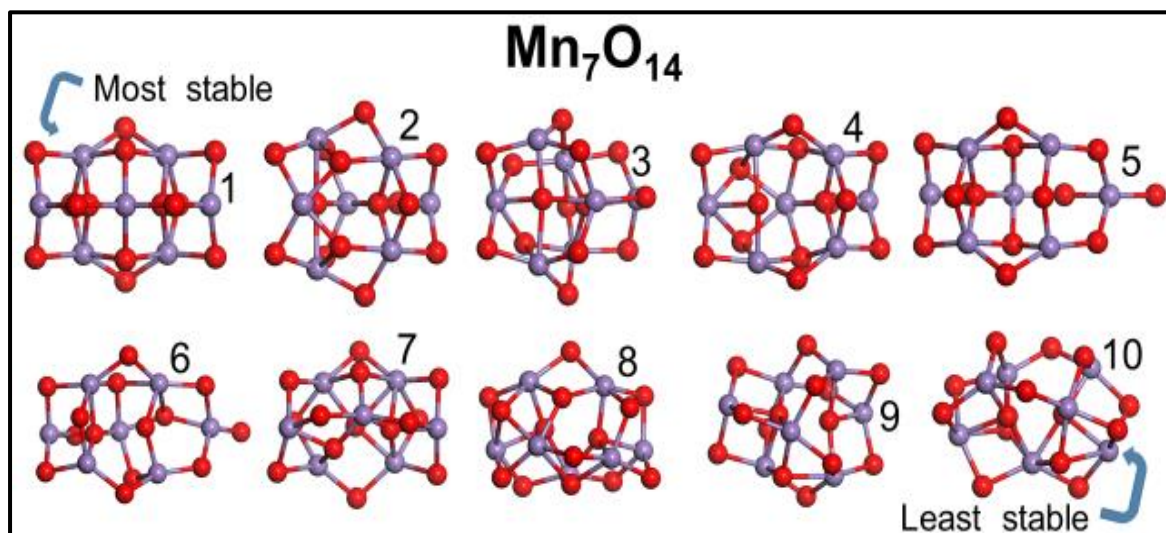
Appendix B1-4: Mn_5O_{10}



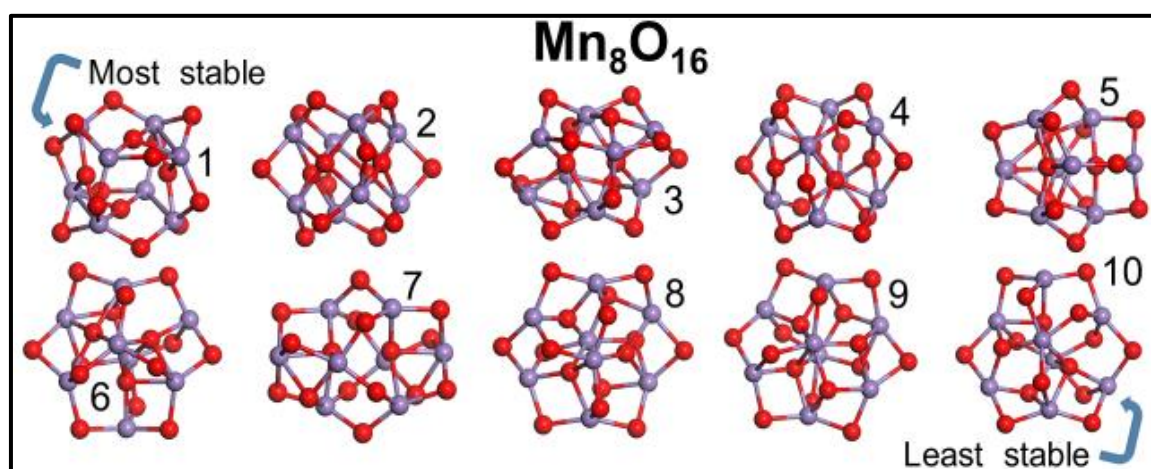
Appendix B1-5: Mn_6O_{12}



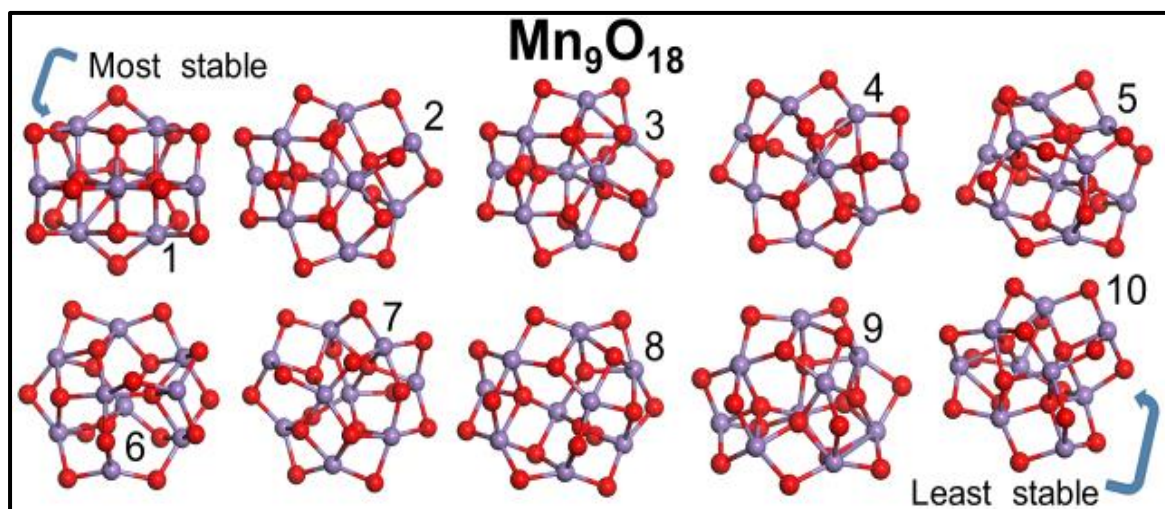
Appendix B1-6: Mn_7O_{14}



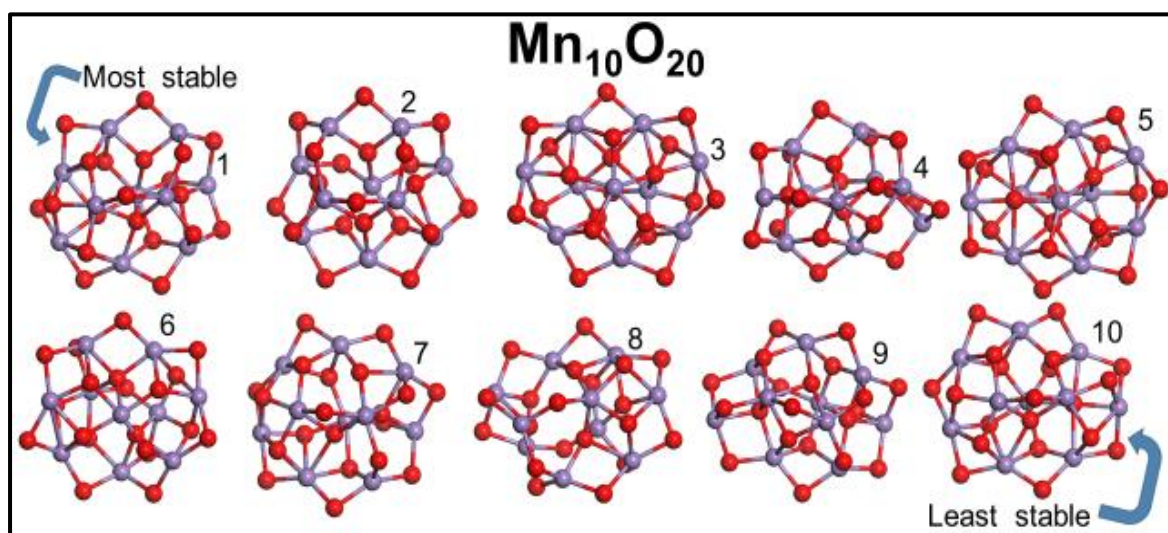
Appendix B1-7: Mn_8O_{16}



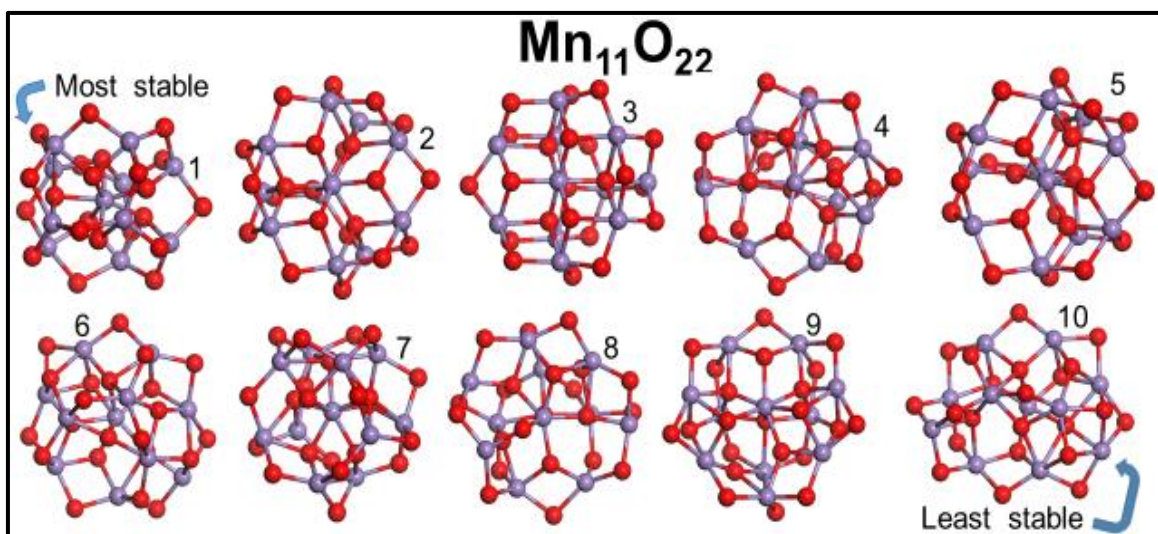
Appendix B1-8: Mn_9O_{18}



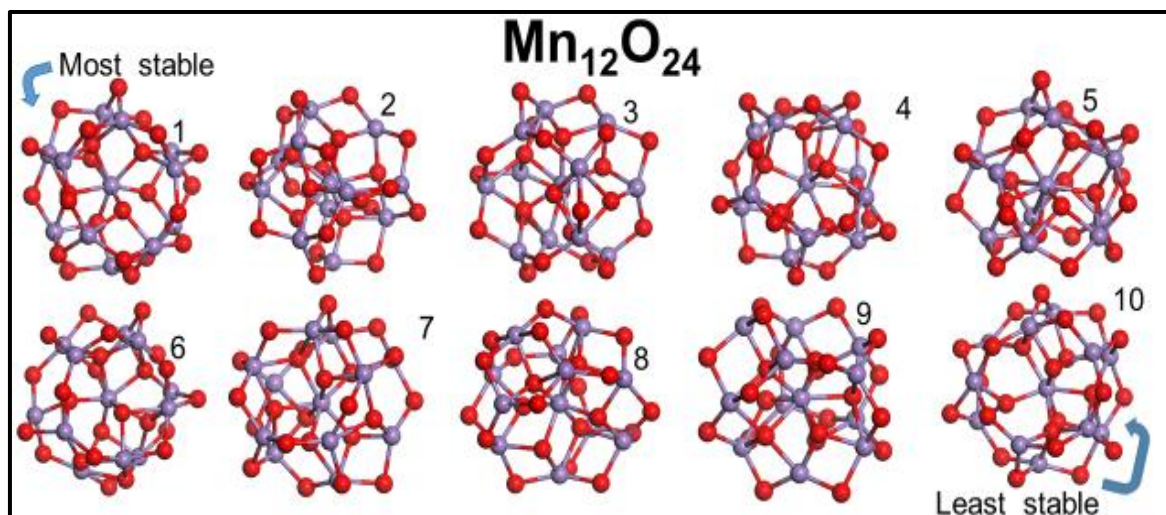
Appendix B1-9: $\text{Mn}_{10}\text{O}_{20}$



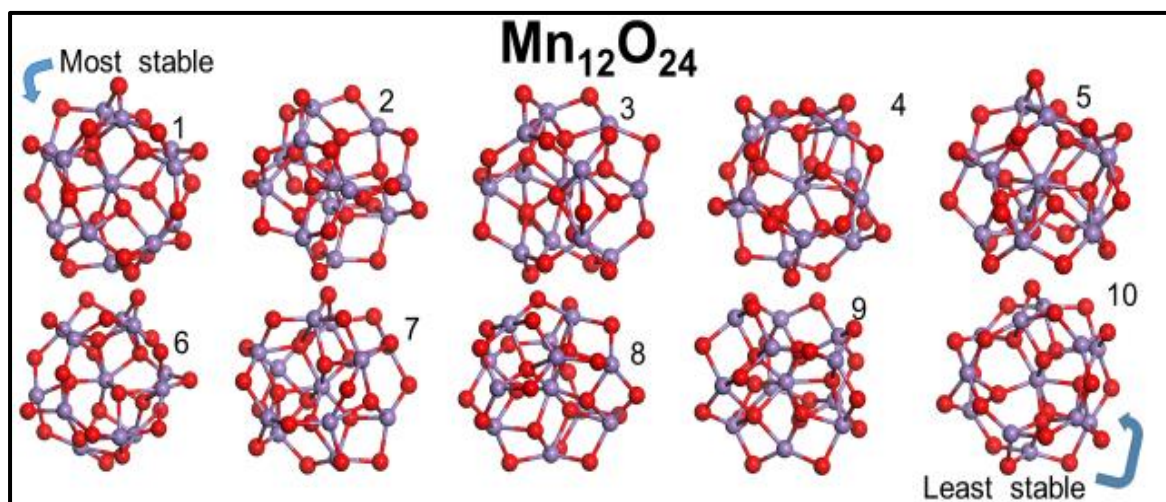
Appendix B1-10: $Mn_{11}O_{22}$



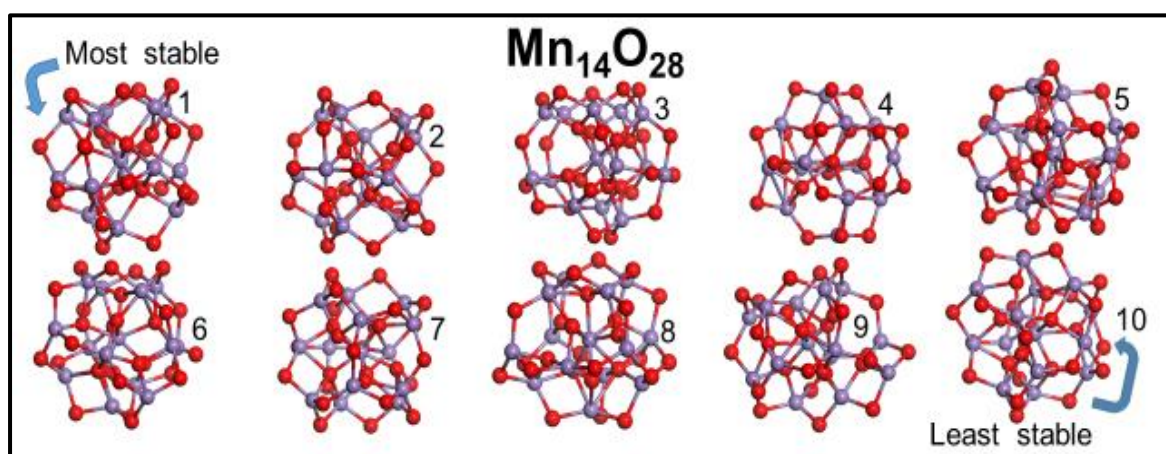
Appendix B1-11: $Mn_{12}O_{24}$



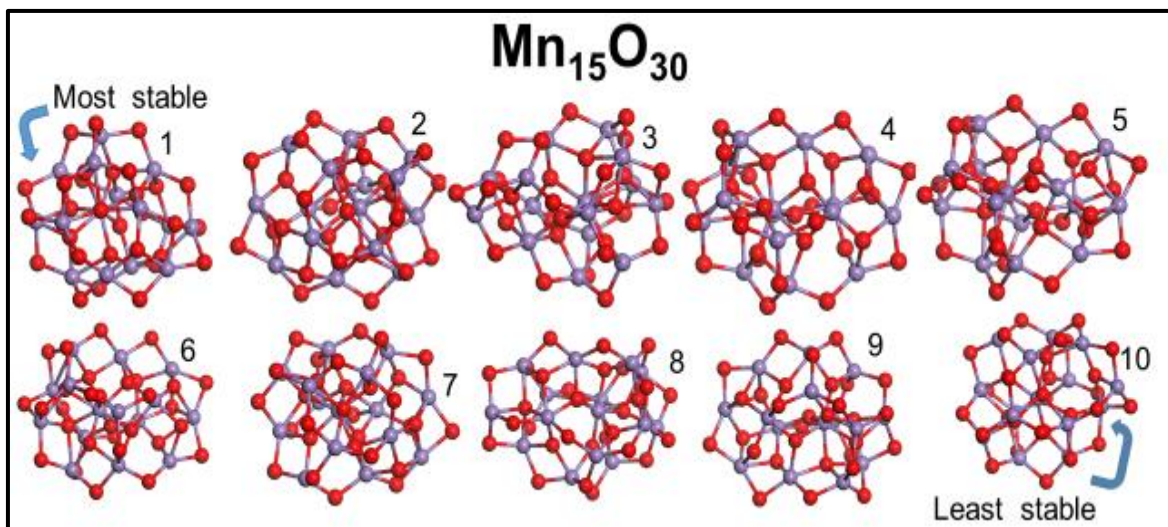
Appendix B1-12: $\text{Mn}_{13}\text{O}_{26}$



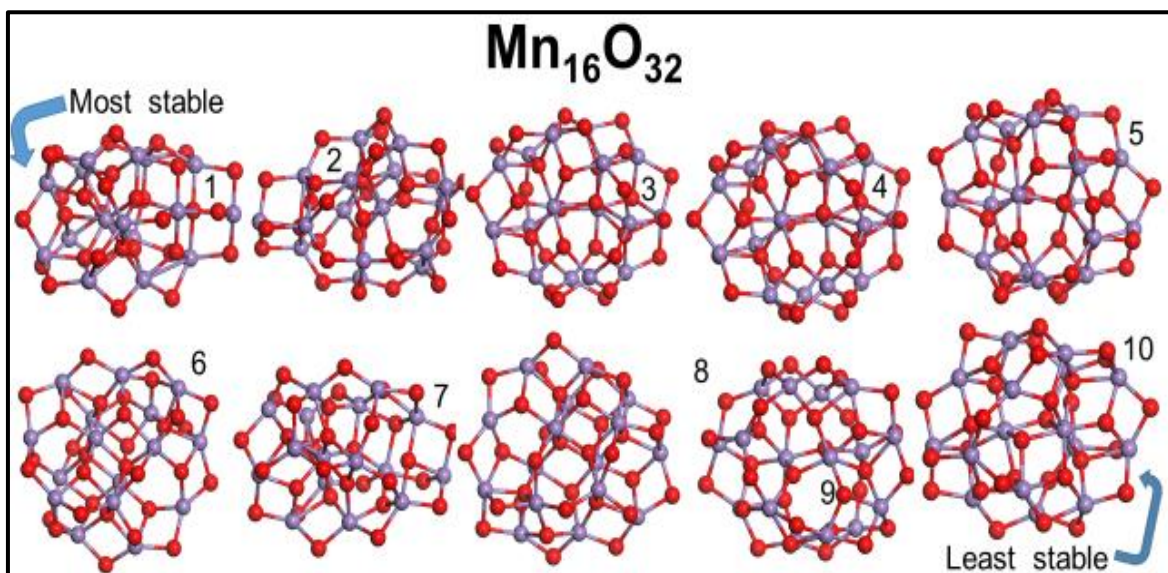
Appendix B1-13: $\text{Mn}_{14}\text{O}_{28}$



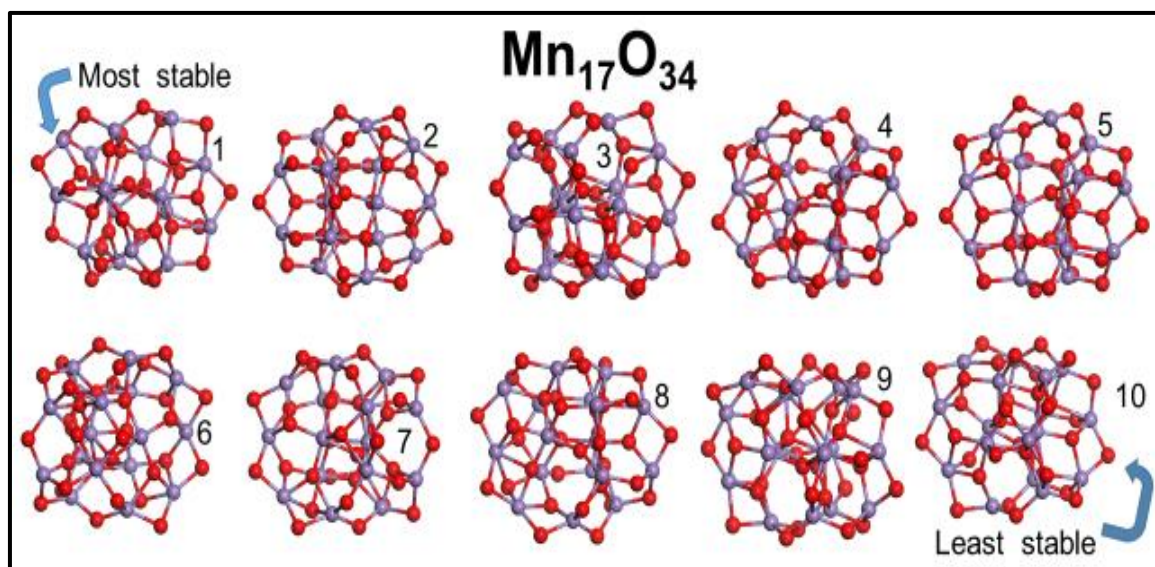
Appendix B1-14: $\text{Mn}_{15}\text{O}_{30}$



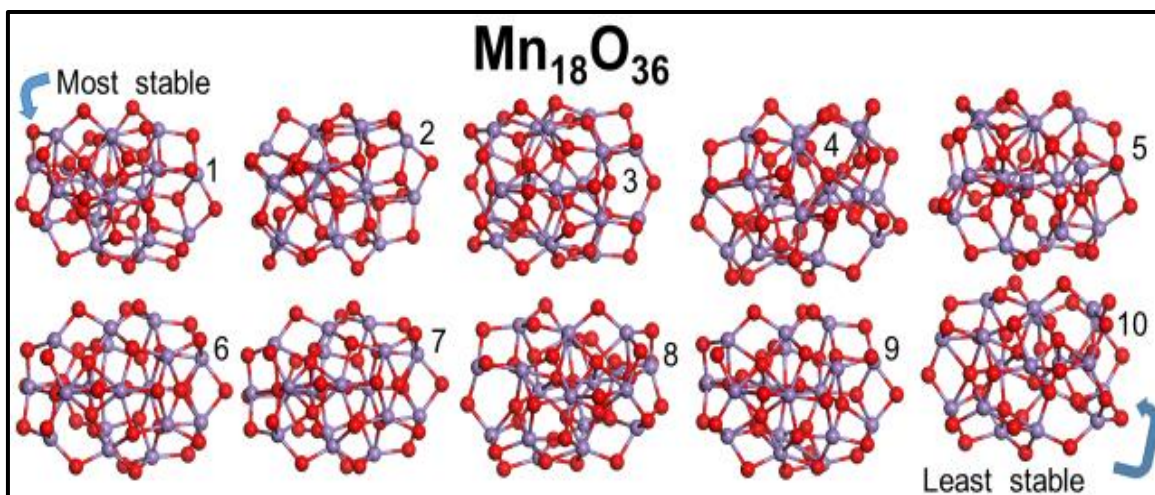
Appendix B1-15: $\text{Mn}_{16}\text{O}_{32}$



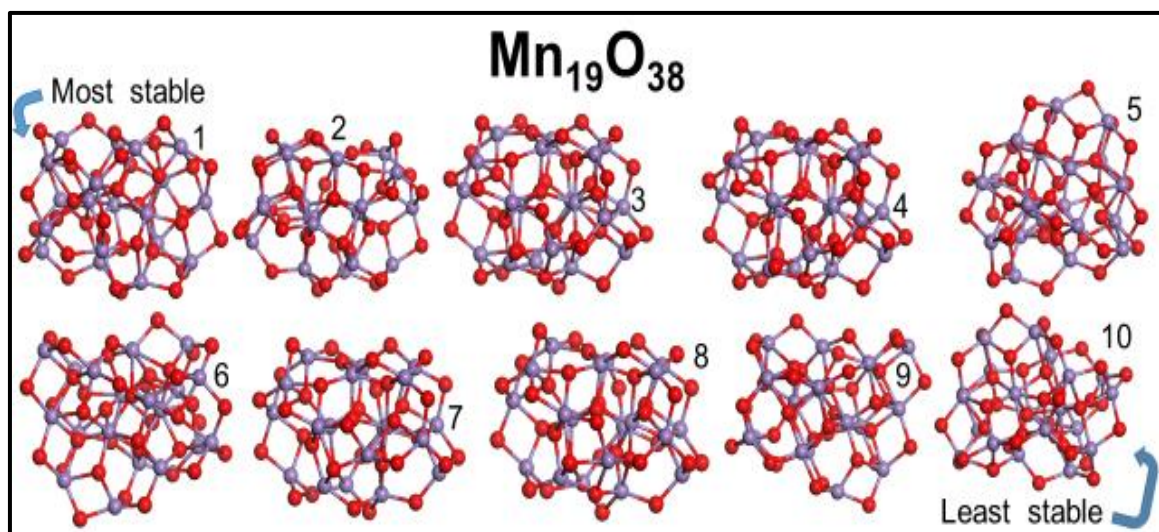
Appendix B1-16: $Mn_{17}O_{34}$



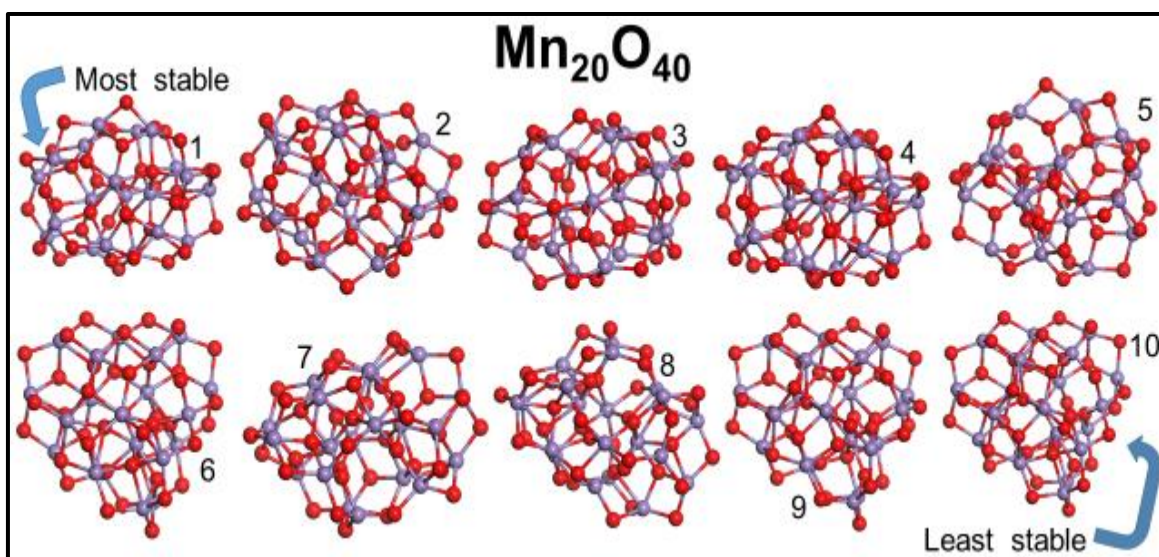
Appendix B1-17: $Mn_{18}O_{36}$



Appendix B1-18: $\text{Mn}_{19}\text{O}_{38}$



Appendix B1-19: $\text{Mn}_{20}\text{O}_{40}$



```

[masoga@sebata5 ~]$ ls
fhi-aims.160328_2  klmc  lustre  n20
[masoga@sebata5 ~]$ qstat
Job id          Name          User          Time Use S Queue
-----
5431.sebata5    MS_BLCBL      biovia        13382:54 R workq
5852.sebata5    MS_ZJBPW      biovia        00:30:11 R workq
6085.sebata5    klmc-n19      masoga        1199:22: R workq
6086.sebata5    klmc-n20      masoga        1200:34: R workq
6919.sebata5    MS_2YJNV      biovia        386:52:1 R workq
6920.sebata5    MS_2YVPH      biovia        386:18:4 R workq
6922.sebata5    MS_2YQQU      biovia        385:37:5 R workq
6923.sebata5    MS_2YGS7      biovia        385:27:1 R workq
7299.sebata5    300K_AGAIN    mehlope       36:40:37 R workq
[masoga@sebata5 ~]$

```

Screen capture image showing the duration of a calculation that was ongoing at the time, of a Genetic Algorithm sequential calculation performed by KLMC to generate the most stable nanoclusters of the largest size in this study; n19 and n20. The time already taken during this calculation was already at 1200 hours and still ongoing which is equivalent to 50 days and counting.

Appendix C: Presentations, awards and publications

Local/National Conference Presentations

1. Masoga P.W., Ngoepe P.E. and Maphanga R.R. “Evolutionary algorithm simulation study of MnO₂ nanoclusters”. The South African Institute of Physics Annual Conference (SAIP2015). Boardwalk Convention Centre, Port Elizabeth, Nelson Mandela Bay, South Africa. 29 June – 03 July 2015. – Oral
2. Masoga P.W., Ngoepe P.E. and Maphanga R.R. “Computer simulation study of MnO₂ nanoclusters for use in Lithium-ion batteries”. Centre for High Performance Computing (CHPC) National Meeting. CSIR International Convention Centre, Pretoria, South Africa. 30 November – 04 December 2015. – Poster
3. Masoga P.W., Maphanga R.R. and Ngoepe P.E. “Structural prediction of β -MnO₂ nanoclusters using global search techniques”. The South African Institute of Physics Annual Conference (SAIP2016), University of Cape Town, South Africa. 4 – 8 July 2016. – Poster
4. Masoga P.W., Ngoepe P.E. and Chauke H.R. “Evolutionary algorithm simulation study of Manganese Dioxide Nanoclusters.” Faculty of Science and Agriculture Annual Research Day. Bolivia Lodge, Polokwane, South Africa. 20 – 21 September 2018. – Oral
5. Masoga P.W., Lazauskas T., Sokol A.A., Woodley S.M., Catlow C.R.A., Ngoepe P.E. and Chauke H.R. “Generation of β -MnO₂ nanoclusters using global search techniques”. CHPC National Conference, Century City Convention Centre, Cape Town, South Africa. 02 – 06 December 2018. – Poster

International Conference Presentations

1. Masoga P.W., Ngoepe P.E. and Maphanga R.R. “Evolutionary algorithm simulation study of MnO₂ nanoclusters”. International Symposium on Macro- and Supramolecular Architectures and Materials. Emperors Palace Hotel, Johannesburg, South Africa. 23 – 27 November 2014. – Poster
2. Masoga P.W., Ngoepe P.E., Maphanga R.R. and Chauke H.R. “Structural prediction and electronic properties of β -MnO₂ nanoclusters”. Hands-on Workshop, Density-Functional Theory and Beyond. Humboldt University, Berlin, Germany. 31 July to 11 August 2017. – Oral and Poster
3. Masoga P.W., Maphanga R.R., Ngoepe P.E. and Chauke H.R. “Density functional theory studies of β -MnO₂ nanoclusters”. CCP5 DL Software Training. Daresbury, United Kingdom. 19 – 22 February 2018. – Oral and Poster
4. Masoga P.W., Ngoepe P.E. and Chauke H.R. “The use of β -MnO₂ nanoclusters for enhancement of lithium-ion rechargeable batteries”. NANOAFRICA Conference. Cape Town, Somerset West, Lord Charles Hotel, 26 – 29 October 2022. – Oral
5. Masoga P.W., Ngoepe P.E. and Chauke H.R. “Structural and electronic properties of β -MnO₂ nanoclusters”. RAPDASA-RobMech-PRASA-CoSAAMI. Cape Town, Somerset West, Lord Charles Hotel, 08 – 11 November 2022. – Oral

Publications

1. Masoga P.W., Ngoepe P.E. and Maphanga R.R. “Evolutionary algorithm simulation study of β -MnO₂ nanoclusters”. ISBN: 978-0-620-77094-1, page 31 – 36. Conference proceedings of SAIP2016.
https://events.saip.org.za/event/86/attachments/2181/2898/SAIP2016_31.pdf
2. Masoga P.W., Ngoepe P.E. and Chauke H.R. “Structural and electronic properties of β -MnO₂ nanoclusters”. Conference proceedings of RAPDASA-RobMech-PRASA-CoSAAMI. MATEC Web of Conferences 370, 09004 (2022)
<https://doi.org/10.1051/mateconf/202237009004>
3. Masoga P.W., Ngoepe P.E. and Chauke H.R. “The generation and stability of manganese dioxide nanoclusters.” Manuscript ready for publication
4. Masoga P.W., Ngoepe P.E. and Chauke H.R. “Computational simulation study investigating the effect of doping on the structural stability of Manganese dioxide nanoclusters.” Manuscript ready for publication

Achievements

1. Judge: Eskom EXPO for young Scientists.
University of Limpopo, Mankweng, Polokwane, South Africa. 14 August 2014.
2. Laboratory assistant and supervisor
Physics first year and second year laboratories. 2010 – 2018 University of Limpopo, Mankweng, Polokwane, South Africa
3. Lecturer: Physical Science Education. Department of Mathematics, Science and Technology Education. School of Education. Faculty of Humanities. University of Limpopo.
4. School Academic Development Practitioner (CAE Baditi Mentor Supervisor–SADP: KINDI) 2020 – Present. University of Limpopo. Mankweng, Polokwane, South Africa
5. Certified Professional Physicist – Mr. P.W. Masoga (Pr.Phys - 2015060) (South African Institute of Physics, 2021-2026).
6. First place oral presentations in the Faculty of Science Annual research day in 2018 and first place oral presentations at the RAPDASA-COSAAMI in 2022.

Awards

Best Poster Presentations

1. Masoga P.W., Ngoepe P.E. and Maphanga R.R. “Evolutionary algorithm simulation study of MnO₂ nanoclusters”. The South African Institute of Physics Annual Conference (SAIP2015). Boardwalk Convention Centre, Port Elizabeth, Nelson Mandela Bay, South Africa. 29 June – 3 July 2015.
2. Morukuladi M.T., Masoga P.W., Ngoepe P.E. and Maphanga R.R. “Computational Modelling of graphene mediated sodium-air batteries.” Faculty of Science and Agriculture Annual Research Day. Bolivia Lodge, Polokwane, South Africa. 19 – 20 October 2017.

1st Place Oral Presentations

1. Masoga P.W., Ngoepe P.E. and Chauke H.R. “Evolutionary algorithm simulation study of Manganese Dioxide Nanoclusters.” Faculty of Science and Agriculture Annual Research Day. Bolivia Lodge, Polokwane, South Africa. 20 – 21 September 2018.
2. Masoga P.W., Ngoepe P.E. and Chauke H.R. “Structural and electronic properties of β -MnO₂ nanoclusters”. RAPDASA-RobMech-PRASA-CoSAAMI annual conference. Lord Charles Hotel, Somerset West, Cape Town, South Africa. 8 – 11 November 2022.
3. Mamabolo P.M. and Masoga P.W. “ Developing grade 12 learners’ conceptual understanding of chemical equilibrium using problem-based learning”. SAIP Annual Conference, 3 – 7 July 2023, Richards Bay.